MAGNETIC PROPERTIES OF NANOCRYSTALLINE Fe-(Al,Cr)-Co-Si ALLOYS PREPARED BY MECHANICAL ALLOYING PROCESS

A thesis submitted

by

Shyni P C

to

Indian Institute of Technology Guwahati

in

Partial fulfillment of the requirement for the award of the degree of
Doctor of Philosophy in Physics

Department of Physics
Indian Institute of Technology Guwahati
Guwahati 781 039, Assam, India
December 2014

MAGNETIC PROPERTIES OF NANOCRYSTALLINE Fe-(Al,Cr)-Co-Si ALLOYS PREPARED BY MECHANICAL ALLOYING PROCESS

A thesis submitted

by

Shyni P C

to

Indian Institute of Technology Guwahati

in

Partial fulfillment of the requirement for the award of the degree of
Doctor of Philosophy in Physics

Department of Physics
Indian Institute of Technology Guwahati
Guwahati 781 039, Assam, India
December 2014

Statement

The work contained in the thesis entitled “Magnetic properties of nanocrystalline Fe-(Al,Cr)-Co-Si alloys prepared by mechanical alloying process” has been carried out by me under the supervision of Dr. Perumal Alagarsamy at the Department of Physics, Indian Institute of Technology Guwahati. This work has not been submitted elsewhere for the award of any degree.

December 2014

(Shyni P C)
Roll No: 09612118
Department of Physics
Indian Institute of Technology Guwahati
Guwahati – 781039
India.

Certificate

It is certified that the work contained in the thesis entitled “Magnetic properties of nanocrystalline Fe-(Al,Cr)-Co-Si alloys prepared by mechanical alloying process” submitted by Shyni P C, a Ph. D. student of the Department of Physics, Indian Institute of Technology Guwahati for the award of degree of Doctor of Philosophy has been carried out under the supervision of Dr. Perumal Alagarsamy. This work has not been submitted elsewhere for the award of any degree.

December 2014

(Dr. Perumal Alagarsamy)
Professor
Department of Physics
Indian Institute of Technology Guwahati
Guwahati – 781039
India.

Dedicated to my

beloved brother and parents

Acknowledgements

Pursuing a PhD is an enjoyable as well as a painful experience at the same time. It is just like climbing a big mountain, step by step, accompanied with hardships, bitterness, enthusiasm, trust, encouragement and with so many people's kind support. Though it will not be enough to express my gratitude in words to all those people who helped me, I would still like to give my heartfelt thanks to all of them.

First of all, I would like to express the deep sense of gratitude to my thesis supervisor Dr. Perumal Alagarsamy for his resourceful guidance, constructive criticisms and careful supervision throughout my research work. His continuous encouragements and intellectual discussions have been a driving force for me to excel in my work. I have learned a lot from him and his advice on research as well as on career has been priceless. I am grateful to my doctoral committee members, Prof. A. Srinivasan, Dr. Subhradip Ghosh and Dr. Vinayak Kulkarni for reviewing my research work regularly and providing valuable comments and suggestions for the improvement of my research work. I am thankful to Prof. S. Basu, HOD Department of Physics, and Prof. S. Ravi, the former HOD, Department of Physics for their immense support. I extend my whole hearted thanks to all the faculty members of Physics department who supported me in several ways during my research life in IIT Guwahati (IITG). I am thankful to IITG for providing me with financial assistantship during the research period.

I express my sincere thanks to Dr. Sidananda Sarma, scientific officer in the department of physics, for guiding me to handle various high precision instruments in the department of physics. Also, I thank Mr. Chandan Borgohain, Dr. Kula Kamal Senapati, Mr. Madhurjya Borah and Mr. Kh. Kesho Singh, the scientific officers of CIF, who have patiently and enthusiastically extended their expertise in handling various instruments that I have used for my research work.

I am fortunate to have my seniors Dr. Debabrata Mishra and Dr. Rahul Das, who helped me in various ways during my PhD period.

Dr. Akhilesh Kr. Singh, Dr. Santhosh, Dr. Batakrushna, Deepanwita, Poulami, Tribedi, Munendhar, Padam, Indrajeet, Mukesh, Bhargab, Suresh, Arun, Jithin, Abhijith, Rajitha, Bhagaban, Anabil, Ravi, Camelia, Gobinda, Arnab, Nisha, Rajkumar, Buddhadeb, Ranganadha, Bipul, Junmoni, Mahesh, Prahlad and all other research scholars of physics department will always be remembered for the wonderful time we shared together.

I thank my malayali seniors Meera, Veena, Sangeetha and Aneesh for their company during the initial days of IITG which made me to feel comfortable here. A special thanks to Meera chechy for playing the dual roles of an elder sister and a good friend with whom I felt like in my home. The hours long chit-chats we had sometimes about 'anything under the sky' were a great

relief from the busy schedule of PhD life for both of us and the funny moments we shared during those times will remain as some of the unforgettable moments of my IITG life.

I thank Bijita, Sajitha, Jismy, Gayathri, Dhanya, Sangkha and all other friends of IITG for their wonderful company which gifted me a memorable life in IITG campus. I extend my thanks to my best friends Sajna, Aparna and Deepak for providing immense support and motivation throughout my PhD period. They were always been there during both the good and bad times of my life. The encouragement, advices, trust and care they extended helped me a lot to cross all the hurdles and to emerge with enhanced courage and confidence. They made me to laugh even in the midst of thousands of problems. Big thanks to my ever best buddies for being the source of my positive energy and inspiration.

I am extremely indebted to my most favorite teacher and one of the best teachers I have ever had in my life, Dr. Rajan K. John for his kindness and support. Without his inspiration I would not have been able to achieve this goal. He taught me to dream high and made me to understand the value of hard work. I can never forget the moral support, courage and motivation received from him during my post-graduation period which eventually lead me to pursue a career in research field.

Words cannot express how grateful I am to my family for all the sacrifices they have made on my behalf. The prayers, support, love and care they have shed on me was what sustained me this far. I am so fortunate to have such great parents who had taught me the value of education and given me the freedom to continue my studies as long as I wish. Countless thanks to my one and only brother who took all the family responsibilities on his shoulder in my absence without any complaints. He always provided unconditional love, trust, support and encouragement which motivated me to work harder and do my best in my career. My family is the origin of my happiness and the backbone of my success. I extend my thanks to my sister-in-law and all other relatives for their love and prayers for my progress.

I am thankful to all my school and college friends for their well wishes and to my teachers for their kind blessings which motivated me to complete this voyage. I thank Neethu chechy who inspired me a lot to do PhD in prestigious institutions like IITs. Also, my sincere thanks are due to all those, who have been helped me in whatever manner and bring me to this position, some of whom I may have inadvertently forgotten to mention in this acknowledgement.

Finally and foremost I thank the almighty God for giving me the good times which I enjoyed a lot and the bad times from which I learned many lessons. I remain thankful to the God for the courage and ability given to face all the adverse situations to come out with flying colors.

Shyni P C

PREFACE

Over the past few decades, nanocrystalline materials characterized by ultrafine grains and significant volume fraction of grain boundary regions have received considerable research interest due to their unusual physical, chemical and mechanical properties. In the area of magnetic materials, soft magnetic nanocrystalline materials are one of the recent emphases of material scientists and physicists due to their promising applications in various emerging fields such as magnetic field screening, magnetic sensors, reading heads of information storage systems, magnetic refrigeration, tape wound cores for common mode chokes and high frequency transformers. Soft magnetic materials are characterized by low coercivity (H_C), large saturation magnetization (M_S), high effective permeability, low magnetostriction and controllable magnetic anisotropy, when their average crystallite size is less than the ferromagnetic exchange correlation length which is typically of the order of tens of nanometers. The main reason for the excellent soft magnetic properties in the nanocrystalline materials is their characteristic two-phase microstructure, which not only yields an averaging out of magnetocrystalline anisotropy, but also enhances the values of M_S and permeability. In addition, the strong ferromagnetic inter-granular exchange interaction and long range ferromagnetic ordering result in very high Curie temperature (T_C). Therefore, to obtain soft magnetic nanocrystalline materials, it is very much essential to understand the correlation between the structural and magnetic properties. These materials in general can be obtained through two diverse processes, viz., melt spinning and mechanical alloying. In the melt spinning technique, a thin stream of molten alloys is ejected onto the rotating wheel cooled either by water or liquid nitrogen causing rapid solidification of the molten alloys. This process can induce high cooling rates of the order of $10^4 – 10^7$ K per second which results in producing an amorphous ribbon of the molten material. Subsequently, the nanocrystalline materials can be obtained by controlled crystallization of amorphous precursors by heat treatment at elevated temperatures. On the other hand, mechanical alloying is a well-known and powerful method for the synthesis of various metastable powders through a process involving deformation, fragmentation, cold welding and micro-diffusion of elements in the solid state in a highly energetic grinding media. This technique is relatively inexpensive and there is a potential to scale up production for commercial quantities. The obtained nanostructured powders either consist of particles composed of nanometer sized crystalline grains linked one to another through grain

boundaries or has amorphous structure depending on the constituents and mechanical alloying conditions. It also forms highly refined and strained alloy powders, resulting a high H_C in the range of 10 – 1000 Oe and therefore relatively hard as compared to those prepared by melt spinning technique. Therefore, the powders have to be consolidated and given appropriate heat treatment in a way which is analogous to the preparation technique of nanocrystalline melt-spun ribbons.

Among various nanocrystalline soft magnetic materials, Fe rich Fe-Si based alloys are traditionally well known materials suited for various applications such as transformers, magnetic cores of electrical appliances, magnetic sensors and electromagnetic noise suppression, *etc*. These materials can be prepared using various preparation techniques such as Inert gas condensation, spray conversion processing, rapid solidification, mechanical alloying, physical vapor deposition, chemical vapor deposition and crystallization of amorphous phases. The introduction of Si into Fe results in a decrease of magnetic anisotropy thereby leading to a decrease of H_C. The presence of Si also enhances the electrical resistivity and hence reduces eddy current loss. These results make Si as one of the prime choices of alloying element with Fe. Nanocrystalline Fe-Si based materials prepared from melt-spun amorphous precursors exhibit ultrasoft magnetic properties with H_C as low as 10^{-3} Oe. However, the study of high Si content Fe-Si alloys prepared by melt-spun technique could not provide systematic compositional dependence of physical properties owing to the limited alloying range available for this method. With the increasing demand for powder core technologies, the study of low-cost, high Si content soft magnetic Fe-Si alloys become important. Interestingly, mechanical alloying process involves alloy formation through a solid state process where some of the restrictions of equilibrium phase formation are easily overcome. Extensive studies have been carried out using mechanical alloying process to produce a variety of Fe-Si based alloys with tunable properties. Most of the literatures reported the substitution of Si (< 20 at.%) in Fe-Si to produce non-equilibrium solid solution having crystallite size between 10 and 20 nm with controllable magnetic properties. The increase of Si content above 20 at.% in Fe-Si leads to the formation of various phases such as Fe-Si intermetallic compounds, DO_3-type structures and Fe-Si solid solutions, resulting in a drastic change in the magnetic properties. A careful review of the literatures reveals that the properties of nanocrystalline materials prepared by mechanical alloying strongly depend on the milling parameters. Hence, a comparison of results obtained through different preparation conditions for different alloy compositions becomes difficult and prevents a systematic correlation between the microstructure and magnetic properties.

Nevertheless, there have been continuous attempts to improve the soft magnetic properties by tailoring composition, choice of substituting elements, selection of preparation parameters, optimization of nanostructure and annealing conditions. However, only limited reports deal with systematic investigations of structural and magnetic properties of Fe-Si based alloys with different substitution elements prepared by a single preparation technique.

Therefore, this thesis work aims (i) to understand the evolution of nanocrystalline microstructure and resulting magnetic properties of mechanically alloyed $Fe_{100-x}Si_x$ ($5 \leq x \leq 50$) binary alloys over a wide range of compositions with different milling conditions, (ii) to study the effects of substituting elements (Co, Al, Cr) in selected Fe-Si parent systems and the annealing process to tailor the microstructural and magnetic properties, and (iii) to investigate the correlation between the microstructure and magnetic properties of these mechanically alloyed powders and to explore the possibility to enhance their soft magnetic properties. The following atomic compositions have been taken up for the investigations: (i) $Fe_{100-x}Si_x$ ($5 \leq x \leq 50$) binary alloys, (ii) $Fe_{100-x-y}Co_ySi_x$ ($x = 10$ and 15, $y = 0 – 20$) ternary alloys, and (iii) $Fe_{95-x-z}(Al,Cr)_zCo_5Si_x$ ($x = 10$ and 15, $z = 0 – 10$) quaternary alloys. The present thesis comprises of eight chapters.

Chapter 1 presents a brief introduction to the content of the thesis along with a detailed review of the literature relevant to the present thesis work. The motivation and objectives of the thesis work are also explained in this chapter. The fundamental aspects of magnetism and various theoretical methods employed in the analysis of the data of the presently investigated samples are summarized in **Chapter 2**. **Chapter 3** describes the experimental techniques including the sample preparation methodologies used in the present study. The basic principle and theory behind the experiments, the experimental set up and measurement / methodology used for the determination of the physical properties are also briefly discussed here.

In **Chapter 4**, the results and discussion on $Fe_{100-x}Si_x$ ($5 \leq x \leq 50$) powders milled for various time periods with different milling speeds over a wide range of compositions have been presented. Milling was carried out up to 100 hours in a planetary ball mill with a ball to powder weight ratio of 10:1 under argon atmosphere. With increasing milling time, (i) the procedure yields non-equilibrium solid solutions of α-Fe(Si) with the average crystallite size of about 10 nm and dislocation density of the order of 10^{17} m^{-2} within 100 hours of milling and (ii) the milling process also led to the formation of finer particles of homogeneous size and spherical shape as confirmed by electron microscopy. The milling

parameters (milling time and milling speed) required for forming the solid solution in high Si content Fe-Si alloys increases with increasing Si content. The formation of solid solution could be achieved up to 40 at.% Si and the increase of Si content above 40 at.% results in the formation of finite intermetallic compounds and other equilibrium phases. Occurrence of atomic disorder with increasing milling time has been evidenced from the variation of lattice parameters and magnetization values. All the Fe-Si samples exhibit an increase in H_C with increasing milling time due to the introduction of dislocations, reduction of crystallite size, formation of extended grain boundaries and change in magnetic anisotropy in the course of milling process. As-milled Fe-Si powders show H_C in the range of 150 to 250 Oe and the magnetization decreases to about 100 emu/g as Si content is increased up to 40 at.%. H_C shows nearly linear variation with dislocation density over the entire range of milling for low Si content (< 20 at.%). The region of linear variation of H_C with dislocations reduces as Si content is increased beyond 20 at.%. High temperature thermomagnetization studies reveal that $Fe_{100-x}Si_x$ samples with $x \leq 20$ display a single magnetic phase transition from ferromagnetic to paramagnetic state, while the samples with $x \geq 25$ exhibit destruction and generation of magnetic phases, which depends strongly on the milling time and composition. In addition, T_C of the solid solution is found to be higher than that of the melt-spun ribbons of same composition and decreases gradually at a rate of 1.45 K per at.% Si with increasing Si in Fe-Si solid solution. Such higher T_C and the slower variation of T_C with Si content have been attributed to the presence of strain in the milled powders and the dissolution process of Si in Fe matrix. The observed results show good correlation between structural and magnetic properties with milling parameters and compositions. However, the structural and magnetic parameters have been found to be strongly dependent on the alloy compositions.

Chapter 5 discusses the effect of Co substitution on the structural, microstructural and magnetic properties of nanocrystalline $Fe_{100-x-y}Co_ySi_x$ (x = 10 and 15, y = 0 – 20) alloy powders. All the powders were milled for 40 hours under the milling speed of 600 rpm. Structural investigations using X-ray diffraction (XRD) and electron microscopy techniques confirmed complete dissolution of both Si and Co in Fe matrix to form a non-equilibrium α-Fe(Co,Si) solid solution within 40 hours of milling. The average crystallite size was found to be in the range of 7 to 11 nm, but increases initially for Co substitution up to 10 at.% and then decreases for further increase in Co content. The dislocation density (ρ) is found to be of the order of 10^{17} m^{-2}. ρ decreases considerably for Co substitution up to 10 at.% and then

increases with further increase in Co. On the other hand, the lattice constant increases slowly in as-milled $Fe_{100-x-y}Co_ySi_x$ alloys powders with increasing Co content up to 10 at. % and then decreases for further increase in Co. The amount of decrease in lattice constant strongly depends on the Si content, which has been attributed to the delay in the dissolution of Co in Fe matrix by the introduction of more Si. Co substitution increases both M_S and H_C, but the amount of increase depends on the Si content in $Fe_{100-x-y}Co_ySi_x$ alloys. This behavior could be correlated to the atomic pair ordering and induced magnetic anisotropy in the solid solution with the increased Co substitution. Thermomagnetization studies at high temperatures revealed that T_C increases at a rate of 4 K per at.% Co for the Co substitution up to 10 at.% and the rate of increase in T_C drops down to 1.4 K per at.% Co for higher Co substitution. Furthermore, the crystallization temperature decreases with increasing Co content resulting in an increase in magnetization at high temperature with increasing Co content above 5 at.%.

The effects of Al and Cr substitution on the evolution of nanocrystalline microstructure and the resulting magnetic properties of $Fe_{95-x-z}(Al,Cr)_zCo_5Si_x$ (x = 10 and 15, z = 0 – 10) alloy powders are discussed in **Chapter 6.** All the powders were milled for 40 hours with a milling speed of 600 rpm. Structural analysis reveals that (i) a solid solution of α-Fe(Al,Co,Si) and α-Fe(Cr,Co,Si) is formed within 40 hours of milling and (ii) with increasing Al and Cr content, the XRD peak broadening increases along with a considerable shift in the peak position. This confirms the formation of highly refined crystallites with size less than 8 nm. Although the extent of Cr dissolution could not be inferred directly from XRD patterns, the variations of structural, compositional and magnetic properties indirectly confirmed the presence of Cr in $Fe_{95-x-z}Cr_zCo_5Si_x$ alloys. While the average crystallite size decreases to about 6 nm with increasing Al and Cr substitution, the dislocation density increases significantly for low Al and Cr content (< 5 at.%) and tends to saturate with increasing Al and Cr above 2 at.%. The lattice constant increases slowly in as-milled $Fe_{95-x-z}(Al,Cr)_zCo_5Si_x$ (x = 10 and 15, z = 0 – 10) powders with increasing Al and Cr substitution. The amount of increase in the lattice constant is significantly low as compared to Fe-Al and Fe-Cr binary alloys due to the compositional dependent dissolution process and extended grain boundaries in multicomponent alloys. The study of room temperature magnetic properties confirms that M_S decreases for both Al and Cr substituted in Fe-(Al,Cr)-Co-Si samples, but Cr substitution exhibits a faster decrease in M_S. While the general decrease in M_S can be attributed to a partial filling of d bands of Fe by the substitutions of Si, Al and Cr in Fe-(Al,Cr)-Si-Co powders, the large decrease of M_S upon Cr substitution is

attributed to the formation of various types of exchange interactions. In addition, considerable amount of Fe atoms are expected to be present in the grain boundaries, resulting as a spatial variation of inter-atomic distance between Fe neighbors. On the other hand, H_C decreases from 90 Oe to 44 Oe and 60 Oe for small amount of Al and Cr substitution (2 at.%) in $Fe_{80-z}(Al,Cr)_zCo_5Si_{15}$, but increases sluggishly above 2 at.% at a rate of 1.5 and 0.3 Oe/at.% of Al and Cr content, respectively. The evolution of H_C is explained on the basis of different phenomena such as dislocation density, grain refinement, and compositional dependent grain boundary formation. The observed results showed a promising approach to reduce average crystallite size considerably in as-milled nanocrystalline alloys by proper choice of substituting elements.

Chapter 7 discusses the effect of annealing on the structural, microstructural and magnetic properties of Al and Cr substituted $Fe_{80-x-z}(Al,Cr)_zCo_5Si_{15}$ with $z = 0 – 10$ alloy powders annealed at selected annealing temperatures for 5 hours. Annealing has been found to have a significant effect on the microstructure and improvement of soft magnetic properties of the powders. With increasing annealing temperature, the peak broadening of XRD peaks decreases along with a considerable shift in the peak position indicating that the average size of the crystallites increases and the dislocation density decreases along with a considerable change in the lattice parameters. The samples annealed at 500 °C shows almost no change in average crystallite size, but a large reduction in dislocation density. Interestingly, the average crystallite size of Al and Cr substituted Fe-(Al,Cr)-Co-Si samples annealed at 900 °C decreases considerably with increasing Al and Cr content, suggesting that Al and Cr substitution controlled growth of nanocrystallites in quaternary alloys. As a result, H_C of the annealed powders was found to reduce rapidly. $Fe_{70}Al_{10}Co_5Si_{15}$ powders annealed at 900 °C yielded the lowest coercivity of 14 Oe among the powders studied in this work with moderate magnetization of 160 emu/g. This could be attributed to achieving an optimum nanocrystalline microstructure with fine crystallites of about 18 nm with reduced dislocation density by the annealing process. M_S values decrease with increasing annealing temperature due to the development of atomic ordering. The variations of magnetic parameters with annealing temperatures are observed to be dependent on the alloy compositions. The observed results showed a promising approach to control the growth of the average crystallite size efficiently in the annealed nanocrystalline alloys by proper choice of substituting elements and enhance the soft magnetic properties of mechanically alloyed Fe-Si based nanocrystalline alloys.

The above results have been used to understand the evolution of nanocrystalline microstructure with fine crystallites and the resultant magnetic properties on the basis of milling parameters (milling time and milling speed), compositions, substituting elements and annealing conditions in shaping the structural and magnetic properties of nanocrystalline Fe-(Al,Cr)-Co-Si alloy powders. Furthermore, conclusions have been drawn on the basis of variations in average crystallite size, density of dislocations, effective magnetic anisotropy, compositional effects and the development of grain boundaries. **Chapter 8** provides a summary of the results obtained in the thesis and suggests possible directions of future work in this topic.

CONTENTS

Chapter 1

Prologue

1.1. Introduction:

Magnetic materials have stimulated human imagination for millennia and for many centuries they have enthused progress in science and technology. For a long time, the focus was only on naturally occurring magnetic materials such as Fe and magnetite. Later on, the focus shifted to improvement of magnetic properties of coarse-grained magnetic materials [VISS2006, SCHA2009]. Over the past few decades, research on soft magnetic materials has moved over from coarser-grained materials to amorphous and nanocrystalline materials [BOLL1983, YOSH1988, INOU2001, ZHAN2004, IDZI2005, LIUY2006, SELL2006, WITK2006]. Although high saturation magnetization (M_S) can be easily realized in conventional crystalline magnetic materials, when concentrations of Fe are increased, their soft magnetic properties become poor due to large magnetocrystalline anisotropy of the iron. Interestingly, the effect of magnetocrystalline anisotropy can be suppressed dramatically either by preparing amorphous materials or by reducing average crystallite size to nanometer scale in nanocrystalline magnetic materials. As a result, exceptionally controllable M_S and excellent soft magnetic properties could be obtained in Fe-rich nanocrystalline alloys [MCHE1999, HONO2002, SELL2006]. Therefore, nanocrystalline materials characterized by ultrafine grains and significant volume fraction of grain boundary regions have received considerable research interest due to their unusual physical, chemical and mechanical properties [GLEI1989]. One of the most successful industrial applications of nanostructured materials is with magnetic materials. Hence, in the area of magnetic materials, soft magnetic nanocrystalline materials are one of the recent emphases of material scientists and physicists due to their promising applications in various emerging fields such as magnetic field screening, magnetic sensors, reading heads of information storage systems, magnetic refrigeration, tape wound cores for common mode chokes and high frequency transformers [MCHE1999, HONO2002, ZHAN2004, WITK2006].

Soft magnetic materials are generally characterized by low coercivity (H_C), large M_S, high effective permeability, low magnetostriction and controllable magnetic anisotropy, when the average crystallite size is less than ferromagnetic exchange correlation length which is typically of the order of tens of nanometers (~ 35 nm) [DING2001, ZUOB2004]. The main reason for the excellent soft magnetic properties in the nanocrystalline materials is their characteristic two-phase microstructure, in which nanosized (< 20 nm) crystals of soft ferromagnetic phase are embedded in ferromagnetic amorphous matrix. Such microstructure not only has an averaging out on magnetocrystalline anisotropy, but also enhances the values of M_S and permeability [HERZ1995]. In addition, the strong ferromagnetic inter-granular

exchange interaction and long range ferromagnetic ordering result in very high Curie temperature (T_C) [HERN19951, GORR1996]. Therefore, to obtain soft magnetic properties in the nanocrystalline materials, it is very much essential to understand the correlation between the structural and magnetic properties.

In general, magnetic materials can be prepared by various preparation techniques. In the early days, magnetic materials were mainly prepared by casting process. Such magnetic materials are known to be harder when their crystallite size is decreased. Therefore, early research activities on soft magnetic materials were mainly confined to the development of suitable magnetic alloys with large crystallite sizes. This approach was changed after the discovery of amorphous magnetic materials prepared by rapid solidification technique [BOLL1983] and the advent of nanocrystalline materials with crystallite size of the order of nanometer (~ 10 – 20 nm) prepared by controlled crystallization of melt-spun amorphous precursor [YOSH1988, HERZ1993, HONO2002, ZHAN2004]. More recently, the development of amorphous and nanocrystalline materials was achieved by alternative and commercially inexpensive technique called mechanical alloying [SURY2001].

In the melt spinning technique, a thin stream of molten alloys is ejected onto the rotating wheel cooled either by water or liquid nitrogen [LIEB1976, CAHN1983]. This process causes a rapid solidification of the molten alloys. This process can induce high cooling rates of the order of $10^4 – 10^7$ K per second which results in producing an amorphous ribbon of the molten material. Subsequently, the nanocrystalline materials can be obtained by controlled crystallization of amorphous precursors by heat treatment at elevated temperatures [LUK1996, MCHE1999, MARI2000]. On the other hand, mechanical alloying technique is a well-known and powerful method for the synthesis of various metastable powders involving deformation, fragmentation, cold welding and micro-diffusion of elements in the solid state in a highly energetic grinding media [KOCH1993, SURY2001, ZHAN2004, WITK2006]. This technique is relatively inexpensive and there is a potential to scale up production for commercial quantities. The obtained nanostructured powders either consist of agglomerated particles composed of nanometer sized crystalline grains linked one to another through grain boundaries or has amorphous structure. This technique also forms highly refined and strained alloy powders. The nanocrystalline materials can also be prepared by using other preparation techniques such as inert gas condensation [GLEI1989], electro-deposition [VOJT1974], physical vapor deposition [MORL2011] and vapor quenching method [MANG1978].

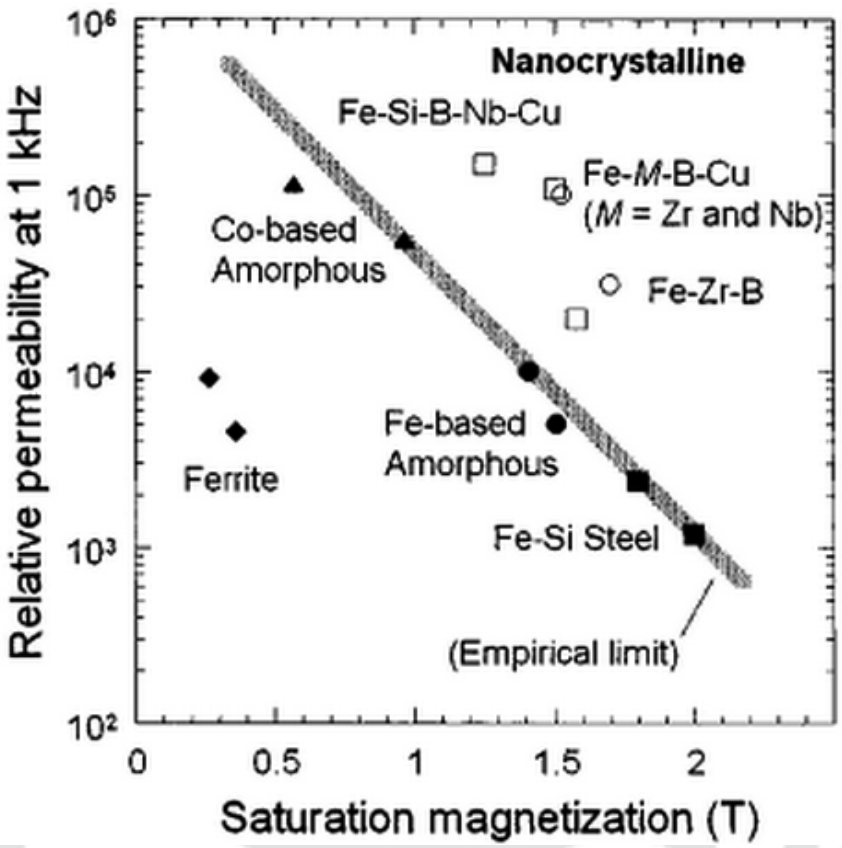

Figure 1.01. Relative permeability and saturation magnetization of various soft magnetic materials. The open circles and open squares denote FINEMET [YOSH1988, YOSH2001] and NANOPERM [BITO1997] alloys, respectively.

1.2. Motivation and preview of the thesis work:

The study of soft magnetism in nanocrystalline ribbons has brought a revolutionary change in understanding of magnetism and in the design of soft magnetic alloys. Fe-Si based alloys are one of the earliest known and widely used soft magnetic alloys [BARR1900]. Nanocrystalline Fe-Si based alloys derived from melt-spun amorphous ribbons exhibit ultrasoft magnetic properties with H_C as low as 10^{-3} Oe due to their two-phase microstructure [YOSH1988, HERZ1990, SELL2006]. Among various nanocrystalline soft magnetic materials, Fe rich Fe-Si based alloys are traditionally well known materials suitable for various applications such as transformers, magnetic cores of electrical appliances, magnetic sensors and electromagnetic noise suppression, *etc*. [MCHE1999, MARI2000]. There are two major alloy systems in this family of nanocrystalline magnetic materials viz., Fe-Si-B-Nb-Cu alloys [YOSH1988] commercially known as FINEMET and Fe-Zr-B-(Cu) alloys known as NANOPERM

[SUZU1990, SUZU19911]. Figure 1.01 shows saturation magnetization and relative permeability of various types of soft magnetic materials. As nanocrystalline materials have superior soft magnetic properties with high T_C, they find wide applications in high performance magnetic components and high temperature applications. However, the soft magnetic properties of these nanocrystalline materials are strongly dependent on the average grain size as shown in Figure 1.02.

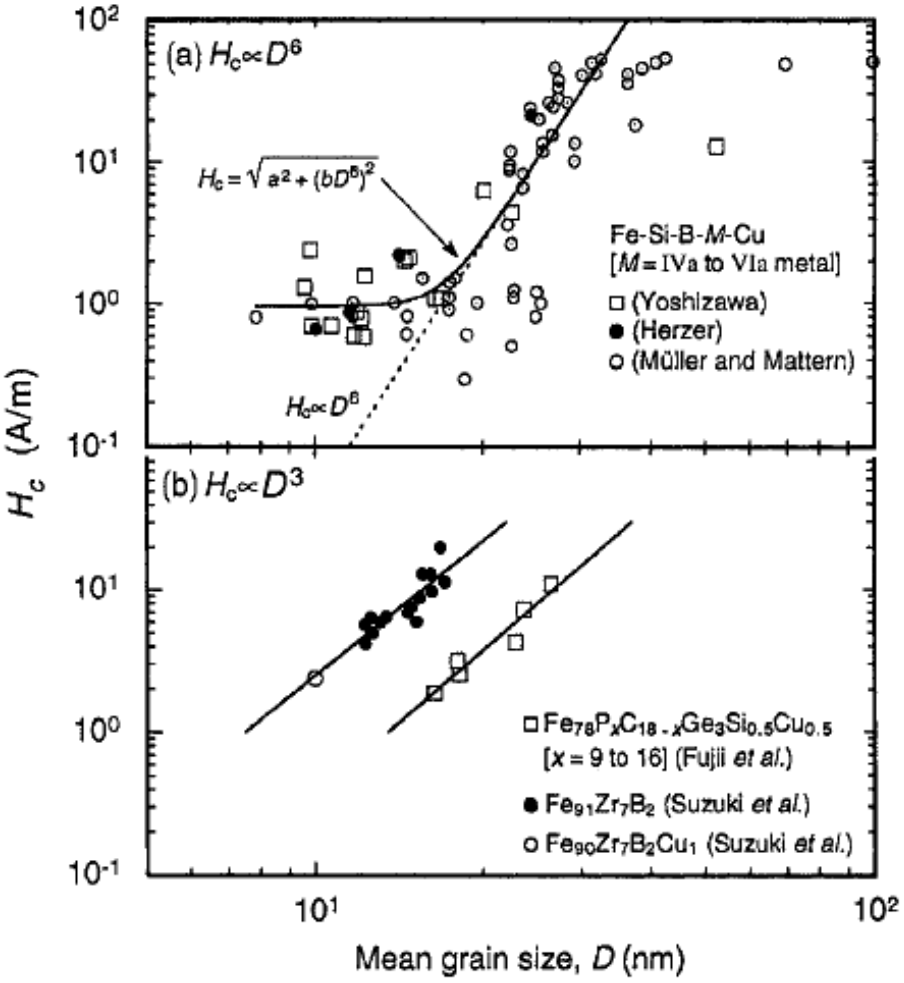

Figure 1.02. Grain size dependence of coercivity for (a) Fe-Si-B-M-Cu [MULL1994, HERZ1995] and (b) Fe-P-C-Ge-Si-Cu [FUJI1991] and Fe-Zr-B-(Cu) [SUZU1990, SUZU1996] alloys.

It is well understood that pure Fe exhibits high M_S, large magnetocrystalline anisotropy and low resistivity. As a result, they exhibit large H_C and high eddy current losses. The introduction of Si into Fe results in a decrease of magnetic anisotropy [ZHOU1999] and

thereby leading to a decrease of H_C. The presence of Si in Fe-Si based alloys also enhances the electrical resistivity and thereby reduces the eddy current loss. These results make Si as one of the prime choice of alloying element with Fe. A further reduction of the core losses is demanded with Si steels to solve energy saving problems. It has been reported that the core loss decreases with increasing the Si content, but at the cost of increasing the brittleness and reduction of magnetization [BOZO1993]. Therefore, the study of high Si content Fe-Si alloys prepared by melt-spun technique could not provide systematic compositional dependence of physical properties owing to the limited alloying range available for this method. Further, melt spun nanocrystalline ribbons are thin and usually brittle which restricts their applications mainly to toroidal cores. With the increasing demand for powder core technologies, the study of low-cost, high Si content soft magnetic Fe-Si alloys become important [VARG2001]. In this respect, mechanical alloying being a completely different approach of processing of nanocrystalline alloys provides a huge scope for exploring the properties of nanocrystalline alloys. As mechanical alloying process involves alloy formation through a solid state process where some of the restrictions of equilibrium phase formation are easily overcome [DAVI1987], extensive studies were carried out using mechanical alloying process to produce a variety of Fe based and Fe-Si based alloys with tunable properties. Table 1.01 summarizes H_C of various mechanically alloyed nanocrystalline soft magnetic powders reported in the literature. Data on other similar systems have also been included to facilitate a comparison.

Table 1.01. Coercivity of mechanically alloyed nanocrystalline powders.

Material	**Processing**		**Coercivity (Oe)**	**Reference**
	Mechanical alloying (Milling time in hours)	**Annealing** (time; Temperature)		
$Fe_{50}(SiC)_{50}$	0 – 40	-	154 - 320	[SHEN1992]
$Fe_{100-x}M_x$ (M = Al, Si, Cu; x = 0 – 50)	60	-	3.8 - 50	[KUHR1993]
$Fe_{100-x}Si_x$ (x = 6.5 – 25)	40	-	120 - 140	[ZHOU1999]
$Fe_{100-x}Co_x$ (x = 0 – 80)	100	30 min.; 973 – 1273 K	6.3 - 17	[KIMY2000]

$Fe_{73.5}Cu_1Nb_3Si_{13.5}B_9$; $Fe_{82}Si_{18}$	0 – 60	-	85 - 125	[RAJA2000]
$Fe_{100-x}Si_x$ (x = 0 – 40)	40	20 min.; 473 – 973 K	2.4 - 7.4	[DING2001]
$Fe_{73.5}Cu_1Nb_3Si_{13.5}B_9$	0 – 3500	-	80 - 320	[FECH2004]
$Fe_{80}Cu_{20}$; $Fe_{92}Al_2Si_6$	30	60 min.; 373 – 673 K	10 - 100	[SHEN2005]
$Fe_{75}Si_{25}$	0 – 100	573 – 853 K	-	[ZUOB2005]
Fe; $Fe_{50}Co_{50}$	0 – 40	-	50 - 72	[AZZA2006]
$Fe_{75}Si_{20}Ni_5$	35 – 100	-	30 - 80	[BAHR2006]
$Fe_{67}Si_{33}$	0 – 50	-	50 – 65	[KIMS2006]
Fe-Co-B	0 – 10	-	15 - 70	[ZENG2007]
Co; $Co_{90}Ni_{10}$	0 – 100	-	40 - 160	[GUES2008]
$Fe_{75}Si_{20}M_5$ (M = Al, B and Cr)	0 – 80	-	50 – 300	[KALI20083]
$Fe_{90}Ni_{10}$; $Fe_{80}Ni_{20}$	0 –100	-	50 - 200	[KOOH2008]
$Fe_{100-x}Si_x$ (x = 6.5 – 20); $Fe_{83.5}Si_{13.5}Nb_3$	40	20 min.; 643 - 773 K	53 - 65	[MIRA2008]
$Fe_{75}Nb_{10}Si_5B_{10}$	5 – 200	600K, 800 K	50 – 95	[SUNO2008]
$Fe_{75}Si_{25}$	0 – 80	-	50 – 120	[KALI20081]
$Fe_{94}Si_6$	0 – 10	-	-	[BENS2009]
$Fe_{75}Si_{25}$	0 – 80	573 – 1273 K	40 – 100	[KALI2009]
$FeSi_{10}Cr_{10}$	0 – 30	-	30 – 70	[BENS2010]
$(Fe_{65}Co_{35})_{100-x}Si_x$	0 – 80	-	20 – 90	[YOUS2012]
$Fe_{80-x}Ni_{20}Si_x$	0 – 36	-	30-90	[BAHR2013]
$[Fe_{65}Co_{35}]_{100-x}Si_x$	0 – 80	-	20 - 70	[YOUS2014]

A careful review of the literature reveals that the properties of nanocrystalline materials prepared by mechanical alloying strongly depends on the milling parameters. For example, Taghvaei et al. [TAGH2011], Yousefi et al. [YOUS2012], Bahrami et al. [BAHR2013] and Gomez-Esparza et al. [GOME2014] reported that H_C increases initially up to certain milling time period and then decreases with further increase in milling time period. This results in a maximum in H_C after certain milling time periods, which depends strongly on the alloying

materials. In contrast, Kim et al. [KIMS2006] and Bensebaa et al. [BENS2010] showed a decreasing tendency in H_C with increasing milling time period in Fe-Si based alloy powders. On the other hand, Guittoum et al. [GUIT2008] showed that H_C of Fe-Ni alloy prepared by mechanical alloying exhibits oscillatory variation of H_C up to 12 hours of milling and then increases continuously with increasing milling time up to 50 hours. These different results clearly suggest that any change in the magnetic properties of as-milled powders with milling time period strongly depends on the milling parameters and alloying materials. Furthermore, despite having the average crystallite of the nanocrystalline powders in the range of 10 – 20 nm, H_C of mechanically alloyed nanocrystalline powders (see Table 1.01) has been reported to be considerably larger as compared to nanocrystalline melt-spun ribbons ($H_C \sim 10^{-3}$ Oe). The higher values of H_C have been mainly attributed to the high strain caused by the existence of large dislocations induced during the milling process. In most of these reports, the values of M_S have been reported to be slightly lower than that of pure Fe, but strongly depends on the composition of Fe-Si based alloys. Comparison of results obtained through different preparation conditions for different alloy compositions becomes difficult and there is not much systematic study carried out to obtain a correlation between the microstructure and magnetic properties. Nevertheless, there have been continuous attempts to improve the soft magnetic properties by tailoring the alloy composition [SUNO2008, YOUS2012], changing substituting elements [ZENG2007, GUIT2008, BENS2010], varying preparation parameters, optimizing nanostructure, and changing annealing conditions.

In the literature, there are some reports on systematic studies pertaining only to the structure of as-milled and annealed Fe-Si powders [PERE1996, ZUOB2004] and structural and magnetic properties of Fe-Si based alloy powders [MIRA2008, BENS2010, BAHR2013, YOUS2014]. Perez et al. [PERE1996] reported the synthesis of nanocrystalline $Fe_{80}B_{13}Si_7$ powders. The lattice parameter estimated from X-ray peak positions indicated about 75 % dissolution of Fe and only 35 % dissolution of B after 128 hours of milling. Zuo et al. [ZUOB2004] and Kalita et al. [KALI20081, KALI20083] reported the effect of annealing in the temperature range 573 K – 973 K on the structure of Fe-Si and Fe-Si-Al milled powders. Bahrami et al. [BAHR2013] and Yousefi et al. [YOUS2014] performed systematic studies on the degree of alloying, dissolution of substituting elements in Fe matrix using energy dispersive spectroscopy mapping and development of fraction of grain boundaries for Fe-Si based alloys milled at different milling time periods. There are only a few reports on the high temperature ferromagnetic properties of mechanically alloyed Fe-Si alloys [FALL1936, CARM1991,

ESCO1991, KOHO1994, VARG2001, FECH2004] over a wide range of compositions prepared under similar preparation conditions. Furthermore, there are only limited number of reports available on the systematic investigations of structural and magnetic properties of Fe-Si based alloys with different substitution elements prepared by a single preparation technique under optimized preparation conditions [BENS2010]. Therefore, the present work attempts to gather a comprehensive understanding of the correlation between structural, microstructural and magnetic properties of Fe-Si based nanocrystalline alloys prepared by mechanically alloying process.

1.3. Objective of the thesis work:

- To prepare nanocrystalline $Fe_{100-x}Si_x$ ($5 \leq x \leq 50$) binary alloy powders over a wide range of compositions under different milling conditions to understand the evolution of nanocrystalline microstructure and resulting magnetic properties of mechanically alloyed Fe-Si binary alloys.
- To prepare nanocrystalline $Fe_{100-x-y}Co_ySi_x$ (x = 10 and 15, y = 0 – 20) ternary alloys under the optimized milling conditions and to understand the effect of Si and Co substitution on the structural and magnetic properties of $Fe_{100-x-y}Co_ySi_x$ alloy powders.
- To study the effect of substituting elements such as Al and Cr on the refinement of nanocrystalline microstructure and the resulting magnetic properties of $Fe_{95-x-z}(Al,Cr)_zCo_5Si_x$ system.
- To investigate the effect of post annealing temperatures on the strain relaxation, the formation of nanocrystalline microstructure, control of crystallite growth and the improvement of soft magnetic properties of nanocrystalline $Fe_{80-z}(Al,Cr)_zCo_5Si_{15}$ alloy powders.
- To understand the correlation between structural, microstructural and magnetic properties of the nanocrystalline powders in the as-milled and annealed conditions and to optimize the samples with suitable preparation parameters and compositions to obtain enhanced soft magnetic properties in Fe-(Al,Cr)-Co-Si alloy powders.

Chapter 2

Fundamental aspects and theoretical modeling

2.1. Introduction:

Magnetism is the phenomenon by which materials affirm an attractive or repulsive force. Although it has been known for thousands of years, i.e., the history of magnetism is coeval with the history of science, the underlying principles and mechanisms that explain the magnetic properties of the materials are still complicated and mysterious. Nevertheless, it is well established that most of the modern technological devices such as electrical power generators, transformers, electric motors, sensors, computers and components of sound and video reproduction systems largely depend on magnetism and magnetic materials. Hence, during last few decades, extensive studies on various types of magnetic materials have been carried out from both fundamental and application points of views. In this regard, the understanding of development of magnetic properties in new types of materials and optimization of the magnetic properties for different applications are very much essential. This chapter provides a brief description of the origin of magnetism in solids, the phenomenon of ferromagnetism and the various phenomena affecting the ferromagnetic properties of materials prepared by different techniques and suitability of these materials for various applications.

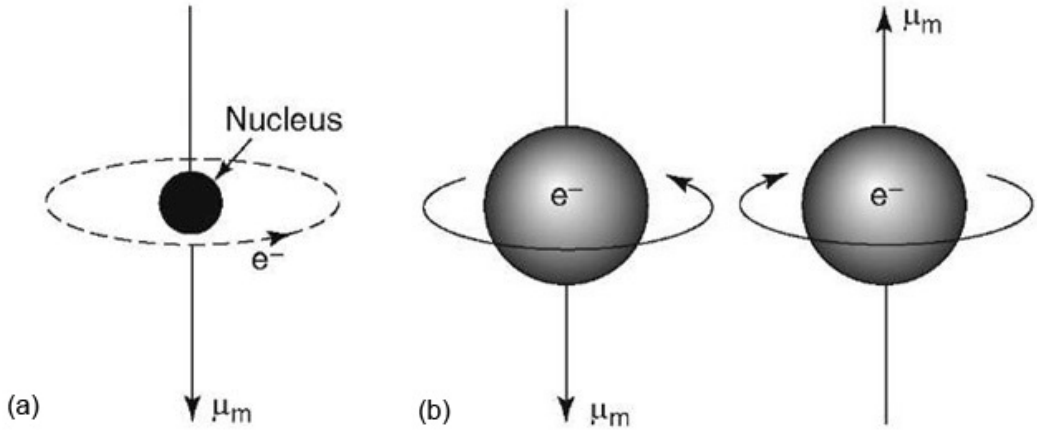

Figure 2.01. Schematic representation of (a) orbiting electron around the nucleus and (b) electrons spinning around their own axis.

2.2. Origin of magnetism:

It is known that the macroscopic magnetic properties of materials are consequences of magnetic moments associated with individual electrons in an atom [OHAN2000, KITT2004]. The magnetic moment originates from two different sources as demonstrated in Figure 2.01.

One is orbital motion of electron around the nucleus (see Figure 2.01(a)), which generates small magnetic fields with magnetic moment along the axis of rotation. The other magnetic moment originates from the electron spin, which is directed along the spin axis either up or down depending on the mode of rotation as shown in figure 2.01(b). Therefore, each electron in an atom can be imagined of being a small magnet having permanent orbital and spin magnetic moments. The net magnetic moment for an atom is the sum of the magnetic moments of each of the constituting electrons, including both orbital and spin contributions and taking into account of the moment cancellation. These electrons occupy empty states in an atom according to the Pauli's exclusion principle and Hund's rule. Hence, for an atom having completely filled electron shells or subshells, there is a total cancellation of both the moments. Note that such materials are not capable of being permanently magnetized. Based on the number of unpaired electrons in an atom, their orientation in the orbitals and the spin-orbit interaction between the electron orbital angular momentum and spin angular momentum and their response in external applied field, magnetic materials are majorly classified into diamagnetic, paramagnetic, ferromagnetic, antiferromagnetic and ferrimagnetic [KRON2003].

Diamagnetism is a manifestation of Lenz law, i.e., if one applies a magnetic field to a system of moving charges, then their motions change in such a way that they create a magnetization, which opposes the original applied magnetic field [OHAN2000]. This effect is present in all materials, but is often obscured by other types of magnetism. However, for some solid materials, each atom possesses a permanent dipole moment by virtue of incomplete cancellation of electron spin and/or orbital magnetic moments. These magnetic moments are random in nature in the absence of any applied magnetic field, resulting in zero macroscopic magnetization. Upon applying external magnetic field, these atomic dipoles are free to rotate and paramagnetism occurs when they preferentially align to field direction by rotation [KITT2004]. Both diamagnetic and paramagnetic materials are generally assumed to be non-magnetic as they show zero magnetization in the absence of any external magnetic field. On the contrary, certain materials possess a permanent magnetic moment resulting from strong interaction between the magnetic moments even in the absence of an external field. Such interactions dominate over thermal energy, displaying an alignment of magnetic moment in a particular direction. This kind of behavior is exhibited by the transition metals and some of the rare earth metals and known as ferromagnetic materials. In antiferromagnetic materials, moments of equal magnitude are aligned in an antiparallel arrangement with zero net moment in the absence of external field at temperatures below the ordering temperature called Néel

temperature [KITT2004]. Some ceramics exhibit a permanent magnetization, termed ferrimagnetism. When two antiferromagnetically coupled sublattices in a material have unequal moments due to different species at different sites, the net moment is not zero and such materials are called ferrimagnets. As the primary motivation of the thesis work is to study the ferromagnetic properties of magnetic materials with nanocrystalline microstructure, we concentrate on the phenomenon of ferromagnetism, the various phenomena affecting the ferromagnetic properties of materials and the applications of magnetic materials in the rest of this chapter.

2.3. Ferromagnetic materials:

As discussed earlier, ferromagnetic materials are spontaneously magnetized materials when placed in a small magnetic field. At a given constant temperature, the response of a ferromagnetic material to an applied magnetic field (***H***) is non-linear and characterized by a magnetic hysteresis phenomenon as displayed in Figure 2.02. The dotted curve from origin to the point '*a*' represents the initial magnetization curve of a demagnetized material. Magnetization increases with increasing ***H*** and saturates at higher magnetic fields. The maximum (saturated) magnetization achievable is known as saturation magnetization (M_S). The typical magnetic hysteresis (***M***–***H***) loop of a ferromagnetic material is shown by the solid curve '*a-d-a*' in Figure 2.02(a). Significant parameters characterizing a magnetic material associated with the *M-H* loop are retentivity or remanence (M_R, value of magnetization when $\boldsymbol{H} = 0$, point *b*) and coercivity (H_C, the reverse magnetic field required to reduce the net magnetization to zero, point *c*). Another important parameter is the magnetic induction [$\boldsymbol{B} = \mu_o (\boldsymbol{H} + \boldsymbol{M})$, where μ_o is the permeability of free space], which is the total flux of magnetic field lines through a unit cross sectional area of the material. From the initial magnetization curve, the initial magnetic permeability μ_I ($= \boldsymbol{B}/\boldsymbol{H}$, for very small applied magnetic field) and maximum permeability μ_{max} [$=(\boldsymbol{B}/\boldsymbol{H})_{max}$] can be obtained. These parameters indicate the amount of induction generated by the material in a given magnetic field and are useful in characterizing magnetic materials. μ_I and H_C have a reciprocal relationship. So, materials exhibiting low H_C necessarily have a high μ_I. When the ferromagnetic material is heated, they become paramagnetic above a particular temperature as shown in Figure 2.02(b). The temperature at which the magnetic phase transition from ferromagnetic to paramagnetic state occurs is known as Curie temperature (T_C), which is also an important parameter characterizing a ferromagnetic material. Ferromagnetic materials exist in different forms, e.g. crystalline,

amorphous and oxide states. These materials can be engineered for specific applications with suitable selection of elements and composition.

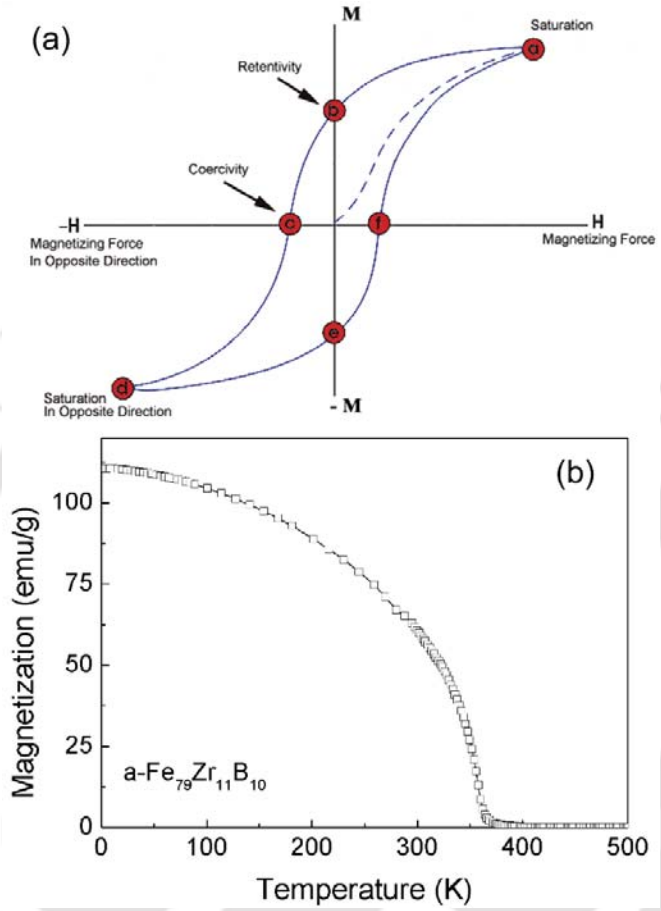

Figure 2.02. Response of a ferromagnetic material to (a) applied magnetic field at a particular temperature and (b) temperature at a constant applied magnetic field.

Ferromagnetic materials are classified into two groups as depicted in Figure 2.03. They are hard ferromagnetic materials, which exhibit very high H_C (> 1000 Oe), which are generally used as permanent magnets and information storage media, and (ii) soft ferromagnetic materials with low H_C (< 10 Oe) which are used as transformer cores, read heads and magnetic sensors applications.

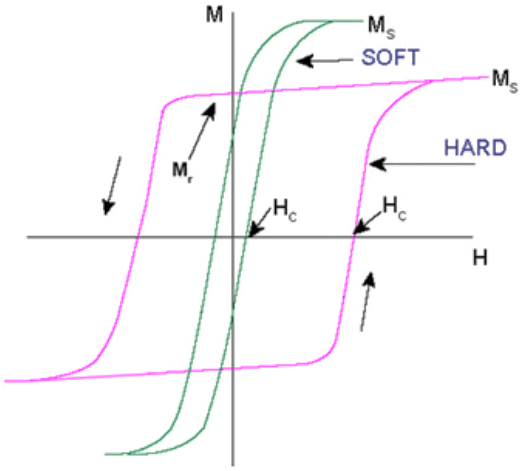

Figure 2.03. Typical magnetic hysteresis loops of soft and hard ferromagnetic materials.

2.4. Intrinsic and extrinsic properties of magnetic materials:

Intrinsic properties of ferromagnetic materials are M_S, T_C and magnetocrystalline anisotropy (MCA). They, in general, describe the equilibrium properties of the material on the atomic scale. On the other hand, extrinsic magnetic properties such as H_C and M_R reflect the magnet's real-structure (microstructure and morphology) [BLOC1932, LAND1935, SKOM19991]. A brief discussion on both intrinsic and extrinsic properties of magnetic materials is presented below:

2.4.1. Itinerant ferromagnetism:

Magnetism in transition metals (Fe, Co and Ni) arises from the 3*d* levels which are partly filled according to Hund's rule [JILE1991]. In general, the atomic orbitals overlap in metals to form bands. However, for these 3*d* metals, the high lying 3*d* electrons are delocalized and become itinerant. Therefore, the origin of ferromagnetism in 3*d* metals can be simply explained by the band theory of ferromagnetism proposed first by Stoner [STON1993] and later worked out independently by Slater [SLAT1936]. This is a simple extension of band theory of paramagnetism by the introduction of exchange coupling between the electrons. The Stoner criterion of ferromagnetism is briefly reviewed below.

Let us consider that paramagnetic density of states (DOS) is known and it does not depend on the band filling. Thus, the energy of electrons of the band is

$$E_B = \int_0^{E_\uparrow} E D_S(E) dE + \int_0^{E_\downarrow} E D_S(E) dE \qquad (2.01)$$

where $E_{\uparrow}$ and $E_{\downarrow}$ are the Fermi energies of the spin up and spin down bands, respectively. $D_S(E)$ is the paramagnetic DOS per spin which can be related to the number of electrons in the *d* band, *N* and spin polarization, *s*, through the relation

$$\int_0^{E_{\uparrow}} D_S(E)dE - \int_0^{E_{\downarrow}} D_S(E)dE = sN \tag{2.02}$$

By assuming a small spin polarization, replacing $D_S(E)$ by $D_S(E_F)$ and subtracting the zero point energy term, the electron energy can be simplified as

$$\Delta E_B = \frac{N^2}{4D_S(E_F)}s^2 \tag{2.03}$$

The exchange interaction term can be expressed in terms of the energy term as proposed by Stoner [STON1938] as

$$E_{ex} = -\frac{I}{4}(N_{\uparrow} - N_{\downarrow})^2 = -\frac{I}{4}s^2N^2 \tag{2.04}$$

where *I* is the Stoner exchange parameter, $N\uparrow$ and $N\downarrow$ are number of electrons with up and down spins, respectively. The above equation contains a contribution from the Coulomb repulsion that arises from the fact that two electrons with the same spin cannot occupy the same local orbital (*cf.* Pauli's exclusion principle for atoms). Furthermore, it contains the magnetic exchange between the electrons. Addition of equations (2.03) and (2.04) gives

$$\Delta E_B = \frac{N^2}{4}\left(\frac{1}{D_S(E_F)} - I\right)s^2 \tag{2.05}$$

To obtain a spontaneous spin polarization, the factor inside the parenthesis has to be negative, that is

$$D_S(E_F) \geq \frac{1}{I} \tag{2.06}$$

This is known as Stoner criterion of ferromagnets, which is satisfied only by the elements Fe, Co and Ni [JANA1977, SKOM19992].

The reason for magnetism in the metals at the end of the 3*d* series is mainly due to the large DOS at the Fermi level. Similarly, the reasons for the large DOS for the late 3*d* metals are

several. First of all, the 3*d* band must accommodate 10 electrons, and secondly the *d* band is contracted with increasing atomic number due to the increasing nuclear charge. In fact, it is also spontaneous to be believed that elements such as Rh and Pd should also exhibit ferromagnetism. But, the 4*d* electrons are further away from the core and they also extend further out. Consequently, the bands broaden and have a lower DOS at the Fermi level. Hence, the only pure transition metals that exhibit ferromagnetism are the late 3*d* metals.

2.4.2. Magnetic moment:

As discussed earlier, the magnetic moment in an atom arises due to the motion of the electron and interaction between them. Orbital and spin magnetic moments are main contributions to the total magnetic moment of the atom. The contribution from nuclear magnetic moment is quite negligible by comparison. The maximum magnetic moment ($\boldsymbol{\mu}$) of a single atom in a particular direction is given by [BLUN2001],

$$\boldsymbol{\mu} = g\boldsymbol{J}\mu_B \tag{2.07}$$

where g is the landé g-factor (ratio of the magnetic moment to the angular momentum), μ_B is the Bohr magneton ($1\mu_B = 9.274\times10^{-24}$ JT^{-1}) and $\boldsymbol{J}$ is the total angular momentum of the atom. $\boldsymbol{J}$ is defined as $\boldsymbol{J} = \boldsymbol{L} \pm \boldsymbol{S}$, where $\boldsymbol{L}$ is orbital angular momentum and $\boldsymbol{S}$ is the spin angular momentum. The sign ± is determined by the Hund's rule.

The magnetic moment of the transition metal elements Fe, Co and Ni originates due to the 3*d* band electrons. The value of magnetic moment for Fe, Co and Ni is determined to be 2.23 μ_B, 1.73 μ_B and 0.62 μ_B, respectively. In order to explain the measured magnetic moments in a meek way, the concept of strong and weak ferromagnetism has been introduced. Co and Ni are the strong ferromagnets, where the spin up band is completely filled with 5 electrons. On the other hand, Fe is an example of weak ferromagnet in which the spin up band is partially filled. Since a strong ferromagnet has the spin up band completely filled, its magnetic moment can be estimated from the number of valence electrons in the atom [JILE1997]. When the spin up band is completely filled and contains 5 electrons and the atom has n valence electrons in total (number of 3*d* and 4*s* electrons), the atomic magnetic moment can be calculated as

$$\boldsymbol{\mu} = [5 - (n - x - 5)]\mu_B = (10 - n + x)\mu_B \tag{2.08}$$

where x is the number of 4*s* electrons per atom. In isolated atoms of Fe, Co and Ni, the number of 4*s* electrons is 2 but in a metallic crystal, the 4*s* electrons will fill into 3*d* band. In order to

reproduce the measured magnetic moments, the 4*s* band must contain only about 0.65 electrons [SKOM19991]. Therefore, eqn.(2.08) turns out to be

$$\boldsymbol{\mu} = (10.65 - n)\mu_B \tag{2.09}$$

The above equation yields the magnetic moments of 2.65 μ_B, 1.65 μ_B and 0.65 μ_B for Fe (n = 8), Co (n = 9) and Ni (n = 10), respectively. These estimated values fairly agree well with the measured values of 2.23 μ_B, 1.73 μ_B and 0.62 μ_B for Fe, Co and Ni, respectively.

2.4.3. Exchange interaction:

Weiss, in 1907, reported that in addition to any externally applied field H, there is an internal molecular field or exchange field in a ferromagnetic material proportional to its magnetization as given in eqn.(2.10),

$$\boldsymbol{B_E} = \lambda \boldsymbol{M} \tag{2.10}$$

where λ is a constant and independent of temperature. According to eqn.(2.10), each spin sees the average magnetization of all the other spins. Note that this molecular field is not really a magnetic field. In order to explain this field, Heisenberg introduced the concept of exchange interaction in 1928 [HEIS1928]. The origin of the Heisenberg exchange interaction is electrostatic, but the explanation involves quantum mechanics. The charge distribution of a system of two spins depends on whether the spins are parallel or antiparallel. Although Pauli's exclusion principle dismisses the occupation of two identical electrons in the same quantum state simultaneously, it does not exclude two electrons of opposite spin. Therefore, the electrostatic energy of a system depends on the relative orientation of the spins, i.e., the difference in energy defines the exchange energy. The energy of interaction between the atoms i and j bearing electron spins S_i and S_j is defined from the Heisenberg model as [OHAN2000],

$$E_{exch} = -2\sum_{i<j} J_{ij} S_i . S_j \tag{2.11}$$

where J_{ij} is the exchange integral related to the overlap of the charge distribution of the atoms i and j. Assuming that the exchange interaction is the same for each nearest-neighbor pair, eqn.(2.11) turns out to be

$$E_{exch} = -2J \sum_{i<j}^{nn} S_i . S_j \tag{2.12}$$

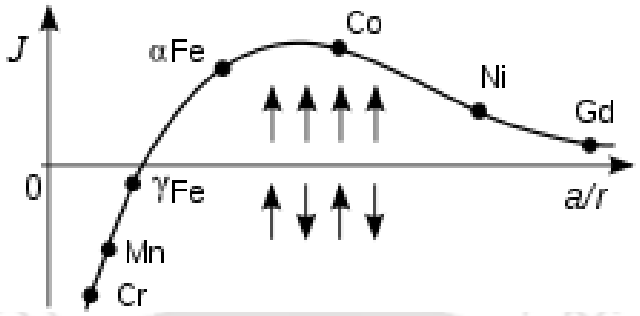

Figure 2.04. Bethe-Slater curve: Elements above and below the horizontal axis are ferromagnets and antiferromagnets, respectively.

For parallel orientation of the magnetization (ferromagnet), *J* should be positive and for antiparallel alignment of spins, *J* should be negative. The variation of *J* with respect to inter-atomic distance is shown in Figure 2.04. This curve is also known as the Bethe-Slater curve. It is clear from the Figure 2.04 that the value of *J* and hence the short-range exchange interaction depends strongly on the inter-atomic distance. The eqn.(2.12) can be further simplified by considering the energy of a particular atom *i* interacting with its *j* nearest neighbor:

$$E_{exch}^{i} = -2JS_i \sum_{j} S_j \tag{2.13}$$

while for the entire material,

$$E_{exch} = -\frac{1}{2} \sum_{j} E_{exch}^{i} \tag{2.14}$$

Thus, the discrete, pairwise interaction can be replaced by assuming that the magnetic moment $\mu_m^i = g\mu_B S_i$ at site *i* interacts with a molecular field H_{eff} given by the net effect of the *z* nearest neighbor spins:

$$E_{exch}^{i} = -\mu_0 \mu_m^i H_{eff} = -g\mu_0 \mu_B S_i H_{eff} \tag{2.15}$$

where g is the landé g-factor, μ_B is Bohr magneton and μ_0 is the permeability of the free space (= $4\pi\times10^{-7}$ H/m or 1.256×10^{-6} H/m). Comparing eqn.(2.15) with eqn.(2.13) provides the effective field as,

$$H_{eff} = \frac{2J}{g\mu_0\mu_B}\sum_j S_j \cong \frac{2zJ}{g\mu_0\mu_B}\langle S_j\rangle \tag{2.16}$$

Here, the sum over z neighboring spins has been replaced by z times the average spin value $\langle S_j\rangle$. Using $M = N_v g\mu_B\langle S_j\rangle$, eqn.(2.16) gives,

$$H_{eff} \cong \frac{2zJ}{N_v g^2 {\mu_B}^2 \mu_0} M \tag{2.17}$$

From eqn.(2.17), it can be seen that the H_{eff} is the Weiss molecular field defined as $H_{mol} = \lambda M$, provided

$$\lambda = \frac{2zJ}{N_v g^2 {\mu_B}^2 \mu_0} \tag{2.18}$$

Using the value of molecular field coefficient λ as 10^3, J is calculated to be 2×10^{-21} J or 0.01 eV/atom. Exchange interactions are weaker than the Coulomb interactions that distinguish levels of different principal and orbital quantum numbers, but stronger than spin-orbit interaction. Following the treatment of Weiss molecular field that $T_C = \lambda C$ with $C = N_v {\mu_m}^2 \mu_0/3k_B$, the expression for T_C can be obtained from eqn.(2.18) as

$$T_C = \frac{2zJ{\mu_m}^2}{g^2{\mu_B}^2 3k_B} = \frac{2zJs(s+1)}{3k_B} \tag{2.19}$$

where ${\mu_m}^2 = g\mu_B s(s+1)$. Another important relation between exchange energy and the magnetization is defined as,

$$\frac{E_{exch}^{ij}}{V} = \frac{s^2 b^2 J N_v'}{2}\left(\frac{\nabla M}{M}\right)^2 = A\left(\frac{\nabla M}{M}\right)^2 \tag{2.20}$$

where b is the distance between the spins, A is called the exchange stiffness constant having 1-2×10^{-11} J/m for most ferromagnets and N_v' is number of nearest neighbour atoms per unit volume (V). Therefore, it is clear from the above equations that the exchange energy or the Heisenberg exchange interaction depends strongly on temperature due to the dependence of

interatomic distance on temperature. In particular, the disorder ferromagnetic system is the subject of low T_C due to the low value of J.

2.4.4. Anisotropy:

When a material exhibits direction dependent physical property, then such a material is supposed to exhibit anisotropy. Particularly, in magnetic materials, the preference of magnetization to lie in a particular direction of sample is called magnetic anisotropy. As anisotropy plays an important role in tuning the nature and shape of *M–H* loop, it is very much essential to understand the various possible sources of magnetic anisotropy and its influence on the control of the magnetic properties. Figure 2.05 demonstrates a typical situation where for zero applied field, the magnetization would point along the easy axis shown ($\alpha = 0$). When a magnetic field is applied, the magnetization is pulled towards the field direction and approaches closer to the field direction with increasing the applied field. For any intermediate values of α, the magnetization is being attracted in opposite directions, i.e., up by the field and down by the anisotropy.

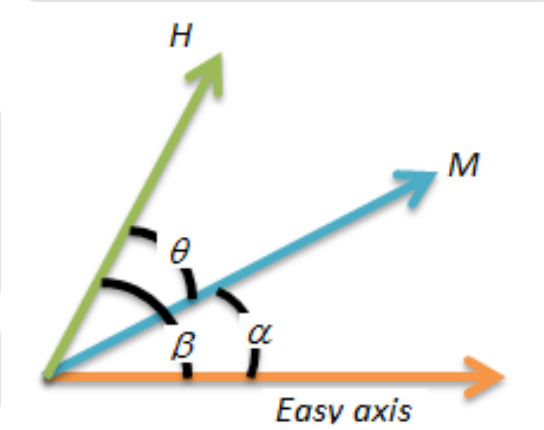

Figure 2.05. Schematic diagram of magnetization, applied field and easy axis for a given material.

Let us assume that all the magnetic moments are pointing in the same direction in a magnetic material and the material exhibits an easy axis of magnetization. In such a scenario, we can describe the energy per unit volume of the magnetization of this material by

$$E = K \sin^2\alpha \qquad (2.21)$$

where K is called anisotropy constant with an unit of energy per unit volume (J/m^3). In general, the magnitude of uniaxial anisotropy is described in terms of the anisotropy field, which is defined as the field needed to saturate the magnetization of a uniaxial crystal in the hard axis direction and is given as

$$H_k = \frac{2K}{\mu_0 M} \tag{2.22}$$

In general, the energy of the magnetization is given by

$$E = K\,sin^2\alpha - \mu_0 MH\,cos(\beta - \alpha) \tag{2.23}$$

where the first term is the anisotropy energy. The second term is due to the magnetic field and the difference in the angle (β - α) is the angle between $\boldsymbol{H}$ and $\boldsymbol{M}$. In order to get equilibrium, we require the first derivative to be zero. Therefore, taking derivative of eqn.(2.23) with respect to the angle we get,

$$\frac{dE}{d\alpha} = 2K \sin\alpha \cos\alpha - \mu_0 MH\,sin(\beta - \alpha) = 0 \tag{2.24}$$

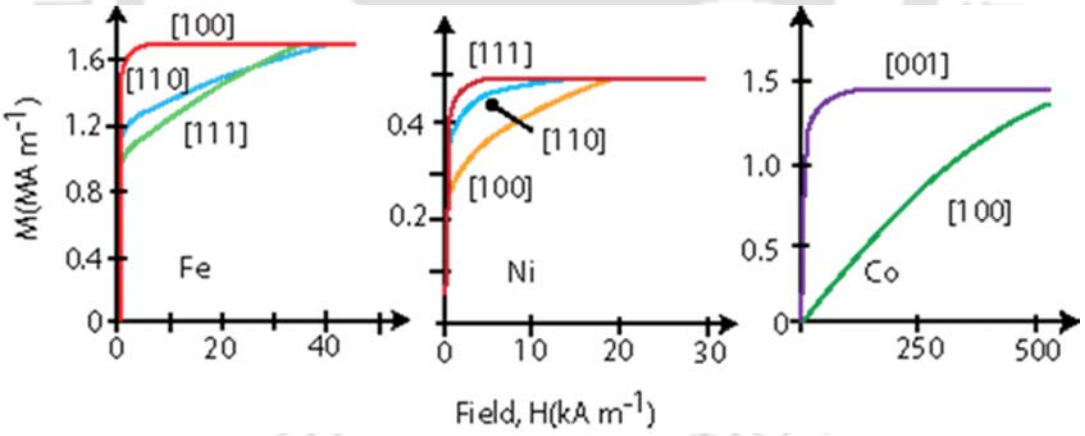

Figure 2.06. Magnetization of single crystals of Iron, Nickel and Cobalt.

Taking the value of β as 90^o for the equilibrium angle for the magnetization relative to the easy axis and considering the eqn.(2.22) gives

$$\sin\alpha = \frac{H}{H_k} \tag{2.25}$$

The above equation suggests that when field is zero, the magnetization points along the easy axis and when the field is equal to H_k, the magnetization points along the direction of field. For any intermediate value of the applied field, the magnetization points at a value of angle given by eqn.(2.25) rotating smoothly between the easy axis and the applied field.

2.4.4.1. Magnetocrystalline anisotropy:

Figure 2.06 shows initial magnetization curves of single crystals of different 3*d* ferromagnetic elements. It could be clearly seen that the magnetization approaches to saturation in different ways when magnetized in different directions. Iron displays ⟨100⟩ as easy direction and ⟨111⟩ as hard direction, while nickel exhibits ⟨111⟩ as easy axis and ⟨100⟩ as hard directions. This behavior can be understood by analyzing the development of anisotropy energy in different symmetries as given below:

For Hexagonal system

$$E_a = K_1 \sin^2\theta + K_2 \sin^4\theta + K_3 \sin^6\theta + K_3' \sin^6\theta \sin 6\phi \tag{2.26}$$

For Tetragonal system

$$E_a = K_1 \sin^2\theta + K_2 \sin^4\theta + K_2' \sin^4\theta \cos 4\phi + K_3 \sin^6\theta + K_3' \sin^6\theta \sin 6\phi \tag{2.27}$$

For Cubic system

$$E_a = K_{1c}(\alpha_1^2\alpha_2^2 + \alpha_2^2\alpha_3^2 + \alpha_3^2\alpha_1^2) + K_{2c}(\alpha_1^2\alpha_2^2\alpha_3^2) \tag{2.28}$$

where α_i are the direction cosines of the magnetization. K_{1c} term is equivalent to $K_{1c}(\sin^2\theta\, cos^2\phi \sin^2\phi + \cos^2\theta \sin^2\theta)$. When, $\theta = 0$, $\phi = 0$, this term reduces to eqn.(2.21) [COEY2010].

Origin of MCA: There are two different sources of MCA: (i) single-ion contributions and (ii) two-ion contributions. The first one is essentially due to the electrostatic interaction of the orbitals containing the magnetic electrons with the potential created at the atomic site by the rest of the crystal. This crystal field interaction stabilizes a particular orbital and by spin-orbit interaction the magnetic moment is aligned in a particular crystallographic direction. For example, the uniaxial crystal having 2×10^{28} ions/m^3 described by a spin Hamiltonian DS^2 with D/k_B = 1 K and S = 2 will have anisotropy constant $K_1 = nDS^2 = 1.1\times10^6$ J/m^3. On the other

hand, the later contribution replicates the anisotropy of the dipole-dipole interaction. Considering the broadside and head-to-tail configurations of two dipoles each with moment *m*, as shown in Figure 2.07, the energy of the head-to-tail configuration is lower by $3\mu_0 m^2/(4\pi r^3)$ and hence the magnets tend to align head-to-tail. In non-cubic lattices, the dipole interaction is an appreciable source of ferromagnetic anisotropy.

Figure 2.07. Schematic drawing of broadside and head-to-tail configurations for a pair of ferromagnetically coupled magnetic moments.

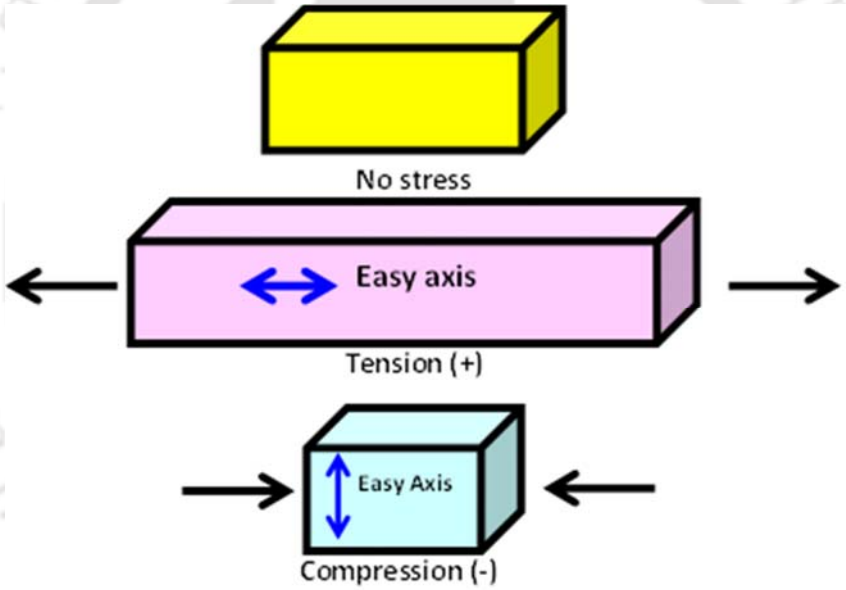

Figure 2.08. Schematic drawing of bars to demonstrate methods of inducing an easy-axis in a material with positive magnetostriction.

Table 2.01. MCA constants of Fe, Co and Ni [JILE1997].

Material	K_1 **(10^4 Jm^{-3})**	K_{u1} **(10^4 Jm^{-3})**	K_2 **(10^4 Jm^{-3})**	K_{u2} **(10^4 Jm^{-3})**
Fe (cubic)	4.80	-	0.50	-
Ni (cubic)	-0.45	-	0.23	-
Co (hexagonal)	-	41.0	-	10.0

2.4.4.2. Magnetoelastic anisotropy:

When a ferromagnetic material is exposed to applied magnetic field, the dimensions of the material change and thereby experience strain. This is known as magnetostriction. The inverse effect, *i.e.*, the change of magnetization with stress also occurs and produces a unique easy axis of magnetization giving rise to magnetoelastic anisotropy (MEA). The anisotropy energy associated with the magnetoelastic effect can be expressed as [JOHN1996]

$$E_{mea} = -K_{mea}\cos^2\phi \tag{2.29}$$

where ϕ is the angle between the magnetization and the plane of isotropic anisotropy and

$$K_{mea} = \frac{3}{2}\lambda\sigma = \frac{3}{2}\lambda E\varepsilon \tag{2.30}$$

where λ is the magnetostriction coefficient and σ is the stress which relates to the strain (ε) through the elastic modulus E. The experimental values of λ for Fe, Ni and Fe_3O_4 are -7×10^{-6}, -33×10^{-6} and -40×10^{-6}, respectively. Figure 2.08 shows the schematic views of bars with different applied stress conditions. If λ is positive, then application of a tensile stress to the bar creates an easy axis in the direction of the applied stress. If a compressive stress is applied, then the direction of the easy axis created will be perpendicular to the stress direction. On the other hand, if the magnetostriction constant of the material is negative, then the above phenomena would be reversed: a tensile stress will create an easy axis perpendicular to the stress direction and a compressive stress will create an easy axis in the direction of the applied stress.

2.4.4.3. Induced anisotropy:

In some materials, the magnetic anisotropy can be induced by many other ways, i.e., by (i) fabricating a thin film in the presence of applied magnetic field, (ii) heat treatment of the materials in the presence of external applied magnetic field and (iii) applying uniaxial stress. In the first two cases, after applying magnetic field, the material may exhibit an easy axis of magnetization that points in the direction of the magnetic field. This induced anisotropy is certainly independent of any crystalline anisotropy or any other form of anisotropy that might be present. Figure 2.09 shows the typical example of inducing the anisotropy in ferromagnetic materials by field annealing.

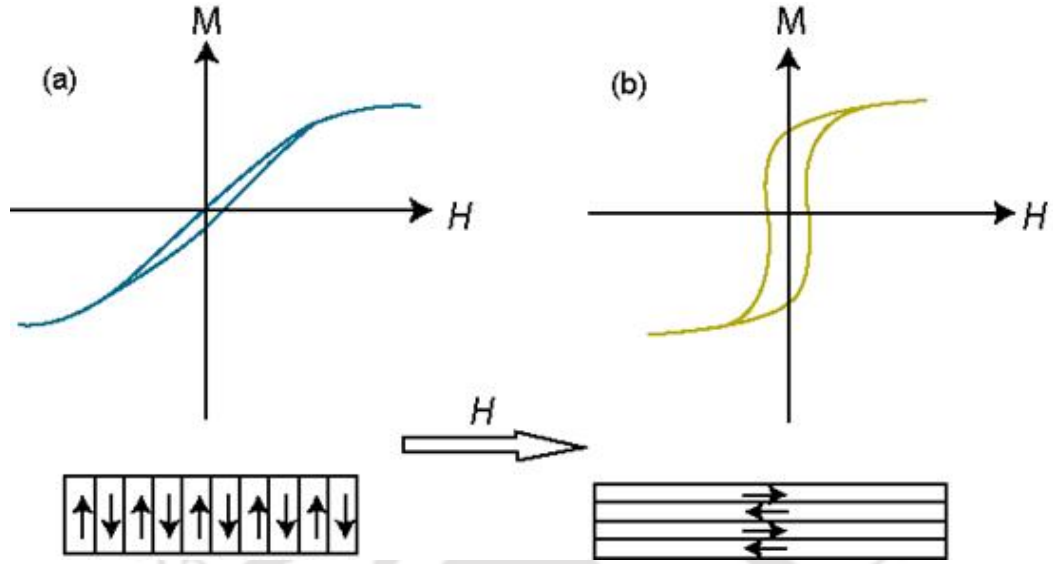

Figure 2.09. Magnetization of a thin film with induced anisotropy created by annealing in a magnetic field. The sheared (a) and open (b) loops are observed when the measuring field ***H*** is applied perpendicular and parallel to the annealing field direction, respectively.

2.5. Magnetic domains and domain walls:

Ferromagnetic materials consist of magnetic domains in which the magnetic moments are aligned parallel within the volumes containing large number of atoms. In the demagnetized state, magnetic domains are randomly oriented resulting in nearly zero magnetization in the absence of any externally applied magnetic field. However, the domains align when a small magnetic field is applied to the material [KITT1949, KITT1956, DILL1963]. The number of domains and size of domains are determined by the balance between magnetostatic energy versus domain wall energy. The change of spontaneous magnetization from a domain to its neighbor occurs at the domain wall. The width of the boundary between magnetic domains (the domain wall) is determined by the balance between the exchange energy and the MCA energy. The spins near to the wall point toward the non-easy directions. Therefore, the anisotropy energy is higher within the wall than in its adjacent domains. The exchange energy tries to make the wall as wide as possible. In order to make the angle between the adjacent spins as small as possible, the anisotropy energy tries to make the wall thin, i.e., reducing the number of spins pointing in non-easy directions. This competition leads to certain finite domain wall width by minimization of the total energy. The domain wall width δ is related to the exchange length [BROW1970, HUBE2009] by the relation

$$\delta = \pi L_{ex} \tag{2.31}$$

where L_{ex} is exchange correlation length given as

$$L_{ex} = \sqrt{\frac{A}{K}} \tag{2.32}$$

where A is the exchange stiffness constant and K is the MCA constant of the material [BLUN2001]. Typical domain wall widths are about 5 and 1000 nm for hard and soft magnetic materials, respectively.

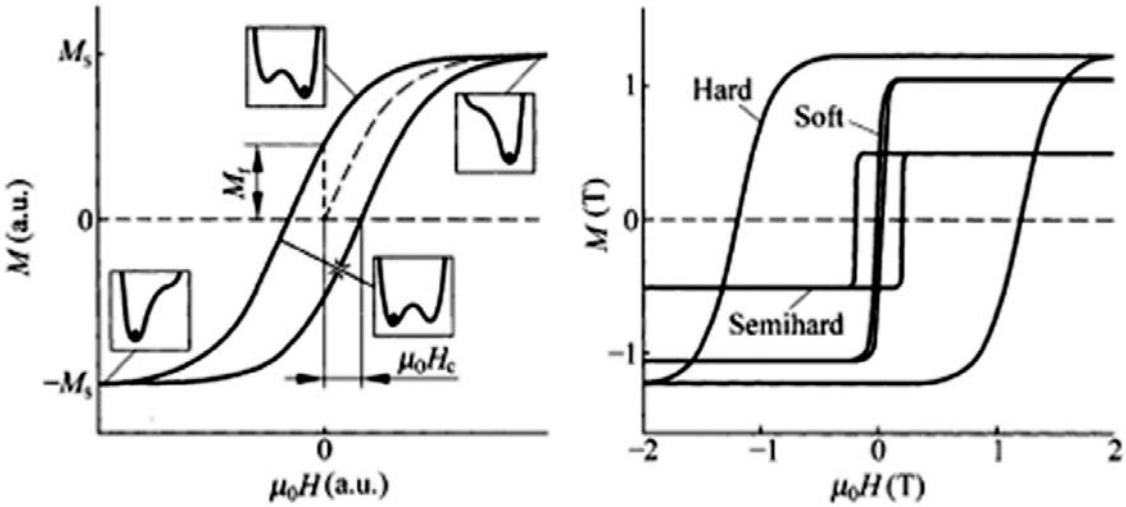

Figure 2.10. Typical *M–H* loops of different types of ferromagnetic materials.

2.6. Magnetic hysteresis:

Magnetic properties are generally derived from the magnetic hysteresis loop, which is extrinsic in nature. In addition, they describe the real structure of the magnet. The response of the ferromagnetic material to an applied magnetic field at a constant temperature is characterized by a magnetic hysteresis phenomenon as discussed in section 2.3. Figure 2.10 shows typical *M–H* loops of different types of ferromagnetic materials. Two very important extrinsic properties derived from *M–H* loops are H_C and M_R. *B–H* loops are used to determine the energy product $(BH)_{max}$, which is the manifestation of the maximum magnetostatic energy per magnet volume stored outside the magnet. Magnetic hysteresis is a complex, nonlinear, non-equilibrium and nonlocal phenomenon as depicted in the insets of Figure 2.10 reflecting the

existence of various metastable energy minima. A change in the applied magnetic field destroys local minima and the magnetization is forced to jump into another minimum. The nonlocal character of extrinsic properties originates due to the magnetostatic dipole interactions [SKOM19991].

2.7. Coercivity:

Coercivity, the most intriguing aspect of the hysteresis, describes the stability of the remanent state and gives rise to the classification of magnets into (i) soft magnetic materials having low H_C (< 100 Oe), (ii) hard materials having high H_C values (> 100 Oe). Hard magnetic materials are further divided into semihard magnetic materials with the coercivity of 2000 Oe ≤ H_C ≤ 10000 Oe which are mainly used for storage media applications and (iii) hard magnetic materials having large H_C (>10000 Oe, permanent magnets). A phenomenological expression for H_C is

$$H_C = p\frac{2K_1}{\mu_0 M_S} - D_{eff}M_S - \Delta H(T,\beta) \qquad (2.33)$$

where p is a Kronmuller parameter [KRON1987, KRON1988], D_{eff} is a magnetostatic interaction parameter and ΔH is fluctuation-field contribution caused by thermal activation [NEEL1951, COEY1996, SKOM19991]. H_C also depends on the field sweeping rate β (= dH/dt). H_C is mainly governed by two mechanisms such as nucleation and pinning. Nucleation-controlled magnets are almost defect-free and the H_C is essentially given by the nucleation field. There are several types of nucleation process such as coherent rotation in very small particles, curling in large perfect ellipsoids of revolution and localized nucleation in imperfect structures [SKOM1998]. In contrast to nucleation type magnets, pinning-type magnets contain many defects, which ensure large H_C by impeding the motion of the domain walls.

2.8. Origin of magnetic softness in nanocrystalline system:

Good soft magnetic properties are generally observed when both the domain wall motion and domain rotation occur within a small change in the energy of the system. The existence of magnetic anisotropies such as MCA, induced anisotropies, shape anisotropy *etc*. strongly affects the energy of the system. Among these anisotropies, MCA reflects the symmetry of the crystal structure. Stress induced anisotropy (MEA) originates from the magnetostriction, which itself is one of the intrinsic magnetic characteristics of materials.

As discussed earlier, H_C of a magnetic material is strongly dependent on its microstructure. The crystallite size and defects like grain boundaries, non-magnetic inclusions and internal stresses influence the values of H_C. According to Mager [MAGE1952], the coercivity determined by grain boundaries is a linear function of the reciprocal of the diameter of the crystallite (D) according to the relation

$$H_C \approx 3\frac{\gamma_W}{B_S}\frac{1}{D} \tag{2.34}$$

where γ_W is the domain wall energy and B_S is the saturation induction. The wall energy can be expressed as [BLUN2001]

$$\gamma_W = \sqrt{k_B T_C K / a} \tag{2.35}$$

where k_B is the Boltzmann constant, K is the MCA and a is the lattice constant. From equations (2.34) and (2.35), one can write

$$H_C \approx 3\frac{\sqrt{k_B T_C K / a}}{J_S}\frac{1}{D} \tag{2.36}$$

However, the D^{-1} dependence on coercivity is valid only when the crystallite size is larger than the ferromagnetic exchange length, where the magnetization is governed mainly by the MCA of the crystallites [HERZ1990]. Ferromagnetic exchange length as shown in Figure 2.11 is a basic parameter in domain theory which characterizes a minimum range over which the magnetization can vary appreciably. Ferromagnetic exchange length also determines the size barrier between multi-domain and single-domain structures.

For crystallite size less than the ferromagnetic exchange length, magnetization process is governed by the interplay of MCA of the crystallites and the ferromagnetic exchange energy. The theoretical model by Herzer known as random anisotropy model (RAM) [HERZ1990] which explains the origin of ultra-low coercivity in nanocrystalline ribbons is briefly discussed below. The RAM was originally proposed by Alben et al. [ALBE1978] for amorphous ferromagnets. Herzer applied it to explain the ultra-low coercivity in nanocrystalline ribbons.

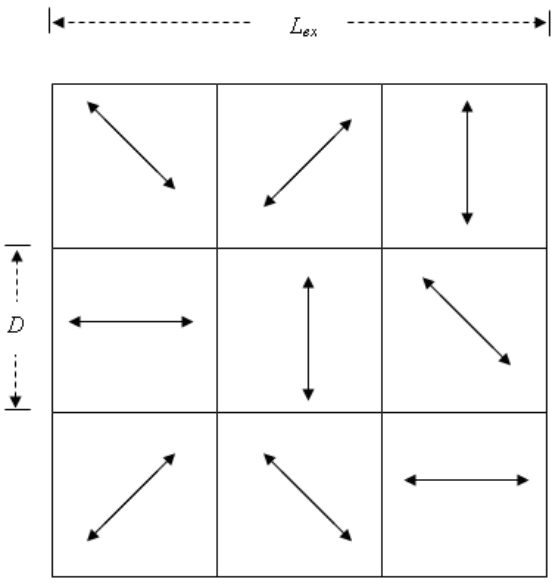

Figure 2.11. Schematic representation of RAM. The solid arrows indicate the randomly fluctuating MCA.

The basic idea of RAM is depicted in Figure 2.11. It shows an assembly of randomly oriented ferromagnetically coupled crystallites of size *D* with MCA constant *K*. The effective MCA affecting the magnetization process results from averaging over the number of crystallites, $N=(L_{ex}/D)^3$ within the volume $V=L_{ex}^{\ 3}$ of the exchange length. For a finite number, there will always be some easiest direction determined by the statistical fluctuations. As a consequence, the resulting anisotropy $\langle K \rangle$ is determined by the mean fluctuating amplitude of anisotropy energy of *N* crystallites, which is given by

$$\langle K \rangle \approx \frac{K}{N} = K\left(\frac{D}{L_{ex}}\right)^{3/2} \tag{2.37}$$

In turn, the exchange constant is now related self consistently to the average anisotropy by substituting $\langle K \rangle$ for *K* in eqn.(2.32), *i.e.*

$$L_{ex} = \sqrt{\frac{A}{\langle K \rangle}} \tag{2.38}$$

As MCA is suppressed by exchange interaction, the scale on which exchange interaction dominate expands and thus local anisotropies are averaged out more effectively. The combination of equations (2.37) and (2.38) results in

$$\langle K \rangle \approx \frac{K^4}{A^3} D^6 \tag{2.39}$$

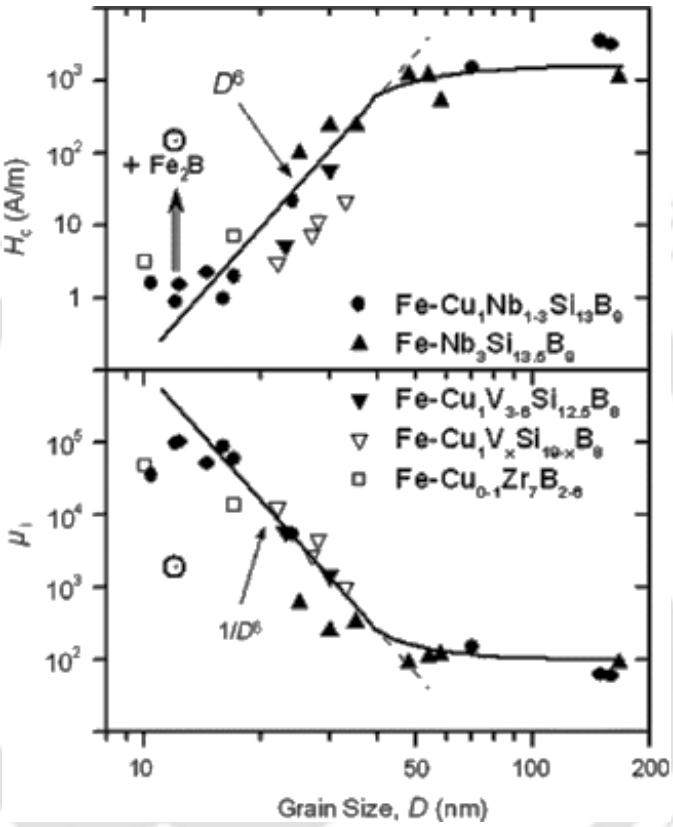

Figure 2.12. Variations of coercivity and permeability with grain size for different nanocrystalline alloys [HERZ2005].

This relation is valid as long as the crystallite size is less than L_{ex}. Furthermore, H_C can be related to $\langle K \rangle$ using the relation between H_C and MCA for coherent rotation of spins [BOZO1951]

$$H_C = p_c \frac{K}{J_S} \approx p_c \frac{KD^6}{J_S A^3} \tag{2.40}$$

where p_c is a dimensionless parameter. Accordingly, H_C varies as D^6 when D is less than L_{ex} and $1/D$ when D is larger than the L_{ex}. The summarized variations of H_C with the average crystallite size for various soft magnetic materials are shown in Figure 2.12. This is known as D^6 law for nanocrystalline materials and it explains the origin of soft magnetism in nanocrystalline system.

2.8.1. RAM in two-phase systems:

Most of the nanocrystalline soft magnetic materials prepared by primary crystallization of amorphous precursor contain two-phase microstructure, i.e., a nanocrystalline precipitate co-exists in a residual amorphous matrix. The extension of RAM model to two-phase system was carried out with two distinct exchange stiffness constants corresponding to amorphous and nanocrystalline phases. It is to be noted that the volume fractions of both of these phases affect the effective anisotropy [HERN19952, HERZ1995, HERN1998, LOFF1999]. A modified RAM for two-phase structure can be expressed as,

$$< K > = p\,(1 - V_{am})^4 K_1^4 D^6 \left[\frac{1}{\sqrt{A_{cr}}} + \frac{(1 - V_{am})^{-0.33} - 1}{\sqrt{A_{am}}}\right]^6 \qquad (2.41)$$

where A_{cr} and A_{am} are the exchange stiffness constants for crystalline and amorphous phase, respectively, and V_{am} is the volume fraction of the amorphous phase.

2.8.2. RAM in the presence of residual stress:

Melt spun nanocrystalline ribbons exhibiting excellent soft magnetic properties are thin and usually brittle in nature. This certainly restricts their applications mainly to toroidal cores. Furthermore, the preparation of nanocrystalline ribbons over a wide composition range is also limited due to easy formation of intermetallic compounds. Therefore, to overcome these limitations, alternative method for preparing soft magnetic alloys was investigated. Mechanical alloying has drawn a lot of research interest over a last two decades because of its versatility to prepare nanocrystalline soft magnetic alloys in a wide range of compositions in powder form with relatively inexpensive equipment. We have already summarized the values of H_C of mechanically alloyed nanocrystalline soft magnetic powders reported in the literature in Table 1.01. The crystallite size of the nanocrystalline powders mentioned in Table 1.01 is mostly in the range 10 – 20 nm. However, H_C in the mechanically alloyed nanocrystalline powders has been reported to be two to three order higher as compared to nanocrystalline melt-spun ribbons

($H_C \sim 10^{-3}$ Oe). The higher values of coercivity have been mainly attributed to the high strain and dislocations induced during the milling process. In most of these reports, saturation magnetization has been reported to be slightly less than that of pure Fe and independent of microstructure. To understand the magnetic properties of mechanically alloyed powders, RAM model is extended in the presence of residual stress, which is briefly discussed in this section.

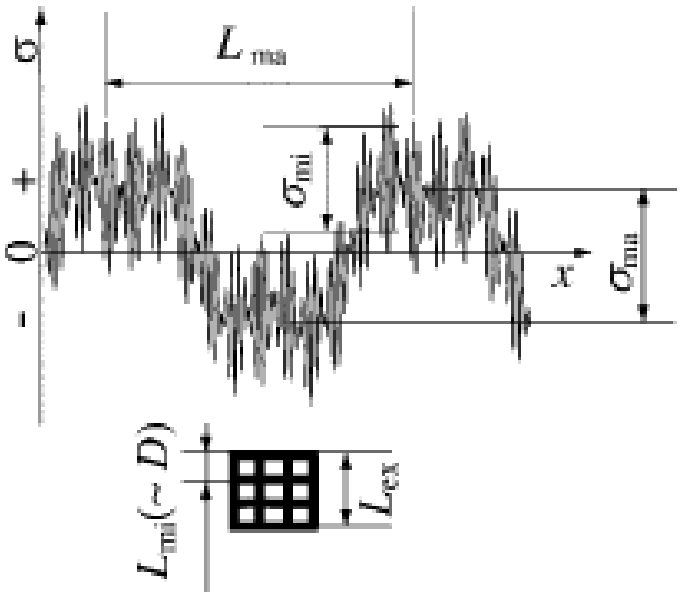

Figure 2.13. Schematic representation of the residual stress along an arbitrary direction within a mechanically alloyed powder particle. The length scale of the microstress is $L_{mi} \approx D \approx 10$ nm. The length scale of the macrostress is L_{ma} = aggregate thickness = 1 μm [SHEN2005].

Figure 2.13 depicts the schematic representation of the residual stress along an arbitrary direction within a mechanically alloyed powder particle. The fluctuating internal stress has a macroscopic range component σ_{ma} and microscopic range component σ_{mi}. The wavelength of the macrostress is L_{ma} which is approximately the size of aggregated particle, while the wavelength of the microstress is equal to the D, which is assumed to be lesser than ferromagnetic exchange length. In mechanically alloyed nanocrystalline alloys, the grain boundaries are considerably diffuse and contain a high density of tangled dislocations, leading to high-frequency fluctuations in the microscopic stress. The stresses σ_{ma} and σ_{mi} produce magnetoelastic anisotropy $K_{\sigma,ma}$ and $K_{\sigma,mi}$ according to eqn.(2.30) [CULL1972]

$$K_{\sigma,ma} = \frac{3}{2}\lambda\sigma_{ma};\ K_{\sigma,mi} = \frac{3}{2}\lambda\sigma_{mi}; \tag{2.42}$$

Both these anisotropies contribute to total effective anisotropy, K_{eff}, as shown in Figure 2.13. Therefore, K_{eff} can be defined as

$$K_{eff} = \sqrt{K_{\sigma,ma}^2 + \langle K_{\sigma,mi}^2 \rangle + \langle K_1 \rangle^2} \tag{2.43}$$

The average value of microscopic anisotropy can be rewritten as

$$\langle K_{\sigma,mi} \rangle = \frac{\frac{3}{2}\lambda\sigma_{mi}}{\sqrt{N}} \tag{2.44}$$

Therefore, the eqn.(2.43) can be written by including all the terms as

$$K_{eff} = \sqrt{\left(\frac{3}{2}\lambda\sigma_{ma}\right)^2 + \left[\left(\frac{3}{2}\lambda\sigma_{mi}\right)^2 + K_1^2\right]\frac{D^3}{A^{3/2}}} \tag{2.45}$$

If one considers negligible residual stress, then the eqn.(2.45) turns into eqn.(2.39) predicted by Herzer's RAM.

2.9. Law of approach to saturation:

The theoretical model based on micromagnetism of ferromagnetic materials was developed by Brown to describe the law of approach to saturation magnetization [BROW1940, BROW1941]. A generalized equation [KRON1959] derived for the high-field magnetization is

$$M(H) = M_S\left(1 - \frac{a_1}{\sqrt{H}} + \frac{a_2}{H} + \frac{a_3}{H^{3/2}} + \frac{a_4}{H^2} + \frac{a_5}{H^3}\right) + \alpha T\sqrt{H} + \chi_p H \tag{2.46}$$

where the terms a_n result from intrinsic properties such as MCA, spin-waves and the Pauli's paramagnetic susceptibility, as well as from extrinsic properties such as point defects, dislocations, grain boundaries and non-magnetic precipitations.

Intrinsic contributions: (1) MCA gives rise to a $1/H^2$ dependence. Local fluctuations of the MCA as in the amorphous alloys result in a $1/H^{1/2}$ term at low fields and a $1/H^2$ term at large fields. (2) The energy gap in the spin-wave spectrum due to the Zeeman energy gives rise the $\sqrt{H}$ term. (3) The linear term $\chi_p H$ is due to the enhanced Pauli's paramagnetism of the band structure.

Extrinsic contributions: Inhomogeneous spin states are produced by the stress sources due to the magnetoelastic interactions. Hence, the corresponding deviations of magnetization from the saturation values [$\Delta M = M_S - M(H)$] depend on the geometry of the defects, spatial variation of the stresses and the correlation between the defects. The change in the values of ΔM due to the defects is as follows: (a) point defects of radius r result in $\Delta M = a_4/H^2$, when $r_o > L_{ex}$, (b) straight dislocation dipoles of width D contribute as $\Delta M = a_2/H$, when $D < L_{ex}$ and $\Delta M = a_4/H^2$, when $D > L_{ex}$, and (c) nonmagnetic spherical precipitations of radius r_0 contribute as $\Delta M = a_{1/2}/H^{1/2}$, when $r_o < L_{ex}$ and $\Delta M = a_{3/2}/H^{3/2}$, when $r_o > L_{ex}$. Similarly, the effect of intrinsic fluctuations of the materials parameters such as local spin density, local magnetic anisotropy energy and local magnetic stray fields resulting from the local fluctuations of the spin density also affect M_S. Magnetoelastic coupling due to the stress induced sources has also effect on M_S of magnetic materials.

2.10. Soft magnetic materials and their applications:

As discussed earlier, soft magnetic materials belong to a class of ferromagnetic materials, which can be easily magnetized and demagnetized. Soft magnetic materials are typically characterized by high M_S and narrow hysteresis loops, *i.e.*, low H_C. The applications of soft magnetic materials are generally fall into two broad categories, *viz.* alternating current (AC) and direct current (DC) applications. For AC applications, the important consideration is how much energy is lost in the system as the material is cycled around its hysteresis. The energy loss originates from two main sources *viz.* hysteresis loss, relating to the area enclosed by the hysteresis, and eddy current loss, which is related to the generation of electric currents in the magnetic material and the associated resistive losses. While, hysteresis losses can be reduced by the reduction of H_C with a consequent reduction in the area enclosed by the hysteresis, eddy current losses can be reduced by increasing the electrical resistivity of the material and by laminating the material. In DC applications, the material is magnetized in order to perform an operation and then demagnetized at the conclusion of the operation.

Therefore, the development of soft magnetic materials has been mainly driven by the search for superior soft magnetic alloys and to meet the requirements of various magnetic applications. Recent research has been focused on achieving materials having large composition range with low H_C, high permeability and high M_S in a cost effective way. The continuing development of better materials has considerably improved the efficiency of key

building blocks of present electrical appliances like motors, generators, transformers, inductors *etc.*

2.10.1. Conventional soft magnetic alloys:

Among the soft magnetic alloys which find wide applications, Fe-Si is one of the earliest to be discovered. Barrett et al. [BARR1900] reported the improvement in the soft magnetic properties of Fe with the addition of Si in 1900. Significant progress occurred after the discovery of grain-oriented Fe-Si alloys (see Table 2.02) and Ni-Fe alloys (Table 2.03) such as permalloy in the 1940s. The range of soft magnetic materials was further extended by the development of ferrites in the 1950s [FISH1990]. The major families of the conventional soft magnetic alloys with important applications are briefly discussed below.

Table 2.02. Selected magnetic properties of some Fe-Si alloys [JILE1991].

Fe-Si Alloy	**Composition**	**Maximum Permeability, μ_{max}**	**H_C (Oe)**	**Saturation Induction, B_S (T)**
Fe-Si (Grain-oriented)	$Fe_{97}Si_3$	40,000	0.1	2.0
Fe-Si (Non-oriented)	$Fe_{96}Si_4$	4,000 – 15,000	0.4 - 1.5	2.1
Fe-Si (Non-oriented)	$Fe_{97.5}Si_{2.5}$	4,000 – 12,000	0.15 - 1.5	2.0

Table 2.03. Selected magnetic properties of some Ni-Fe alloys [JILE1991].

Alloy	**Composition**	**Maximum Permeability, μ_{max}**	**H_C (Oe)**	**Saturation Induction, B_S (T)**
Permalloy	$Ni_{78}Fe_{22}$	8,000	0.05	1.08
Hipernik	$Ni_{50}Fe_{50}$	4,000	0.05	1.60
Supermalloy	$Ni_{79}Fe_{16}Mo_5$	1,00,000	0.005	0.79
Mu-metal	$Ni_{77}Fe_{16}Cu_5Cr_2$	20,000	0.05	0.65

Fe-Si alloys: In electrical power generation and transmission, the highest demand is for transformer cores. Fe-Si alloys are used for transformer cores in exclusion of all other soft magnetic alloys and are commonly known as ‘electrical steels’ or ‘silicon steels’. In the power

industry, electrical voltage is almost always AC and at low frequency. At these frequencies, eddy currents are generated in the transformer core. Silicon is a less costly and easily available material and therefore gets importance to meet the huge demands of transformer core materials in large quantities. Addition of Si in Fe reduces the MCA and magnetostriction (*i.e.* length change on magnetization) of Fe and thereby decreases the coercivity. Further, the resistivity of Fe increases with the addition of Si and thereby reduces the eddy current losses [BARR1900]. The addition of too much of Si makes the material extremely brittle and difficult to produce, resulting in a practical limitation of the additive to 4 wt %. Often Al is added in Fe-Si alloys to increase the ductility of the alloy [BOZO1993]. Alloys with atomic composition $Fe_{75}Si_{15}Al_{10}$ (known as Sendust) are used as electrical steels for some special applications. Selected magnetic properties of some Fe-Si alloys are listed in Table 2.02.

Ni-Fe alloys: Selected magnetic properties of some Ni-Fe alloys are listed in Table 2.03. These alloys, also known as permalloy, are extremely versatile and are used over a wide range of compositions (from 30 to 80 wt% Ni). The properties of Ni-Fe alloys vary considerably over a wide composition range and the optimum composition can be selected depending on the application. There are special grades of Ni-Fe alloys that have zero magnetostriction and zero magnetic anisotropy, such as mu-metal which is produced by a careful heat treatment and minor additions of Cu and Cr. These alloys have extremely high relative permeability (up to 3,00,000) and H_C of 5×10^{-3} Oe. However, low M_S and the high cost of Ni, as compared to Si, limits these alloys only for some special applications.

Table 2.04. Selected magnetic properties of some Fe-Co alloys [JILE1991, LIUY2006].

	Composition	**Maximum Permeability, μ_{max}**	***H*C (Oe)**	**Saturation Induction, *B*S (T)**
Permendur	$Fe_{50}Co_{50}$	5,000	0.05	2.45
Supermendur	$Fe_{49}Co_{49}V_2$	60,000	1	2.40

Fe-Co alloys: Selected magnetic properties of some Fe-Co alloys are listed in Table 2.04. These alloys have higher saturation magnetization than pure Fe. They have both AC and DC applications, but high cost of Co has limited their applications only for some special purposes in high temperature applications.

Table 2.05. Selected magnetic properties of some amorphous alloys prepared by melt spun technique [HERZ1996].

Alloy composition	H_C **(Oe)**	**Saturation Induction,** B_S **(T)**
$Fe_{76}(SiB)_{24}$	0.04	1.45
$Co_{68}Fe_4(MoSiB)_{28}$	0.004	0.55
$Co_{72}(FeMn)_5(MoSiB)_{23}$	0.006	0.8

Table 2.06. Typical structural and magnetic parameters of selected nanocrystalline alloys.

Alloy composition	**Crystallite size,** D **(nm)**	H_C **(Oe)**	**Saturation Induction,** B_S **(T)**	**Reference**
$Fe_{73.5}Cu_1Nb_3Si_{13.5}B_9$	13	0.006	1.24	[YOSH1988]
$Fe_{73.5}Cu_1Nb_3Si_{15.5}B_7$	14	0.005	1.23	[HERZ1996]
$Fe_{84}Nb_7B_9$	9	0.10	1.49	[SUZU19911]
$Fe_{86}Cu_1Zr_7B_6$	10	0.04	1.52	[SUZU19911]
$Fe_{91}Zr_7B_2$	17	0.07	1.63	[SUZU19911]

2.10.2. Amorphous and nanocrystalline soft magnetic alloys:

Remarkable progress in soft magnetic materials took place in 1970s and 1980s with the advent of melt spun technique [BOLL1983, YOSH1988]. This technique provided a route to produce magnetic materials with new compositions and microstructure. Amorphous materials (also called metallic glasses) produced by melt spun technique are attractive candidates to replace the conventional spectrum of soft magnetic materials in both DC and AC applications. Due to the lack of long range order, amorphous alloys have no MCA and hence magnetic softness prevails. Mostly transition metal based alloys such as Fe-(B, P, Si), Fe-(Zr, Nb, Hf) are used as soft magnetic materials. The primary function of magnetic core materials is magnetic flux multiplication which requires both high M_S and high permeability. Both of these parameters are important for miniaturization. The desire for miniaturization also results in steadily increasing the operation frequencies which, of course, require low eddy-current losses. Hence, similar to amorphous materials, their production-inherent low thickness of 20 μm and their high residual resistivity of 100 $\mu\Omega$cm minimize eddy currents in nanocrystalline ribbons and make them attractive up to frequencies of 100 kHz and above. Apart from Fe based amorphous alloys, Fe-Co-B based alloys are used for soft magnetic purposes due to the zero

magnetostriction. By changing the Fe/Co ratio, magnetostriction of the material can be tuned and accordingly soft magnetic properties can be improved. The major advantages of these ferrites are high electrical resistivity and low cost. However, these alloys have low magnetization [MOOR1984, OHAN1987]. Selected magnetic properties of some amorphous materials prepared by rapid solidification technique are listed in Table 2.05.

On the other hand, crystallization of the amorphous precursors is known to yield coarse grain microstructure with crystallite size of about 0.1 – 1 μm with deteriorated soft magnetic properties. However, a milestone in magnetic materials was achieved by Yoshizawa et al. [YOSH1988], who found that crystallization of Fe(Si,B) glasses with the combined addition of small amounts of Cu and Nb yields an ultrafine grain structure of body centered cubic (*bcc*) Fe(Si) with crystalline size of 10 to 15 nm embedded in a minority amorphous matrix. These nanocrystalline alloys were found to exhibit ultralow coercivity of 10^{-3} Oe. The significance of these nanocrystalline alloys is that ultralow H_C could be obtained in Fe-Si based alloys with high saturation polarization of 1.2 T or even more with the potential of a huge impact in all soft magnetic applications. Typical structural and magnetic parameters of some nanocrystalline alloys are listed in Table 2.06. There are mainly three types of nanocrystalline alloys: FINEMET, NANOPERM and HITPERM. Fe-Si-B-Nb-Cu based alloys belong to the FINEMET family. In this case, α-Fe(Si) nanocrystals with a DO_3 structure gives rise to the soft magnetic properties [YOSH1988]. NANOPERM was developed in Prof. Masumoto's laboratory at IMR Tohoku University in 1989. Upon crystallizing the amorphous precursor of NANOPERM alloys, α-Fe nanocrystals developed inside amorphous matrix. The presence of two-phase microstructure is responsible for the magnetic softness in these alloys [SUZU19911, SUZU19912, MAKI1994]. The strong intergranular exchange coupling between the nanocrystals through the ferromagnetic amorphous matrix results very low MCA, which is averaged out and improves the soft magnetic properties. The presence of only α-Fe enhances the saturation induction. HITPERM alloy mainly consists of Fe-Co-Zr-B. The primary crystallization product of HITPERM alloy is α-Fe(Co) upon annealing. Due to the presence of Fe(Co) phase, saturation induction is quite high. Also, T_C is higher than that of NANOPERM type alloys. So, these alloys are used for high temperature applications.

2.10.3. Application of soft magnetic materials:

Soft magnetic alloys are used in numerous applications. Among these, a few prominent ones are summarized in this section. Amorphous based soft magnetic alloys are basically used in

power transformers, inductive mode choke coils, magnetic shields, magneto-elastic transducers and magnetic heads for data storage applications. These materials should have higher permittivity, large magnetic induction and high resistance for the above applications [MARI2000, KRON2007].

Co rich alloys in particular (Fe-Co)-Si-B exhibit vanishing magnetostriction in the as-made state, but exhibits outstanding properties related to a high initial susceptibility despite the low M_S [GOME1993]. A large field induces variations in the impedance of soft magnetic amorphous wires and ribbons, an effect known as the magnetoimpedance effect [PANI1994]. The effect as a magnetic field sensor can be adapted to monitor the passage of moving pieces or vehicles in many industrial processes. This would act as a position sensor based on magnetoimpedance effect. Also, this type of alloy can be used in antitheft system based on ferromagnetic resonance.

NANOPERM type alloys are used in transformer core materials due to the higher thermal stability and higher induction [MAKI1995]. Apart from that these materials are used as power transformers, common-mode choke coils, pulse transformers and flux gate magnetometers [MAKI1994]. A choke coil is an active filter used to prevent signal distortion in the reactor elements of phase modifying equipment. They provide line current corrections in all current signals. The core material of a choke coil needs large saturation induction, B_S and low core losses as well as small magnetostrictive coefficients. Since NANOPERM alloys have higher B_S values comparable to amorphous Fe-Si based alloys and lower core losses, these materials are suitable for above mentioned applications.

Fe-Co based HITPERM alloys are used in high temperature applications. These materials are used in space power systems. Other applications include core materials and winding wires for audio and radio frequency transformers. Due to the higher T_C of these materials they are used in aero-space applications [PARK1997].

FINEMET type alloys are used for the attenuation of pulse voltages in choke coils. These choke coils can be used over a wide frequency range as well as for protection from high voltage noise caused by lightning. These alloys are superior to Fe based alloys for this type of applications [MCHE1999].

Chapter 3

Experimental Methods

In the course of present investigations, several experimental techniques were used for the preparation and characterization of the samples. This chapter provides a brief description of these experimental techniques.

3.1. Materials processing techniques:

Material processing carried out in the present thesis involves two steps viz., high energy planetary ball milling of the pure elemental powders and heat treatment of as-milled powders under high vacuum. A brief discussion on both the techniques is given below.

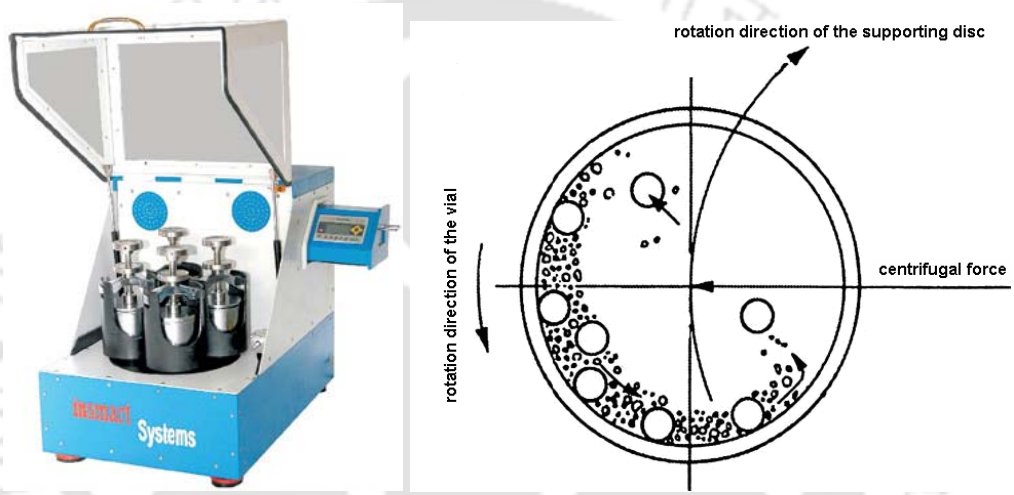

Figure 3.01. (a) Photographic view of the planetary ball mill used and (b) Schematic diagram of the horizontal section of a vial depicting the movement of the balls inside the vial due to its planet like movement.

3.1.1. Mechanical alloying technique:

Mechanical alloying of elemental powders was carried out by high-energy ball milling in a planetary ball mill (Insmart, India). The photographic view of the planetary ball mill comprising of a horizontal support disc on which vials are mounted and the schematic view of mechanical milling process are shown in Figure 3.01. The vial mounted on the horizontal disc rotates in a direction opposite to that of the disc and thereby simulating a planetary motion. This planetary motion results in large centrifugal force acting on the balls kept inside the vial. This causes the balls to collide with themselves and to the wall of the vial with high impact. When a mixture of elemental powders corresponding to a particular composition is placed in the vial along with the balls, the powders are subjected to repeated cold welding and fracture

at the surfaces of the balls and the vial. This process leads to disintegration of the powders, resulting first in refinement of crystallite size and ultimately in atomic level mixing of the elements to produce alloys [SONI2001, SURY2001, KOCH2002, SURY2004]. Hence, crystallite size refinement is a natural consequence of a mechanical alloying process. As the milling time progresses the alloy becomes amorphous. The refinement and alloying processes are determined by the milling parameters such as powder to ball weight ratio, ball size, rotation speed, milling time *etc*. Nature of the milling vial and balls also plays an important role in the process along with the milling media.

In the present thesis work, dry milling of high purity elemental powders has been carried out under high purity argon gas atmosphere. Hardened steel vial and hardened steel balls were used for milling of all the powder compositions. The ball to powder ratio was fixed at 10:1 and the rotating speed was varied between 500 and 600 rotations per minute for milling process. Prolonged milling under dry conditions results in a temperature rise inside the vial which usually deteriorates the final product. Thus, to avoid excessive heating, the mill was paused for 10 minutes after every 15 minutes of continuous milling. In addition, Ar gas was periodically filled inside the vial to avoid oxidation.

3.1.2. Heat treatment at elevated temperatures:

In order to release the strain accumulated during the milling process and to optimize the nanocrystalline microstructure, the selected as-milled powders were undergone heat treatment at elevated temperatures (annealing) using a resistive tubular furnace (Okay, India). This tubular furnace could be used up to a temperature of 1600 ˚C. The temperature of the constant temperature heat zone at the center of the furnace extends to 150 mm. The annealing temperature was controlled to ± 2 ˚C using a commercial temperature controller.

Since the as-milled powders would oxidize if heated to high temperatures under ambient conditions, the powders were sealed in evacuated fused silica ampoules prior to the heat treatment. For this purpose, ampoules of around 80 mm length with a constriction were fabricated from fused silica tubes of 8 mm internal diameter. Subsequently, as-milled powders were transferred into the well cleaned and dried ampoules and connected to a vacuum pumping system. The pumping system (Vacuum Techniques, India) consisted of a diffusion pump and rotary pump combination capable of creating a low pressure of 10^{-4} Pa. After creating the low pressure, the constricted (neck) portion of the ampoule was flame sealed with a neutral oxygen-liquid petroleum gas flame and the sealed ampoule was detached from the tube. These

ampoules were then loaded in the annealing furnace for heat treatment at elevated temperatures for constant duration of annealing.

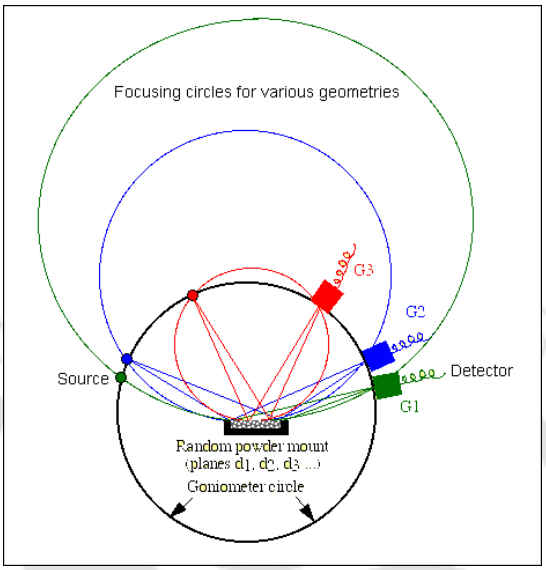

Figure 3.02. Bragg-Brentano geometry of a powder X-ray diffractometer.

3.2. Structural characterizations:

3.2.1. X-ray diffraction technique:

Two different powder X-ray diffractometers *viz.* Seifert 3003 T/T and high power (18 kW) Rigaku TTRAX III were used in the thesis work depending upon the availability. Cu-Kα X-ray radiation with a wavelength of 1.54056 Å was used in all the cases. The theta-theta ($\theta - \theta$) goniometer was used in the reflection (Bragg-Brentano) geometry (*cf.* Figure 3.02) [CULL2001]. The X-ray diffraction (XRD) technique allows identification of various crystalline phases present in the material and provides other structural information such as the size of the crystallites, strain present inside the crystallites, lattice constant *etc*.

It is well-known that an ideal crystal has a periodic arrangement of atoms. Diffraction of X-rays occurs through constructive interference of X-rays scattered from atoms of a set of parallel planes in crystal lattice at a particular angular positions of the incident wave known as Bragg angles [CULL2001]. This condition for obtaining constructive interference is known as Bragg's law given by the relation [CULL2001],

$$2d_{hkl}\sin\theta = n\lambda \qquad (3.01)$$

where d_{hkl} is the inter-planer spacing, θ is the glancing angle, λ is the wavelength of the X-ray and n is the order of diffraction. A series of these angles can be used to determine the Miller indices (hkl) values and the crystal structure can be identified from the systematic behavior of these indices. Figure 3.03 depicts the diffraction of X-rays from crystal lattice planes illustrating Bragg's law.

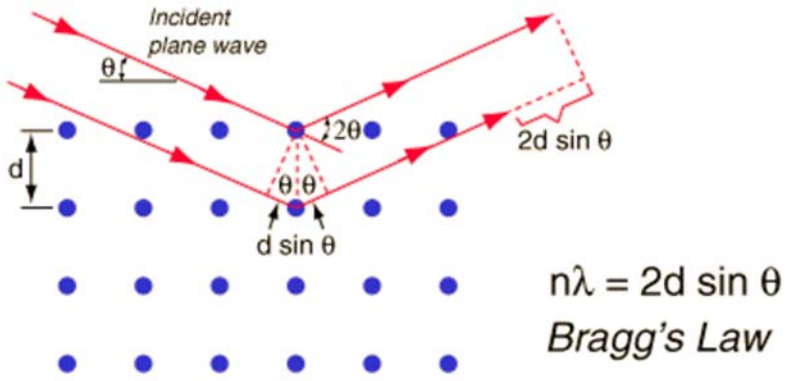

Figure 3.03. Diffraction of X-rays by a crystal.

The crystallite size and the strain present in the crystallites can be estimated from the width of the diffraction peaks. Reduction in the crystallite size results in less number of diffracting planes. This is analogous to the diffraction of light from a grating where the line width is proportional to the number of diffracting grooves in the grating. The broadening $\Delta\theta_{size}$ due to crystallite size can be quantified by Scherrer's formula [CULL2001],

$$\Delta\theta_{size} = \frac{k\lambda}{D\cos\theta} \qquad (3.02)$$

where $\Delta\theta_{size}$ is broadening due to crystallite size, θ is the peak position, λ is the wavelength of the X-ray and D is the size of the average crystallite of the material. Presence of strain also broadens the peak which can be quantified as [CULL2001]

$$\Delta\theta_{strain} = 4\eta\tan\theta \qquad (3.03)$$

where $\Delta\theta_{strain}$ is broadening due to strain and η is the lattice strain. To estimate the effects of crystallite size and strain to the broadening, Williamson and Hall [WILL1953] proposed a method by combining both equations (3.02) and (3.03) for a set of Bragg peaks. This method is a linear representative of the total broadening effect expressed as

$$\Delta\theta = \frac{k\lambda}{D_{WHP}\cos\theta} + 4\eta\tan\theta \tag{3.04}$$

or

$$\Delta\theta\cos\theta = \frac{k\lambda}{D_{WHP}} + 4\eta\sin\theta \tag{3.05}$$

In case of elastically anisotropic materials, certain Bragg peaks are more affected by strain than others. In such cases, the use of Williamson – Hall Plot (WHP) method for the analysis of size and strain is questionable. In order to consider the different strain contribution to different peaks, Modified Williamson-Hall Plot (MWHP) method [UNGA19991, UNGA19992] can be used to analyze the diffraction peaks. According to this model, the individual contribution to the broadening of XRD peaks can be expressed as

$$(\Delta K)^2 = \left(\frac{0.9}{D}\right)^2 + \left(\frac{\pi b^2\rho}{2B}\right)K^2 C_{hkl} \tag{3.06}$$

where ΔK [= ($2\cos\theta\Delta\theta/\lambda$], $\Delta\theta$ is full width at half maximum (FWHM) of the Bragg reflections (in radian) after correcting instrumental broadening, λ is wavelength of the X-ray, $K = 2\sin\theta/\lambda$, b is modulus of Burgers vector of dislocations, B is a constant (taken as 10 for a wide range of dislocation distributions [SHEN2005]), $C_{hkl} = C_{h00}\left(1 - qH^2\right)$ is dislocation contrast factor introduced to take care elastically anisotropic materials, where the residual strains affect some Bragg reflections more than the others, $H^2 = \left(h^2k^2 + k^2l^2 + l^2h^2\right)/\left(h^2 + k^2 + l^2\right)$ for a cubical system and q is a constant. To correct the instrumental broadening in XRD, the starting pure iron powder annealed at 1273 K for 24 hours was used as the reference powder. The instrumental broadening corrected line profile breadth ($\Delta\theta$), in radians, of each reflection was calculated from the parabolic approximation correction [KALI20082] described as,

$$(\Delta\theta)^2 = F^2\left(1 - \frac{f^2}{F^2}\right) \tag{3.07}$$

where F and f are the breadths of the same Bragg peak (in radians) from the XRD scans of the experimental and reference powders, respectively. Both F and f can be determined by the computer software Origin as the FWHM after automatic background removal. In the MWHP

formulation, Ungar et al. [UNGA19991, UNGA19992] considered that dislocations are main contributors to the strain. The plots between $(\Delta K)^2$ and K^2C_{hkl} can be fitted using a straight line and the values of D and ρ could be calculated from intercept and slope of the fitted straight line, respectively.

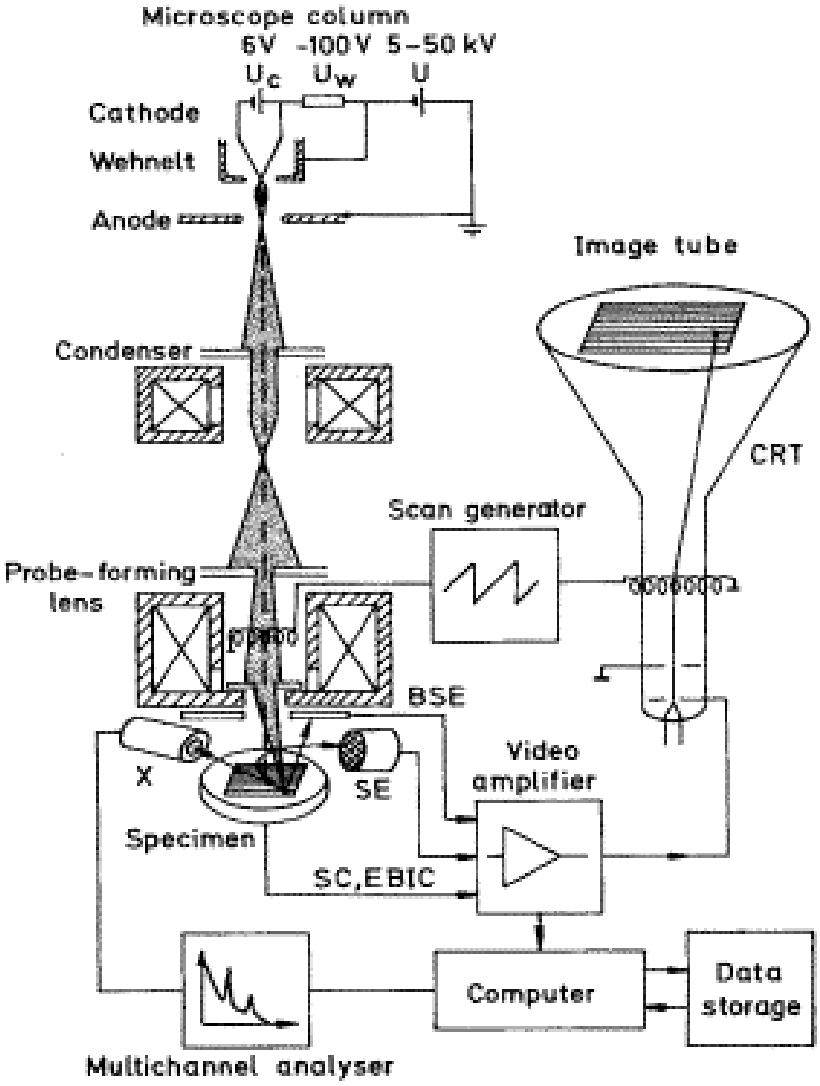

Figure 3.04. Schematic view of scanning electron microscope [MILT1992].

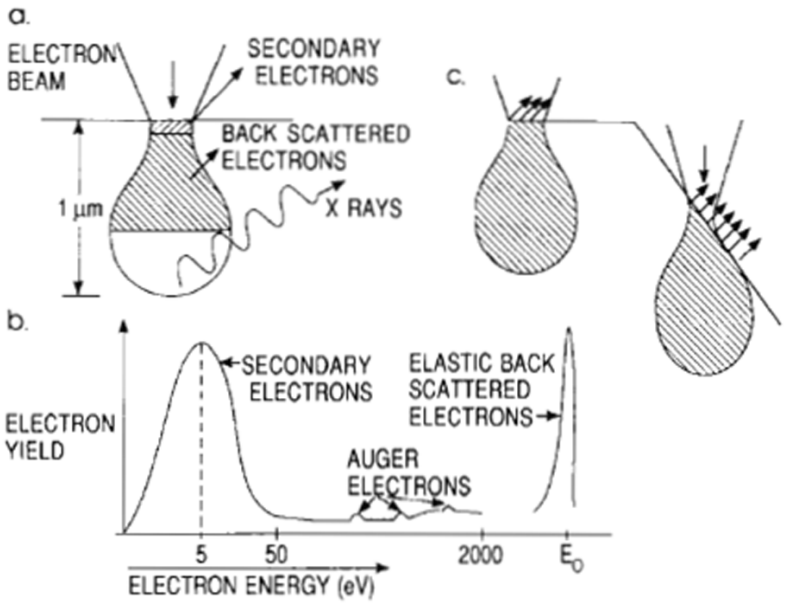

Figure 3.05. (a) Electron and photons signals emanating from tear-shaped interaction volume during electron beam impingement on specimen surface, (b) Energy spectrum of electrons emitted from the specimen surface, and (c) Effect of surface topography on electron emission.

3.2.2. Scanning electron microscopy:

Scanning electron microscope (SEM, Leo 1430VP) with energy dispersive spectroscopy (EDS) attachment (Oxford) was used to study the surface morphology and elemental compositions of the alloy powders. SEM is a microscopic technique that uses electrons to form an image of objects and to study surface morphology, fractured components, foreign particles and residues, polymers, electronic components, biological samples and countless others. The schematic view of SEM is shown in Figure 3.04. The thermionically emitted electrons from a tungsten filament or field emission controlled electrons are drawn to an anode, focused by two successive condenser lenses into a beam with a narrow fine spot size (~ 50 Å). The shorter wavelength of electrons permits image magnifications of up to 100,000 times in SEM. Pair of scanning coils located at the objective lens deflects the beam either linearly or in raster fashion over a rectangular area of specimen surface. Figure 3.05 displays the interaction of electrons on the surface of the sample. Upon electron impingement on the surface, the interaction volume assumes a tear shape. These primary bombarding electrons on the surface of the specimen dislodge electrons called as secondary electrons from the specimen. These dislodged secondary electrons are attracted and collected by a positively biased grid or detector, and then translated

into a signal. These signals are then amplified, analyzed and translated into images of the topography being inspected. Finally, the image is shown on a cathode ray tube. The most common imaging mode relies on the detection of the very lowest portion of the emitted energy distribution. Their very lower energy means they are originated from a subsurface depth of no longer than several angstroms.

Apart from secondary electrons, the primary electron beam results in the emission of backscattered (or reflected) electrons from the specimen. Backscattered electrons possess more energy than secondary electrons and have a definite direction. As such, they cannot be collected by a secondary electron detector, unless the detector is directly in their path of travel. All emissions above 50 eV are considered to be backscattered electrons. It may be noted that the backscattered electron imaging is useful in distinguishing one material from another, since the yield of the collected backscattered electrons increases monotonically with the specimen's atomic number Z (~ 0.05 $Z^{1/2}$). Backscatter imaging can distinguish elements with atomic number differences of at least 3, *i.e*. elements with atomic number differences of at least 3 would appear with good contrast on the image.

EDS analysis is quite useful in identifying materials and contaminants as well as estimating their relative concentrations on the surface of the specimen. During EDS analysis, the specimen is bombarded with an electron beam inside the SEM. The bombarding electrons colliding with the specimen knock off some of the electrons from the atoms. A position vacated by an ejected inner shell electron is eventually occupied by a higher-energy electron from an outer shell. To be able to do so, however, the transferring outer electron must give up some of its energy by emitting X-rays. The amount of energy released by the transferring electron depends on which shell it is transferring from, as well as which shell it is transferring to. Furthermore, the atom of every element releases X-rays with unique amounts of energy during the transferring process. Thus, by measuring the amounts of energy present in the X-rays being released by a specimen during electron beam bombardment, the identity of the atom from which the X-ray was emitted can be established. The output of an EDS analysis is an EDS spectrum, which is just a plot of how frequently an X-ray is received for each energy level. An EDS spectrum normally displays peaks corresponding to the energy levels for which the most X-rays had been received. Each of these peaks is unique to an atom, and therefore corresponds to a single element. The higher a peak in a spectrum, the more concentrated the element is in the specimen.

In the present work, a thin layer of powder was spread on carbon coated tape. Gold coating was then applied over it to yield an electrically conducting surface for SEM observation.

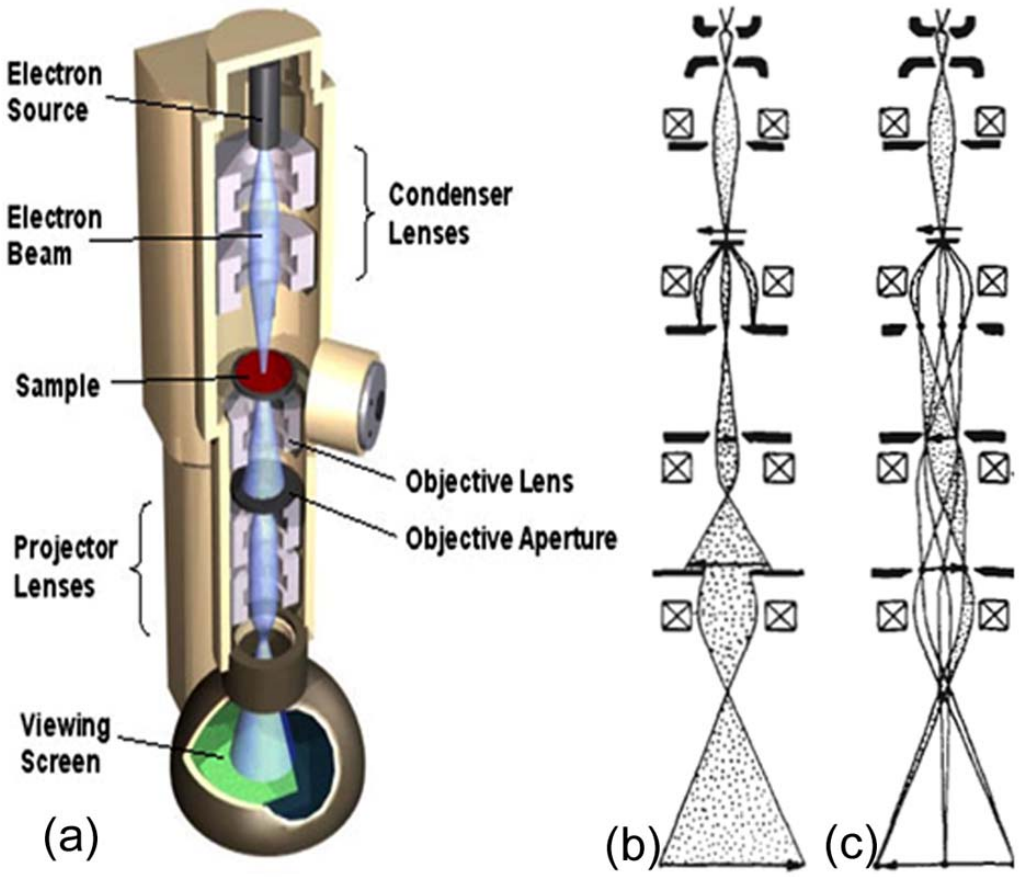

Figure 3.06. (a) Cut view of transmission electron microscope and (b) Schematic ray diagrams of image mode and (c) diffraction mode.

3.2.3. Transmission electron microscopy:

Transmission electron microscope (TEM, Jeol 2100) has been used to study the microstructure of the powders. TEM is an optical analogue to the conventional light microscope. It is based on the fact that electrons can be ascribed a wavelength (of the order of 0.25 nm), but at the same time interact with magnetic fields as a point charge. A beam of electrons is applied instead of light and the glass lenses are replaced by magnetic lenses. The lateral resolution of the best microscopes is down to atomic resolution. A schematic diagram of a TEM is shown in Figure 3.06.

Electrons emitted thermionically from a hot filament (electron gun) are accelerated to 100 keV or higher and first projected on to the specimen by means of the electromagnetic lens systems. The scattering processes experienced by electrons during their passage through the specimen determine the kind of information obtained as shown in Figure 3.07. Elastic

scattering involving no energy loss when electrons interact with the potential field of the ion cores gives rise to diffraction pattern. In-elastic scattering between beam and matrix electron at heterogeneities such as grain boundaries, dislocations, second-phase particles, defects, density variations cause complex absorption and scattering effects. The generation of characteristic X-rays and Auger electrons also occurs, but these by-products are not usually collected in a typical TEM measurement.

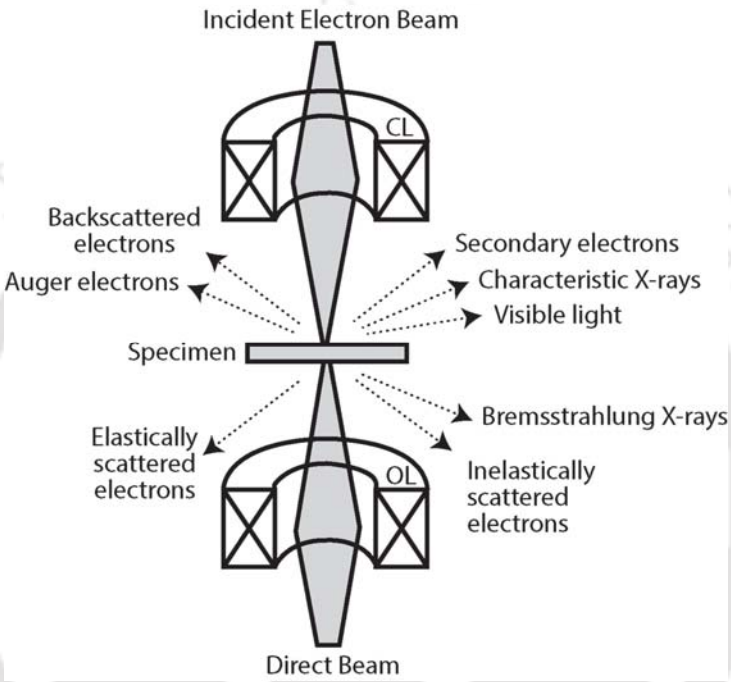

Figure 3.07. Various signals generated as a result of electron beam interaction with a thin solid specimen in TEM.

The emergent primary and diffracted electron beams are now made to pass through a series of post-specimen lenses. The objective lens produces the first image of the object. Depending on how the beams reaching the back focal plan of the objective lens, the beams are subsequently processed using different operation modes. Basically, either magnified images or diffraction patterns are obtained. The image can be studied directly by the operator or photographed with a camera.

Images can be formed in a number of ways. The bright-field image is obtained by intentionally excluding all diffracted beams and only allowing the selected portion of the central beam passed through the specimen. This is done by placing suitably sized apertures in the back focal plane of the objective lens. Intermediate and projection lenses then magnify this

central beam. Dark-field images are also formed by magnifying a single beam. Here, one of the diffracted beams is chosen by means of an aperture that blocks the central beam and the other diffracted beams. By selected area diffraction pattern, ring like structure is imaged, which corresponds to the particular plane of that element or compound. If only diffused rings appear then the system must have single amorphous phase. The high-resolution TEM image obtained by allowing both the central beam passing through the specimen and one or more of the diffracted beams helps to evaluate the average grain size and dislocations more precisely.

For TEM observation, the sample in the form of powder was dispersed in dimethyl formamide solvent using an ultrasonicator. A drop of the colloidal solution was placed on a carbon coated TEM grid and allowed to dry in a clean environment. The grid with the dried powder particles was then used for the TEM observation.

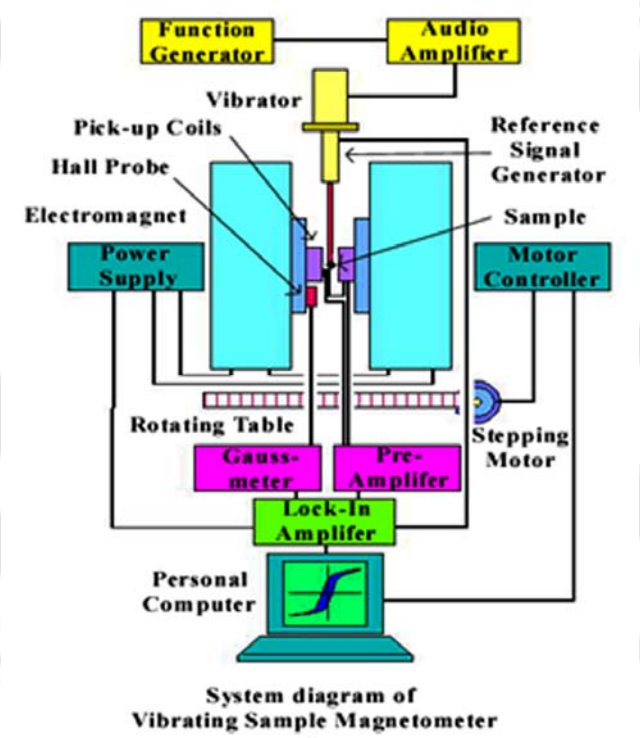

Figure 3.08. Schematic diagram of a vibrating sample magnetometer.

3.3. Magnetic property characterization:

Magnetic properties of a material can be characterized by using various experimental techniques such as vibrating sample magnetometer, superconducting quantum interference device, Faraday balance, ac susceptometer *etc.* In this section, a brief outline of the principle involved in vibrating sample magnetometer used in the present work is given.

3.3.1. Vibrating sample magnetometer:

Vibrating sample magnetometer (VSM, Lakeshore model 7410, USA) was used to investigate the magnetic properties at room temperature and temperature dependent magnetic properties. VSM [SVOB2004, CZIC2006] measures the net dipole moment when the material is exposed to magnetic field. The magnetic moment of the sample can be obtained either as a function of field (magnetic hysteresis loop) or as a function of temperature (thermomagnetization data) to investigate the variation of magnetic properties with temperature and understand the magnetic phase transition of the samples. Figures 3.08 and 3.09 display schematic diagram and a photographic view of VSM, respectively.

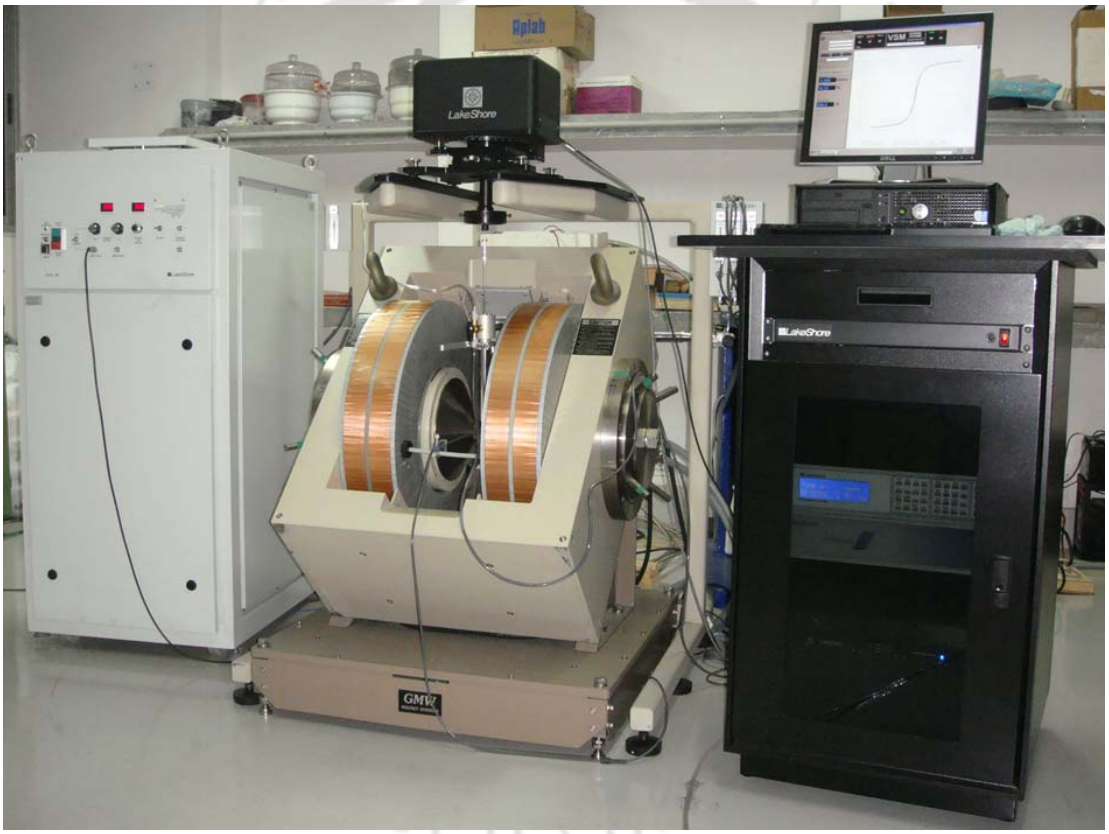

Figure 3.09. Photographic view of a vibrating sample magnetometer (Lakeshore Model 7410, USA).

When a sample is placed in uniform magnetic field, a dipole moment proportional to the product of the sample susceptibility and the applied field is induced in the sample. If the sample is made to undergo sinusoidal motion, an electrical signal can be induced in suitably located stationary pickup coils, as shown in Figure 3.07. This signal has amplitude proportional to the

magnetic moment of the sample, the vibrating amplitude and the vibration frequency. Through the use of lock-in-amplifier and feedback techniques, only that portion of the signal arising from the magnetic moment is picked up and is converted into direct read-out in the unit of magnetization (e.g. *emu*) on a digital panel meter. The VSM consists of the following major parts: 1. Water cooled electromagnet and power supply, 2. Vibration exciter and sample holder (with angular position indicator), 3. Sensing coils, 4. Hall probe, 5. Amplifier, 6. Control chassis, 7. Lock-in amplifier and 8. Computer interface.

The sample was fixed at the lower end of the sample holder after completing the calibration procedure using standard Ni sample. Subsequently, the measurement sequence is programmed using the IDEAVSM software provided with the instrument. The vibration exciter is started and the signal received from the probe and the pick-up coils is converted into the magnetic moment value of the sample. Magnetic fields in the range of 10,000 Oe to 15,000 Oe were applied to the sample. Normally, magnetic field is automatically increased in steps at a constant temperature (magnetization *versus* magnetic field (*M*-*H*)) by setting the program. For high temperature measurements (magnetization *versus* temperature (*M*-*T*)), a high temperature attachment (Lakeshore) capable of providing a controlled heating/cooling of the sample from room temperature to 1273 K was used. For $M - T$ measurements, we used a constant heating rate of 5 K per minute using the IDEAVSM software supplied with the instrument.

Chapter 4

Mechanical alloying of binary $Fe_{100-x}Si_x$ alloy powders

4.1. Introduction:

The study of magnetism in Fe based alloys has been the topic of research for the material scientists and condensed matter physicists due to its complex magnetic phenomena [PEPP2001, GORR2006] and technological applications [HONO2002, ZHAN2004, WITK2006]. Fe-Si based magnetic materials with nanocrystalline microstructure have been extensively investigated because of their remarkable soft magnetic properties [YOSH1988, HERZ1990, ZUOB2004, MIRA2008]. However, Fe-Si alloys with high Si content prepared by melt spun technique could not provide systematic compositional dependent physical properties owing to the limited alloying range available for this method. With the increasing demand for powder core technologies, the study of cheap and high Si content soft magnetic Fe-Si alloys become important [VARG2001]. In this regard, mechanical alloying technique was used to produce variety of Fe-Si based alloys with tunable properties [DAVI1987, KUHR1993, WALI1994, DING2001, SURY2001, KIMS2006, MIRA2008, RODR2008, BENS2009, BENS2010, BAHR2013, YOUS2014].

A careful review of the literature reports reveals that the properties of Fe-Si based nanocrystalline materials prepared by mechanical alloying strongly depend on the milling parameters. This makes it difficult to compare the properties of Fe-Si alloys reported by various research groups for different composition ranges prepared under different conditions. It may be noted that structural analysis using XRD limits the identification of finite amount of phases in the as-milled powders [PERE1996]. The development of various magnetic phases during the course of milling can also be investigated by performing thermomagnetic studies [CARM1991, ESCO1991]. However, no systematic investigations describing phase formation in Fe-Si alloys using thermomagnetization data in correlation with structural properties were reported. Since the properties of the materials are strongly dependent on their structure and composition, the understanding of correlation between structure and physical properties of a material is of fundamental importance in materials science. This eventually helps in designing and developing new materials for various technological applications [GORR2005]. However, most of the published results narrated the study of $Fe_{100-x}Si_x$ alloys at a few selected compositions and only limited investigations were focused over a wide range of Si content. Thus, in this chapter, we carry out systematic investigations on the effect of milling conditions and compositions on the structural and magnetic properties of $Fe_{100-x}Si_x$ ($5 \leq x \leq 50$) powders milled for various milling time periods with different milling speeds over a wide range of compositions.

4.2. Experimental details:

Fe-Si binary alloys corresponding to desired compositions of $Fe_{100-x}Si_x$ ($5 \leq x \leq 50$) were prepared from high purity (> 99.8%) elemental Fe and Si powders (>99.9%) by mechanical alloying method in a high energy planetary ball mill (Insmart India). In order to investigate the effect of various milling parameters carefully on the end product, the alloy powders were prepared at different milled speed such as 500 and 600 rotations per minute (rpm) and different milling time periods ranged between 5 and 100 hours. In the first part of the study, powder mixtures corresponding to the compositions $Fe_{100-x}Si_x$ (x = 10, 15, 20, 25, 30, 35, 40 and 50) were milled for 5, 10, 20, 30, 40, 60 and 100 hours under the milling speed of 500 rpm. The milling speed was increased to 600 rpm in the second part and studied the preparation of Fe-Si alloy powders corresponding to the compositions of $Fe_{100-x}Si_x$ (x = 5, 10, 15, 20, 25, 30, 35 and 40) milled at selected milling time periods (40 hours, 70 hours and 100 hours). The ball to powder weight ratio was fixed at 10:1 for all the sample preparation. For the milling process, the weighed quantities of powder mixtures and hardened steel milling balls (8 mm diameter) were loaded into a hardened steel bowl in the mill station. The bowl was filled with high purity argon gas to minimize oxidation during milling. The milling process was paused for 10 minutes after every 15 minutes of milling to minimize excessive temperature rise.

The evolution of nanocrystalline microstructure and other structural properties were characterized by X-ray diffraction (XRD) in a high-power X-Ray diffractometer (Rigaku TTRAX III 18 kW) using Cu-K_α radiation. XRD data were collected at a slow scan rate of 0.005°/s to analyze the structural parameters such as lattice constant, average crystallite size, dislocation density and fraction of grain boundaries using different structural analysis methods. The changes in the surface morphology and evolution of nanocrystalline microstructure were investigated by scanning electron microscope (SEM, Leo 1430VP), field emission scanning electron microscope (FE-SEM, ZEISS) and transmission electron microscope (TEM, JEOL 2100), respectively. Overall composition of the milled powders was verified using energy dispersive spectrometer (EDS, Oxford) attached to SEM. Magnetic properties of the as-mixed and milled powders were characterized by using vibrating sample magnetometer (VSM, LakeShore Model 7410, USA) by performing magnetic hysteresis (*M-H*) loops at room temperature and high temperature thermomagnetization (*M-T*) curves under constant applied magnetic field.

4.3. Properties of Fe-Si binary alloy powders milled at 500 rpm:

4.3.1. Structural evolution during milling:

Figure 4.01 shows typical room temperature XRD patterns of as-mixed and 100 hours milled $Fe_{90}Si_{10}$ powders. The as-mixed powders show the Bragg reflections from the planes of the individual elements Fe (body centered cubic (*bcc*)) and Si (diamond cubic). However, after 100 hours of milling, the reflections corresponding to Si disappeared completely leaving behind only the *bcc* α-Fe reflections. This suggests that Si has dissolved in α-Fe matrix and hence forming a non-equilibrium solid solution of α-Fe(Si). Further, the width of α-Fe(Si) reflections increased considerably indicating the formation of highly refined and strained alloy powders. In addition, there is a measurable shift in the peak positions of the milled powders to higher angles. This suggests that there is a considerable change in the lattice constant during the milling process. In order to understand the evolution of non-equilibrium solid solution carefully, we have carried out systematic analysis of XRD patterns collected at different milling time periods between 5 hours and 100 hours.

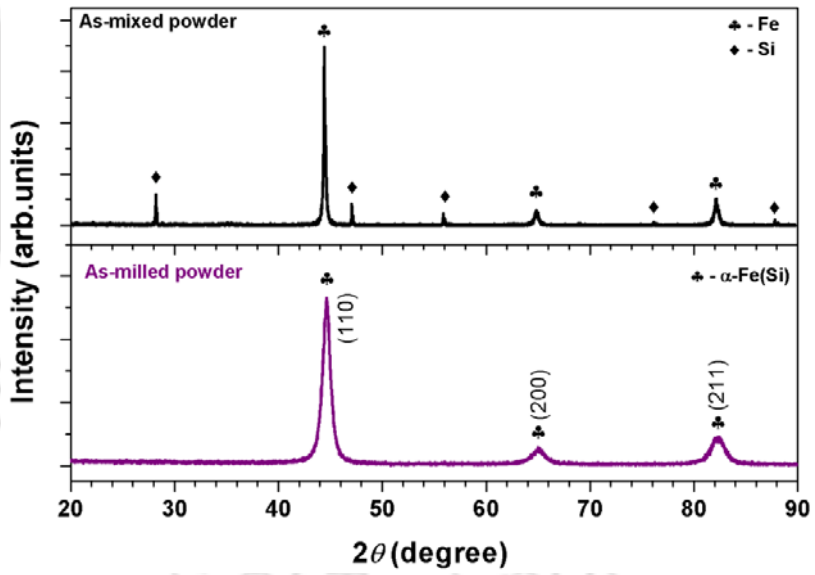

Figure 4.01. Typical room temperature XRD patterns of as-mixed and 100 hours milled $Fe_{90}Si_{10}$ alloy powders.

Figure 4.02 depicts the XRD patterns of $Fe_{90}Si_{10}$ alloy powders milled for various milling time periods. With increasing milling time, the reflections corresponding to Si decrease progressively and disappear completely within the resolution of high-power XRD technique after 20 hours of milling. In addition, the broadening of the α-Fe(Si) peak increases and the peak position shifts slightly to higher angles with increasing milling time. A careful analysis

of the lattice constant from the XRD patterns of the milled powders reveals that the lattice constant decreases from 0.28715±0.00007 nm to a nearly stable value of 0.28656±0.00008 nm after 40 hours of milling. This reveals a maximum lattice change of 0.00059 nm in the as-milled powders. This could be attributed to the substitutional dissolution of Si in Fe matrix with milling since atomic radius of Si (0.118 nm) is smaller than Fe (0.125 nm).

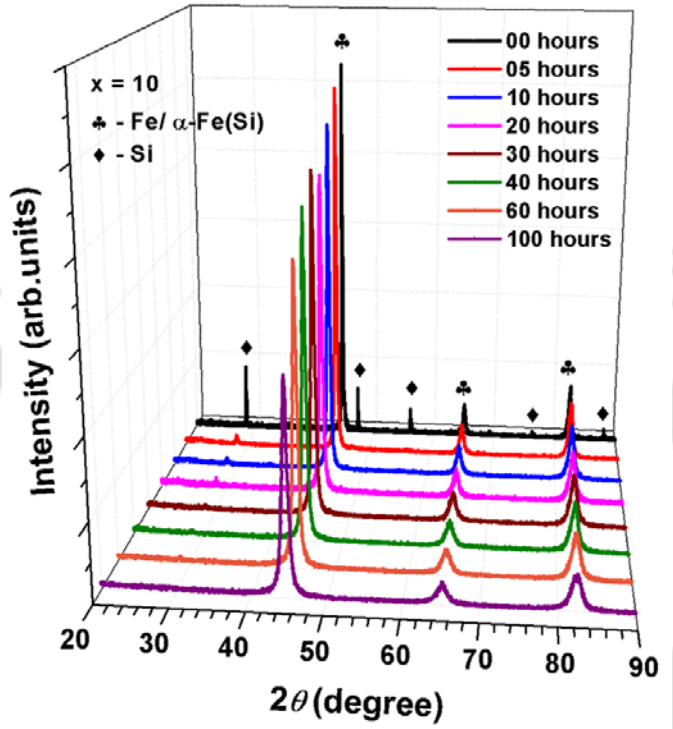

Figure 4.02. Room temperature XRD patterns of $Fe_{90}Si_{10}$ alloy powders milled for different time periods.

The degree of dissolution of Si in α-Fe is estimated by following the results reported on the rapidly quenched Fe-Si alloys [PERE1996]. According to Perez et al. [PERE1996], the introduction of Si into Fe decreases the lattice constant at a rate of 0.000065 nm per at.% Si. This suggests that the addition of 10 at.% Si should decrease the lattice constant of Fe from 0.28715 nm to 0.2865 nm. A comparison between the experimental observation and the above calculation confirms that nearly 90 % of Si occupy in *bcc* α-Fe with the rest 10 % predominantly residing in grain boundaries. This is in better agreement with the earlier reports on $Fe_{75}Si_{25}$ system [KALI20081]. On the other hand, the $Fe_{90}Si_{10}$ samples milled for 100 hours exhibit a slight increase in the lattice constant from 0.28656±0.00008 nm to 0.28682±0.00010 nm. This could be caused by the defects introduced at the interfaces by the prolonged milling. Zeng et al. [ZENG2007] reported that in the nanostructured materials the less dense structure

of the interfaces can result in some negative pressure on the interfaces which can lead to an increase in the lattice constant. Further, the introduction of lattice defects during mechanical alloying and the existence of a solid solution with a high volume fraction of grain boundaries could raise the free energy of the system and provide a condition in which the substituted Si atoms will be able to leave the grains toward grain boundaries. This will reduce the energy of the system, resulting in an increase in the lattice constant [STEV1999, BENS2009, BAHR2013].

It is well known that broadening of XRD peaks occurs due to the refinement of average crystallite size (D), instrumental broadening, and strain caused by the density of dislocations (ρ) induced during mechanical alloying process [DING2001, SURY2001]. In order to calculate the effective variation in the values of D and ρ, the contribution from instrumental broadening must be corrected properly. Therefore, to correct the instrumental broadening in XRD data, the starting pure iron powder annealed at 1273 K for 24 hours was used as the reference powder. The instrumental broadening corrected line profile breadth ($\Delta\theta_B$), in radians, of each reflection was calculated from the parabolic approximation correction [KALI20082] described as,

$$(\Delta\theta_B)^2 = F^2\left(1-\frac{f^2}{F^2}\right) \tag{4.01}$$

where F and f are breadths of the same Bragg peak (in radians) from the XRD scans of the experimental and reference powders, respectively. Both F and f were determined by the computer software Origin as the FWHM after automatic background removal. Subsequently, to separate the individual contributions from D and ρ, XRD patterns were analyzed using Williamson-Hall Plot (WHP) method [WILL1953] described by the formula given in eqn.(4.02),

$$\Delta\theta_B\cos\theta_B = \frac{k\lambda}{D_{WHP}} + 4\eta\sin\theta_B \tag{4.02}$$

where $\Delta\theta_B$ is full width at half maximum (FWHM) of Bragg reflections (in radians), λ (= 1.5406Å) is wavelength of X-ray, θ_B is angle of Bragg reflection, D_{WHP} is average crystallite size, k is constant taken as 0.9 by assuming spherical nature of particles and η is effective strain. In order to validate the WHP fit to XRD data, the eqn.(4.02) is modified to

$$\Delta K = \frac{k}{D_{WHP}} + K\eta \qquad (4.03)$$

where ΔK [= $(\Delta\theta_B \cos\theta_B)/\lambda$] and $K = 4\sin\theta_B/\lambda$.

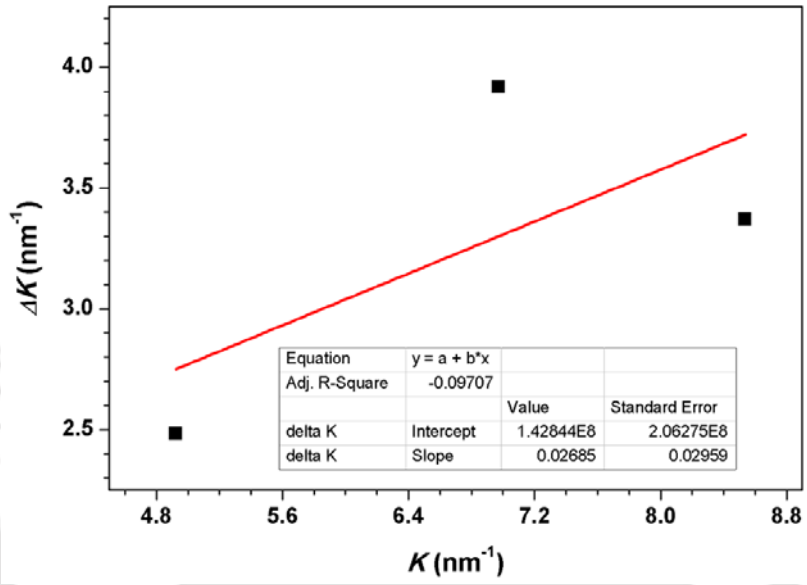

Figure 4.03. WHP fit for $Fe_{90}Si_{10}$ alloy powders milled for 60 hours. The straight line passing through the data points is the linear fit to eqn.(4.03).

Figure 4.03 depicts the plot of ΔK versus K for as-milled $Fe_{90}Si_{10}$ powder and the typical linear fit to the data using eqn.(4.03). It is quite obvious from figure that the data do not fall into straight line and hence not entirely obey the linear fit to WHP formulation. The deviation observed in the data can be correlated to the existence of anisotropic variation in the residual strain. Hence, certain Bragg reflections may exhibit large strain component than others. Ungar et al. [UNGA19991, UNGA19992] suggested a modification to WHP method by including dislocation contrast factor in order to consider the anisotropic distribution of dislocation effects on different Bragg peaks. Hence, to separate the size and strain effects effectively for the presently investigated samples, the XRD patterns were analyzed using Modified Williamson-Hall Plot (MWHP) method. According to this method, individual contribution to the broadening of reflections can be expressed as

$$(\Delta K)^2 = \left(\frac{0.9}{D}\right)^2 + \left(\frac{\pi b^2 \rho}{2B}\right) K^2 C_{hkl} \qquad (4.04)$$

where ΔK [= $(2\cos\theta_B \Delta\theta_B)/\lambda$], $K = 2\sin\theta_B/\lambda$, b is modulus of Burgers vector of dislocations taken as $b = \left(\sqrt{3}/2\right)a$ [SHEN2005], D is average crystallite size, a is lattice constant, ρ is average dislocation density, B is constant (taken as 10 for a wide range of dislocation distributions), C_{hkl} is the dislocation contrast factor calculated using the relation [UNGA19991, UNGA19992]

$$C_{hkl} = C_{h00}\left(1 - qH^2\right) \tag{4.05}$$

where $H^2 = \left(h^2k^2 + k^2l^2 + l^2h^2\right)/\left(h^2 + k^2 + l^2\right)^2$ for a cubic crystal system, q is a constant and C_{h00} = 0.252 [KALI20081, UNGA19992, SHEN2005, MHAD2010] introduced to take care of elastically anisotropic materials. To deduce the optimal values of D, ρ and q, we have followed the procedures given by Ungar et al. [UNGA19992] to carry out a series of linear fits by combining equations (4.04) and (4.05). The obtained value of q in the presently investigated samples is ranged between 1.6 and 2.5.

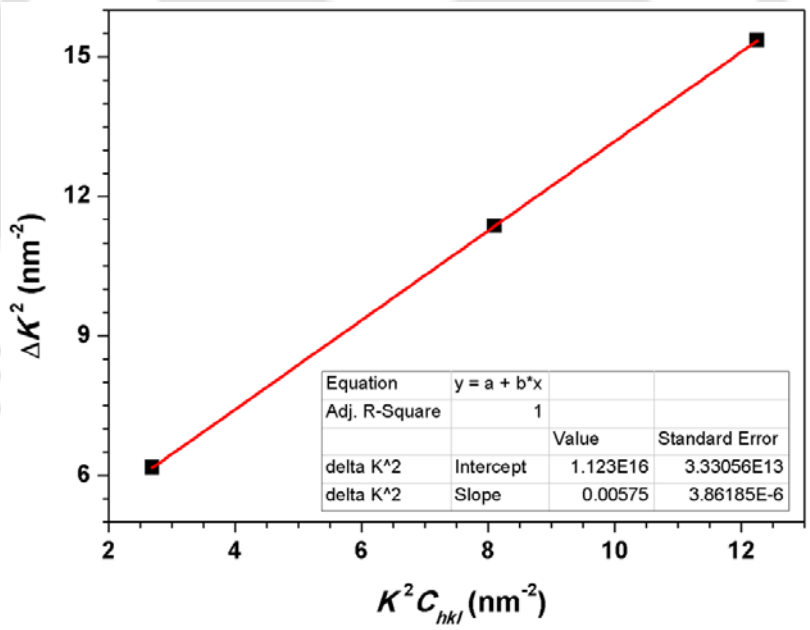

Figure 4.04. MWHP fit for $Fe_{90}Si_{10}$ alloy powders milled for 60 hours. The straight line passing through the data points is the best fit to eqn.(4.04).

Figure 4.04 depicts the typical plot of $(\Delta K)^2$ versus K^2C_{hkl} and the linear fit using eqn.(4.04). It is clear from the figure that all the XRD data fall into straight line showing the applicability of the MWHP method as compared to WHP method for the present data. The plot

between $(\Delta K)^2$ and K^2C_{hkl} was fitted using a straight line as described in eqn.(4.04) and the values of D and ρ were calculated from intercept and slope of the fitted straight line, respectively. This fitting procedure provides supporting evidence to the fact that in the mechanically milled powders dislocations are the major reasons of residual strain and they affect each Bragg reflections differently.

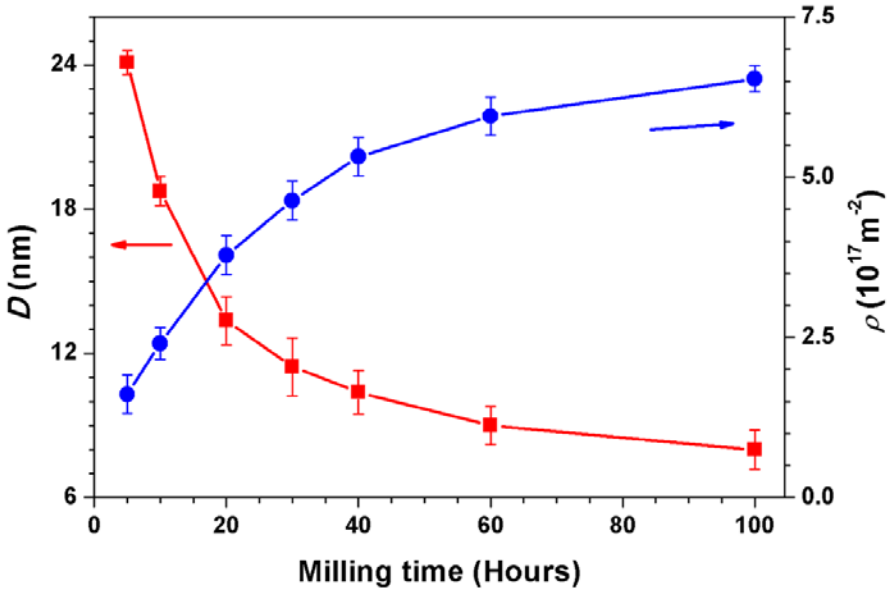

Figure 4.05. Variations of D and ρ as a function of milling time for $Fe_{90}Si_{10}$ alloy powders milled for different time periods.

Figure 4.05 summarizes the variations of D and ρ for $Fe_{90}Si_{10}$ powders as a function of milling time. The values of D decrease progressively up to 40 hours of milling and then attain a nearly constant value, while the ρ values increase with increasing milling time and ultimately show a tendency to saturate at longer milling time. The values of ρ reach up to the order of 10^{17} m^{-2} after milling for 60 hours. This indicates the formation of one to seven dislocations for every 10 nm^2 area by the mechanical alloying process [KALI20081, KALI20082, BOUK2012]. This systematic study reveals the development of non-equilibrium solid solution of α-Fe(Si) with nanocrystalline microstructure during the mechanical alloying process. The formation of solid solution with nanosized crystallites suggests that the solid solution would be harder and stronger than pure metal [AGUI2010]. As discussed earlier, mechanical alloying is a simple method to produce large variety of nanomaterials at the solid state. In order to enhance the solubility, the exterior energy should be supplied. The energy is eventually transferred to the powders during the milling process. Further, intense deformation is

introduced into the particles during the mechanical alloying process. It was reported that the rates of dissolution of the powders were directly related to the dislocation densities introduced by the comminution [ALBA1987]. Therefore, dislocation density is one of the major structural parameters influencing the final nanocrystalline microstructure. As the milled powders subjected to severe plastic deformation, the density of dislocations can be correlated by [HULL2001],

$$\rho = 2\sqrt{3}\frac{\langle \eta_{rms} \rangle}{Db} \tag{4.06}$$

where $\langle \eta_{rms} \rangle$ is root mean square lattice strain, b is modulus of Burgers vector of dislocations, as defined in eqn.(4.04). It is clear from the above equation that the development of large density of dislocations increases the probability of forming highly refined crystallites. On the other hand, when the crystallite size reaches a saturation value, further milling will not produce more dislocations due to the difficulty of generating dislocations at smaller crystallites. It may be noted that at this stage the existing dislocations will be rearranged and some dislocations may be annihilated due to prolong milling [AGUI2009]. This process also promotes the formation of grain boundaries in the final nanocrystalline alloys. It is well understood that the basic underlying mechanism of grain refinement involves an increase in the dislocation density by heavily deforming the materials as shown in Figure 4.05. These dislocations form an ordered arrangement of walls and as the deformation continues these walls transform into grain boundaries. The crystallites in severely deformed materials are divided into subcrystallites which are separated from each other by low-angle grain boundaries. These grain boundaries eventually affect the movement of dislocation significantly. As the average crystallite size decreases largely with increasing milling time period in the presently investigated samples, we have tried to estimate the development of fraction of grain boundaries (f_{GB}) in as-milled powders. The fraction of grain boundaries is in inverse proportion to grain size defined as [YOUS2012],

$$f_{GB} = 1 - \frac{(D - d_{eGB})^3}{D^3} \tag{4.07}$$

where D is the average crystallite size calculated from XRD pattern using MWHP method, d_{eGB} is the effective grain boundary thickness which is associated with the average atomic diameter (D_{aad}) of the major elements in the nanocrystalline materials given as [SONG1999],

$$d_{eGB} = 84 D_{aad} - 21.7 \quad (4.08)$$

where both d_{eGB} an D_{aad} are in nanometer scale. This relation suggests that larger the atomic diameter, the wider the effective grain boundary. In most of the nanostructured alloys, the estimated thickness of the interfaces was roughly found to be 2 to 3 atomic layers [YOUS2012]. The values of f_{GB} were determined using eqn.(4.07) for the powders milled at different milling time periods and depicted in Figure 4.06. As expected, the fraction of grain boundaries increases to a great extent with increasing milling time period and attains a maximum value of nearly 20 % for 100 hours milled powders. Similar increase in the fraction of grain boundaries with increasing milling time period in mechanically alloyed nanocrystalline Fe-Co-Si powders was reported by Yousefi et al. [YOUS2014]. Bahrami et al. [BAHR2013] shown the value of f_{GB} as 13 %, 18 % and 28 % when the average crystallite size is 14, 10 and 6 nm, respectively in Fe-Ni-Si alloy powders milled for 36 hours. These results suggests that the fraction of grain boundaries in the as-milled powders strongly depends on the composition of the alloys and milling parameters.

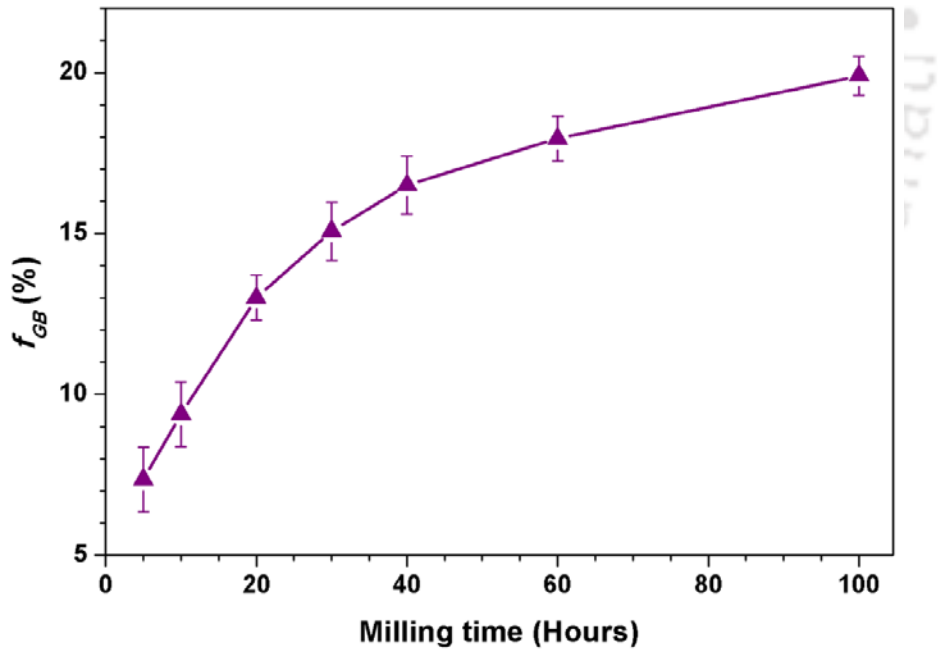

Figure 4.06. Variation of f_{GB} as a function of milling time for $Fe_{90}Si_{10}$ alloy powders milled for different time periods.

In order to understand the development of nanocrystalline microstructure and to analyze the existence of defects in the nanostructure, TEM observations were carried out for as-milled

powders. Figure 4.07 displays typical bright-field TEM (BF-TEM) image, selected area electron diffraction (SAED) pattern, high-resolution TEM (HR-TEM) image and inverse-Fast Fourier Transform (i-FFT) image of selected area of HR-TEM image of $Fe_{90}Si_{10}$ powders milled for 60 hours. BF-TEM micrograph displays the existence of fine-grain microstructure, which is a typical characteristic of mechanically alloyed powders. The non-uniform contrast inside each grain and along the grain boundaries observed in BF-TEM image indicates the presence of high degree of strain in the as-milled powders. SAED pattern shows the polycrystalline nature of the powders with the rings corresponding to reflections from (110), (200) and (211) planes of α-Fe(Si). The *d*-spacing and lattice constant were calculated from the electron diffraction pattern for the 60 hours milled samples. These results agree well with the values obtained from XRD peak analysis. HR-TEM image also supports the presence of fine nanometer sized crystallites with high degree of strain.

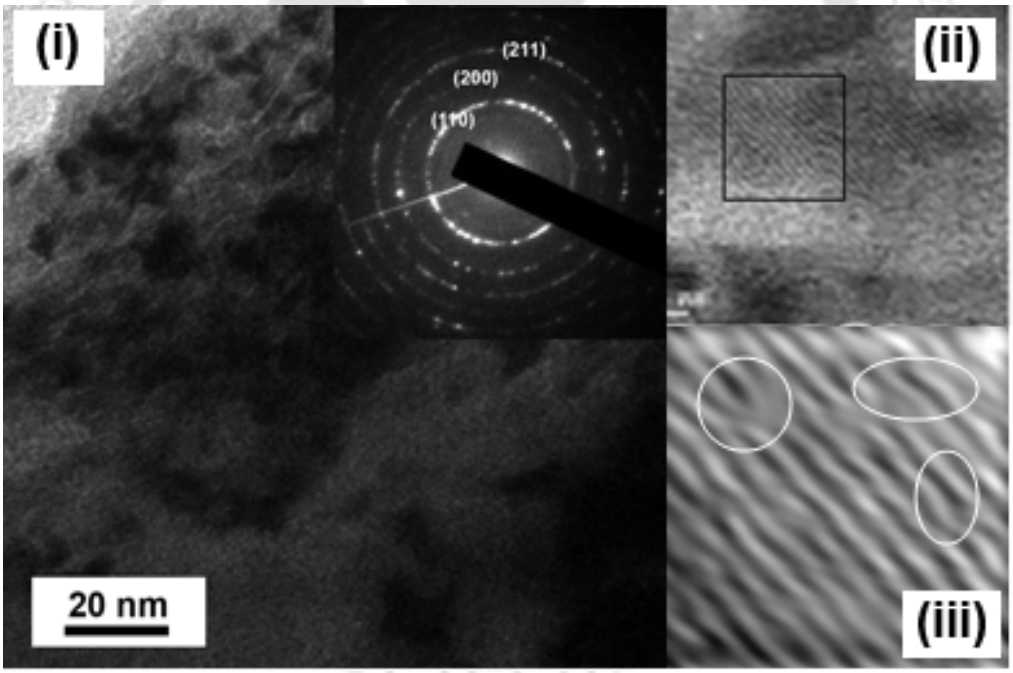

Figure 4.07. (i) BF-TEM micrograph and SAED pattern (ii) HR-TEM image and (iii) i-FFT image of selected area of HR-TEM image [highlighted by square box in Figure 4.07(ii)] of $Fe_{90}Si_{10}$ alloy powders milled for 60 hours.

However, the existence of defects in the crystallites could not be directly observed from the HR-TEM images. This is mainly due to the limitation of the TEM instrument used for observing such high resolution images. In order to analyze the existence of possible defects,

the HR-TEM image was resolved by inverse-fast Fourier Transform (i-FFT) method using GATAN digital micrograph software and shown in Figure 4.07(iii) for 60 hours milled $Fe_{90}Si_{10}$ powders. The i-FFT image of the selected area of the HR-TEM image clearly confirms the presence of dislocations, which are highlighted by circles. These results show that a highly strained and defective nanostructure has been formed after 60 hours of milling in the presently investigated sample.

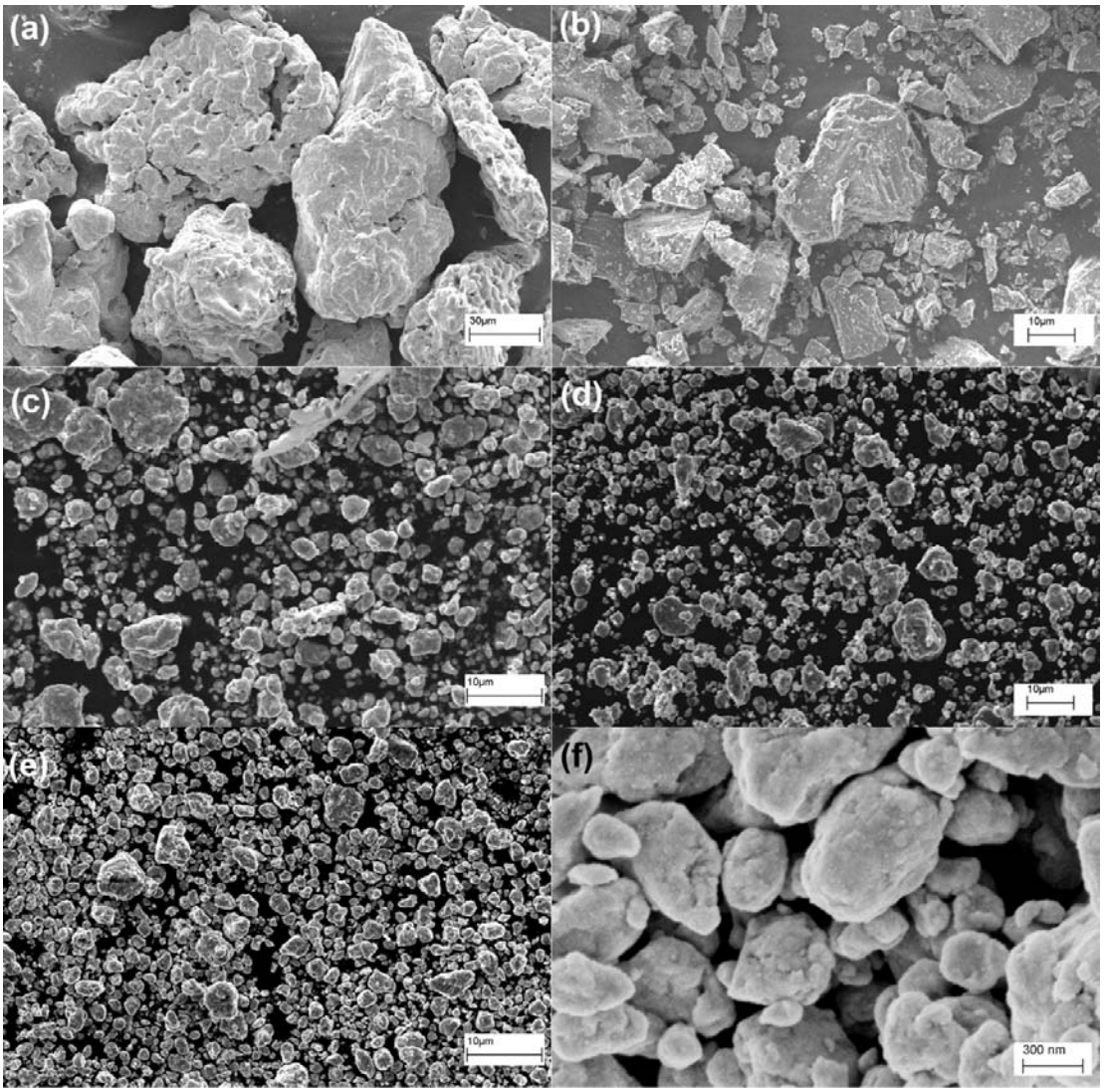

Figure 4.08. SEM micrographs of pure (a) Fe, (b) Si and $Fe_{90}Si_{10}$ alloy powders milled for various time periods: (c) 5 hours, (d) 10 hours, (e) 30 hours and (f) 60 hours.

Changes in the surface morphology of the powders with increasing milling time periods were observed from the SEM micrographs of pure powders and powders milled for various milling time periods and presented in Figure 4.08. As shown in the Figures 4.08 (a) and (b),

pure Fe powder exhibits predominantly rounded shape with large sized particles in the range between 60 and 100 μm [DEME2013], whereas the Si powder shows plate-like morphology [BAHR2013] and contains finer particles in the size range of 5 to 30 μm as compared to the Fe powder. After the initial milling stage, the average particle size resulting from the aggregation of many crystallites has reduced significantly, but has an irregular morphology up to 10 hours of milling. The particle size distribution is also found to be relatively inhomogeneous. Such aggregates are typical of mechanically alloyed powders and result from the repeated cold-welding and fracture of powders during ball milling [LUL1998]. For higher milling time periods, the particle size becomes smaller in the size range of 300 to 600 nm and the size distribution becomes narrower with spherical shape in nature. However, no significant change in particle size of the powders could be observed after 30 hours of mechanical alloying. The average crystallite size calculated from the XRD analysis is about 10 nm for 60 hours milled powders. These results suggest that the particles with sizes ranging from few hundred nanometers to few micrometers observed in SEM micrographs are agglomerations of nanosized (~10 nm) crystallites oriented randomly within the particles. Composition analysis was performed on 60 hours milled powders using EDS. The results of the analysis showed the overall average composition to be $Fe_{90.3}Si_{9.7}$. This indicates the presence of Si in the form of solid solution in α-Fe.

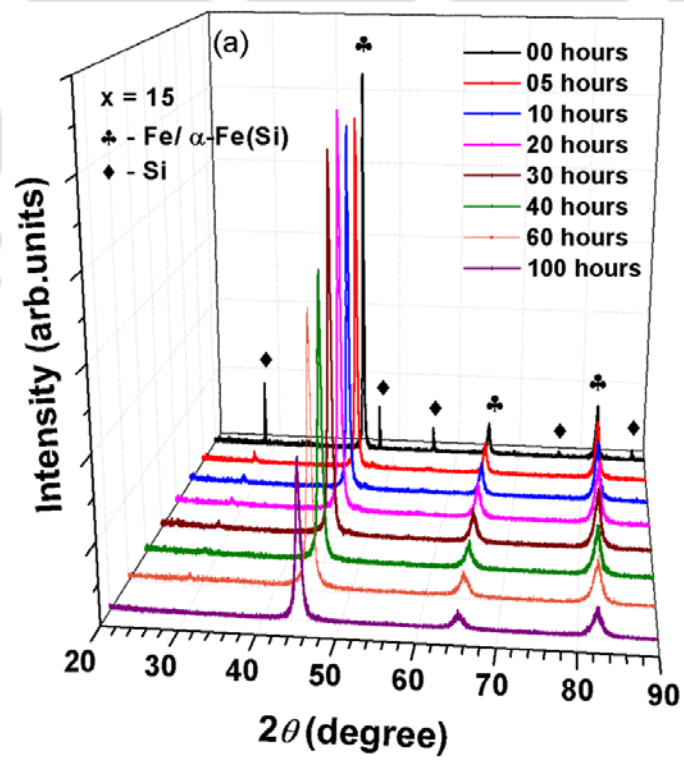

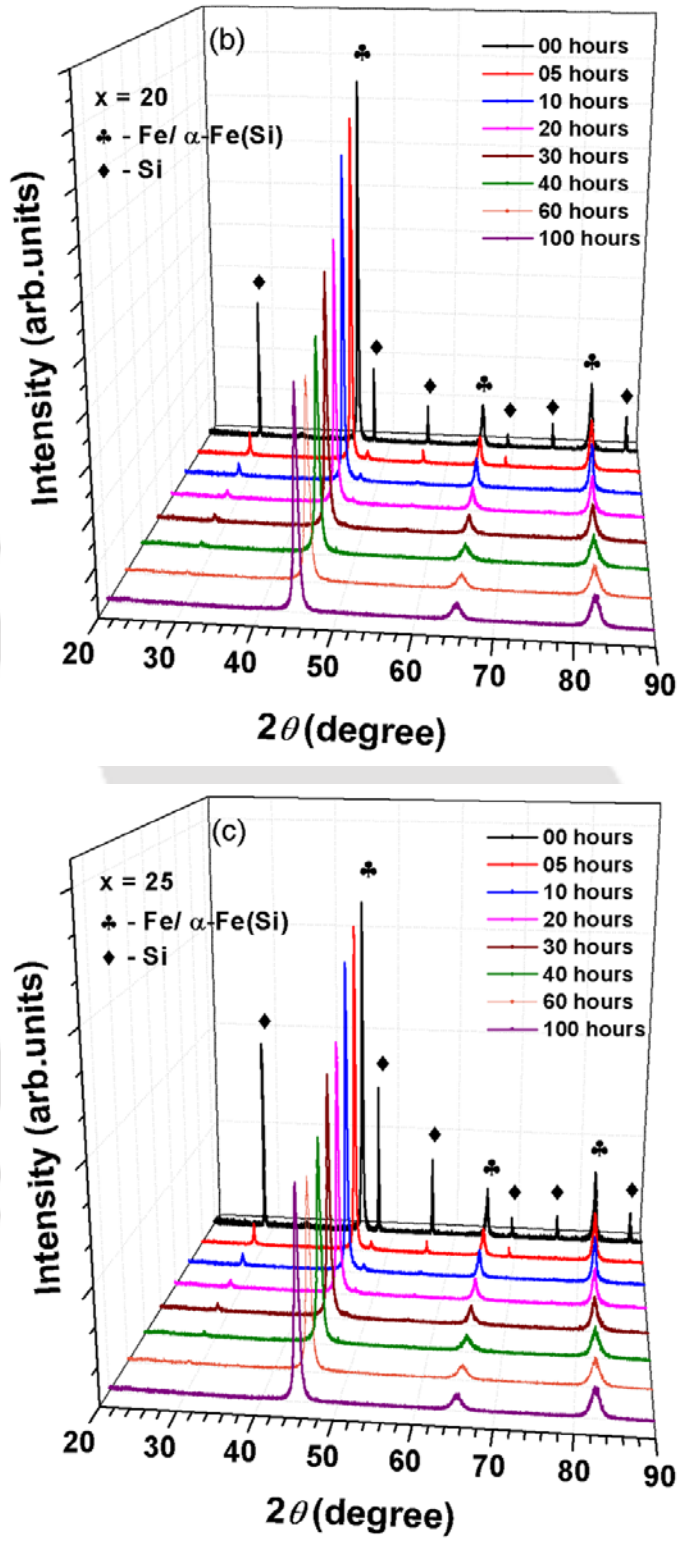

Figure 4.09. Room temperature XRD patterns of $Fe_{100-x}Si_x$ alloy powders with (a) x = 15, (b) x = 20 and (c) x = 25 milled for various milling time periods.

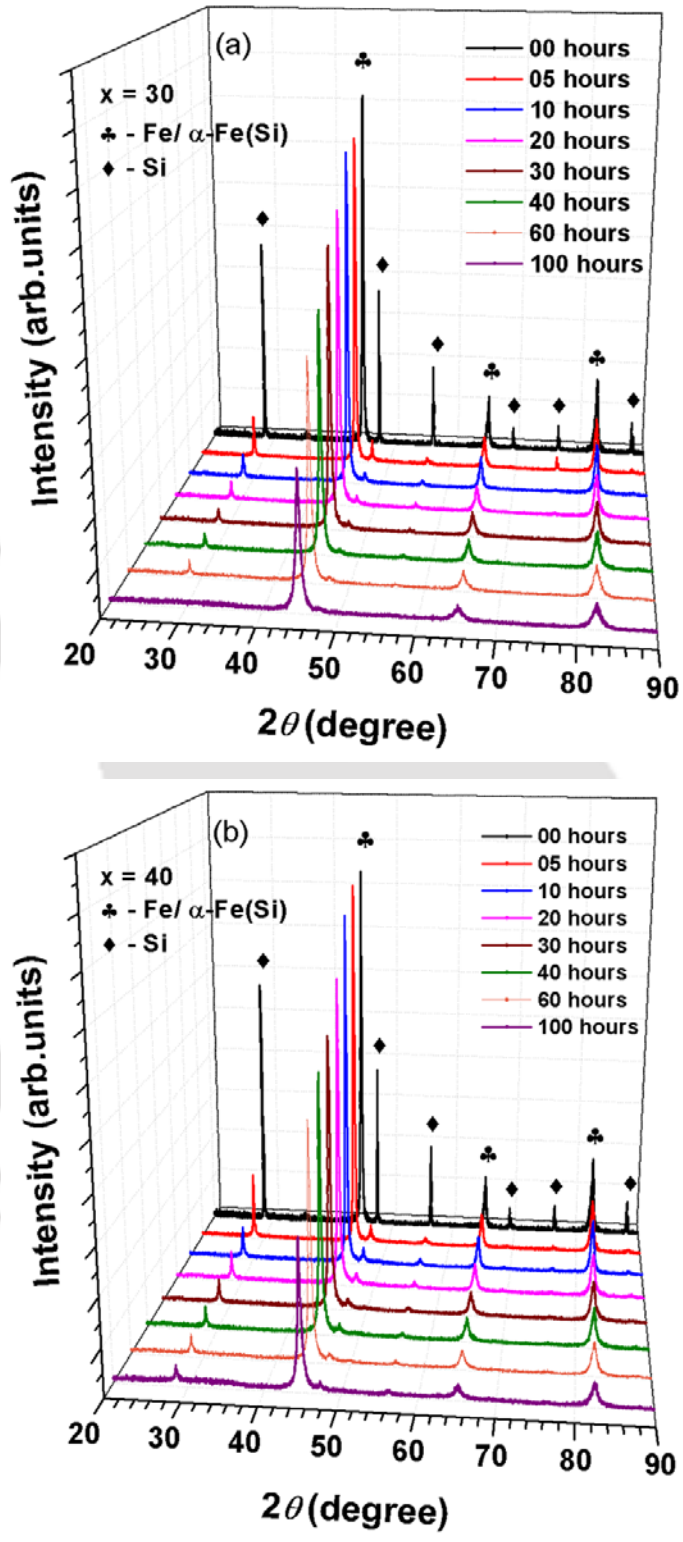

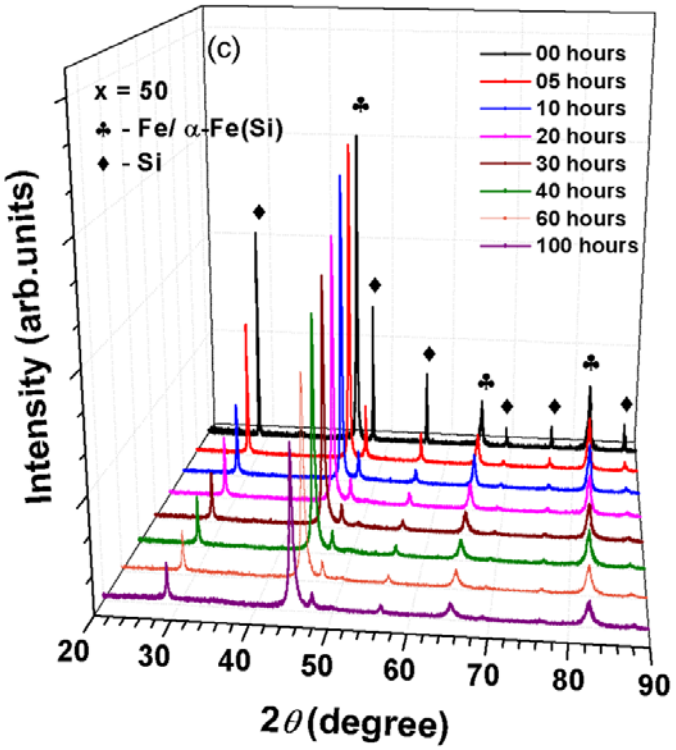

Figure 4.10. Room temperature XRD patterns of $Fe_{100-x}Si_x$ alloy powders with (a) x = 30, (b) x = 40 and (c) x = 50 milled for various milling time periods.

4.3.2. Structural properties of $Fe_{100-x}Si_x$ (x = 15 – 50):

Figures 4.09 and 4.10 depict the room temperature XRD patterns of the $Fe_{100-x}Si_x$ alloy powders with x = 15 – 50 milled for various milling time periods. The following features were observed from the XRD patterns: (i) For the Fe-Si samples with x up to 30, with increasing milling time, the reflections corresponding to Si decrease progressively and disappear completely after 100 hours of milling. This indicates the formation of non-equilibrium solid solution of α-Fe(Si). A close observation confirms that the milling time required for forming the solid solution increases with increasing Si content in $Fe_{100-x}Si_x$ alloy powders. For example, the milling time of 40 hours, 60 hours and 100 hours is required for forming solid solution in $Fe_{80}Si_{20}$, $Fe_{75}Si_{25}$ and $Fe_{70}Si_{30}$ samples, respectively. (ii) On further increasing the Si content above 30 at.%, the milling time of 100 hours is also not sufficient to form the solid solution in Fe-Si binary alloys. This could be due to the delay in the dissolution behavior of Si into Fe with increasing Si content under the present milling conditions. (iii) In addition, the broadening of the α-Fe(Si) peak increases and the peak position shifts to higher angles with increasing milling time periods and Si contents. As discussed earlier, the broadening of the peaks confirms

the formation of nanocrystalline microstructure with highly refined and internally strained grains, while the shifting of peak positions suggests the atomic disorder due the dissolution of Si in Fe matrix leading to a change in lattice constant.

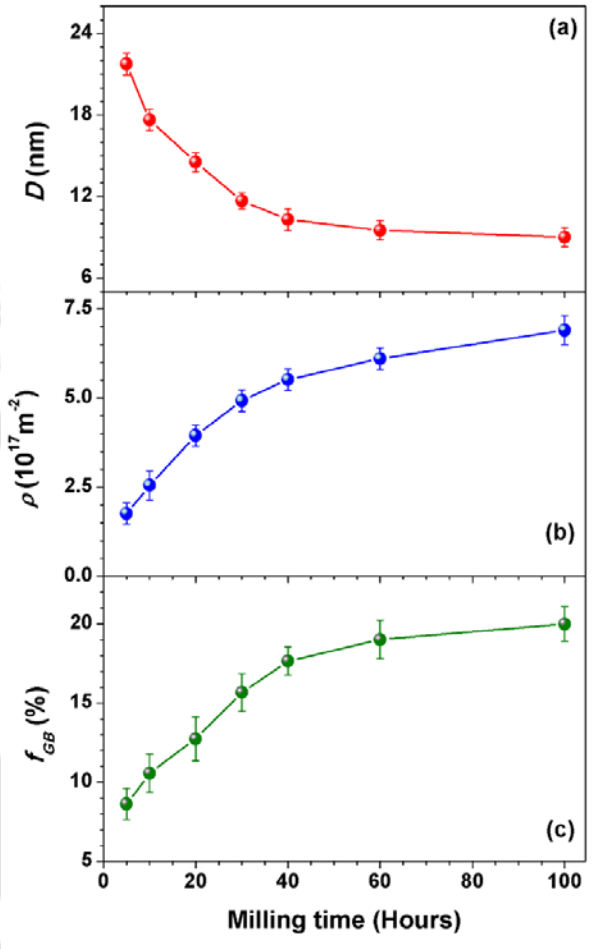

Figure 4.11. Variations of D, ρ and f_{GB} for $Fe_{85}Si_{15}$ alloy powders milled for various time periods.

A careful analysis of the XRD patterns of the milled $Fe_{100-x}Si_x$ alloy powders with different Si content reveals that the lattice constant decreases from 0.28715 nm for un-milled powder to nearly stable values of 0.2863 nm, 0.28607 nm, 0.28585 nm and 0.28576 nm in $Fe_{85}Si_{15}$, $Fe_{80}Si_{20}$, $Fe_{75}Si_{25}$ and $Fe_{70}Si_{30}$ alloy powders, respectively after obtaining the non-equilibrium solid solution of α-Fe(Si). This reveals a maximum lattice change of 0.00085 nm, 0.00108 nm, 0.0013 nm and 0.00139 nm with increasing Si content from 15 to 30 at.%. Following the procedures for calculating the degree of dissolution discussed in earlier section for $Fe_{90}Si_{10}$

alloy powders, the above changes in the lattice constant accounts for nearly 87 %, 83 %, 80 % and 73 % Si occupancy in *bcc* α-Fe for the samples of $Fe_{85}Si_{15}$, $Fe_{80}Si_{20}$, $Fe_{75}Si_{25}$ and $Fe_{70}Si_{30}$ alloy powders, respectively and the rest of the Si mostly residing in grain boundaries.

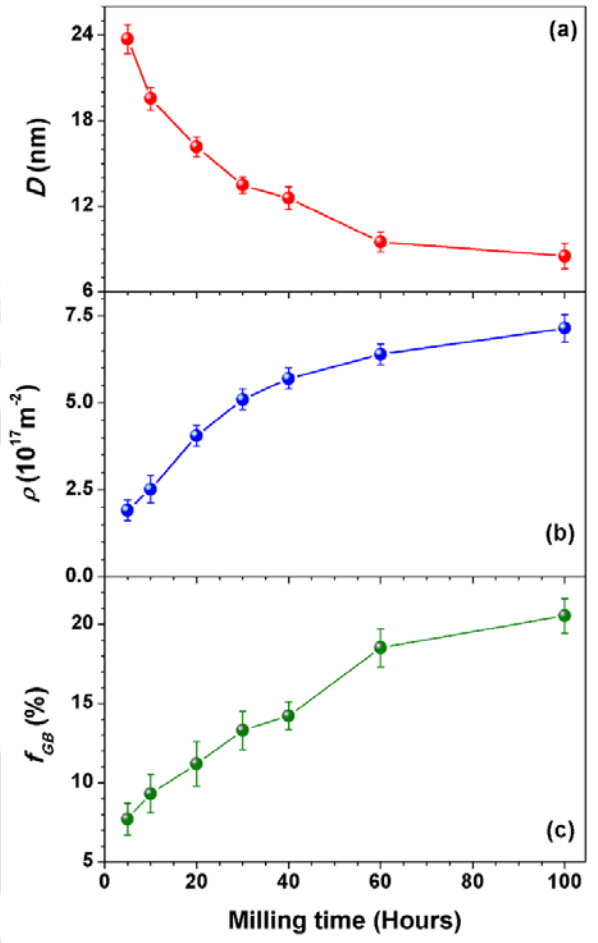

Figure 4.12. Variations of D, ρ and f_{GB} for $Fe_{80}Si_{20}$ alloy powders milled for various time periods.

The observation of 80 % Si occupying *bcc* α-Fe sites for $Fe_{75}Si_{25}$ alloy powder is in close agreement with the report of occupancy of 82 % Si in *bcc* α-Fe for $Fe_{75}Si_{25}$ system [KALI20081]. These results suggests that the amount of Si occupying *bcc* α-Fe sites decreases significantly with increasing Si content. This could be attributed to the difficulty in dissolving all the Si into Fe matrix with the present milling conditions. This is also in good agreement with the reports given by Yousefi et al. [YOUS2014]. Since the formation of non-equilibrium solid solution in high Si content Fe-Si alloys could not be achieved, the calculation of lattice constant was not extended for the $Fe_{100-x}Si_x$ alloy powders with $x > 30$.

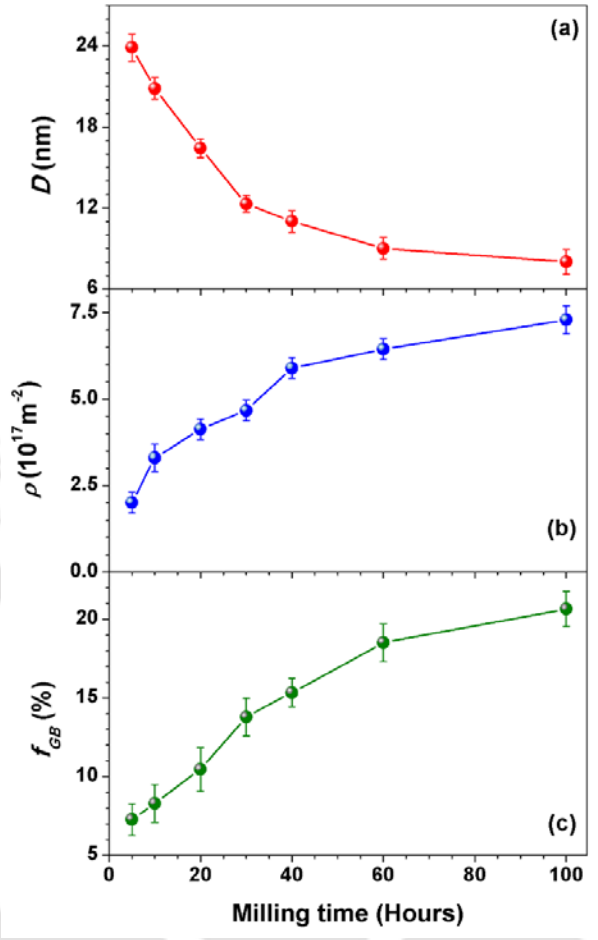

Figure 4.13. Variations of D, ρ and f_{GB} for $Fe_{75}Si_{25}$ alloy powders milled for various time periods.

The structural parameters such as D and ρ determined using MWHP fit procedure as described in eqn.(4.04) and f_{GB} calculated using eqn.(4.07) were depicted as a function of milling time periods in Figures 4.11 to 4.14 for $Fe_{100-x}Si_x$ alloy powders with x = 15, 20, 25 and 30, respectively. The values of D decrease with increasing milling time periods and reach about 8 – 10 nm after 100 hours of milling. On the other hand, the values of ρ increase drastically for the initial period of milling and tend to saturate at higher milling time periods. Nevertheless, the values of ρ are found to be of the order of 10^{17} m^{-2}. The variations of D and ρ exhibit almost similar behavior for all samples, but the actual values depend significantly on the composition of the alloys. Furthermore, the fraction of grain boundary region increases with increasing milling time period and reaches a saturation value in the range of 19 to 21 %. With increasing Si content, a slight increase in fraction of grain boundaries was also observed.

This could be due to the enhanced work hardening rate of the Fe matrix by the brittle nature of the Si particles [BAHR2013]. These results show a strong correlation between the microstructural refinement and formation of grain boundary regions in these mechanically alloyed powders.

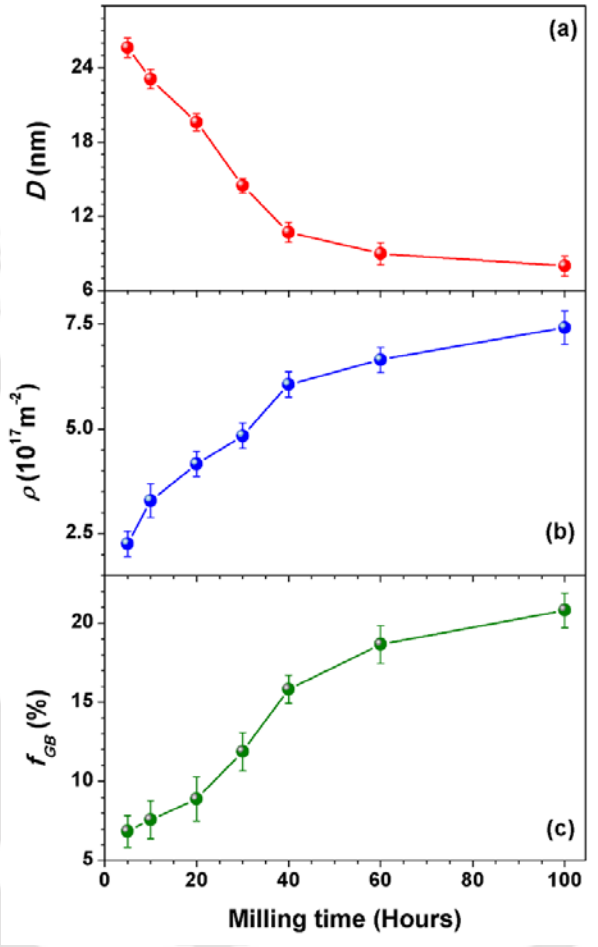

Figure 4.14. Variations of D, ρ and f_{GB} for $Fe_{70}Si_{30}$ alloy powders milled for various time periods.

To understand the effect of Si content on the surface morphology changes, SEM micrographs of the as-milled powders with non-equilibrium solid solutions were observed. The average particle size resulting from the aggregation of many crystallites becomes smaller and the size distribution becomes narrower with spherical shape in nature. Further, the average size of the particles decreases not only with increasing milling time periods, but also decreases significantly with increasing the Si content. The actual variation of particle size of the milled powders with increasing Si content is presented in the later part of the chapter for the powders milled at 600 rpm speed. Composition analysis performed on as-milled powders using EDS

showed the overall composition to be $Fe_{85.4}Si_{14.6}$, $Fe_{80.7}Si_{19.3}$, $Fe_{75.8}Si_{24.2}$ and $Fe_{71.1}Si_{28.9}$ for $Fe_{100-x}Si_x$ alloy powders with x = 15, 20, 25 and 30, respectively. This indicates the presence of Si in the form of solid solution in α-Fe and compositional homogeneity obtained in the powder supports the claim of formation of α-Fe(Si) solid solution.

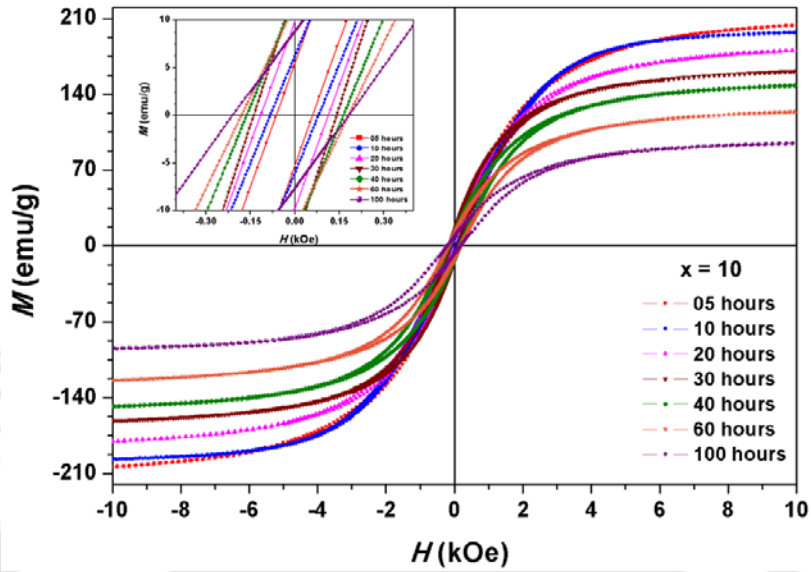

Figure 4.15. Room temperature *M-H* loops of $Fe_{90}Si_{10}$ alloy powders milled for various time periods. Inset: Expanded view of *M-H* loops close to origin.

4.3.3. Evolution of magnetic properties during milling:

In order to understand the effect of milling on the magnetic properties, room temperature magnetic hysteresis (*M-H*) loops were obtained for all the as-milled powders. Figure 4.15 depicts typical *M-H* loops for the $Fe_{90}Si_{10}$ powders milled for various milling time periods and expanded view of the *M-H* loops close to origin in the inset. The shape of the loops is typical of a soft magnetic material. The magnetization value measured at high field decreases gradually with increasing the milling time periods. To monitor the effect of milling on the magnetic parameters such as saturation magnetization (M_S) and coercivity (H_C), M_S and H_C were obtained from the *M-H* loops. In order to determine the actual value of M_S, the initial magnetization curves were fitted to power series defined as in eqn.(4.09)

$$M(H) = M_S\left(1 - \frac{a_1}{H} - \frac{a_2}{H^2} + \ldots\right) \qquad (4.09)$$

where $M(H)$ is the magnetization in an applied magnetic field H and a_1 and a_2 are constant coefficients [KRON2003].

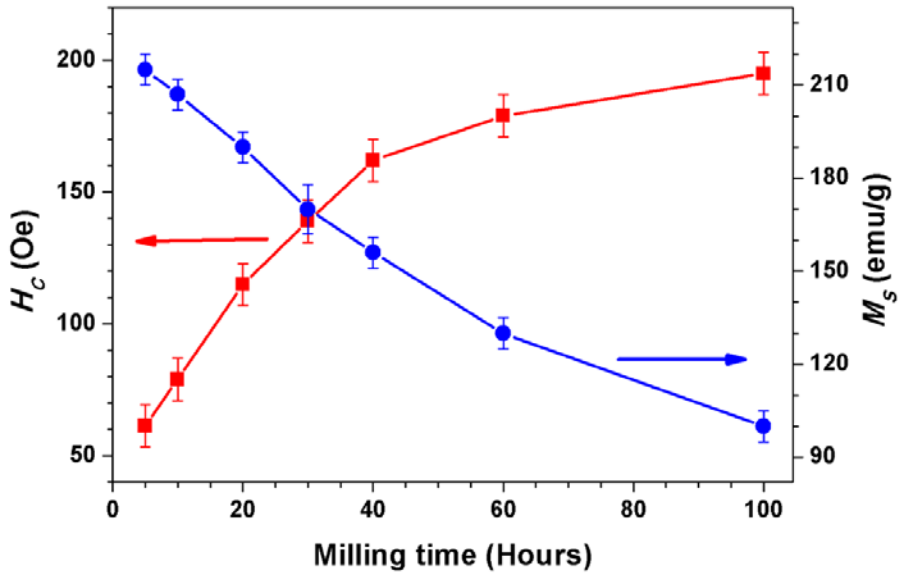

Figure 4.16. Variations of H_C and M_S of $Fe_{90}Si_{10}$ alloy powders milled for various time periods.

Figure 4.16 displays the variations of H_C extracted from the *M-H* loops and M_S determined from eqn.(4.09) as a function of milling time. M_S decreases gradually at a rate of 1.8 emu/g up to 40 hours of milling. On further milling, the rate of decrease in M_S with increasing milling time reduces to 1.02 emu/g. Progressive Si substitution in Fe during the milling process induces a partial filling of the Fe 3*d* bands with 3*p* electrons which results in the decrement of magnetic moment of Fe [SHEN2005, BLAN2006, MARI2001]. Since the fraction of grain boundaries increases with increasing milling time, one would expect a considerable amount of Fe atoms to be present in the grain boundaries which can result in an increase in the inter-atomic distances spatially between Fe neighbours [BLAN2006, KALI20082]. Note that the increase in inter-atomic distances between Fe neighbours can contribute to the lowering of M_S values. On the other hand, H_C of the powder increases with increasing milling time periods. The severe plastic deformation during the milling process produces a large density of defects like dislocations and grain boundaries, which could hinder the motion of the domain walls and increase the coercivity. Such variation is in good agreement with the earlier reports on similar systems [BAHR2006, KALI20081, SUNO2008]. However, it may be noted that the actual variation of H_C with milling strongly depends on the milling conditions and alloying materials. For example: Taghvaei et al. [TAGH2011], Yousefi et al. [YOUS2012], Bahrami et al. [BAHR2013] and Gomez-Esparza et al. [GOME2014] reported that H_C increases initially up

to certain milling time period and then decreases with further increase in the milling time. This results a maximum in H_C after certain milling time periods. However, the milling time at which the maximum H_C appears strongly depends on the alloying materials. In contrast, Kim et al. [KIMS2006] and Bensebaa et al. [BENS2010] showed decreasing tendency in H_C with increasing milling time period for the Fe-Si based alloy powders. On the other hand, Guittoum et al. [GUIT2008] showed that H_C of FeNi alloy prepared by mechanical alloying exhibit oscillatory variation up to 12 hours of milling and then increases continuously with increasing milling time up to 50 hours. These different results clearly suggest that any changes in the magnetic properties of as-milled powders with milling time strongly depends on the milling parameters and alloying materials.

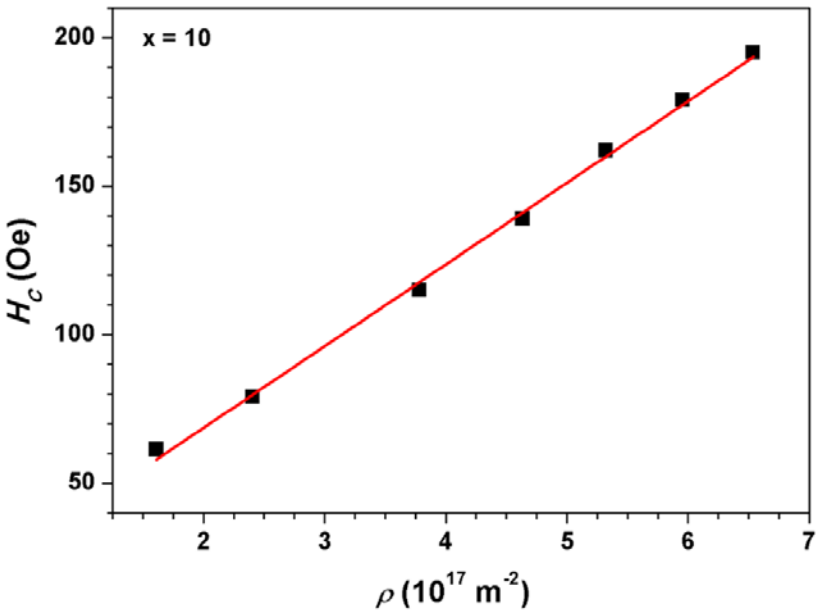

Figure 4.17. Variation of H_C of $Fe_{90}Si_{10}$ alloy powders as a function of ρ. The straight line passing through the data points is the best fit for the linear equation.

In order to understand the various contributions to H_C in the present investigation, H_C has been plotted as a function of ρ in Figure 4.17. It could be clearly seen from the figure that the variation of coercivity with dislocation density shows almost linear behavior for the entire range of milling time periods. The solid line passing through the data point is typical linear fit to the data. According to Néel's theory [NEEL1946], randomly distributed internal stresses (σ) introduced during milling in the samples with local magnetostriction constant (λ) are expected to increase the coercivity. In addition, if the magneto-elastic energy ($\lambda\sigma$) is larger than the anisotropy energy, the coercivity is likely to be proportional to the dislocation density.

Thus, the linear relationship between coercivity and dislocation density obtained in the as-milled powders suggests that dislocation defect is the major factor responsible for the increase in H_C, which is in good agreement with Néel's theory.

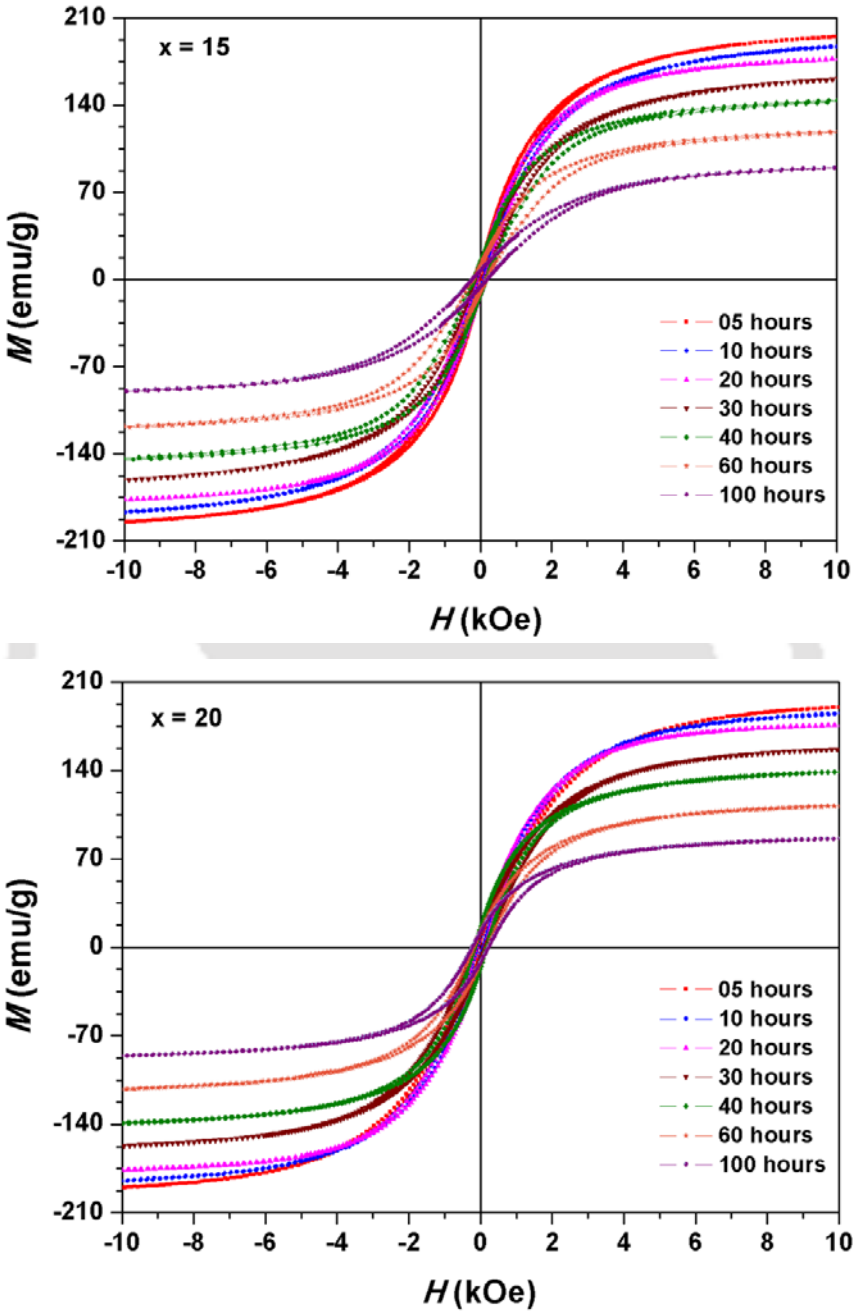

Figure 4.18. Room temperature *M-H* loops of $Fe_{100-x}Si_x$ alloy powders with x = 15 and 20 milled for various time periods.

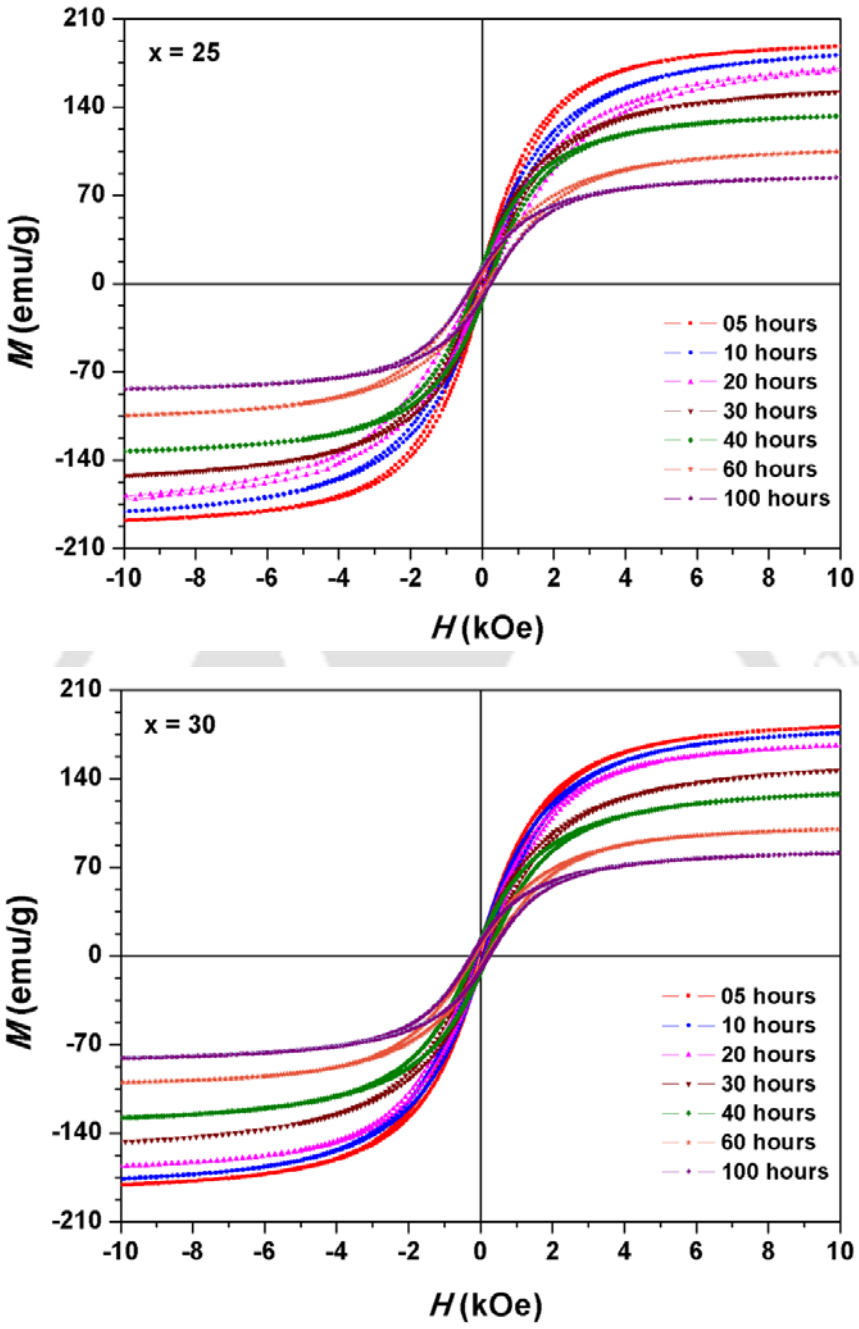

Figure 4.19. Room temperature *M-H* loops of $Fe_{100-x}Si_x$ alloy powders with x = 25 and 30 milled for various time periods.

4.3.4. Magnetic properties of $Fe_{100-x}Si_x$ (x = 15 – 30):

Figures 4.18 and 4.19 show the room temperature *M-H* loops of the $Fe_{100-x}Si_x$ alloy powders with x = 15 and 20 and x = 25 and 30, respectively. The loops shown in the figures are typical of soft magnetic materials. The magnetization value measured at high field decreases gradually

for all the samples with increasing the milling time periods. To study the effect of milling process on the magnetic parameters, the values of M_S were determined using eqn.(4.09) and H_C were extracted directly from the *M-H* loops.

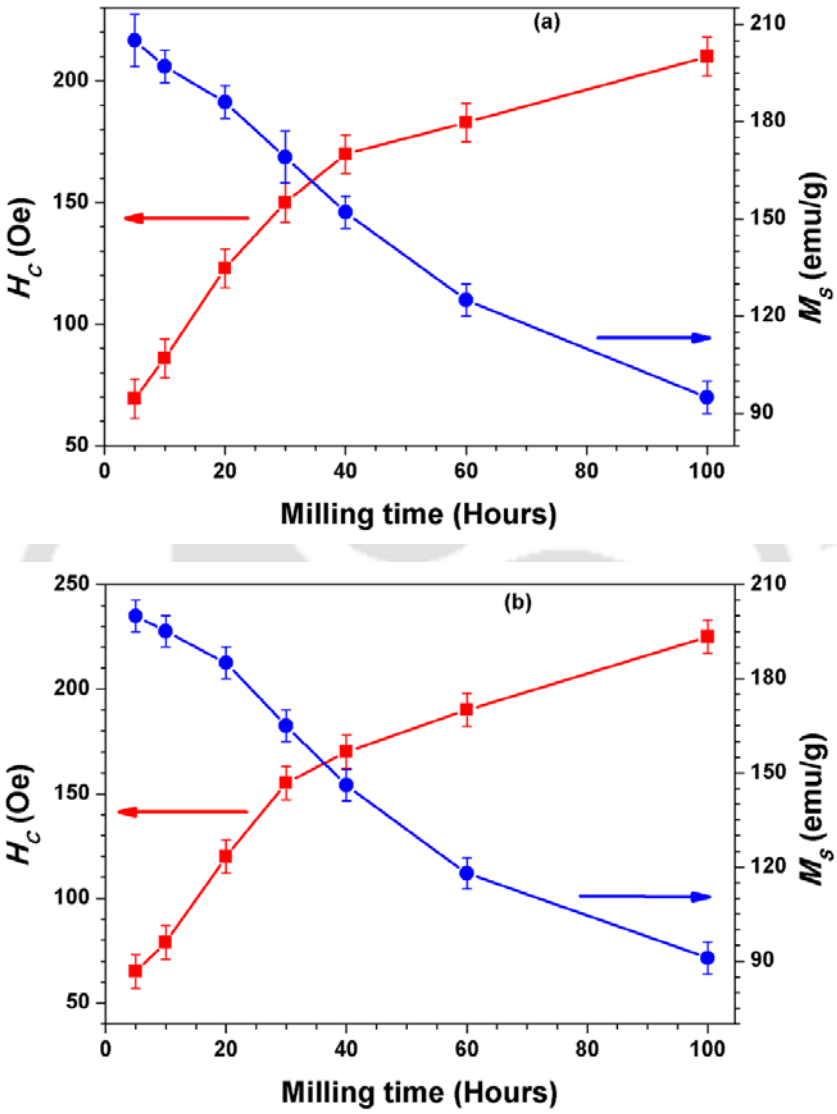

Figure 4.20. Variations of H_C and M_S of $Fe_{100-x}Si_x$ alloy powders with (a) $x = 15$ and (b) $x = 20$ milled for various time periods.

Figures 4.20 and 4.21 show the variations of H_C and M_S of the $Fe_{100-x}Si_x$ alloy powders with $x = 15$ and 20 and $x = 25$ and 30, respectively. M_S decreases and H_C increases with the increase in milling time for all the compositions. However, the rate of variation of M_S and H_C depends on the composition and change in the alloying process with Si substitution. A close observation of the magnetic data reveals that the values of M_S also decrease with increasing Si

content. This could be correlated to partial filling of the Fe 3*d* bands with 3*p* electrons which results in the decrement of magnetic moment of Fe with increasing Si content. On the other hand, a significant increase in H_C was observed with increasing Si content in Fe-Si alloy powders. This could be attributed to the increase of internal strain which has been introduced during the milling process and undissolved solute atoms in the grain boundaries acting as inclusions and hinder the domain wall motion [KHAJ2011].

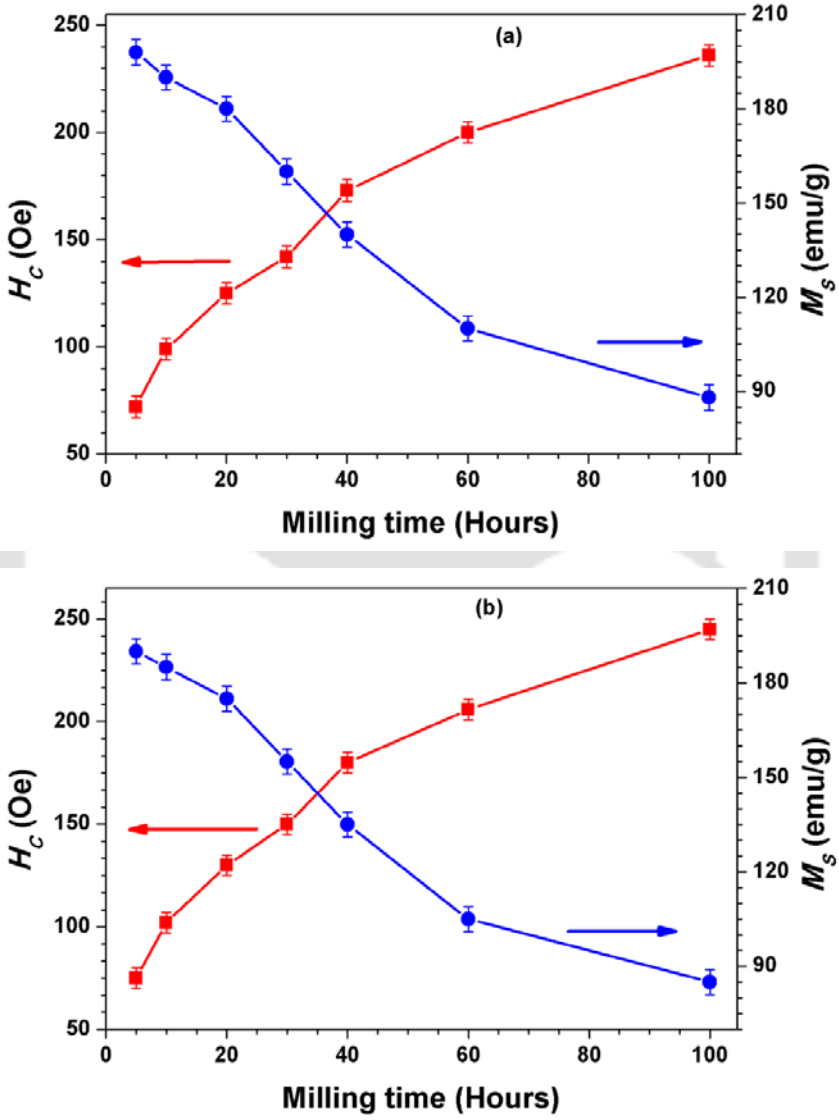

Figure 4.21. Variations of H_C and M_S of $Fe_{100-x}Si_x$ alloy powders with (a) $x = 25$ and (b) $x = 30$ milled for various time periods.

In order to understand the effect of Si content on the H_C behaviour of the as-milled samples, the variation of H_C is plotted as a function of ρ for all the samples in Figure 4.22. It is clear

from the figure that (i) For $Fe_{85}Si_{15}$ sample, the variation of H_C with ρ shows a nearly linear behavior for almost the entire range of milling time. (ii) However, with increasing the Si content, the region of linear variation of H_C is reduced and for higher milling hours, the variation of H_C exhibits another rate of increase.

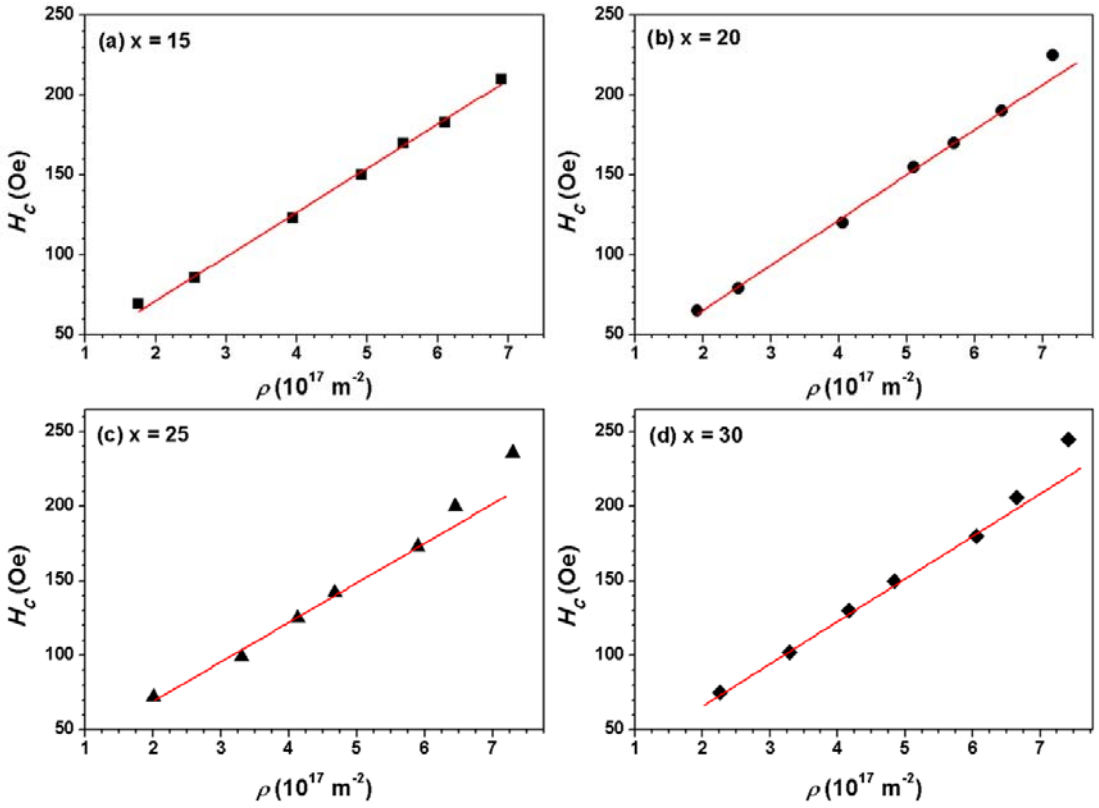

Figure 4.22. Variations of H_C of $Fe_{100-x}Si_x$ milled powders with (a) x = 15, (b) x = 20, (c) x = 25 and (d) x = 30 as a function of ρ. The straight line passing through the selected data points is best fit for the linear equation.

These results suggest that if dislocation defect is the only factor responsible for the increase of H_C with milling time periods, then the linear relationship between ρ and H_C is expected to hold for the entire range of milling time as observed for x = 10 and 15. Therefore, the appearance of second linear region of variation for higher Si content suggests that there exists additional contributions other than dislocation defects to H_C. Since the average particle size decreases with increasing milling time periods and with increasing Si contents, it can be expected that H_C of the powders also depends on the average particle size. This is in good agreement with the earlier reports on similar systems [HERN2005, KALI20081, YOUS2014].

4.4. Properties of Fe-Si binary alloy powders milled at 600 rpm:

The study of structural and magnetic properties of $Fe_{100-x}Si_x$ (x = 10 - 50) alloy powders milled at a speed of 500 rpm revealed that the formation of α-Fe(Si) solid solution was limited up to 30 at.% Si within 100 hours of milling. Since the choice of milling parameters plays a major role on controlling the properties of end product in mechanical alloying process, the milling speed was increased from 500 rpm to 600 rpm to extend the formation of solid solution to higher Si content Fe-Si alloys.

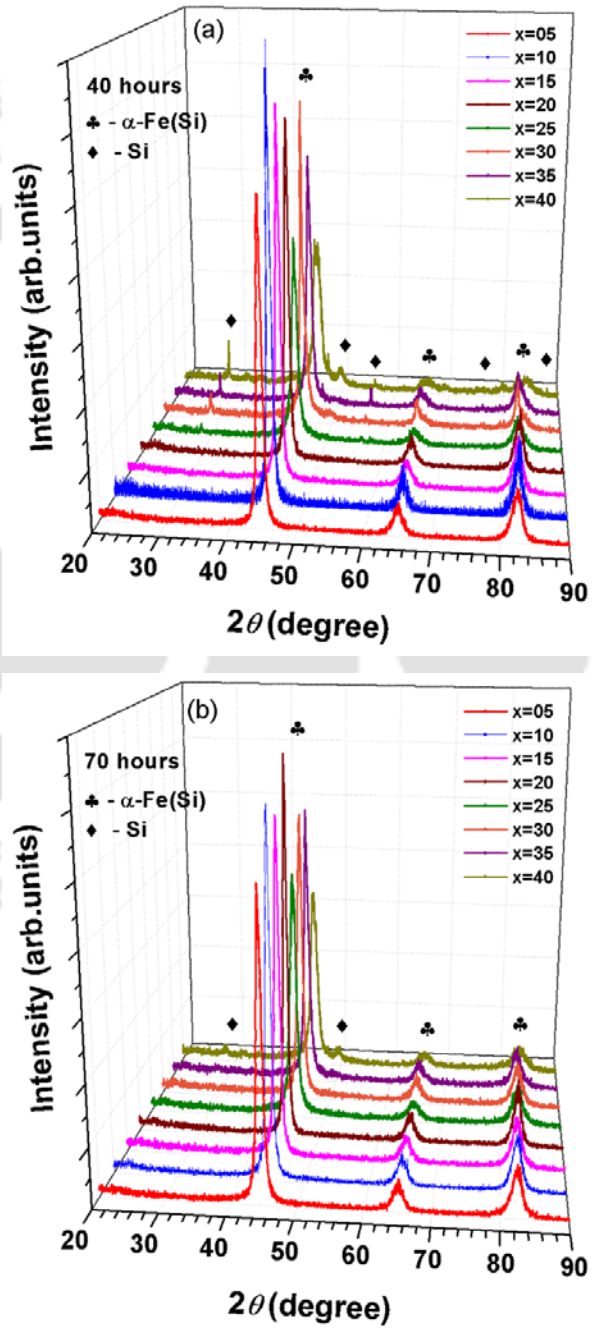

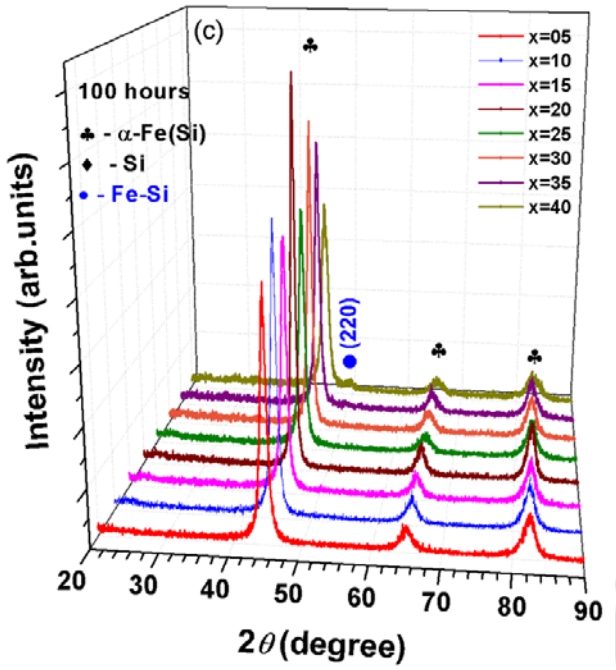

Figure 4.23. Room temperature XRD patterns of $Fe_{100-x}Si_x$ alloy powders milled for various time periods: (a) 40 hours, (b) 70 hours and (c) 100 hours.

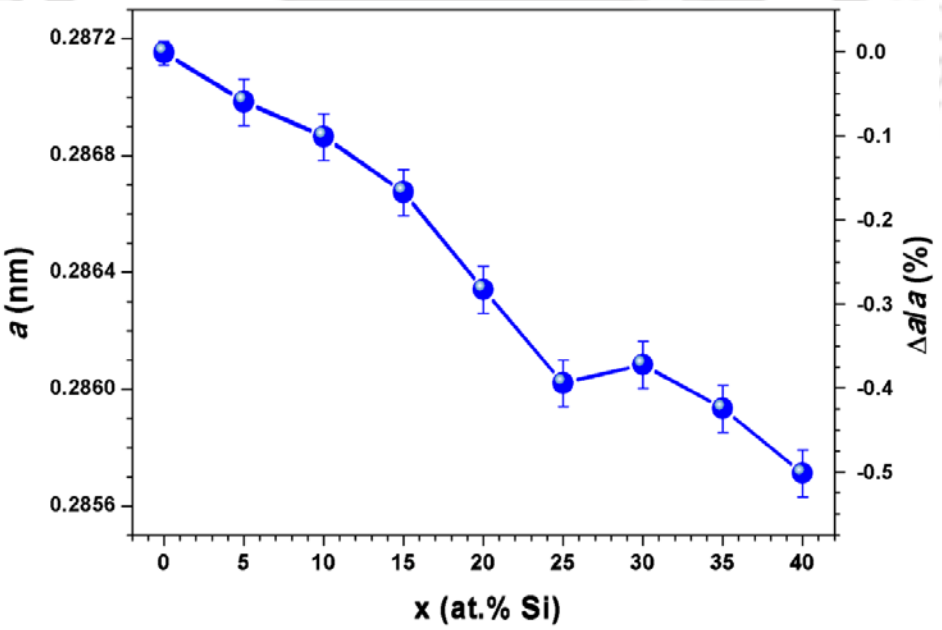

Figure 4.24. Variation of lattice constant and fractional change in the lattice constant of $Fe_{100-x}Si_x$ solid solution as a function of Si content.

In the following section, we report the study of structural and magnetic properties of $Fe_{100-x}Si_x$ (x = 5 - 40) alloy powders milled at 600 rpm as a function of milling time period and Si content. As we have studied the evolution of structural and magnetic properties of Fe-Si alloy powders as a function of milling time period in detail, we hereby focus mainly on the effect of Si content on the structural and magnetic properties of $Fe_{100-x}Si_x$ (x = 5 - 40) alloy powders exhibiting non-equilibrium solid solution of α-Fe(Si).

4.4.1. Evolution of structural properties:

Figure 4.23 shows typical XRD patterns of $Fe_{100-x}Si_x$ (x = 5 – 40) powders milled for different milling periods such as (a) 40 hours, (b) 70 hours and (c) 100 hours. It is observed that (i) With increasing milling time to 40 hours, the reflections corresponding to Si observed in as-mixed powders (see Figure 4.01) disappear leaving behind only *bcc* Fe reflections for Si content up to 20 at.%. This confirms the formation of *bcc* α-Fe(Si) non-equilibrium solid solution. (ii) The samples with $x > 20$ do not form the solid solution completely within 40 hours of milling, (iii) On further increasing the milling time to 100 hours (see Figure 4.23 (c)), the formation of solid solution could be enhanced up to 40 at.% Si in Fe-Si alloy powders. (iv) However, a careful observation of XRD patterns reveals the existence of finite Fe_5Si_3 and/or Fe-Si intermetallic compounds (represented by filled circle) in $Fe_{60}Si_{40}$ sample. (v) The sharp diffraction lines observed for as-mixed powders are broadened with increasing milling time and a measurable shift in the peak positions to higher angle has also perceived. These results suggest that the mechanical alloying induces disordering of *bcc* Fe structure, dissolution of Si in Fe matrix, creation of large interfacial area and grain boundaries with randomly oriented and highly strained nanocrystalline grains and formation of solid solution and compounds during milling. As a result, Fe-Si solid solution could easily be obtained for $x \leq 20$ at low milling hours and the milling time required for forming solid solution in samples with $x \geq 25$ increases with increasing Si content. This is in good agreement with the earlier reports on similar systems [FECH1992, BENS2009]. In order to understand the effect of Si content on the structural parameters, the XRD patterns of the as-milled powders exhibiting non-equilibrium solid solutions were analyzed using eqn.(4.04). It is observed that the values of q and C_{hkl} are in the range of 1.65 – 2.32 and 0.105 to 0.148, respectively for the presently investigated samples.

Figure 4.24 displays the changes in the lattice constant of non-equilibrium solid solution of α-Fe(Si) with increasing Si content. The lattice constant decreases gradually with increasing

Si content confirming the occurrence of atomic disorder during mechanical alloying, which is mainly due to the dissolution of Si in Fe matrix. This is expected since atomic radius of Si (0.118 nm) is smaller than Fe (0.125 nm) [KALI20081, MIRA2008]. A maximum lattice constant change of 0.5% was obtained by substituting 40 at.% Si in Fe-Si alloy powders.

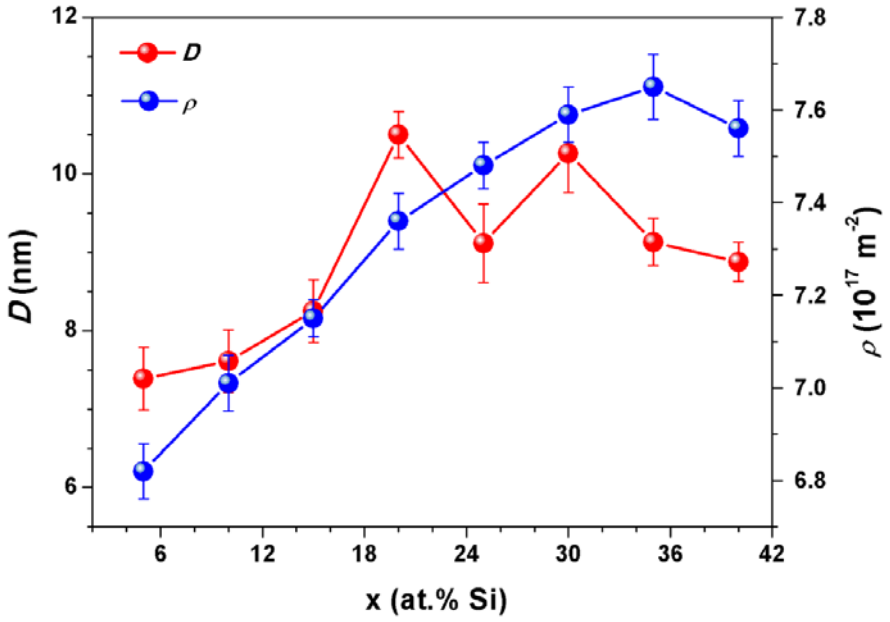

Figure 4.25. Variations of D and ρ of $Fe_{100-x}Si_x$ solid solution as a function of Si content.

The average crystallite size of the powder decreases largely down to around 10 nm due to milling. However, the average values of crystallite size display a weak dependence on Si content as shown in Figure 4.25. This behavior is in close agreement with the earlier reports on similar systems [MIRA2008], where the average crystallite size of Fe-Si alloy powders exhibits oscillating behavior between 15 nm and 13.2 nm with increasing Si content from 6.5 at.% to 25 at.%. On the other hand, the dislocation density of the powder raises to a value of order of 10^{17} m^{-2} for the solid solution. In addition, dislocation density increases with increasing Si content up to 35 at.% and decreases slightly for $Fe_{60}Si_{40}$ sample. As discussed earlier, the decreasing of crystallite size after milling could be attributed to formation of defects such as dislocations that can appear in different ways such as formation of dense regions of these dislocations into the grains, pile up the grain boundaries or untidy clusters into the grain [SCHI1996]. All these possibilities guide to formation of sub-grain structures inside the original grain and therefore decreasing the effective size in crystalline region. On the other hand, the increasing of dislocation density of solid solution can be attributed to the enhanced severe plastic deformation during the milling process by the introduction of brittle nature of

the Si particles. The decrease in dislocation density for $Fe_{60}Si_{40}$ sample might be due to the formation of finite Fe-Si intermetallic phases. Furthermore, the fraction of grain boundaries calculated using eqn.(4.07) increases from 19 % to 22.8 % with increasing Si content from 5 at.% to 35 at.% in α-Fe(Si) solid solution. This could be attributed to the enhanced work hardening rate of the matrix induced by the Si particles [BAHR2013].

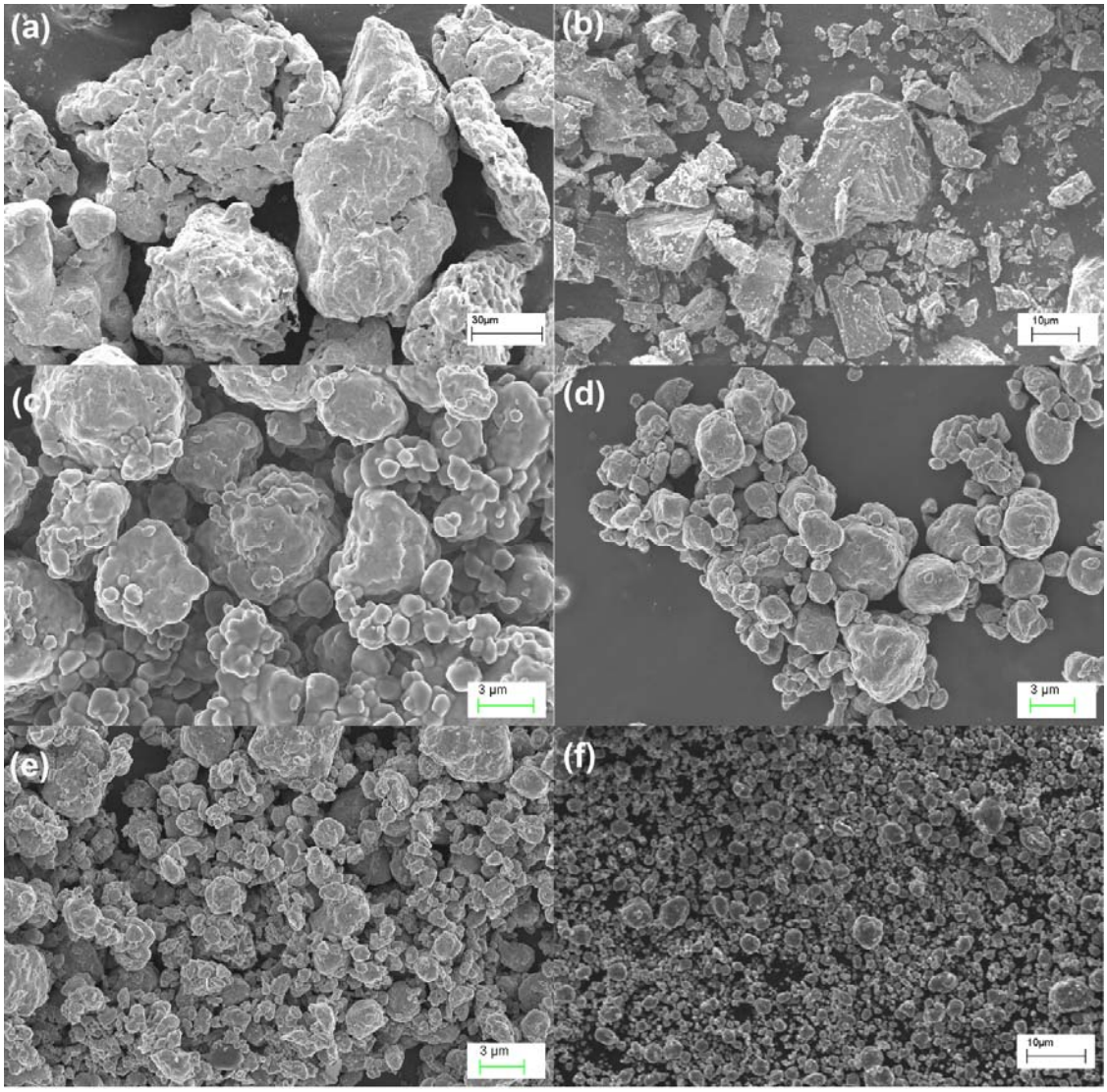

Figure 4.26. SEM micrographs of pure (a) Fe, (b) Si, and $Fe_{100-x}Si_x$ solid solution with different Si content: (c) $x = 5$, (d) $x = 10$, (e) $x = 20$ and (f) $x = 30$.

The changes in the surface morphology of the non-equilibrium solid solution with different Si contents were investigated using SEM microscopy technique. Figure 4.26 shows the SEM micrographs of un-milled Fe and Si powders and milled Fe-Si alloy powders with increasing Si content from 5 at.% to 30 at.%. As discussed earlier, the un-milled Fe and Si exhibits large

sized particles. The average size of the particles in the Fe-Si solid solution decreased significantly with increasing Si content and relatively become homogenous. The average size distribution of the particles also becomes narrower with spherical shape in nature. Comparative studies between XRD and SEM reveal that the particles seen in the SEM micrographs consist of crystallites with a size of about 8 – 11 nm oriented randomly with respect to each other. Composition analysis performed on as-milled powders using EDS showed the overall composition to be $Fe_{95.1}Si_{4.9}$, $Fe_{90.4}Si_{9.6}$, $Fe_{85.2}Si_{14.8}$, $Fe_{80.5}Si_{19.5}$, $Fe_{75.9}Si_{24.1}$, $Fe_{71}Si_{29}$ and $Fe_{66.1}Si_{33.9}$ for $Fe_{100-x}Si_x$ alloy powders with x = 5, 10, 15, 20, 25, 30 and 35, respectively. This confirms the presence of Si in the solid solution of α-Fe. These changes in the structural and surface morphology of the Fe-Si alloyed powders are expected to modify the magnetic properties considerably.

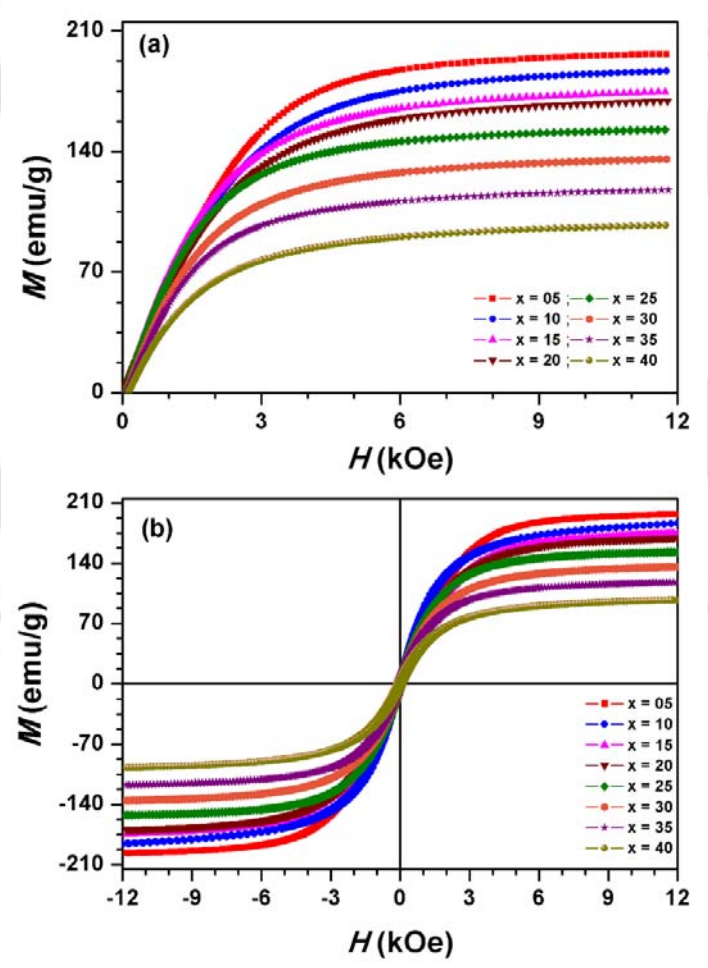

Figure 4.27. Room temperature (a) initial magnetization curves and (b) *M-H* loops of $Fe_{100-x}Si_x$ solid solution as a function of Si content.

4.4.2. Evolution of magnetic properties:

Figure 4.27 depicts room temperature initial magnetization curves and *M-H* loops measured for Fe-Si non-equilibrium solid solution with different Si contents. All the *M–H* curves exhibit a similar nature and attain saturation above 10 kOe applied field. The loops shown in the figures are typical of soft magnetic materials. The magnetization value measured at high field decreases gradually for all the samples with increasing Si content. To study the effect of Si substitution on the magnetic parameters, the values of M_S were determined using eqn.(4.09) and H_C were extracted directly from the *M-H* loops and displayed in Figure 4.28.

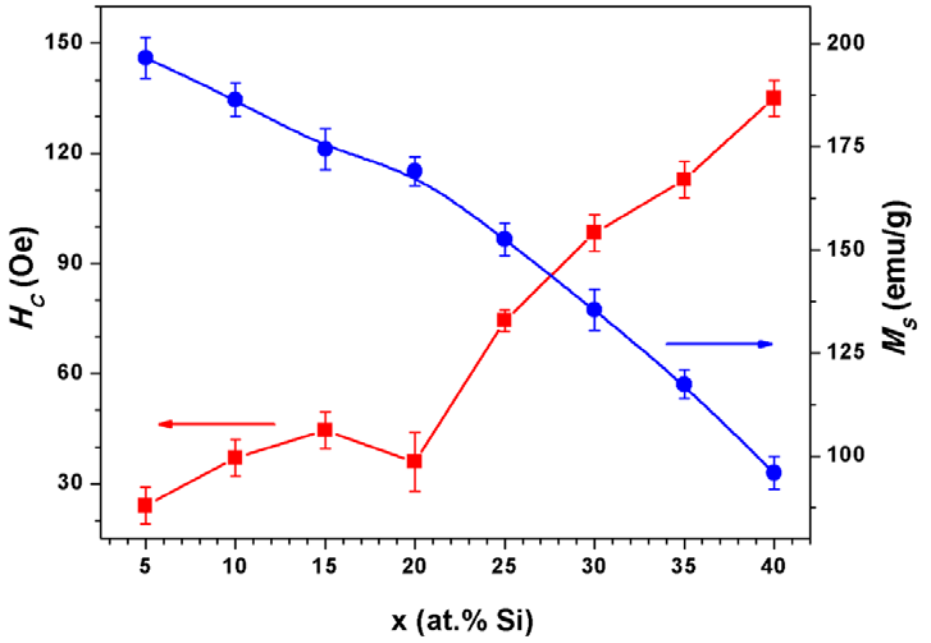

Figure 4.28. Variations of H_C and M_S of $Fe_{100-x}Si_x$ solid solution as a function of Si content.

M_S decreases gradually in Fe-Si solid solution with increasing Si content. This follows a similar trend of lattice constant variation with increasing Si as shown in Figure 4.24. Therefore, the substitutional dependence of M_S can be attributed to a partial filling of Fe 3*d* band with 3*p* electrons in Fe-Si powders [SHEN2005, BLAN2006, MARI2001]. In addition, considerable amount of Fe atoms is expected to be present in grain boundaries, which varies the inter-atomic distance between Fe neighbors spatially leading to reduction in M_S. On the other hand, H_C increases slowly with increasing Si up to 15 at.% and exhibits a small decrease for $Fe_{80}Si_{20}$ sample. On further increasing Si content, H_C increases significantly at a faster rate. It is well known that H_C in the mechanically alloyed powders increases with increasing ρ, while the reduction in *D* exhibits a large decrease in H_C [KALI20083, BENS2010]. Zhou et al.

[ZHOU1999, ZHOU2000] reported that H_C decreases with increasing Si content up to 20 at.% and then increases significantly with further increase in Si content. This was attributed to a reduction in effective magnetic anisotropy by the substitution of Si, induced strain and grain boundaries. Similarly, Varga et al. [VARG2001] reported that the effective magnetic anisotropy constant decreases significantly with increasing the Si content up to 20 at % and remains more or less constant up to 35 at.% Si for Fe-Si alloys prepared by rapid solidification method.

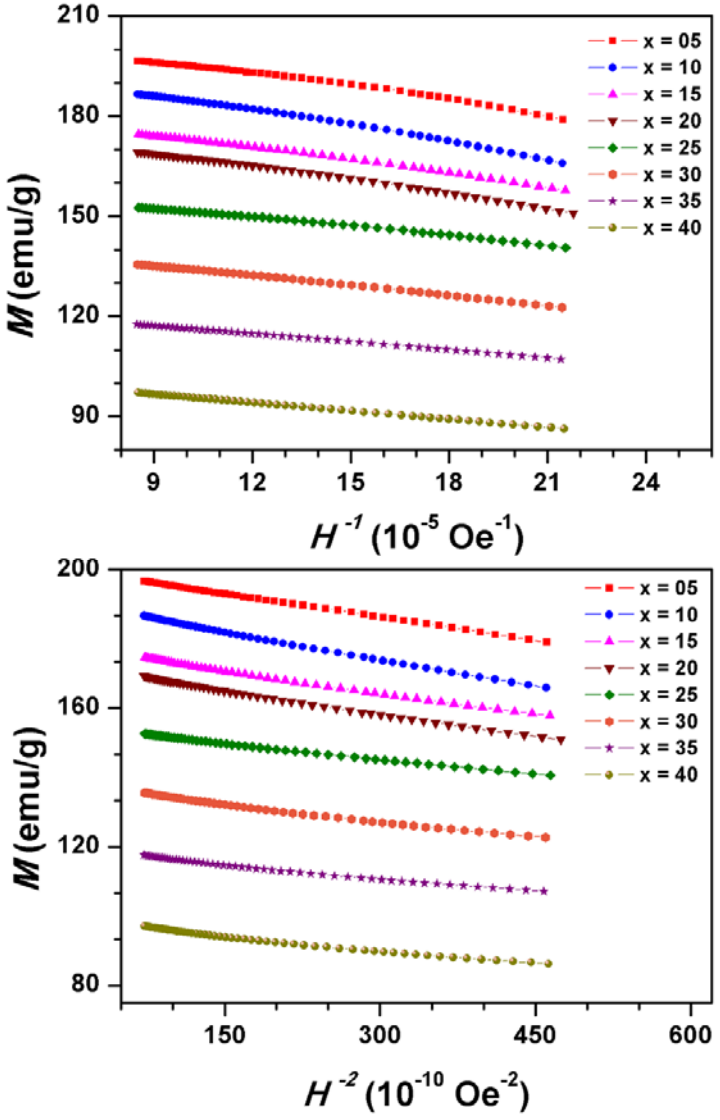

Figure 4.29. The representation of M as a function of H^{-1} and H^{-2} for $Fe_{100-x}Si_x$ solid solution with different Si content.

Therefore, to study the role of effective magnetic anisotropy (K_{eff}) and its dependence on the Si content, the initial magnetization curves were fitted to eqn.(4.09) to extract the values of the constants a_1 and a_2. While the coefficient a_1 has been shown to be caused by the dislocation dipoles provided the distance between the two dipole is smaller than the exchange correlation length, the coefficient a_2 is related to the effective magnetic anisotropy of cubic crystal materials given as [KRON2003],

$$a_2 = \left(\frac{8}{105}\right)\left(\frac{K_{eff}^2}{\mu_0^2 M_S^2}\right) \tag{4.10}$$

If the value of a_2 can be obtained from eqn.(4.10) by analyzing the initial magnetization curves using eqn.(4.09), then the values of K_{eff} can be determined out using

$$K_{eff} = \mu_0 M_S \sqrt{\frac{105}{8} a_2} \tag{4.11}$$

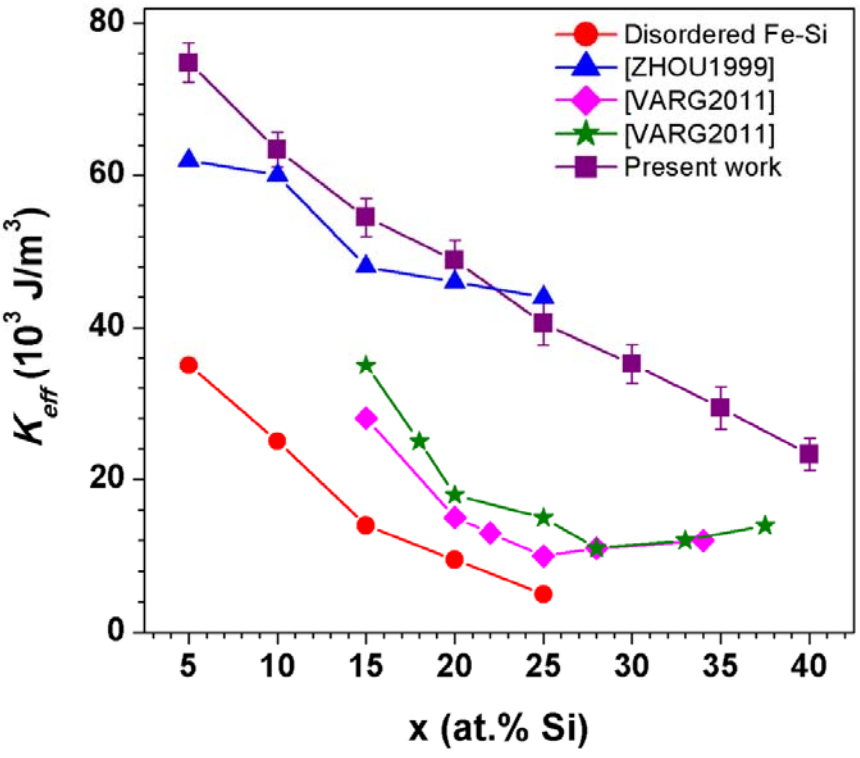

Figure 4.30. Variation of K_{eff} of $Fe_{100-x}Si_x$ solid solution as a function of Si content. The values extracted from literature results are also shown for comparison.

In order to verify the applicability of eqn.(4.09) to analyze the experimental magnetization data, the plots of magnetization against H^{-1} and H^{-2} for the presently investigated samples are demonstrated in Figure 4.29. Considering the validity of the data, the magnetization data were fitted to eqn.(4.09) to obtain the values of a_2 and hence K_{eff} using eqn.(4.11). Figure 4.30 displays the values of K_{eff} as a function of Si content. As a comparison, the absolute values of the magnetocrystalline anisotropy of the disordered polycrystalline $Fe_{100-x}Si_x$ alloys [BOZO1951, BECK1991], nanocrystalline Fe-Si powders [ZHOU1999] and rapidly quenched $Fe_{100-x}Si_x$ alloys [VARG2001] are also shown in the figure. While the value of anisotropy for disordered polycrystalline Fe-Si decreases largely [BOZO1951, BECK1991], the K_{eff} values of nanocrystalline alloys decreases gradually with increasing Si content. This observed results are in good agreement with the reports of Zhou et al. [ZHOU1999]. However, the values of H_C were found to increase with increasing Si content as shown in Figure 4.28. Shen et al. [SHEN2005] reported that for the alloys containing large values of dislocation density, H_C is dominated by the residual strain generated by dislocations. The presence of such strains remarkably rescinds all the advantages of having nanosized grains and results high values of H_C. Yousefi et al. [YOUS2014] and Bahrami et al. [BAHR2013] also showed an increase in H_C of the as-milled Fe-Co-Si and Fe-Ni-Si based alloys prepared by mechanical alloying technique with increasing Si content.

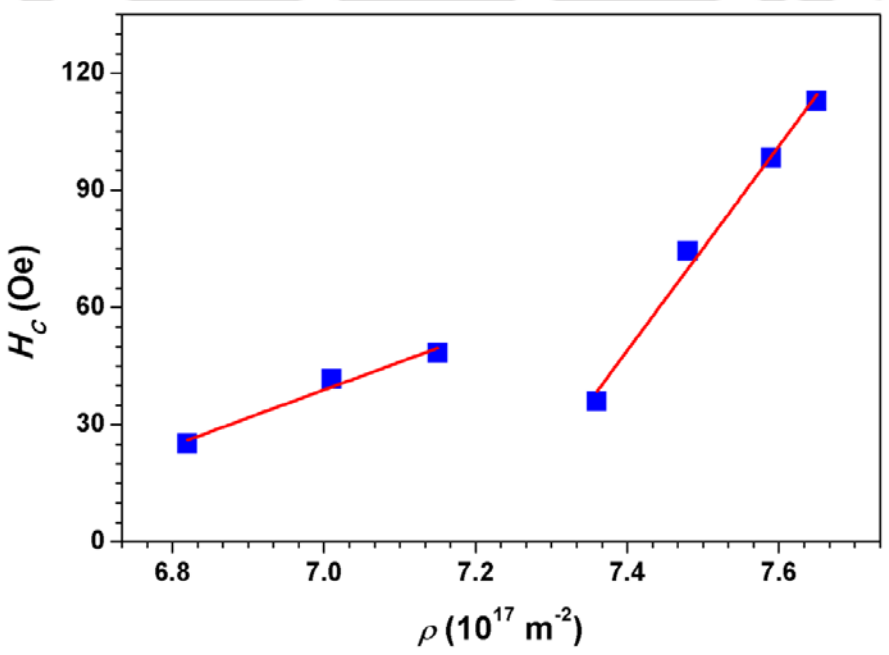

Figure 4.31. Variation of H_C of $Fe_{100-x}Si_x$ solid solution as a function of ρ.

To understand the increasing H_C nature with Si substitution, we have tried to interpret the variation of H_C with all the structural parameters. As explained earlier, there is no clear correlation between D and H_C of Fe-Si solid solution, as the effective changes in D and H_C with Si content are significantly different. This suggests that H_C depends not only on D, but also on other structural factors. Figure 4.31 displays the variation of H_C as a function of ρ. It is clear from the figure that there are two distinct regions of nearly linear behavior. As discussed earlier, according to Néel's theory [NEEL1946], if the magneto-elastic energy is larger than the anisotropy energy, the coercivity is likely to be proportional to the density of dislocations. Therefore, if dislocation defect is the only factor responsible for the increase of H_C with increasing Si content, then the linear relationship between dislocation density and coercivity is expected to hold for the entire composition range. However, the observed deviation in the initial linear behavior of H_C with ρ indicates that factors other than dislocation defects contribute to H_C of the powders at higher Si content. Since the average particle size decreases with increasing Si content, it can be correlated that the coercivity of the powders also depends on the average particle size at higher Si content Fe-Si non-equilibrium solid solution [HERN2005, KALI20081]. As the coercivity is a microstructure sensitive property, it would also depend on other microstructural parameters such as fraction of grain boundaries. Hence, H_C increases significantly with increasing Si content and inclusions [CHIT2011].

To investigate the presence of various magnetic phases in high Si content samples in correlation with the structural studies, high temperature *M–T* measurements were carried out systematically for all the compositions milled at different milling hours under 100 Oe applied field at a heating rate of 5 K per minute. In order to compare the *M-T* data, the temperature dependent magnetization data is normalized with respect to corresponding room temperature magnetization value. Figure 4.32 depicts the normalized *M-T* curves for the samples milled for different time periods. A close observation of the Figure 4.32 and a comparative study between the structural properties reveals that Fe-Si solid solution with $x \leq 20$ exhibit a single magnetic phase transition from ferromagnetic to paramagnetic phase as shown in Figure 4.32(a). On the other hand, *M-T* curves of samples with $x \geq 20$ show strong dependence on the milling time, and the destruction and generation of various magnetic phases were evident from Figure 4.32(b). Two different magnetic phase transitions were observed for $Fe_{100-x}Si_x$ ($25 \leq x \leq 35$) powders milled for 40 hours. While the first one at comparatively low temperature can be assigned to the formation of Fe_3Si compound [WALI1994, VARG2001], the phase transition observed at higher temperatures (T_C) is due to the solid solutions of Si in Fe [BERK1969].

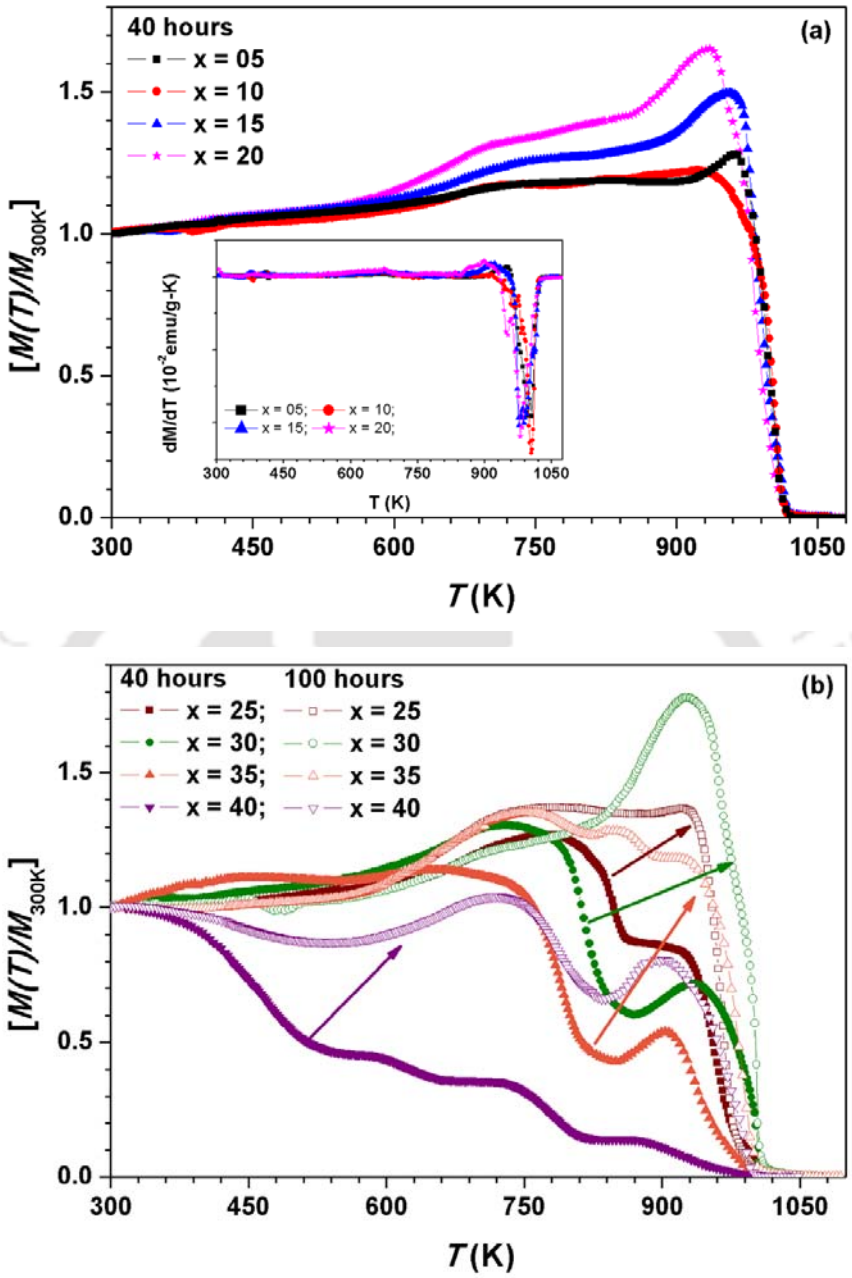

Figure 4.32. Normalized *M-T* curves of $Fe_{100-x}Si_x$ solid solution with (a) $x \leq 20$ milled for 40 hours and (b) $x \geq 25$ milled for 40 hours and 100 hours.

On further increasing the Si content to 40 at.%, we observed multiple phase transitions due to the presence of Fe_5Si_3, Fe-Si compounds (Fe_2Si and Fe_3Si) and Fe-Si solid solution. However, with increasing the milling time to 100 hours, the multiple phase transitions transform into a single phase transition corresponding to Fe-Si solid solution as shown by arrow marks in Figure 4.32(b) except for $Fe_{60}Si_{40}$ sample, which exhibits both Fe_5Si_3 and Fe-

Si solid solution. It is understood that the mechanical alloying process involving a repeated cold welding and fracturing to form nanocrystalline structure results the formation of various phases such as solid solutions, intermetallic compounds and amorphous states depending on the milling intensity and milling period. Hence, the formation of intermetallic compounds such as Fe_5Si_3, Fe_3Si and Fe_2Si are also observed for alloys with $x \geq 25$.

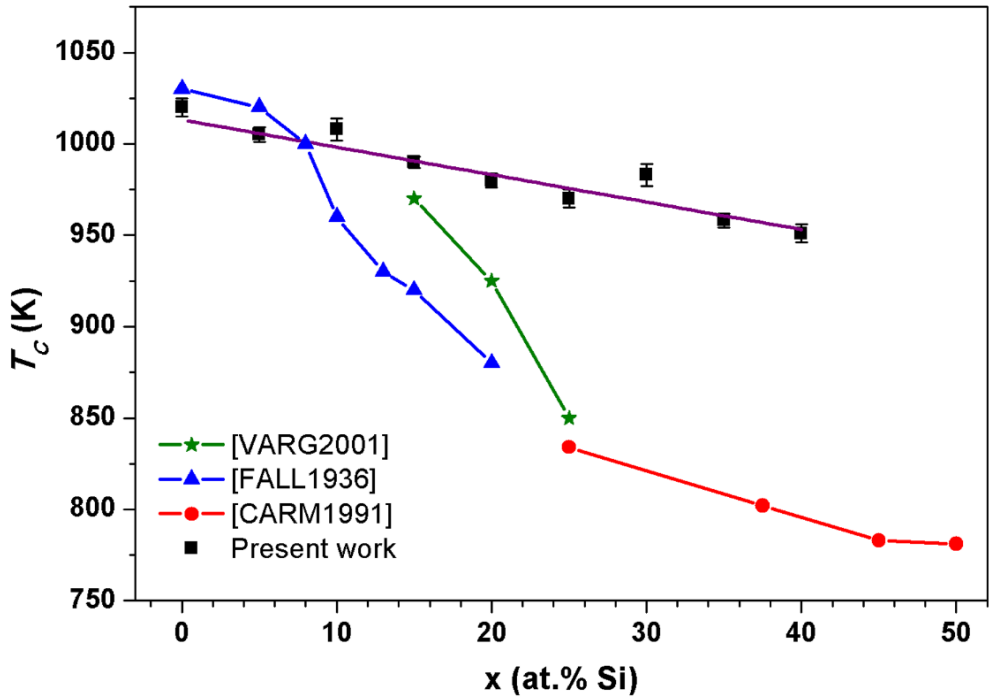

Figure 4.33. Variation of T_C of $Fe_{100-x}Si_x$ solid solution as a function of Si content. T_C values reported in Fe-Si system [FALL1936, CARM1991, VARG2001] are also shown for comparison.

To understand the variation of Curie temperature (T_C) of the solid solution with Si content, the value of T_C of various magnetic phases was obtained from the thermal derivative of *M-T* data. Figure 4.33 depicts the variation of T_C of Fe-Si solid solution for the presently investigated samples along with the literature results for comparison. A careful analysis of the present data and in comparison with the literature results, we interpret that T_C lies in the range 910 – 1043 K for Fe-Si solid solution [ESCO1991], 800 – 840 K for Fe_3Si [WALI1994, VARG2001], 543 K for Fe_2Si [ESCO1991], 300 – 623 K for amorphous Fe-Si and 378 – 393 K for Fe_5Si_3 [VARG2001, GIRO1987]. The obtained results for the presently investigated samples suggest that the end products of mechanical alloying process are produced according to following reaction;

$(100-x)$ Fe + x Si → α-Fe (Si); for $x \leq 20$

$(100-x)$ Fe + x Si → a-Fe-Si + Fe_5Si_3 + Fe_3Si + Fe_2Si + α-Fe (Si); for $x \geq 25$

It is interesting to note that T_C of Fe-Si solid solution decreases gradually at a rate of 1.45 K per at.% Si. Carmona et al. [CARM1991] reported a T_C variation of 2.56 K per at.% Si for the composition between $Fe_{75}Si_{25}$ and $Fe_{62.5}Si_{37.5}$ prepared by mechanical alloying process. On further increasing the Si content to 75 at.% in $Fe_{100-x}Si_x$ alloy powder, T_C decreases down to 768 K at a rate of 0.9 K per at.% Si. On the other hand, T_C decreases largely at a rate of 6.6 K per at.% Si in rapidly quenched $Fe_{100-x}Si_x$ alloys in the composition range of $5 \leq x \leq 20$ [FALL1936]. The slow decrease of T_C with Si content in mechanically alloyed powders can be attributed to presence of considerable strain in the as-milled powders [GORR2009], which is evident from the non-smooth variation of magnetization with increasing temperature [ESCO1991]. These results reveal a good correlation between the structural and thermomagnetic properties in the presently investigated Fe-Si nanocrystalline alloy powders.

4.5. Summary:

A systematic study on the evolution of structural and magnetic properties of $Fe_{100-x}Si_x$ (x = 5 - 50) alloy powders prepared by mechanical alloying process in a planetary ball mill has been carried out as a function of milling time periods and Si contents under different milling conditions over a wide range of compositions. The salient features of the Fe-Si binary alloys from the current investigations are as follows:

- Mechanical alloying produces non-equilibrium solid solutions of α-Fe(Si) with the average crystallite size of nanometer range (around 10 nm) and dislocation density of the order of 10^{17} m^{-2}. Milling time and milling speed required for forming the solid solution in high Si content Fe-Si alloys increases with increasing Si content. The formation of solid solution could be extended up to 40 at.% Si.
- Occurrence of atomic disorder with increasing milling time and Si content was evident from the changes in the lattice parameter and magnetization values.
- Milling process lead to the formation of finer particles of nearly homogeneous size and spherical shape in nature.
- Presence of dislocations introduced during the mechanical alloying process and the formation of grain boundaries increases the possibility of domain wall pinning and resulting an increased coercivity with increasing Si content. The linear variation of

coercivity with dislocation density over a complete range of milling time periods depends strongly on the Si content.

- Strain induced during milling has affected the Curie temperature of the powder, which decreases at a rate of 1.45 K per at.% Si with increasing Si content in Fe-Si solid solution.
- Although similar correlation between structure and magnetic properties has been observed in powders of all the alloy compositions, the structural and magnetic parameters have been found to be strongly dependent on the composition of the alloys.

Chapter 5

Mechanical alloying of ternary $Fe_{100-x-y}Co_ySi_x$ alloy powders: Effect of Co substitution

5.1. Introduction:

The mechanical alloying of binary $Fe_{100-x}Si_x$ alloy powders discussed in Chapter 4 revealed the formation of non-equilibrium solid solutions of α-Fe(Si) over a wide range of compositions. However, the milling time and speed required for forming the solid solution in high Si content alloys increased considerably with increasing Si content. While the average crystallite size was obtained to be 8 to 12 nm, the dislocation density increases slightly with Si addition up to 35 at.%. The occurrence of atomic disorder with milling and Si content has been discussed based on the variation of lattice constant (a) and saturation magnetization (M_S). Recently, there has been growing demand to develop new soft magnetic materials with high M_S, high permeability and low core loss for saving energy in electric power transmission and automotive applications. In this context, Fe based nanocrystalline alloys have been extensively investigated [SELL2006, OHIT2007]. The substitution of Si in Fe based alloys not only increases the electrical resistivity and thereby reduces eddy current losses, but also decreases the effective magnetic anisotropy (K_{eff}). In addition, M_S values are also observed to be decreased significantly. In such cases, the substitution of Co for Fe in Fe-based amorphous and nanocrystalline alloys is expected to enhance M_S and Curie temperature (T_C) [VACC1981, MISH2010]. Yousefi et al. [YOUS2012] reported the effect of simultaneous addition of Co and Si to Fe in nanostructured Fe (Fe-Co-Si alloys) prepared by mechanical alloying process and showed that the magnetic properties are strongly dependent on the composition of Si content due to the competition between Si and Co in the alloying process in nanostructured Fe. However, a systematic investigation on the evolution of nanocrystalline microstructure and the resulting magnetic properties of Co substituted $Fe_{100-x-y}Co_ySi_x$ alloys with different Si contents has not been performed yet. Therefore, in this chapter, we present the effect of Co substitution on the structural and magnetic properties of nanocrystalline $Fe_{100-x-y}Co_ySi_x$ alloy powders prepared by mechanical alloying process by employing high energy ball mill.

5.2. Experimental details:

The starting materials used in this study include high purity (> 99.8 %) Fe, Co and Si powders with different particle sizes of 60 – 100 μm, 2 – 4 μm and 5 – 30 μm respectively. Weighed quantities of elemental Fe, Si and Co powders corresponding to the compositions of $Fe_{100-x-y}Co_ySi_x$ with x = 10 and 15 and y = 0 – 20 were milled in a hardened steel bowl together with 8 mm diameter hardened steel milling balls. The ball to powder weight ratio was maintained at 10:1. The bowl was filled with high purity argon gas to prevent oxidation of the powders

during milling. The planetary ball mill (Insmart, India) was operated at 600 rpm and the samples were milled for 40 hours duration. The milling process was programmed such that the milling was paused for 10 minutes after every 15 minutes of milling to minimize excessive temperature rise. To determine the variations of a, average crystallite size (D), dislocation density (ρ) and the fraction of grain boundaries (f_{GB}), the powder specimens were analyzed using X-ray diffraction (XRD) in a high-power X-Ray diffractometer (Rigaku TTRAX III 18 kW) using Cu-K_α (λ = 1.54056 Å) radiation. XRD data were collected at a slow scan rate of 0.005°/s to analyse the structural parameters using Modified Williamson Hall Plot (MWHP) method [UNGA19991, UNGA19992]. As described in Chapter 4, the instrumental broadening was corrected using eqn.(4.01) for the calculations of structural parameters. The surface morphology and evolution of nanocrystalline microstructure were investigated by field emission scanning electron microscope (FE-SEM, ZEISS) and transmission electron microscope (TEM, JEOL 2100) respectively. Overall compositions of the as-milled powders were characterized using energy dispersive spectrometer (EDS, Oxford) attached to scanning electron microscope (SEM, Leo 1430VP). Magnetic properties of the samples were investigated by performing room temperature magnetic hysteresis (M-H) loops and temperature dependent magnetization measurements (M-T) by using vibrating sample magnetometer (VSM, LakeShore Model 7410 USA).

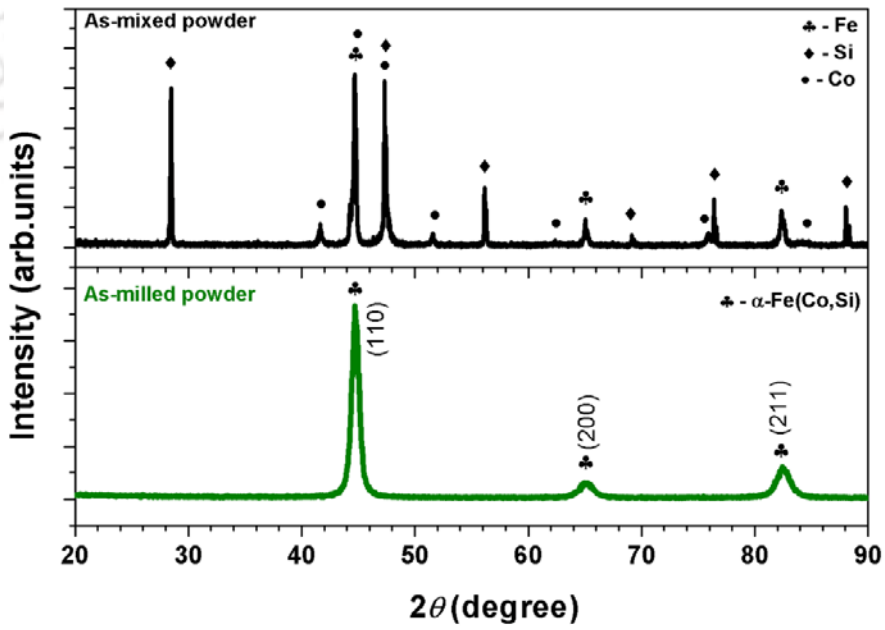

Figure 5.01. Typical room temperature XRD patterns of as-mixed and 40 hours milled $Fe_{85}Co_5Si_{10}$ powders.

5.3. Properties of nanocrystalline ternary $Fe_{90-y}Co_ySi_{10}$ alloy powders:

5.3.1. Structural evolution with Co substitution:

Figure 5.01 displays typical XRD patterns of as-mixed and 40 hours milled $Fe_{85}Co_5Si_{10}$ alloy powders. It is observed that as-mixed powders exhibit sharp characteristic Bragg reflections corresponding to all three constituting elements, i.e., Co (face centred cubic and hexagonal close-packed structures), Si (diamond cubic) and Fe (body centred cubic). However, the peaks corresponding to Co and Si disappear after milling for 40 hours. This is mainly due to the diffusion of Co and Si in Fe matrix forming body centred cubic (*bcc*) solid solution of α-Fe(Co,Si). Note that no additional peaks corresponding to any other compounds were observed.

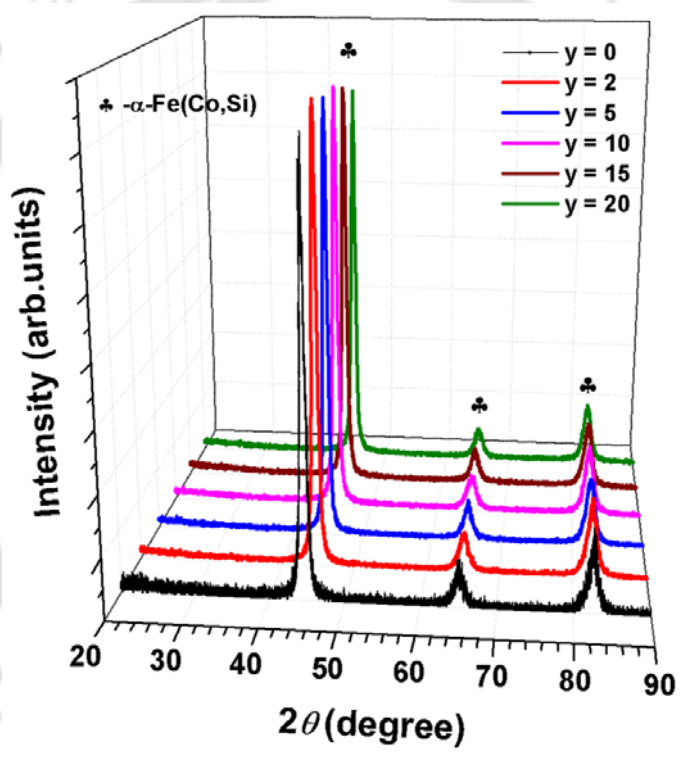

Figure 5.02. Room temperature XRD patterns of 40 hours milled $Fe_{90-y}Co_ySi_{10}$ alloy powders with y = 0 - 20.

Figure 5.02 shows the XRD patterns of $Fe_{90-y}Co_ySi_{10}$ with y = 0 – 20 alloy powders milled for 40 hours. The as-milled powders exhibit significant peak broadening along with a considerable shift in the peak positions. As discussed in the earlier chapter, the broadening of the peaks confirms the formation of nanocrystalline microstructure with highly refined and internally strained grains, while the shifting of peak positions suggests the atomic disorder due the dissolution of substituting elements Co and Si in Fe matrix leading to a change in lattice

constant. The solid solubility levels have been generally determined from the changes in the lattice constant deduced from peak positions in the XRD pattern [KOOH2008, LOUD2011]. To understand the dissolution of Co and Si into Fe, the lattice constant determined from the peak positions is depicted as a function of Co content in Figure 5.03. It is clear from the figure that the lattice constant is observed to increase slightly up to 10 at.% Co substitution and then decreases with further increase in Co content. A maximum lattice constant change of 0.1% was observed with Co substitution in $Fe_{90-y}Co_ySi_{10}$ alloy powders.

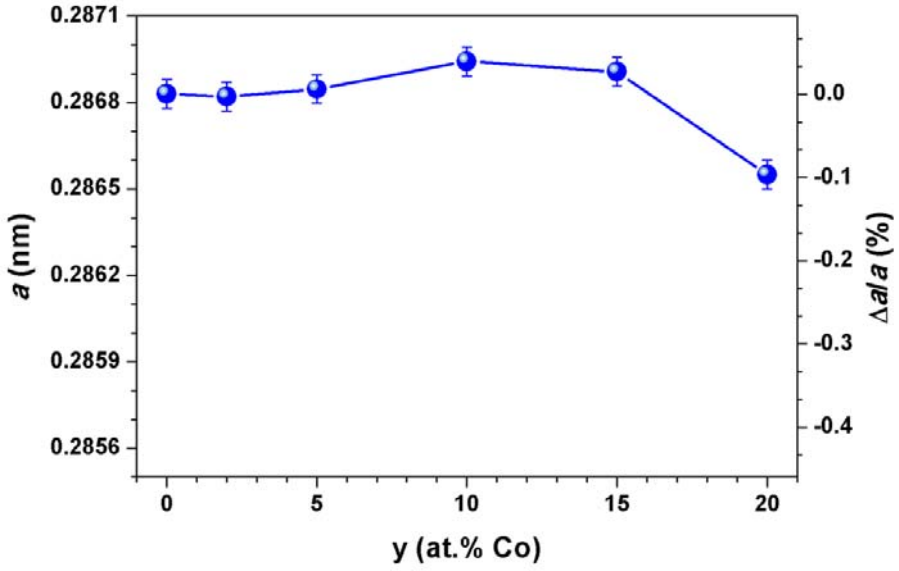

Figure 5.03. Variation of lattice constant and fractional change in the lattice constant of 40 hours milled $Fe_{90-y}Co_ySi_{10}$ alloy powders.

All the other structural parameters were determined by using MWHP method as discussed in Chapter 4. Figure 5.04 displays the variations of D and ρ determined using eqn.(4.04) fitted to the XRD data and f_{GB} calculated using eqn.(4.07) as a function of Co content. The values of D are found to increase slightly from about 8 nm to 10 nm with increasing Co content up to 10 at.% and then decreases sluggishly for high Co content. On the other hand, the values of ρ are found to be of the order of 10^{17} m^{-2}, but decrease by small amount for initial Co addition up to 10 at.% and then increases slightly with further increase in Co content. Similarly, the values of f_{GB} are also found to decrease from nearly 20 % to 16.5 % with increasing Co content up to 10 at.% and increases slowly for higher Co content. These results show close agreement to each other and can be understood as follows: The slow increase of lattice constant with Co substitution suggests that the milling process leads to the dissolution of Si and Co atoms in Fe matrix and forms solid solution. Such variation of lattice constant with Co substitution is in

good agreement with the earlier report on Fe-Co system [SHIG1974]. However, with increasing Co content above 10 at.%, we observed a considerable drop in the lattice parameter, which could be attributed to the delay in the dissolution of Co by the presence of Si [YOUS2012]. Being Co as ductile [COTT1981, KELL1987, CHRI2013], the continuous dissolution of Co in Fe decreases the work hardening rate of the Fe matrix and hence resulting an increase in the average values of D. As a result, both the values of ρ and f_{GB} decrease with increasing Co content up to 10 at.%. These results are adequate as per the expectation by following the eqns.(4.06) and (4.07). On further increasing the Co content, due to delay in the Co dissolution, work hardening of Fe matrix is modified mainly by the presence of Si. This results as a decrease in the values of a and D. Therefore, the values of ρ and f_{GB} increase gradually at higher Co substitution.

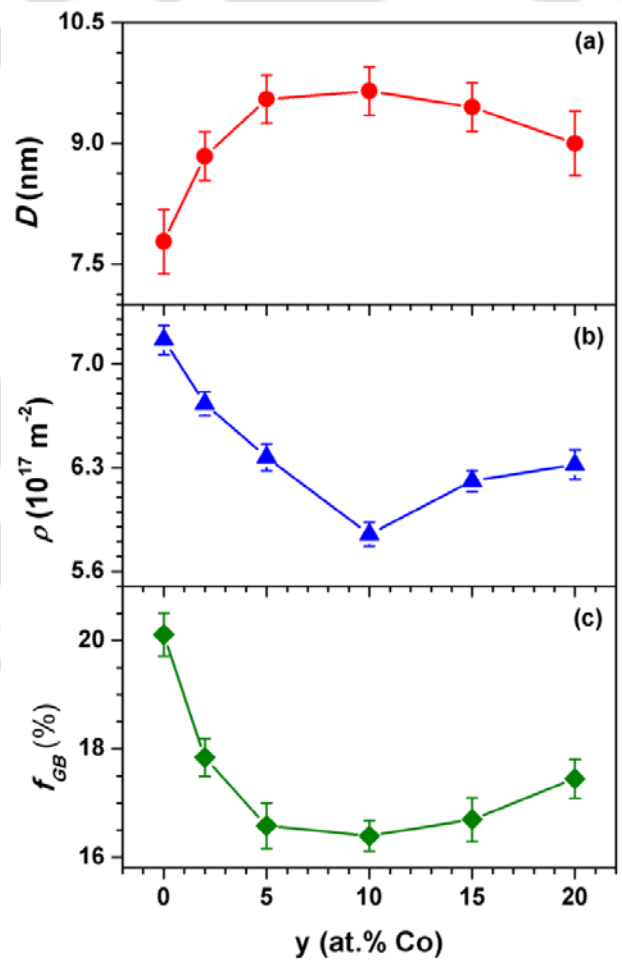

Figure 5.04. Variations of D, ρ and f_{GB} of 40 hours milled $Fe_{90-y}Co_ySi_{10}$ alloy powders.

In order to understand the development of nanocrystalline microstructure with the Co substitution, TEM observations were carried out on the milled $Fe_{90-y}Co_ySi_{10}$ alloy powders. Figure 5.05 displays typical bright field TEM (BF-TEM) images and selected area electron diffraction (SAED) patterns of $Fe_{85}Co_5Si_{10}$ and $Fe_{70}Co_{20}Si_{10}$ alloy powders milled for 40 hours. BF-TEM micrograph displays the existence of fine-grain microstructure which is a typical characteristic of mechanically alloyed powders. The non-uniform contrast inside each grain and along the grain boundaries observed in BF-TEM images are the indicative of high degree of strain present in the as-milled powders. The average crystallite size calculated from the BF-TEM micrographs are about 10 nm and 9 nm for the 5 and 20 at.% Co content samples, respectively. On the other hand, SAED patterns show the polycrystalline nature of the powders with the rings corresponding to reflections from (110), (200), (211), (220) and (310) planes of α-Fe(Co,Si). The *d*-spacing and lattice parameter calculated from the SAED patterns for the 40 hours milled samples are in close agreement with those values obtained from XRD peak analysis.

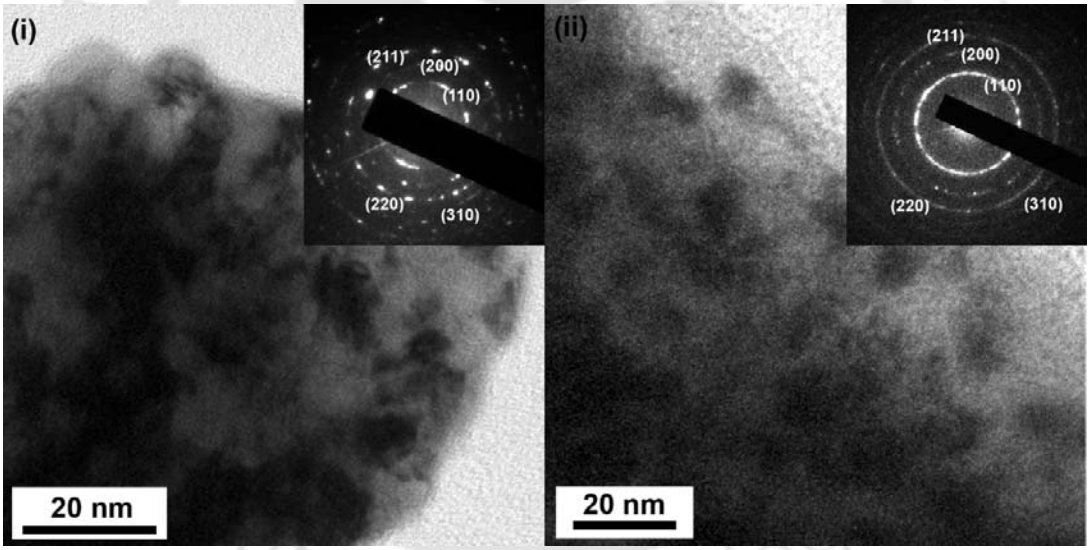

Figure 5.05. BF-TEM images and SAED patterns of 40 hours milled $Fe_{90-y}Co_ySi_{10}$ alloy powders with (i) $y = 5$ and (ii) $y = 20$.

Changes in the surface morphology of the powders with increasing Co substitution were observed from the SEM micrographs of pure elemental powders and powders milled for 40 hours. Figure 5.06 depicts typical SEM micrographs of pure Fe (a), Si (b) and Co (c) and powders milled for 40 hours with Co content 5 at.% (d), 10 at.% (e) and 20 at.% (f). While pure Fe exhibits predominantly rounded shape with large size of the particles in the range between 60 and 100 μm [DEME2013], the Si powder shows plate-like morphology

[BAHR2013] and contains finer particles in the size range of 5 to 30 μm. Cobalt powder exhibit irregular shape morphology with the average particle size of 2 - 4 μm. After the milling process, the particle size distribution of the milled powders is found to be relatively inhomogeneous, which are typical of mechanically alloyed powders and result from the repeated cold-welding and fracture of powders during ball milling [LUL1998]. The particle size of the powders was found to be ranging from few hundred nanometer to few micrometer, which are agglomerations of nanosized (~10 nm) crystallites oriented randomly within the particles.

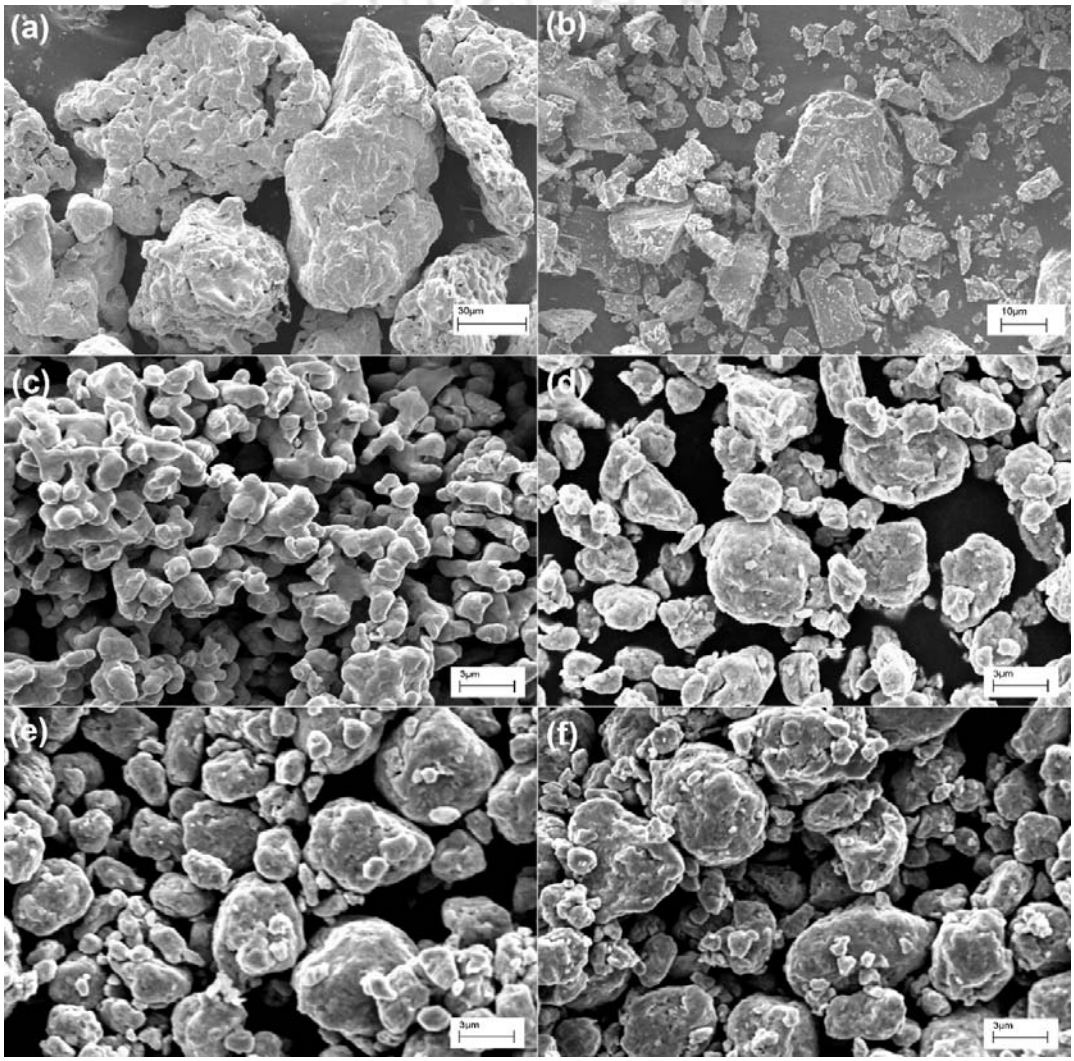

Figure 5.06. SEM micrographs of (a) pure Fe, (b) pure Si, (c) pure Co, and 40 hours milled $Fe_{90-y}Co_ySi_{10}$ alloy powders with (d) y = 5, (e) y = 10 and (f) y = 20.

Composition analysis performed on the milled powders using EDS showed the overall composition of the milled powders to be $Fe_{90.3}Si_{9.7}$, $Fe_{88.4}Co_{1.8}Si_{9.8}$, $Fe_{85.8}Co_{4.6}Si_{9.6}$,

$Fe_{80.9}Co_{9.8}Si_{9.3}$, $Fe_{76.2}Co_{14.3}Si_{9.5}$ and $Fe_{71}Co_{19.2}Si_{9.8}$ for the milled samples with Co content of 0, 2, 5, 10, 15 and 20 at.%, respectively. These results evidently confirm the presence of Si and Co in the form of solid solution in α-Fe.

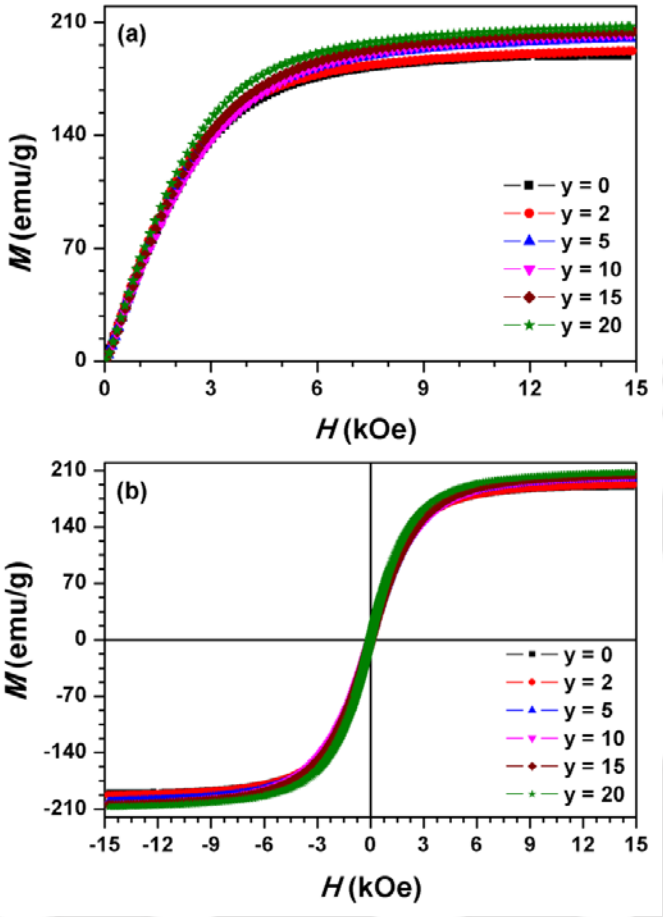

Figure 5.07. Room temperature (a) initial magnetization curves and (b) *M-H* loops of 40 hours milled $Fe_{90-y}Co_ySi_{10}$ alloy powders.

5.3.2. Evolution of magnetic properties with Co substitution:

To understand the effect of Co substitution on the magnetic properties of as-milled $Fe_{90-y}Co_ySi_{10}$ alloy powders, the room temperature initial magnetization curves and magnetic hysteresis (*M-H*) loops were obtained using VSM and depicted in Figure 5.07. While the shape of the loops is typical of a soft magnetic material, a close observation reveals that the substitution of Co fine tunes the slope of the curves towards lower field and increases M_S values. This could be due to the atomic pair ordering in the presently investigated alloys. A similar influence of Co has been reported in large number of Fe based nanocrystalline alloys [IDZI2005]. Shiga reported that the increase of the magnetization due to the magnetic ordering

can influence the change in the lattice constant of Fe-Co alloys with increasing Co content [SHIG1974]. This is in good agreement with the present results. Further, the internal strain induced during mechanical alloying process results in different nature of spin states which leads to considerable deviation of magnetization from attaining saturation. For the field dependence of deviation in magnetization from saturation, the experimental magnetization data were fitted to the power series using eqn.(4.09) as demonstrated in Chapter 4 for the calculation of K_{eff}.

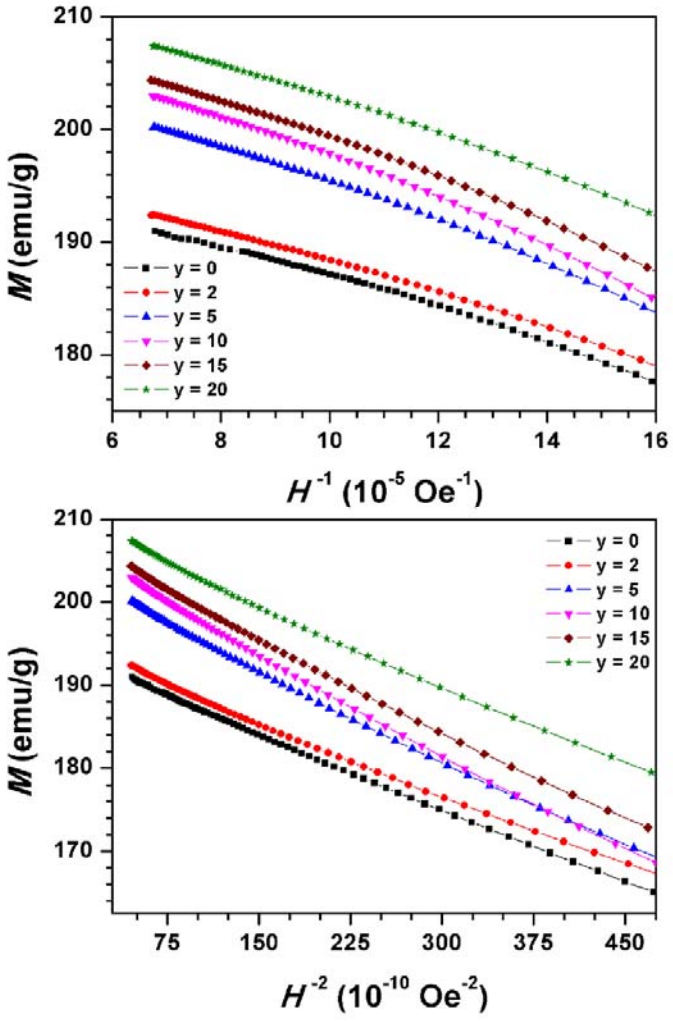

Figure 5.08. The representation of M as a function of H^{-1} and H^{-2} for $Fe_{90-y}Co_ySi_{10}$ alloy powders with y = 0, 2, 5, 10, 15 and 20 milled for 40 hours.

In order to verify the applicability of the power series expression and to analyse the experimental magnetization data, plots of magnetization against H^{-1} and H^{-2} for the as-milled $Fe_{90-y}Co_ySi_{10}$ alloy powders are shown in Figure 5.08. Supported by the validity of the data,

the magnetization data were fitted to eqn.(4.09) to obtain the values of a_2 and hence K_{eff} using eqn.(4.11). Figure 5.09 displays the extracted values of H_C from the *M-H* loops and the determined values of M_S and K_{eff} as a function of Co contents. M_S values increase considerably for low amount of Co substitution, but the rate of increase of M_S decreases with further increase in Co content above 10 at.%. The increase in M_S could be attributed to the atomic ordering and the observed results are in good agreement with the earlier reports on similar systems [SHIG1974, IDZI2005, MISH2009, YOUS2012]. Note that such atomic ordering can induce additional magnetic anisotropy which may deteriorate the soft magnetic properties of the milled powders. This is noticeably evidenced from the plot of coercivity (H_C) variation with Co content. H_C increases slowly at a rate of nearly 1 Oe per at.% Co for initial Co substitution up to 5 at.% and then increases rapidly at a rate of about 3.4 Oe per at.% Co.

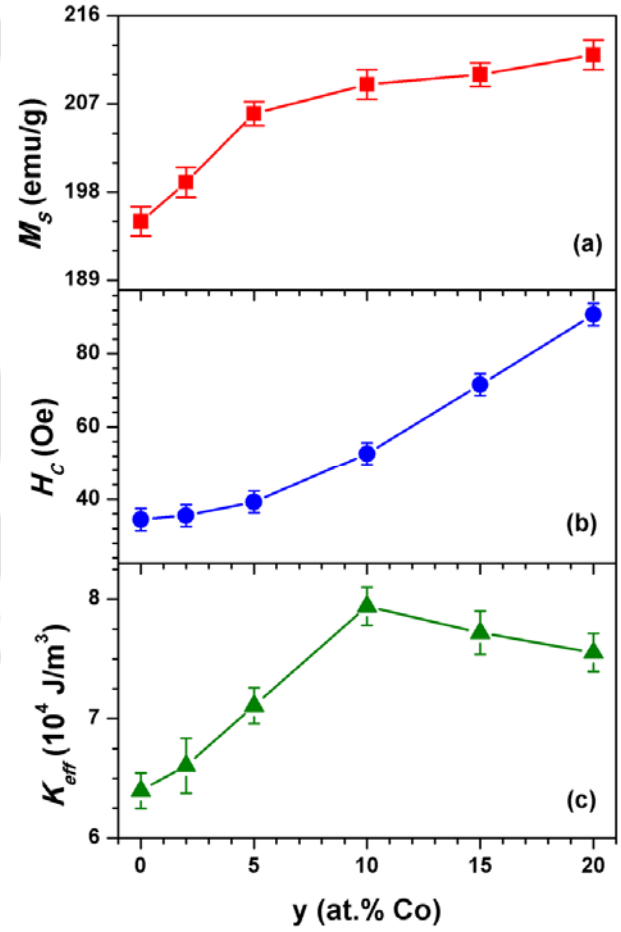

Figure 5.09. Variations of M_S, H_C and K_{eff} of 40 hours milled $Fe_{90-y}Co_ySi_{10}$ alloy powders.

To understand the variation of coercivity with Co content, the determined values of K_{eff} are also plotted in Figure 5.09(c) for comparison. Substitution of Co in $Fe_{90-y}Co_ySi_{10}$ alloy powders

increases the K_{eff} initially up to 10 at.% and then decreases slightly for high Co content. The obtained values of K_{eff} are substantially larger as compared to the magnetic anisotropy values of disordered polycrystalline Fe-Si alloys [BECK1991] and Fe-Si alloys produced by rapid-solidification process [VARG2001]. It has been reported that there exists a correlation between the H_C and K_{eff} in nanocrystalline alloys [SELL2006], but no such direct relation could be obtained from Figure 5.09 for the complete range of presently investigated samples. This might be due to different contributions from the variations of D, ρ and K_{eff} on the variations of H_C with substituting elements. For instance, it is well known that H_C in the mechanically alloyed powders increases with increasing ρ [KALI20082], while the reduction in D exhibits a large decrease in H_C [KALI20083, BENS2010]. In the presently investigated samples, (i) the values of D are found to increase slightly from about 8 nm to 10 nm with increasing Co content up to 10 at.% and then decrease sluggishly for higher Co content, (ii) the values of ρ decrease initially with increasing Co up to 10 at.% and increase slightly for higher Co content, and (iii) the variation of K_{eff} shows an opposite behaviour as compared to the variations of ρ with Co substitution. These results suggest that the variation of H_C in Fe-Co-Si alloy powders is not only controlled by the structural parameters which vary with the alloying process, but also by the atomic ordering with Co addition.

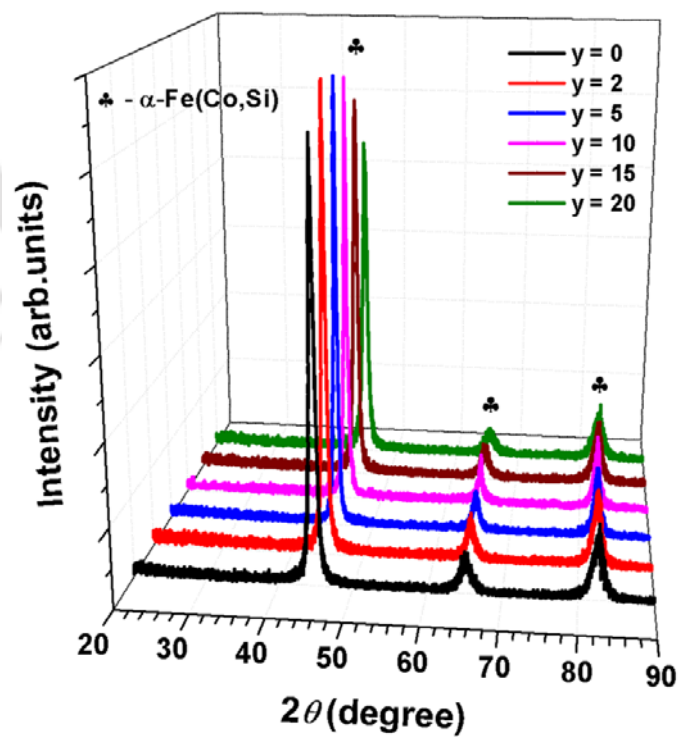

Figure 5.10. Room temperature XRD patterns of 40 hours milled $Fe_{85-y}Co_ySi_{15}$ alloy powders.

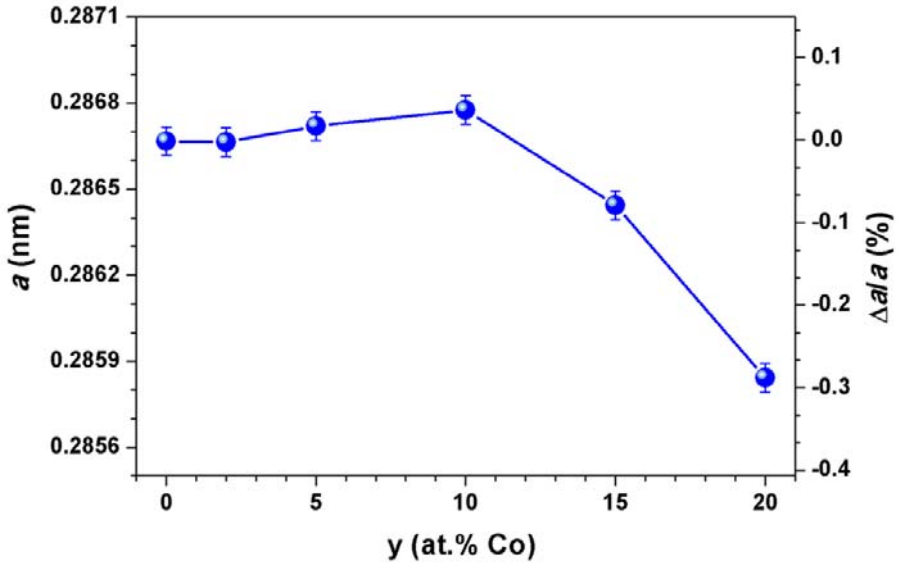

Figure 5.11. Variation of lattice constant and fractional change in the lattice constant of 40 hours milled $Fe_{85-y}Co_ySi_{15}$ alloy powders with y = 0, 2, 5, 10, 15 and 20.

5.4. Properties of nanocrystalline ternary $Fe_{85-y}Co_ySi_{15}$ alloy powders:

In this section, we shall report the structural and magnetic properties of nanocrystalline $Fe_{85-y}Co_ySi_{15}$ alloy powders milled for 40 hours. Yousefi et al. [YOUS2012] reported that the introduction of large amount of Si delays the dissolution of Co into Fe lattices. In the earlier section, we have observed such delay of Co dissolution by the presence of Si only in higher Co contents resulting a significant decrease in lattice constant. In order to understand this feature in detail, we have increased Si content from 10 to 15 at.% in the parent system and studied the effect of Co substitution on the structural and magnetic properties of nanocrystalline $Fe_{85-y}Co_ySi_{15}$ alloy powders.

5.4.1. Structural evolution with Co substitution:

Figure 5.10 displays room temperature XRD patterns of 40 hours milled $Fe_{85-y}Co_ySi_{15}$ alloy powders. It is observed that as-milled powders exhibit no sharp characteristic Bragg reflections corresponding to the substituting elements of Co and Si. This indicates the dissolution of Co and Si in Fe matrix and the formation of a *bcc* solid solution of α-Fe(Co,Si). In addition, we have not observed any additional peaks corresponding to any other compounds. Nevertheless, the as-milled powders exhibit significant peak broadening along with a considerable shift in the peak positions. While the broadening of the peaks confirms the formation of nanocrystalline microstructure with highly refined and internally strained grains, the shifting

of peak positions suggests the occurrence of atomic disorder due the dissolution of substituting elements Co and Si in Fe matrix leading to a change in lattice constant. Figure 5.11 shows the variations of lattice constant determined from the peak positions as a function of Co content. As compared to $Fe_{90-y}Co_ySi_{10}$ alloy powders discussed in section 5.3.1, the as-milled $Fe_{85-y}Co_ySi_{15}$ alloy powders exhibit almost similar increase in lattice constant up to 10 at.% Co, but decrease largely above 10 at.% Co substitution. The maximum lattice constant change of 0.29 % was observed with Co substitution in $Fe_{85-y}Co_ySi_{15}$ alloy powders. The slow increase of lattice constant for the initial substitution of Co indicates that both Si and Co dissolved into Fe lattices for Co content up to 10 %. The large reduction in lattice constant with increasing Co content above 10 at.% is anticipated only if more number of Si atoms are dissolving into Fe as compared to that of Co atoms. Therefore, this could be attributed to the fact that the introduction of more Si into Fe lattice delays the dissolution of Co in Fe matrix with increasing Co content.

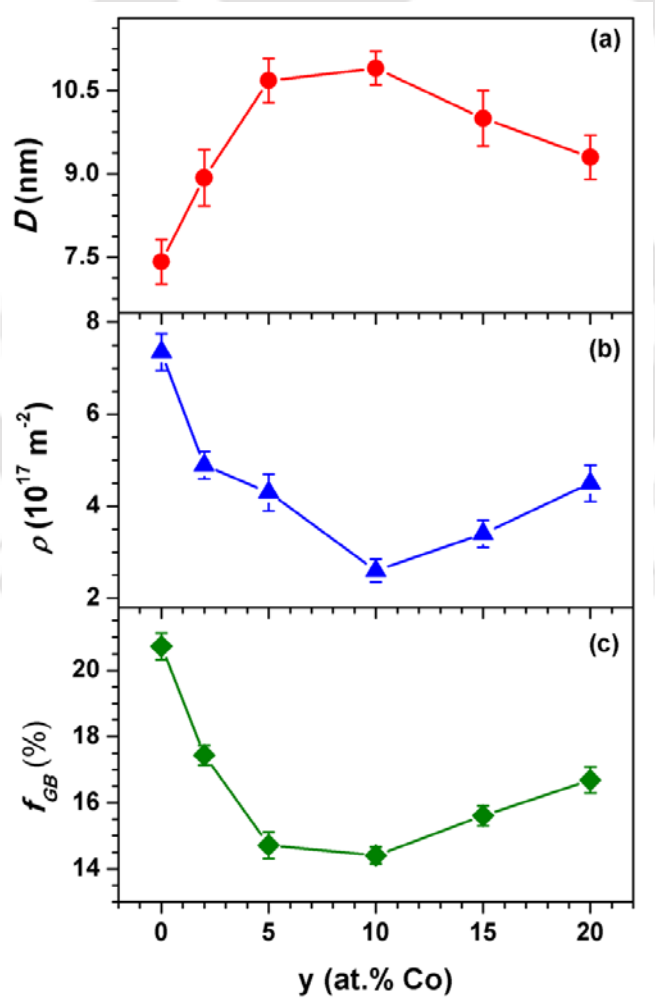

Figure 5.12. Variations of D, ρ and f_{GB} of 40 hours milled $Fe_{85-y}Co_ySi_{15}$ alloy powders.

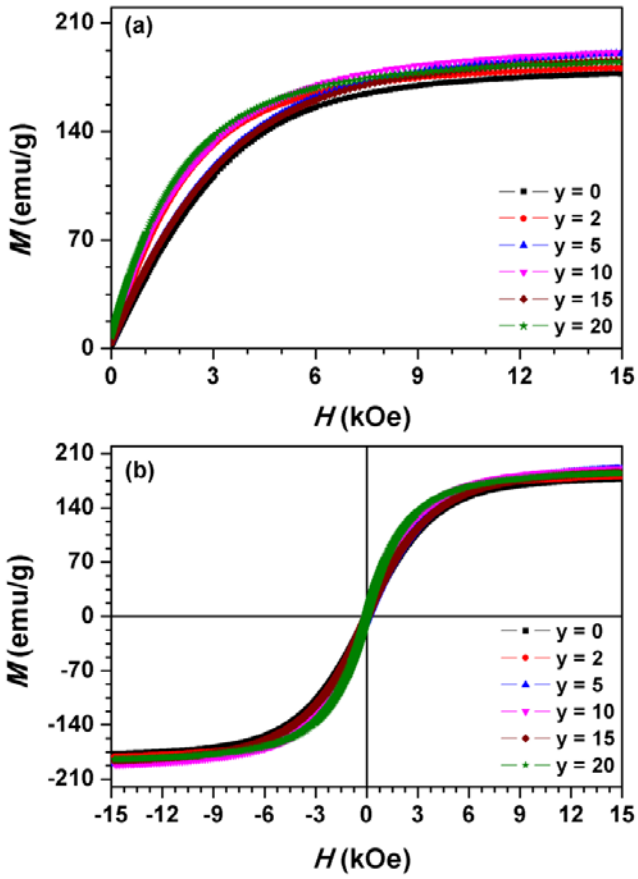

Figure 5.13. Room temperature (a) initial magnetization curves and (b) *M-H* loops of 40 hours milled $Fe_{85-y}Co_ySi_{15}$ alloy powders.

All the other structural parameters were determined by using MWHP method as discussed in Chapter 4. Figure 5.12 displays the variations of D, ρ and f_{GB} as a function of Co content for $Fe_{85-y}Co_ySi_{15}$ alloy powders. The values of D are found to increase slightly from about 7 nm to 11 nm with increasing Co content up to 10 at.% and then decreases down to 9 nm for higher Co substitution. On the other hand, the values of ρ are found to be on the order of 10^{17} m^{-2}, but decreases considerably for initial Co addition and then increases significantly with further increase in Co content. Similarly, the values of f_{GB} are also found to decrease from nearly 21 % to 14 % with increasing Co content up to 10 at.% and increases significantly for higher Co content. These results show similar behaviors of those observed for $Fe_{90-y}Co_ySi_{10}$ alloy powders, but the actual variation of the parameters depends on the alloy composition. Furthermore, the observed results are in close agreement with the recent reports on similar system [YOUS2012] and hence the observed properties could be attributed to the change in dissolution process due to the competition between Si and Co atoms, i.e., the introduction of

more Si into Fe lattice delays the dissolution of Co. Note that such delayed process would enhance the density of dislocations and fraction of grain boundaries at higher Co content. This is in good agreement with the results shown in Figure 5.12. Therefore, the variations of D, ρ and f_{GB} are also strongly depend on the alloying process, which are expected to play a considerable role in the magnetic properties of these alloyed powders.

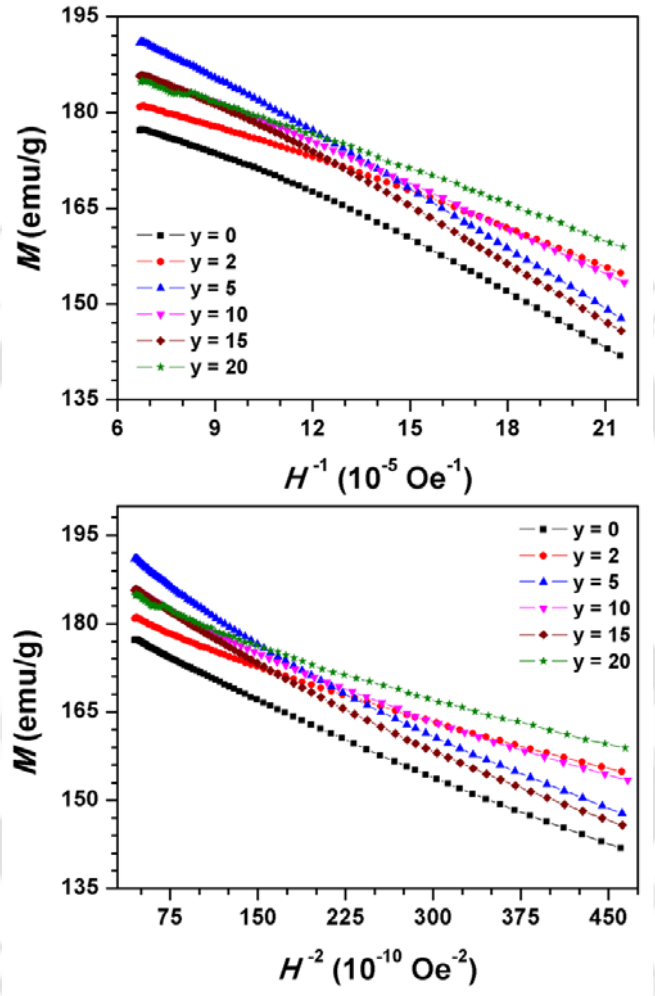

Figure 5.14. The representation of M as a function of H^{-1} and H^{-2} for 40 hours milled $Fe_{85-y}Co_ySi_{15}$ alloy powders.

5.4.2. Evolution of magnetic properties with Co substitution:

To understand the change in the magnetic properties of $Fe_{85-y}Co_ySi_{15}$ alloy powders, room temperature initial magnetization curves, magnetic hysteresis (M-H) loops and high temperature thermomagnetization data (M-T) were obtained using VSM. Figure 5.13 depicts the room temperature initial magnetization curves and M-H loops for $Fe_{85-y}Co_ySi_{15}$ alloy powders milled for 40 hours. The shape of the loops is typical of a soft magnetic material.

However, a careful observation of the loops reveals that the substitution of Co fine tunes the slope of the curves towards lower field as observed in $Fe_{90-y}Co_ySi_{10}$ alloy powders. In order to determine the variation of M_S and K_{eff}, the field dependence of magnetization data were fitted to the power series using eqn.(4.09) after verifying the applicability of power series to analyse the experimental magnetization data as shown in Figure 5.14. The determined values of M_S and K_{eff} and the extracted values of H_C are plotted as a function of Co content in Figure 5.15. M_S increases with increasing Co content up to 10 at.% and then decreases slightly for higher Co substitution. This behaviour is somewhat different from the behaviour observed for $Fe_{90-y}Co_ySi_{10}$ alloy powders (see Figure 5.09(a)) where the values of M_S increase continuously with increasing Co content. This could be correlated to the change in the structural parameters due to the difference in the alloying process as a result of delay in the dissolution of Co into Fe lattice in the presence of more Si content. Nevertheless, the increase in M_S could be attributed to the atomic ordering as discussed earlier. On the other hand, H_C increases at a faster rate initially for low Co substitution and the rate of increase of H_C decreases for high Co content.

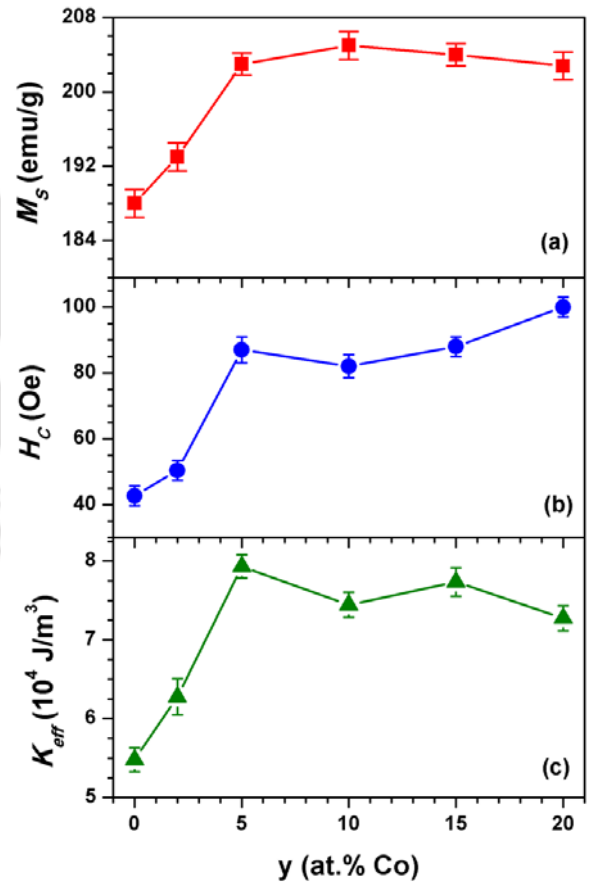

Figure 5.15. Variations of M_S, H_C and K_{eff} of 40 hours milled $Fe_{85-y}Co_ySi_{15}$ alloy powders.

It is well known that H_C is one of the structural sensitive properties of the magnetic materials, which depends strongly on the internal defects such as reduction in grain size, grain boundaries, dislocations and inclusion of additional materials. The increase in H_C can be correlated to the atomic pairing which induces additional magnetic anisotropy and change in the grain boundaries, undissolved solute atoms acts as inclusions and hinder the domain wall motion [KHAJ2011]. To understand the variation of H_C with Co content, the determined values of K_{eff} are also plotted in Figure 5.15(c) for comparison. The variation of K_{eff} shows almost similar behaviour of coercivity up to 15 at.% and then decreases for the samples with 20 at.% Co. This suggests that the effective magnetic anisotropy induced by the internal strain through magnetoelastic coupling and by the atomic pairing by Co substitution plays a major role on the H_C behaviour of the $Fe_{85-y}Co_ySi_{15}$ alloy powders.

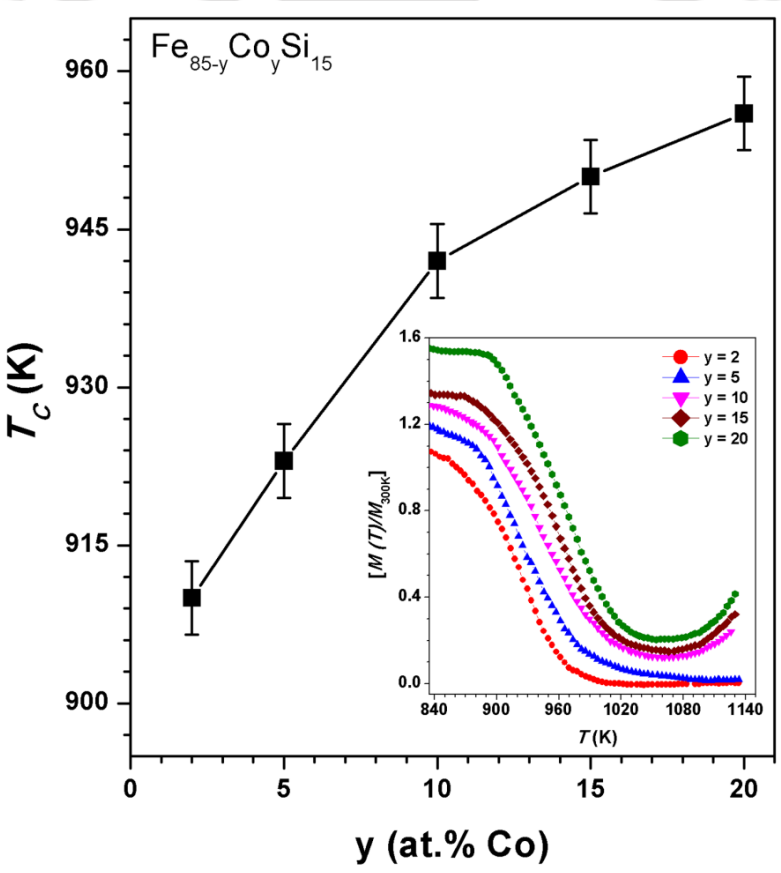

Figure 5.16. Variation of Curie temperature (T_C) of 40 hours milled $Fe_{85-y}Co_ySi_{15}$ alloy powders. Inset: Normalized *M-T* curves as a function of temperature close to magnetic phase transition temperatures.

It has been reported that the substitution of Co in Fe based amorphous and nanocrystalline alloys increases T_C considerably [MISH2010]. To understand the effect of Co on the behaviour of T_C of the as-milled nanocrystalline $Fe_{85-y}Co_ySi_{15}$ alloy powders, high temperature *M-T* measurements were performed at a heating rate of 5 K per minute in the temperature range 300 K to 1123 K under the applied magnetic field of 100 Oe. Figure 5.16 depicts the variation of T_C of as-milled $Fe_{85-y}Co_ySi_{15}$ alloy powders and the normalized thermomagnetization data around the magnetic phase transition temperature (inset). In order to show the transition temperature clearly, *M-T* data for each sample was normalized with respect to their room temperature magnetization value. A close observation of the magnetization data reveals that for $Fe_{85-y}Co_ySi_{15}$ alloy powders with Co content less than 10 at.% exhibit a clear magnetic phase transition from ferromagnetic to paramagnetic state. As a result, the magnetization becomes zero after completing the magnetic phase transition. On further increasing the Co content, we observed an increase in the magnetization above 1050 K and the magnitude of increase in the magnetization increases continuously. This could be attributed to the commencement of crystallization process, which results in growth of the nanocrystalline phase resulting enhanced magnetization. This confirms that the substitution of Co in $Fe_{85-y}Co_ySi_{15}$ alloy powders reduces the crystallization temperature. This is in good agreement with the earlier reports on similar systems [IDZI2005, UMCY2004, MISH2010, MISH2011]. T_C values were determined from the thermal derivative of *M-T* data and plotted as a function of Co content. T_C increases at a rate of nearly 4 K per at.% Co for the Co substitution up to 10 at.%, but the rate of increase in T_C drops down largely to 1.4 K per at.% Co for Co substitution above 10 at.%. The rate of increase in T_C with Co content in the presently investigated alloy is substantially low as compared to the values reported in Co substituted amorphous Fe-based alloys: ~14 K per at.% Co in amorphous $Fe_{82-x}Co_xNb_3Ta_1Mo_1B_{13}$ alloys [UMCY2004] and 12 – 15 K per at.% Co in amorphous $Fe_{89-x-y}Zr_{11}B_xCo_y$ alloys [MISH2009]. This could be mainly due to the sample preparation techniques involving different kinematics on the formation of final alloys. In the presently investigated samples, the formation of nanocrystalline solid solution strongly depends on the milling parameters, solute and the solvents.

5.5. Summary:

The structural and magnetic properties of $Fe_{100-x-y}Co_ySi_x$ (x = 10 and 15, y = 0 – 20) alloy powders with nanocrystalline microstructure prepared by mechanical alloying process in a planetary ball mill were systematically carried out as a function of Co content in this chapter.

The salient features of the ternary alloys obtained from the current investigations are as follows:

- The formation of non-equilibrium α-Fe(Co,Si) solid solution could be obtained for all the $Fe_{100-x-y}Co_ySi_x$ (x = 10 and 15, y = 0 – 20) samples within 40 hours of milling under the milling speed of 600 rpm.
- The lattice constant increases slowly in as-milled $Fe_{100-x-y}Co_ySi_x$ alloy powders with increasing Co content up to 10 at. % due to the substitution of Co in Fe matrix and then decreases with increasing Co above 10 at.%. The amount of decrease in lattice constant strongly depends on the Si content. This was attributed to the delay in the dissolution of Co into Fe lattice by the introduction of more Si.
- The evolution of nanocrystalline microstructure was confirmed through XRD and TEM studies. The average crystallite size was found to be in the range of 7 to 11 nm, but increases initially up to 10 at.% Co substitution and then decreases with further increase in Co content.
- The dislocation density is found to be of the order of $10^{17}m^{-2}$, but decreases slightly with increasing Co substitution up to 10 at.% and then increases for high Co content. The amount of variation strongly depends on the Si content.
- The substitution of Co in $Fe_{100-x-y}Co_ySi_x$ increases both saturation magnetization and coercivity possibly due to atomic ordering which induce additional magnetic anisotropy. However, the amount of increase depends on the extent of Co and Si dissolution in $Fe_{100-x-y}Co_ySi_x$ alloys powders.
- Thermomagnetization studies at high temperatures revealed that Curie temperature increases at a rate of 4 K per at.% Co for the Co substitution up to 10 at.%, but the rate of increase in Curie temperature drops down to 1.4 K per at.% Co for higher Co substitution. Furthermore, the crystallization temperature decreases with increasing Co content resulting an increase in magnetization at high temperature with increasing Co content above 5 at.%.
- Although systematic correlations between structural and magnetic properties have been observed for these Fe-Co-Si alloys, the variation of structural and magnetic parameters has been found to be dependent on the alloy composition.

Chapter 6

Mechanical alloying of quaternary $Fe_{95-x-z}(Al,Cr)_zCo_5Si_x$ alloy powders: Control of Crystallite size

6.1. Introduction:

The effect of Co substitution on the structural and magnetic properties of ternary $Fe_{100-x-y}Co_ySi_x$ alloy powders was discussed in Chapter 5. While the formation of non-equilibrium solid solutions of α-Fe(Co,Si) could be obtained within 40 hours of milling, the substitution of Co helps to improve the saturation magnetization (M_S) and Curie temperature (T_C). However, the coercivity (H_C) also increases significantly with increasing Co content confirming the deterioration of magnetic softness. In general, the nanocrystalline materials produced by mechanical alloying process are magnetically hard [PILA2008] as compared to the nanocrystalline alloys produced by other techniques [ZOLL2012]. This is mainly due to large internal strain, extended imperfections, disordered grain boundaries, substitutional inclusions *etc*. Nevertheless, mechanical alloying process produces nanocrystalline materials of desirable quantity over a wide range of compositions, which are not obtainable by other techniques, with tunable microstructure and physical properties [SURY2001].

In order to release the strain accumulated in the as-milled powders, these powders have to be consolidated at high temperatures to achieve high-density components with improved soft magnetic properties. However, this annealing process unfavorably induces crystallite growth and deteriorates soft magnetic properties. Therefore, a novel methodology or appropriate measure is required to obtain the crystallites of size less than 10 nm. This would help in controlling the subsequent growth of the crystallites during the essential annealing process. It may be noted that the coercivity (H_C) of the nanocrystalline materials decreases drastically with the average crystallite size (D) either as D^6 or as D^3 dependence [HERZ2005, SELL2006] as shown in Figure 1.02. In these regards, there have been continuous attempts either by controlling milling parameters or by substituting suitable alloying elements in shaping the magnetic properties of Fe-Si based alloys [ZUOB2004, BAHR2006, KALI20084, BOUK2012, YOUS2012]. However, a systematic investigation on the evolution of nanocrystalline microstructure with reduced average crystallites and the magnetic properties of Fe-Co-Si based alloys are not explored yet. Hence, in this chapter, we report the influence of substituting elements like Al and Cr on the control of nanocrystalline microstructure and resulting magnetic properties of $Fe_{95-x-z}(Al,Cr)_zCo_5Si_x$ alloy powders prepared by mechanical alloying process.

6.2. Experimental details:

Samples corresponding to the composition of $Fe_{95-x-z}(Al,Cr)_zCo_5Si_x$ (x = 10 and 15; z = 0, 2, 5 and 10) were mechanically alloyed using high energy planetary ball mill (Insmart, India) from

high purity (>99.9%) elemental powders of Fe, Si, Co, Al and Cr under high purity argon atmosphere. The powder mixtures were weighed and loaded into a hardened steel bowl along with hardened steel milling balls of 8 mm diameter each. For the mechanical alloying process, the ball to powder weight ratio was set at 10:1 and the milling was performed at 600 rotations per minute (rpm). The optimum milling time for forming the solid solution was fixed at 40 hours. The milling process was paused for 10 minutes after every 15 minutes of milling to minimize excessive temperature rise. Structural changes were studied by X-ray diffraction (XRD) in a high-power X-Ray diffractometer (Rigaku TTRAX III 18 kW) using Cu-K_α radiation. XRD data were collected at a slow scan rate of 0.005°/s and the structural parameters were determined using Modified Williamson Hall Plot (MWHP) method [UNGA19991, UNGA19992]. The instrumental broadening was corrected using eqn.(4.01) as described in Chapter 4 for the calculations of structural parameters. The morphology and evolution of nanocrystalline microstructure was investigated by scanning electron microscope (SEM, Leo 1430VP) and transmission electron microscope (TEM, JEOL 2100). Overall composition was verified using energy dispersive spectrometer (EDS, Oxford) attached to scanning electron microscope (SEM, Leo 1430VP). Magnetic properties were investigated by measuring room temperature initial magnetization curves and magnetic hysteresis (*M-H*) loops by using vibrating sample magnetometer (VSM, LakeShore Model 7410, USA).

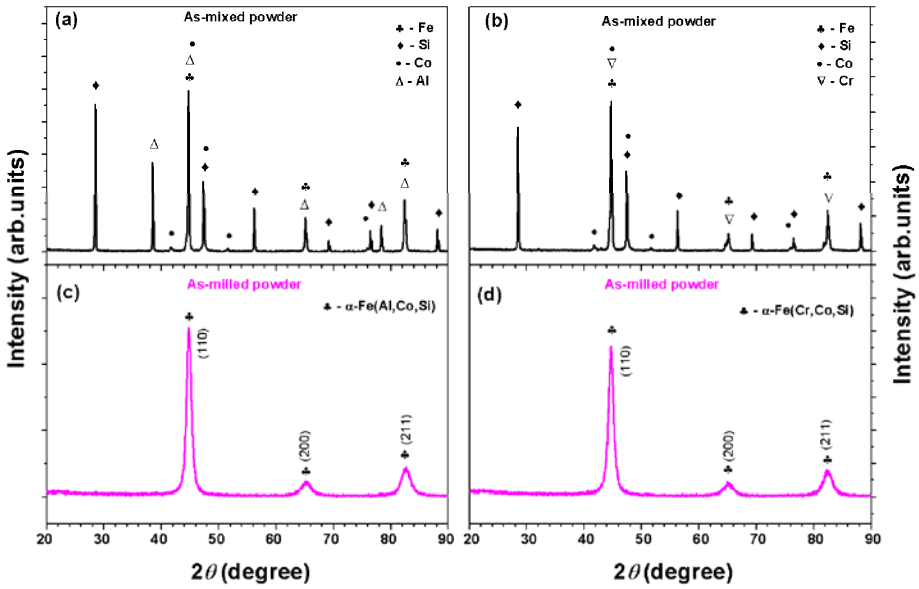

Figure 6.01. Typical room temperature XRD patterns of (a,b) as-mixed and (c,d) 40 hours milled $Fe_{70}Al_{10}Co_5Si_{15}$ and $Fe_{70}Cr_{10}Co_5Si_{15}$ powders.

6.3. Properties of nanocrystalline quaternary $Fe_{80-z}(Al,Cr)_zCo_5Si_{15}$ alloy powders:

6.3.1. Structural evolution with Al and Cr substitution:

Figure 6.01 shows typical room temperature XRD patterns of as-mixed and 40 hours milled $Fe_{80}(Al,Cr)_{10}Co_5Si_{15}$ alloy powders. It is observed that as-mixed powders exhibit sharp characteristic Bragg reflections corresponding to all four constituting elements, i.e., Al (face centered cubic), Co (face centered cubic and hexagonal close-packed structures), Si (diamond cubic) and Fe (body centered cubic) for $Fe_{70}Al_{10}Co_5Si_{15}$ powders and Cr (body centered cubic), Co (face centered cubic and hexagonal close-packed structures), Si (diamond cubic) and Fe (body centered cubic) for $Fe_{70}Cr_{10}Co_5Si_{15}$ powders. However, the Bragg reflections corresponding to Si, Co, Al and Cr disappear after milling for 40 hours. This is mainly due to the diffusion of Si, Co, Al and Cr in Fe matrix resulting the formation of non-equilibrium body centered cubic (*bcc*) solid solutions of α-Fe(Al,Co,Si) and α-Fe(Cr,Co,Si). It is also clear that no additional peaks corresponding to any other phases or compounds were observed within the resolution limit of high power XRD.

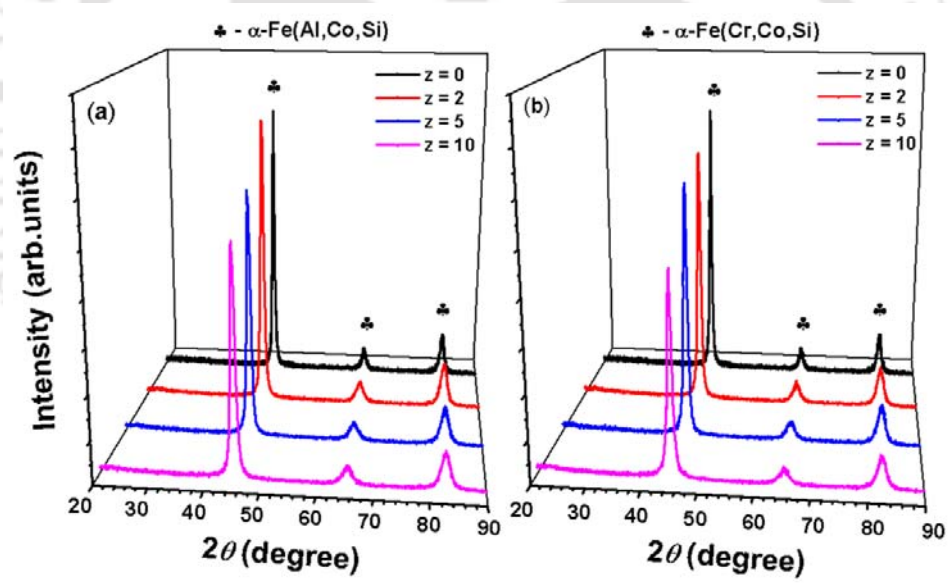

Figure 6.02. Room temperature XRD patterns of (a) $Fe_{80-z}Al_zCo_5Si_{15}$ and (b) $Fe_{80-z}Cr_zCo_5Si_{15}$ alloy powders milled for 40 hours.

To understand the effect of substituting elements on the structural properties systematically, XRD patterns were collected for all the samples milled for 40 hours and depicted in Figure 6.02. A close observation of the XRD patterns reveals that with increasing Al and Cr contents, all the peaks exhibit fairly large peak broadening along with minor shift in peak positions to lower angles. While the first one confirms the formation of nanocrystalline microstructure with highly refined

and internally strained grains with increasing substituting elements, the later one could be attributed to the occurrence of atomic disorder due the dissolution of substituting elements in Fe matrix leading to a change in lattice constant. To study the solid solubility level, the lattice constant was calculated from the peak positions for all the compositions. It is observed that lattice constant increases from 0.28658±0.00005 nm to 0.28698±0.00007 nm and 0.28658±0.00005 nm to 0.28689±0.00004 nm with increasing Al and Cr contents in milled $Fe_{80-z}(Al,Cr)_zCo_5Si_{15}$ alloy powders from 0 to 10 at.%, respectively. These results suggest a maximum lattice change of 0.00004 nm per at.% Al and 0.000031 nm per at.% Cr occurred by the substitution of Al and Cr, respectively. Although the observed variation is in close agreement with the earlier reports on similar systems [SHIG1974, PETR2002, BOUK2012], the increase of lattice constant in the presently investigated alloys is slightly lower than those reported for binary Fe-Al and Fe-Cr alloys. This could be possibly due to the change in the dissolution process in the multicomponent materials as compared to the binary alloys.

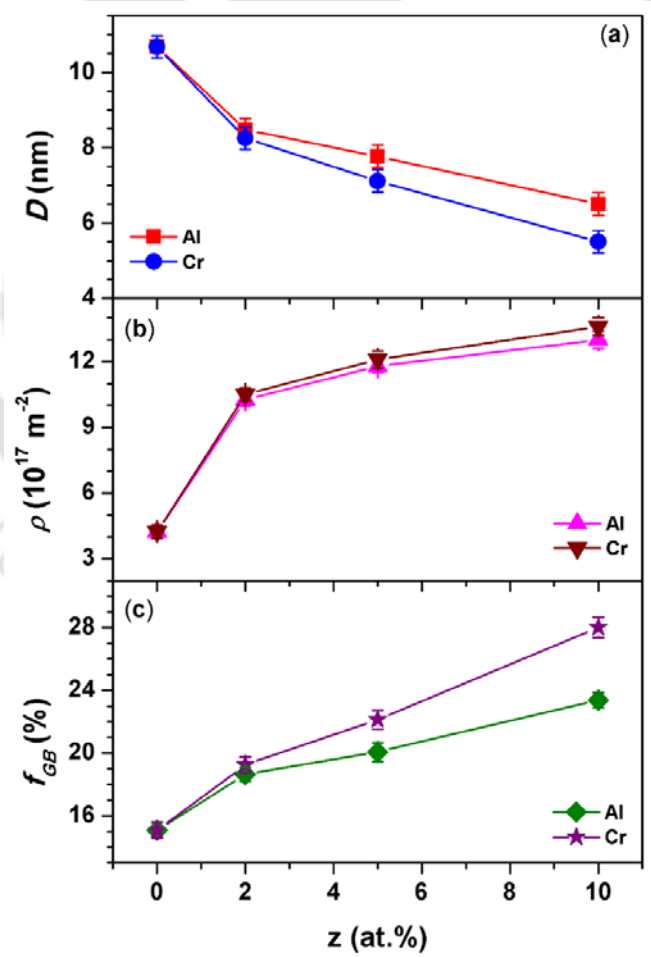

Figure 6.03. Variations of D, ρ and f_{GB} of 40 hours milled $Fe_{80-z}(Al,Cr)_zCo_5Si_{15}$ alloy powders.

In order to separate the contributions of average crystallite size (D) and strain through density of dislocations (ρ) to peak broadening, XRD patterns were analyzed carefully by MWHP method [UNGA19991, UNGA19992] using eqn.(4.04) as demonstrated in Chapter 4. Figure 6.03 depicts the variations of D, ρ and fraction of grain boundaries (f_{GB}) calculated using eqn.(4.07) as a function of Al and Cr contents for as-milled $Fe_{80-z}(Al,Cr)_zCo_5Si_{15}$ alloy powders. It is revealed that Al and Cr substitutions interestingly reduce the values of D from about 11 nm to about 6 nm and increase the ρ values largely from 4.2×10^{17} m^{-2} to 13.6×10^{17} m^{-2}. This indicates that the Al and Cr substitution helps in improving the size refinement and the existence of nearly 0.42 to 1.36 dislocations for every one nm^2 area. This could be attributed to the enhancement in milling intensity with increasing substituting elements [KALI20081, KALI20082, BOUK2012]. Saturated value of dislocation density is achieved more rapidly in these alloys indicating that the solute concentration can strongly affect the mechanical properties. The formation of solid solution with fine crystallite size suggests that the solid solution would be harder and stronger than pure metal [AGUI2010]. The observed results confirm that the behavior of the dislocation density is inversely related to the crystallite size (see eqn.(4.06)), as the large dislocation density occurring in the smallest crystallite size. Furthermore, grain boundary which has a strong effect on the structural properties of nanocrystalline materials increases with decreasing the average crystallite size. It is well understood that the basic underlying mechanism of grain refinement involves an increase in the dislocation density by heavy deformation process. These dislocations form an order arrangement giving rise to dislocation walls, which transform in to grain boundaries, when the formation continues with milling. The grain boundaries affect the movement of dislocations and strain hardening significantly.

As the values of D decrease significantly with the substituting elements, we have tried to estimate the development of grain boundaries in these quaternary alloys using eqn.(4.07). While the values of f_{GB} increase from 15 % to 23 % for the Al substituted powders, the Cr substitution enriches the f_{GB} from 15 % to 28 %. This shows that Cr substitution enhances the formation of grain boundaries as compared to that of Al. Bahrami et al. [BAHR2013] reported the values of f_{GB} as 13%, 18 % and 28 % for x = 0, 10 and 20, respectively in $Fe_{80-x}Ni_{20}Si_x$ system. In this case, the fraction of grain boundaries increases drastically from 13 % to 28 % with increasing the Si content up to 20 at.% and attributed to the enhanced process of microstructural refinement. Similarly, Yousefi et al. [YOUS2014] reported almost 5 % increase in the grain boundaries with increasing 10 at.% Si in mechanically alloyed nanocrystalline $(Fe_{65}Co_{35})_{100-x}Si_x$ powders.

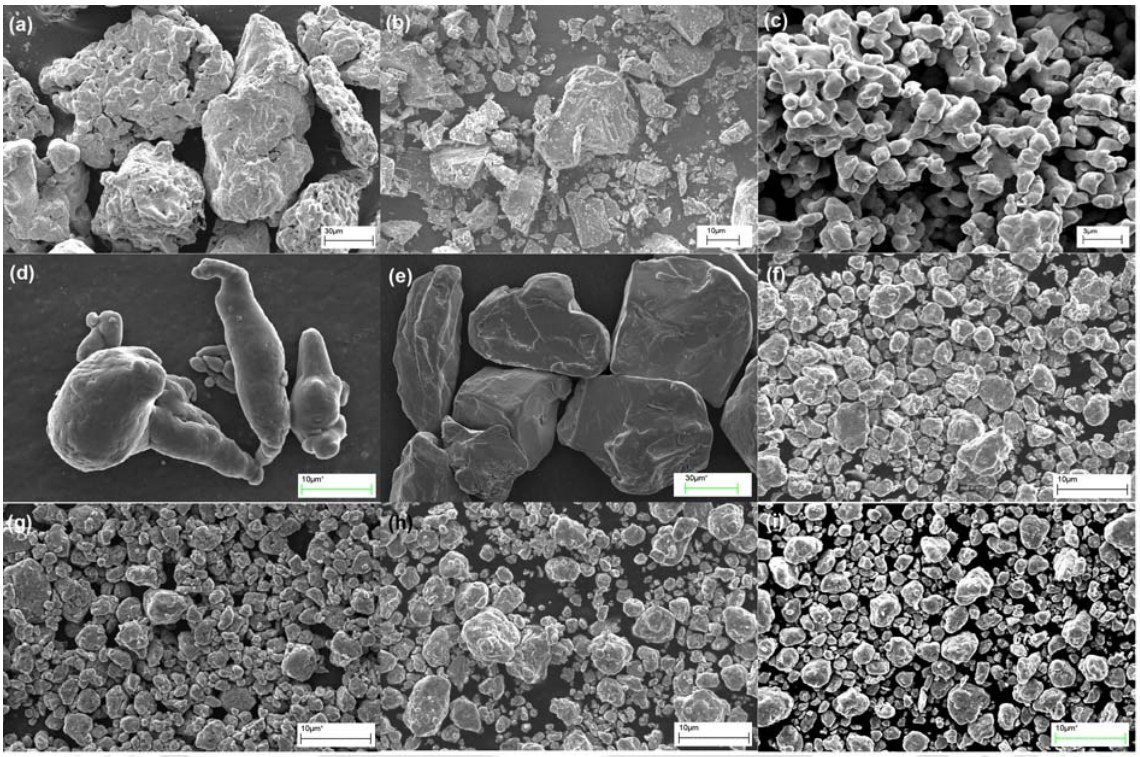

Figure 6.04. SEM micrographs of pure (a) Fe, (b) Si, (c) Co, (d) Al and (e) Cr, and 40 hours milled (f) $Fe_{78}Al_2Co_5Si_{15}$, (g) $Fe_{75}Al_5Co_5Si_{15}$, (h) $Fe_{78}Cr_2Co_5Si_{15}$ and (i) $Fe_{75}Cr_5Co_5Si_{15}$ alloy powders.

To understand the modification of surface morphology of the powders carefully, we have analyzed the morphology of the powders using SEM technique. Figure 6.04 shows the surface morphology of the pure elements (Fe, Si, Co, Al and Cr) and the as-milled powders of $Fe_{78}Al_2Co_5Si_{15}$, $Fe_{75}Al_5Co_5Si_{15}$, $Fe_{78}Cr_2Co_5Si_{15}$ and $Fe_{75}Cr_5Co_5Si_{15}$. SEM micrographs show quasi similarity of particle morphology, i.e., the presence of particles with different sizes. Aggregation of crystallites is a natural consequence of the mechanical alloying process due to repeated cold welding and fracturing. The shape of the aggregated particles is observed to be nearly spherical in nature for both Al and Cr substitution. However, the size distribution of the agglomerated particles is observed to be narrow in Fe-Al-Co-Si powders as compared to Fe-Cr-Co-Si powders. This could be attributed to the different properties of the substituting elements, i.e., Al is soft and ductile and the Cr is hard and brittle resulting different alloying process [CHRI2013]. Over all composition analysis was performed on as-milled powders using EDS attached to SEM unit. It is found that the composition of the as-milled powders to be $Fe_{80.8}Co_{4.6}Si_{14.6}$, $Fe_{79}Al_{1.8}Co_{4.8}Si_{14.4}$ ($Fe_{78.8}Cr_{1.9}Co_{4.6}Si_{14.7}$), $Fe_{75.9}Al_{4.7}Co_{4.7}Si_{14.7}$ ($Fe_{76}Cr_{4.8}Co_{4.7}Si_{14.5}$) and $Fe_{71.6}Al_{9.6}Co_{4.6}Si_{14.2}$ ($Fe_{71.2}Cr_{9.4}Co_{4.8}Si_{14.6}$) for the milled samples

with Al (Cr) content of 0, 2, 5 and 10 at.%, respectively. These results evidently support the presence of Si, Co and Al or Cr in the form of solid solution in α-Fe.

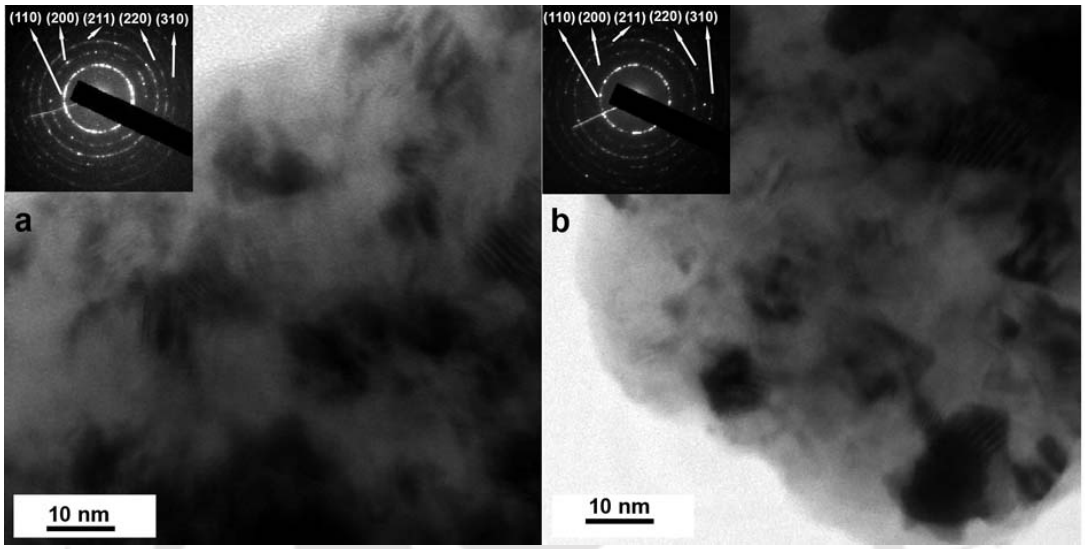

Figure 6.05. BF-TEM micrographs and SAED patterns of 40 hours milled (a) $Fe_{75}Al_5Co_5Si_{15}$ and (b) $Fe_{75}Cr_5Co_5Si_{15}$ alloy powders.

In order to confirm the evolution of nanocrystalline microstructure, the as-milled powders were characterized using TEM technique. Figure 6.05 illustrates bright-field TEM (BF-TEM) micrographs and selected area electron diffraction (SAED) patterns for 40 hours milled $Fe_{75}Al_5Co_5Si_{15}$ and $Fe_{75}Cr_5Co_5Si_{15}$ powders. BF-TEM micrographs confirm the existence of fine-grain structure with the average grain size of about 7 nm having non-uniform contrast inside each grain and along the grain boundaries. This could be attributed to the large strain in the as-milled powders. On the other hand, the rings present in SAED patterns reveal a nanocrystalline microstructure and match with the Bragg reflections in the XRD patterns. The values of average crystallite size and lattice constant calculated from TEM analysis show nearby agreement with those obtained from XRD data as shown in Figure 6.03. These results show that the particles with sizes ranging from few hundred nanometers to few micrometers observed in SEM micrographs are agglomerations of fine nanosized crystallites oriented randomly with respect to each other. The nature of agglomeration, however, strongly depends on the alloy compositions.

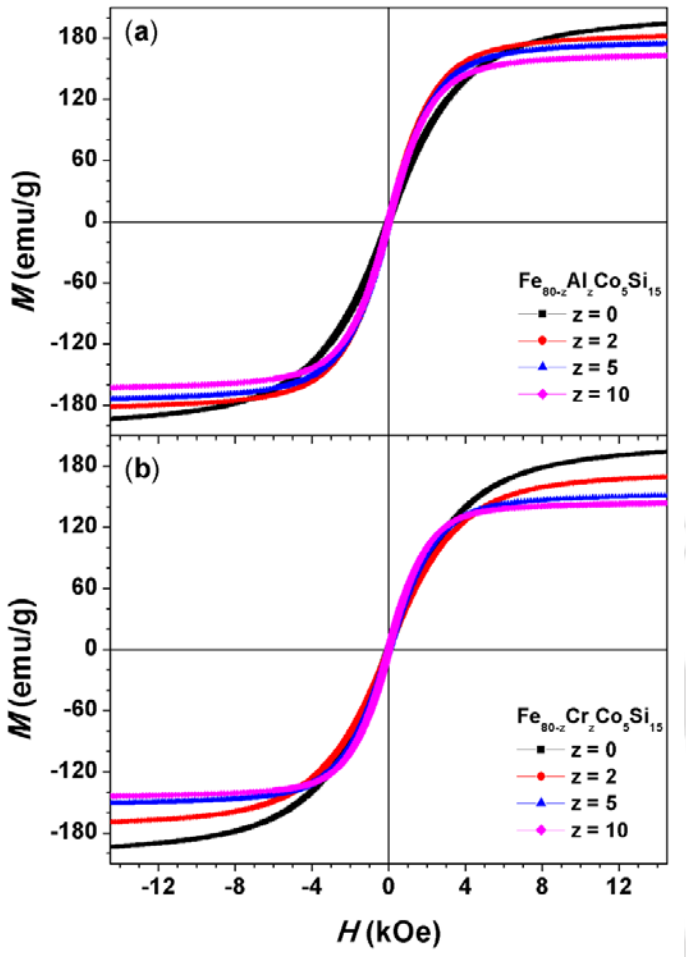

Figure 6.06. Room temperature $M - H$ loops of 40 hours milled $Fe_{80-z}(Al,Cr)_zCo_5Si_{15}$ alloy powders.

6.3.2. Evolution of magnetic properties with Al and Cr substitution:

To study the effect of nanocrystalline microstructure with reduced average crystallites and substituting elements on the magnetic properties, room temperature initial magnetization curves and *M-H* loops were obtained for all the as-milled powders. Figure 6.06 displays the *M-H* loops measured at room temperature for milled $Fe_{80-z}(Al,Cr)_zCo_5Si_{15}$ powders. While the shape of the loops is typical of a soft magnetic material, a close observation reveals that the substitution of Al and Cr reduces the applied field required for saturation behavior and decreases the magnetization considerably. It is known that magnetic domains exist in the nanocrystalline Fe-Si based alloys [ZHOU1996] and the movement of these domain walls is hindered by density of dislocations, grain boundaries as well as the substituting elements resulting in high coercivity (H_C) in mechanically alloyed powders. Perez et al. [PERE1996]

reported that despite XRD patterns showed the formation of non-equilibrium solid solution in Fe-Si-B alloy within 0.5 hours of milling, the electron probe microanalysis and precise lattice parameter measurements revealed that the complete dissolution of substituting elements in Fe matrix varies with the milling conditions and substituting elements. Similarly, Zhou et al. [ZHOU1999] proposed from the Mössbauer analysis of $Fe_{100-x}Si_x$ alloys that the Si concentration located in the grain boundaries might be larger than that located in the crystallites. Following these arguments and comparing the variations of lattice constants for the presently investigated system, we deduce that the existence of the substituting elements in the grain boundaries is possible [PERE1996, ZHOU1999] due to the enhancement in the relative fraction of grain boundaries with increasing Al and Cr contents. This would perhaps help in modifying the structurally disordered environment in grain boundaries and resulting a reduced obstruction to the domain wall movement. As a result, $Fe_{80-z}(Al,Cr)_zCo_5Si_{15}$ alloy powders attain saturation easily.

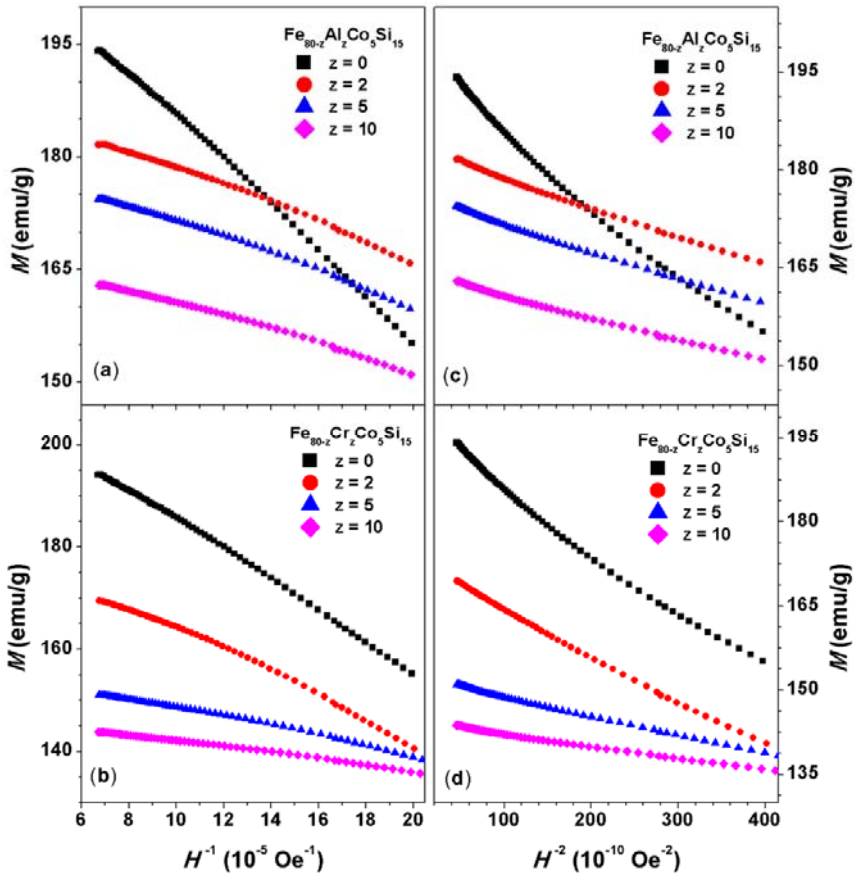

Figure 6.07. The representation of M as a function of H^{-1} and H^{-2} for $Fe_{80-z}(Al,Cr)_zCo_5Si_{15}$ alloy powders milled for 40 hours.

Furthermore, the magnetoelastic coupling energy due to internal strain result different nature of spin states which develops considerable deviations of magnetization from saturation. For the field dependence of deviation in magnetization from saturation, the experimental magnetization data were fitted to power series [KRON2003] using eqn.(4.09) and determined the values of effective magnetic anisotropy (K_{eff}). To verify the applicability of power series analysis to the experimental magnetization data, the plots of magnetization against H^{-1} and H^{-2} for the presently investigated samples are demonstrated in Figure 6.07. Considering the validity of data, the magnetization data was fitted to eqn.(4.09) to determine the values of K_{eff}.

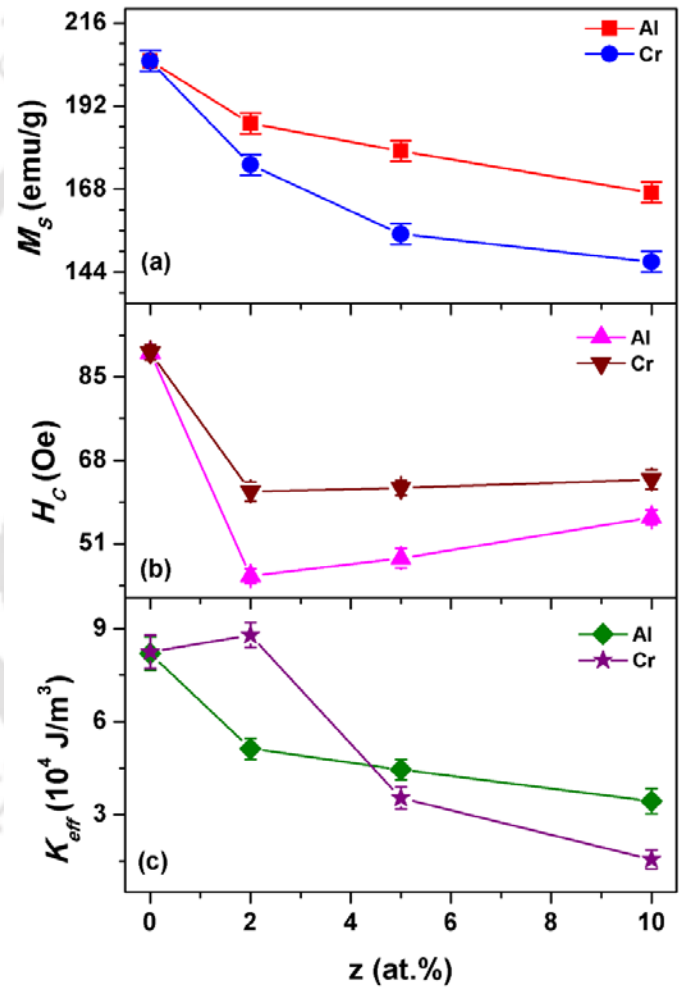

Figure 6.08. Variations of M_S, H_C and K_{eff} of 40 hours milled $Fe_{80-z}(Al,Cr)_zCo_5Si_{15}$ alloy powders.

Figure 6.08 shows the extracted values of coercivity (H_C) from the *M-H* loops and the determined values of M_S and K_{eff} as a function of Al and Cr contents. While M_S decreases slowly from 205 emu/g to 167 emu/g at a rate of 2.5 emu/g per at.% Al with $z > 2$ for $Fe_{80-z}Al_zCo_5Si_{15}$

powders, the substitution of Cr in $Fe_{80-z}Cr_zCo_5Si_{15}$ powder exhibits a non-linear variation of M_S at a faster rate. The general decrease of M_S in $Fe_{80-z}Al_zCo_5Si_{15}$ can be explained from partial filling of *d* bands of Fe by the substituting elements and the presence of considerable amount of Fe atoms in grain boundaries resulting a spatial variation of inter-atomic distance between Fe neighbors. On the other hand, the larger decrease of M_S in $Fe_{80-z}Cr_zCo_5Si_{15}$ might be due to the formation of various types of exchange interactions such as ferromagnetic Fe-Fe and antiferromagnetic Fe-Cr and Cr-Cr interactions [LARE2009]. H_C decreases largely from about 90 Oe to 44 Oe and 60 Oe for small amount of Al and Cr substitution (2 at.%) respectively, and then increases faintly for further increase in Al and Cr contents. In order to understand the coercivity behavior with substituting elements, the values of K_{eff} are also plotted in Figure 6.08(c) for comparison. It is observed that K_{eff} decreases progressively with increasing Al content in $Fe_{80-z}Al_zCo_5Si_{15}$ powders, while the substitution of Cr in $Fe_{80-z}Cr_zCo_5Si_{15}$ increases the K_{eff} slightly for initial Cr substitution and then decreases largely for high Cr content. The obtained values of K_{eff} are significantly larger as compared to the magnetic anisotropy values of disordered polycrystalline Fe-Si alloys [BECK1991]. This reveals that both the internal stress induced by mechanical alloying process and the substituting elements affect the values of K_{eff} in the presently investigated nanocrystalline alloys. However, the decrease of K_{eff} with increasing Al and Cr contents reveals that the magnetoelastic coupling energy, resulting in different nature of spin states, decreases with increasing substituting elements. Furthermore, there may exist, as reported earlier [SELL2006], a correlation between H_C and K_{eff}, but no close correlation could be obtained from Figure 6.08. This might be due to different contributions from the variations of D, ρ and K_{eff} on the variations of H_C with substituting elements. For example, it is well known that H_C in the mechanically alloyed powders increases with increasing the values of ρ, while the reduction in D exhibits a large decrease in H_C [KALI20083, BENS2010]. In the presently investigated samples, the values of D decrease and ρ increase with increasing substituting elements and the variations of K_{eff} show different behaviors as compared to H_C with substituting elements. Therefore, the observed results suggest that both D and ρ play a crucial role on controlling the magnetic properties. Nevertheless, the improved soft magnetic properties were obtained in $Fe_{78}(Al,Cr)_2Co_5Si_{15}$ powders with an average crystallite size of 8 nm. Furthermore, the results confirm the successful tailoring of soft magnetic properties of nanocrystalline $Fe_{80-z}(Al,Cr)_zCo_5Si_{15}$ powders having comparatively low H_C and moderate M_S in the as-milled state itself without any heat treatment.

6.4. Properties of nanocrystalline quaternary $Fe_{85-z}(Al,Cr)_zCo_5Si_{10}$ alloy powders:

As reported in Chapter 5 (see section 5.3), the addition of Co in low Si content $Fe_{90-y}Co_ySi_{10}$ alloy powders increased the coercivity and magnetization progressively. This behavior was observed to be different from the one observed for $Fe_{85-y}Co_ySi_{15}$ alloys and the obtained results were discussed on the basis of compositional dependent dissolution process in $Fe_{100-x-y}Co_ySi_x$ alloy powders. As the dissolution mechanism strongly depends on the composition and to understand the alloying mechanism of Al and Cr in the low Si content $Fe_{85-z}(Al,Cr)_zCo_5Si_{10}$ alloy powders, we are reporting in this section the structural and magnetic properties of quaternary $Fe_{85-z}(Al,Cr)_zCo_5Si_{10}$ alloy powders with low Si content milled for 40 hours.

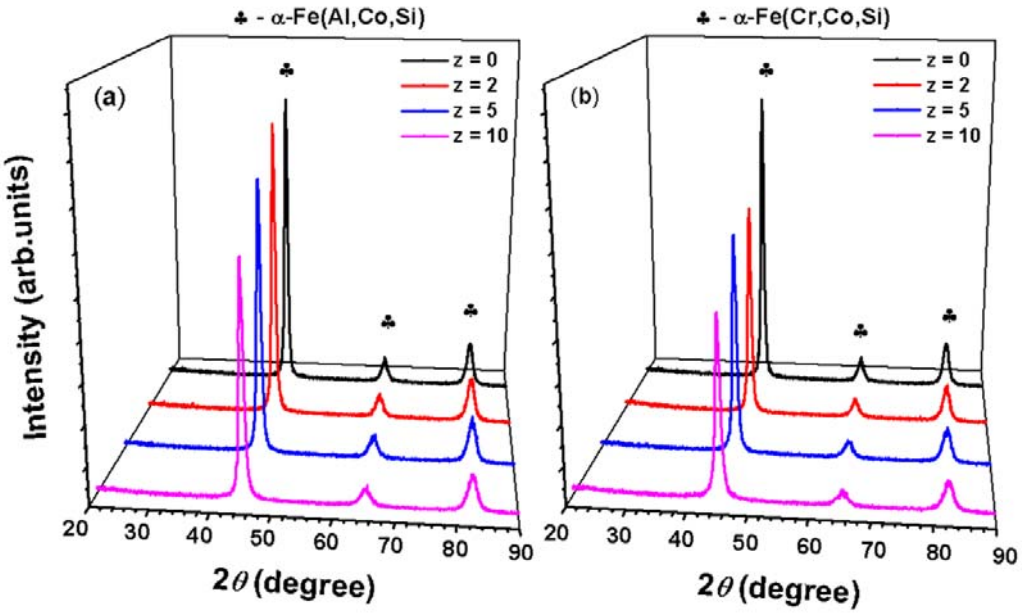

Figure 6.09. Room temperature XRD patterns of 40 hours milled $Fe_{85-z}(Al,Cr)_zCo_5Si_{10}$ alloy powders.

6.4.1. Structural evolution with Al and Cr substitution:

Room temperature XRD patterns of as-mixed and 40 hours milled $Fe_{85-z}(Al,Cr)_zCo_5Si_{10}$ alloy powders are depicted in Figure 6.09. Clearly, the sharp characteristic Bragg reflections corresponding to all substituting elements, i.e., Co, Al and Si for $Fe_{85-z}Al_zCo_5Si_{10}$ and Co, Cr and Si for $Fe_{85-z}Cr_zCo_5Si_{10}$ in as-mixed powders disappear after milling for 40 hours and confirm the formation of non-equilibrium *bcc* solid solutions of α-Fe(Al,Co,Si) and α-Fe(Cr,Co,Si) due to the diffusion of Si, Co, Al and Cr in Fe matrix. In addition, all the peaks exhibit fairly a large peak broadening confirming the formation of nanocrystalline

microstructure with highly refined and internally strained grains, and exhibit small peak shift to lower angles because of atomic disorder due the dissolution of substituting elements in Fe matrix leading to a change in lattice constant. The lattice constant calculated from the peak positions for all the compositions increases from 0.286594±0.00005 nm to 0.28703±0.00007 nm and 0.286594±0.00005 nm to 0.28696±0.00004 nm with increasing Al and Cr contents in milled $Fe_{85-z}(Al,Cr)_zCo_5Si_{10}$ alloy powders from 0 to 10 at.%, respectively. These results confirm the maximum lattice change of 0.0000436 nm per at.% Al and 0.0000366 nm per at.% Cr occurring by the substitution of Al and Cr, respectively. The relative variation of lattice constant is significantly higher in these alloys as compared to $Fe_{80-z}(Al,Cr)_zCo_5Si_{15}$ alloy powders, but in nearby agreement with the literature results [SHIG1974, PETR2002, BOUK2012].

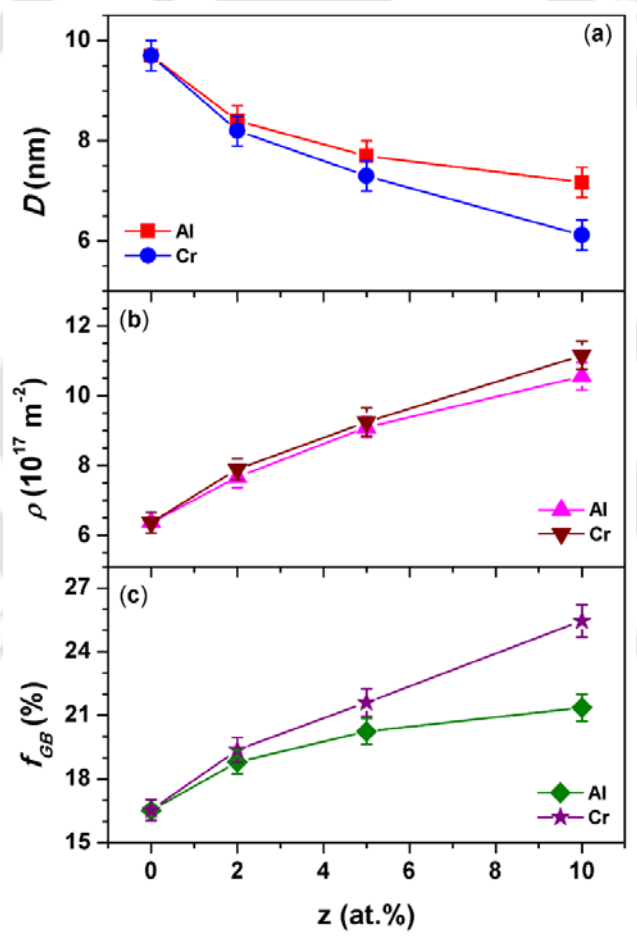

Figure 6.10. Variations of D, ρ and f_{GB} of 40 hours milled $Fe_{85-z}(Al,Cr)_zCo_5Si_{10}$ alloy powders.

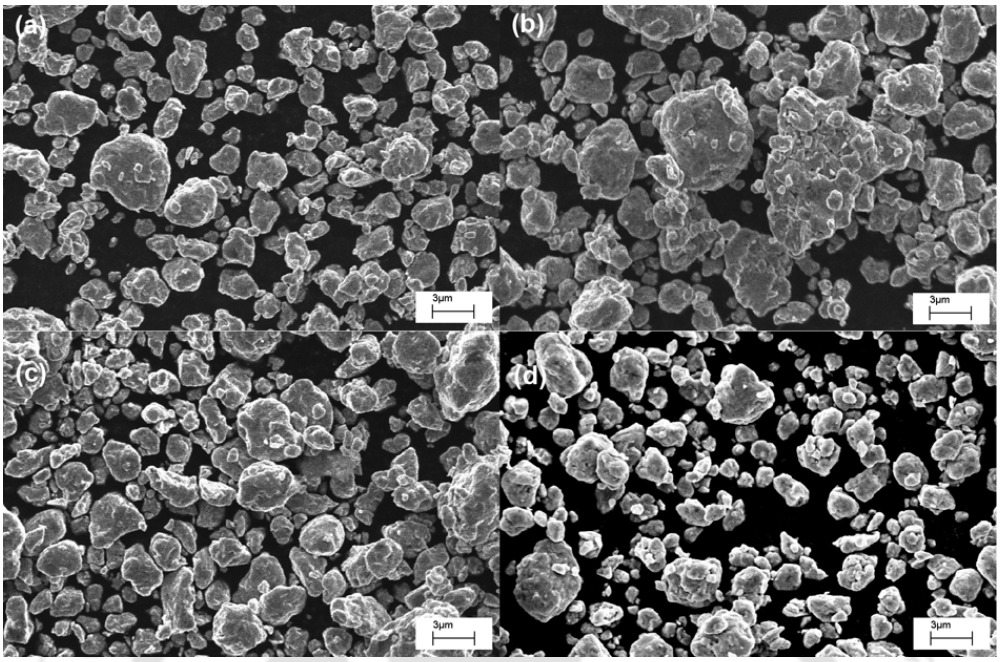

Figure 6.11. SEM micrographs of 40 hours milled (a) $Fe_{83}Al_2Co_5Si_{10}$, (b) $Fe_{83}Cr_2Co_5Si_{10}$, (c) $Fe_{80}Al_5Co_5Si_{10}$ and (d) $Fe_{80}Cr_5Co_5Si_{10}$ alloy powders.

To separate the contributions of D and ρ, XRD patterns were analyzed carefully using MWHP method [UNGA19991, UNGA19992]. The variations of D and ρ as a function of Al and Cr contents are shown in Figure 6.10. While the values of D reduce from 11 nm to about 7 and 6 nm with increasing Al and Cr substitution, the values of ρ increase from 6.3×10^{17} m^{-2} to 10.8×10^{17} m^{-2} indicating the existence of almost 0.63 to 1.08 dislocations for every one nm^2 area. Although the values of D and ρ vary in smaller range as compared to $Fe_{80-z}(Al,Cr)_zCo_5Si_{15}$ alloy powders, a considerable enhancement in milling intensity could be realized with increasing substituting elements [KALI20082, BOUK2012]. In order to understand the development of f_{GB} in these milled powders, the values of f_{GB} were determined by incorporating the structural parameters values in eqns.(4.07). The values of f_{GB} increases from 16.5 % to 21.4 % for the Al substituted powders, while the substitution of Cr enhances the values of f_{GB} from 16.5 % to 25.5 %. The enhancement in the grain boundary is smaller in $Fe_{85-z}(Al,Cr)_zCo_5Si_{10}$ alloy powders as compared to that of $Fe_{80-z}(Al,Cr)_zCo_5Si_{15}$ alloy powders. This could be understood as follows: It is clear from Figures 6.03 and 6.10 that the dislocation density achieves saturation more rapidly in higher Si content alloys. In addition, the higher amount of Si leads to the higher dislocation values. Bahrami et al. [BAHR2013] reported that the f_{GB} values increase from 13% to 28 % with increasing Si from 0 to 20 at.% in $Fe_{80-x}Ni_{20}Si_x$ system.

This suggests that higher Si content enhances the grain boundary formation due to enhanced process of microstructural refinement. This is in good agreement with the present investigation. SEM was used to characterize the surface morphology of the as-milled powders and the typical SEM micrographs for $Fe_{83}Al_2Co_5Si_{10}$, $Fe_{83}Cr_2Co_5Si_{10}$, $Fe_{80}Al_5Co_5Si_{10}$ and $Fe_{80}Cr_5Co_5Si_{10}$ alloy powders are shown in Figure 6.11. SEM micrographs show the quasi similarity of particle morphology and the shape of the aggregated particles is observed to be nearly spherical in nature with wide distribution of particle size for both Al and Cr substitution. Over all composition of the milled powders was determined using EDS. It is found that the composition of the as-milled powders to be $Fe_{85.8}Co_{4.6}Si_{9.6}$, $Fe_{83.6}Al_{1.9}Co_{4.8}Si_{9.7}$ ($Fe_{83.6}Cr_{1.9}Co_{4.7}Si_{9.8}$), $Fe_{81.5}Al_{4.6}Co_{4.5}Si_{9.4}$ ($Fe_{81.1}Cr_{4.4}Co_{4.8}Si_{9.7}$) and $Fe_{76.2}Al_{9.8}Co_{4.5}Si_{9.5}$ ($Fe_{75.8}Cr_{9.6}Co_{4.8}Si_{9.8}$) for the milled samples with Al (Cr) content of 0, 2, 5 and 10 at.%, respectively. These results evidently confirm the presence of Si, Co and Al or Cr in the form of solid solution in α-Fe.

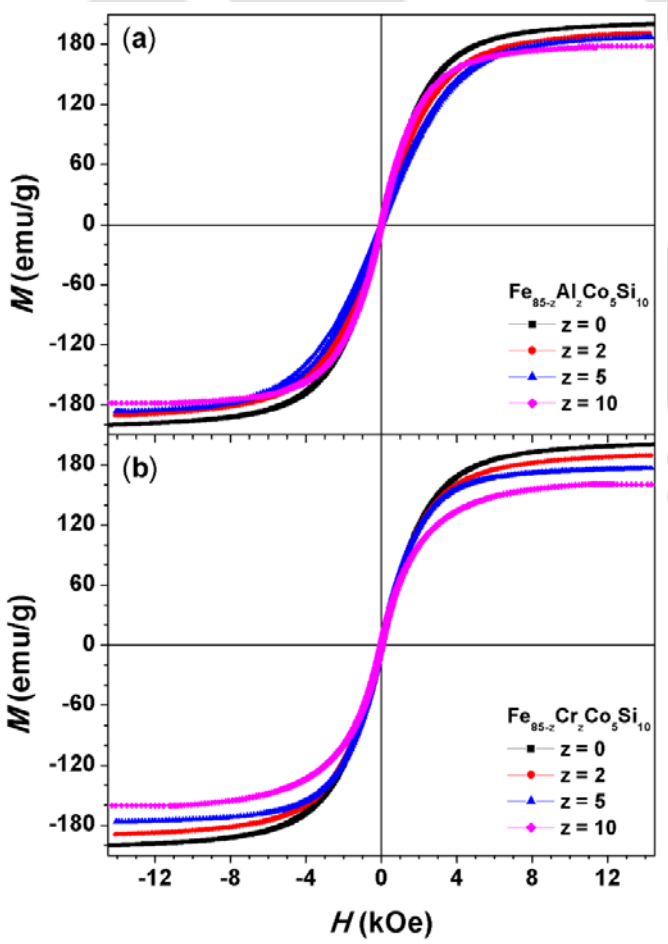

Figure 6.12. Room temperature *M* – *H* loops of 40 hours milled $Fe_{85-z}(Al,Cr)_zCo_5Si_{10}$ alloy powders.

6.4.2. Evolution of magnetic properties with Al and Cr substitution:

To understand the effect of substituting elements on the magnetic properties, room temperature initial magnetization curves and *M-H* loops were obtained for all the as-milled powders. Figure 6.12 displays the *M-H* loops measured at room temperature for as-milled powders. The shape of the loops is typical of a soft magnetic material. However, the substitution of Al and Cr reduces the magnetization significantly to lower values. In order to examine the effect of substituting elements on the magnetic parameters, H_C values are extracted from Figure 6.12 and the values of M_S and K_{eff} were determined from eqn.(4.09) and eqn.(4.11), respectively, by fitting the initial isothermal magnetization data using power series. The applicability of power series analysis to the isothermal magnetization data was verified by plotting the magnetization against H^{-1} and H^{-2} as shown in Figure 6.13.

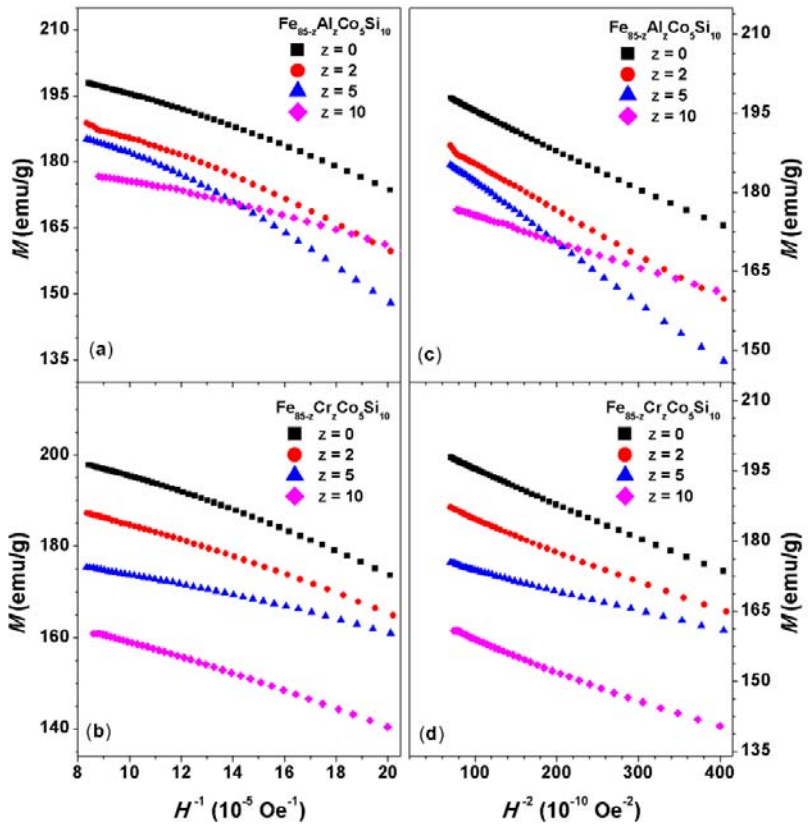

Figure 6.13. The representation of M as a function of H^{-1} and H^{-2} for $Fe_{85-z}(Al,Cr)_zCo_5Si_{10}$ alloy powders milled for 40 hours.

Figure 6.14 shows the values of H_C, M_S and K_{eff} as a function of Al and Cr contents. It is observed that M_S decreases almost linearly with increasing Al and Cr substitution. M_S decreases

from 206 emu/g to 185 emu/g for $Fe_{85-z}Al_zCo_5Si_{10}$ powders at a rate of 2.1 emu/g per at.% Al, while the substitution of Cr in $Fe_{85-z}Cr_zCo_5Si_{10}$ powders exhibits a faster rate of decrease in M_S (3.5 emu/g) from 206 emu/g to 172 emu/g. The relative decrease of M_S is significantly low as compared to $Fe_{80-z}Al_zCo_5Si_{15}$ alloy powders. As discussed earlier, the general decrease of M_S in $Fe_{85-z}Al_zCo_5Si_{10}$ can be explained from partial filling of *d* bands of Fe by the substituting elements and the presence of considerable amount of Fe atoms in grain boundaries resulting a spatial variation of inter-atomic distance between Fe neighbors. However, the larger decrease of M_S in $Fe_{85-z}Cr_zCo_5Si_{10}$ can be correlated to the development of various types of exchange interactions such as ferromagnetic Fe-Fe and antiferromagnetic Fe-Cr and Cr-Cr interactions [LARE2009]. On the other hand, H_C increases from nearly 40 Oe to 46 Oe and 63 Oe with increasing Al and Cr contents, respectively. But, the rate of increase of H_C decreases with increasing the Al and Cr contents.

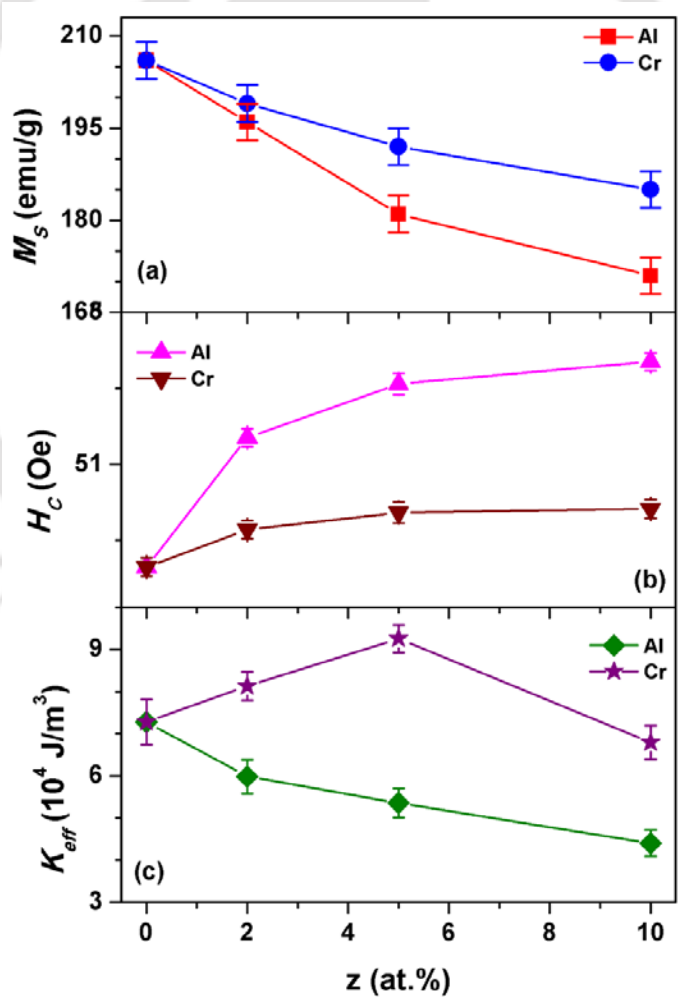

Figure 6.14. Variations of M_S, H_C and K_{eff} of 40 hours milled $Fe_{85-z}(Al,Cr)_zCo_5Si_{10}$ alloy powders.

To understand the behavior of the coercivity, the determined values of K_{eff} from the magnetization data are also plotted in Figure 6.14(c) for comparison. While the values of K_{eff} decreases progressively with increasing Al content in $Fe_{85-z}Al_zCo_5Si_{10}$ powders, the substitution of Cr in $Fe_{80-z}Cr_zCo_5Si_{15}$ increases K_{eff} almost linearly up to 5 at.% and then decreases considerably for 10 at.% Cr content. These results show that there is no close correlation exist directly between H_C and K_{eff} in these series of powders. This further confirms that there are various contributions to the coercivity behavior due to structurally sensitive properties. For example, H_C in the mechanically alloyed powders increases with increasing the values of ρ, while the reduction in D exhibits a large decrease in H_C [KALI20083, BENS2010]. These variations along with the existence of grain boundaries affect the movement of domain walls in the nanocrystalline alloys and exhibit different effective magnetic anisotropy. In the presently investigated samples, the values of D decrease and ρ increase with increasing substituting elements and the variations of K_{eff} show different behaviors with substituting elements. These results propose that the variations of both D and ρ and the formation of compositional dependent grain boundaries [YOUS2014] play a crucial role on controlling the magnetic properties. Nevertheless, H_C has increased by 1.12 and 1.5 times the coercivity of the parent system. A similar variation of coercivity has been reported in Fe-Ni based alloys [DUSW2005], Fe-Ni based alloys [BAHR2013] and Fe-Co-Si alloys [YOUS2014]. These results suggest that the variation of magnetic properties in nanocrystalline materials strongly depends not only on the composition, but also on the alloying mechanism and resulting structural parameters.

6.5. Summary:

In this chapter, we have presented the structural and magnetic properties of nanocrystalline $Fe_{95-x-z}(Al,Cr)_zCo_5Si_x$ (x = 10 and 15, z = 0 – 10) alloy powders prepared by mechanical alloying process in a planetary ball mill as a function of Al and Cr substitution. The following features of the quaternary alloys could be drawn:

- The formation of non-equilibrium α-Fe(Al,Co,Si) and α-Fe(Cr,Co,Si) solid solution could be obtained for all the $Fe_{95-x-z}(Al,Cr)_zCo_5Si_x$ (x = 10 and 15, z = 0 – 10) samples within 40 hours of milling carried out under 600 rpm speed.
- The evolution of nanocrystalline microstructure was confirmed through XRD and TEM studies. The average crystallite size decreases with increasing Al and Cr contents, but

the amount of decrease depends on the parent system. The dislocation density, found to be on the order of $10^{17}m^{-2}$, increases considerably with increasing both Al and Cr contents.

- The lattice constant increases slowly in as-milled $Fe_{95-x-z}(Al,Cr)_zCo_5Si_x$ (x = 10 and 15, z = 0 – 10) powders with increasing Al and Cr substitution. The amount of increase in the lattice constant is significantly low as compared to Fe-Cr and Fe-Al binary alloys due to the compositional dependent dissolution process and grain boundaries in multicomponent alloys.
- While the Al substitution decreases the M_S almost linearly, the substitution of Cr in $Fe_{95-x-z}(Al,Cr)_zCo_5Si_x$ (x = 10 and 15, z = 0 – 10) decreases the M_S largely due to the formation of various types of exchange interactions.
- The coercivity of the milled powder strongly depends on the compositions and varies at different rates for Al and Cr substitution. The evolution of the coercivity was explained on the basis of different phenomena such as dislocation density, grain refinement, and compositional dependent grain boundary formation. No direct correlation between K_{eff} and coercivity was obtained for all the investigated samples due to the different contributions from grain size, dislocation density and compositional dependent grain boundaries.
- The observed results show a promising approach to reduce average crystallite size considerably in the as-milled nanocrystalline alloys by proper choice of substituting elements.

Chapter 7

Effect of annealing on the properties of $Fe_{80-z}(Al,Cr)_zCo_5Si_{15}$ nanocrystalline alloy powders

7.1. Introduction:

From the last few chapters, it is obvious that mechanical alloying technique is a powerful tool to synthesize nanocrystalline alloys of desired composition with tunable structural and magnetic properties. Formation of solid solution could be achieved over a wide composition range in binary Fe-Si alloys. However, the saturation magnetization (M_S) decreased due to Si addition and coercivity (H_C) increased due to strain induced by the mechanical alloying process. Although the substitution of Co in $Fe_{100-x-y}Co_ySi_x$ alloy powders helped to improve M_S, H_C of as-milled powders was also found to increase considerably. Therefore, to obtain nanocrystalline microstructure with refined crystallites, the substitution of fourth elements such as Al and Cr in selected $Fe_{95-x-z}(Al,Cr)_zCo_5Si_x$ (x = 10 and 15, z = 0 – 10) alloy powders was investigated. While the average crystallite size was reduced successfully well below 10 nm by the substituting elements in $Fe_{95-x-z}(Al,Cr)_zCo_5Si_x$ (x = 10 and 15, z = 0 – 10) alloy powders, H_C of powders was still found to be high with a strong dependent on the composition. This is mainly due to the strain induced through dislocations in fine crystallites and compositional dependent grain boundary formation. Hence, to improve the magnetic properties of as-milled powders, appropriate heat treatment at elevated temperatures is inevitable to relax the strain and thereby reducing H_C to improve the soft magnetic properties of mechanically alloyed powders. However, heat treatment at elevated temperatures can induce grain growth, which in turn affects the soft magnetic properties [ZUOB2005], and induce structural modifications including the formation of new and undesired crystalline phases. Therefore, optimization of annealing process for the as-milled powders at selected temperatures and durations is essential to understand the correlation between modification of microstructure with annealing and the resulting magnetic properties. Thus, in this chapter, the effect of optimized annealing on the nanocrystalline microstructure and the resulting magnetic properties of $Fe_{80-z}(Al,Cr)_zCo_5Si_{15}$ alloy powders is presented.

7.2. Experimental details:

Samples corresponding to the composition of $Fe_{80-z}(Al,Cr)_zCo_5Si_{15}$ with z = 0, 2, 5 and 10 prepared by 40 hours of milling under 600 rpm in a planetary ball mill were taken for the annealing (heat treatment) studies. A resistive tubular furnace (Okay, India) having the capability of annealing up to 1600 °C was used to anneal the as-milled powders. As the heat treatment of milled powders at high temperatures under ambient conditions cause oxidization, all the samples were transferred into evacuated silica ampoules of approximately 80 mm length

and 8 mm internal diameter prior to the heat treatment. The ampoules were pumped to the pressure below 10^{-4} Pa using vacuum pumping station consisting of diffusion and rotary pumps combination. Subsequently, flame sealing at a pressure of 10^{-4} Pa was carried out and then the silica ampules with samples inside were loaded in the furnace for annealing at intended temperatures and duration. The annealing temperature in the furnace could be controlled within ± 2 °C to the set temperature using temperature controller. After the careful optimization process, we are herewith presenting the results of the samples annealed at 500 °C and 900 °C for 5 hours duration. The structural changes engendered due to the heat treatment were investigated by using X-ray diffraction (XRD) in a high-power X-Ray diffractometer (Rigaku TTRAX III 18 kW) using Cu-K_α radiation ($\lambda = 1.54056$ Å). The microstructure of the annealed powders was characterized using transmission electron microscope (TEM, JEOL 2100). Room temperature magnetic properties were measured using vibrating sample magnetometer (VSM, LakeShore Model 7410, USA).

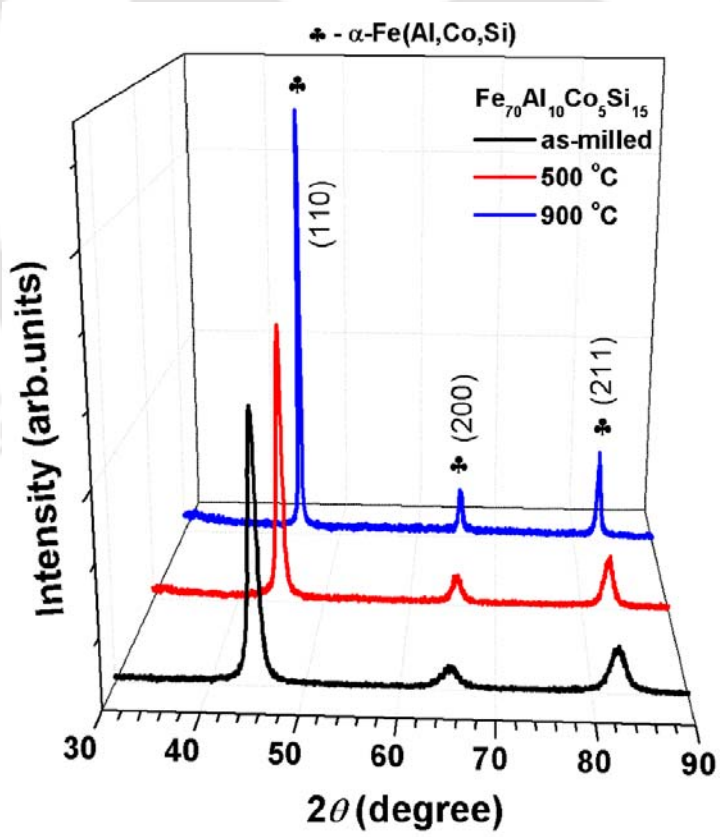

Figure 7.01. Typical room temperature XRD patterns of as-milled and annealed $Fe_{70}Al_{10}Co_5Si_{15}$ alloy powders at different temperatures.

7.3. Effect of heat treatment on the structural properties:

Figure 7.01 shows typical comparison of XRD patterns of as-milled and annealed $Fe_{70}Al_{10}Co_5Si_{15}$ alloy powders at 500 °C and 900 °C for 5 hours duration. While as-milled powder exhibits large peak broadening due to size refinement and induced strain, the powder annealed at 500 °C exhibits almost similar nature but with a slight reduction in the peak width. On further increasing the annealing temperature to 900 °C, the sample depicts not only the reduction in the broadening of the peak, but also a considerable enhancement in the peak intensity. To understand the effect of annealing systematically on the different Al and Cr substituted $Fe_{80-z}(Al,Cr)_zCo_5Si_{15}$ alloy powders, all the samples undergone heat treatment were characterized by XRD and presented in Figures 7.02 and 7.03. It is interesting to note that for the samples annealed at a particular temperature, the width of the peaks increases with increasing Al and Cr contents. This confirms that the presence of Al and Cr helps to control the growth of the crystallites in $Fe_{80-z}(Al,Cr)_zCo_5Si_{15}$ annealed powders. Furthermore, a considerable shift in the peak position is observed, which could be attributed to the atomic ordering and change in lattice constant. In order to understand the effect of annealing on the structural parameters, XRD patterns were analyzed using modified Williamson Hall Plot (MWHP) method [UNGA19991, UNGA19992] using eqn.(4.04).

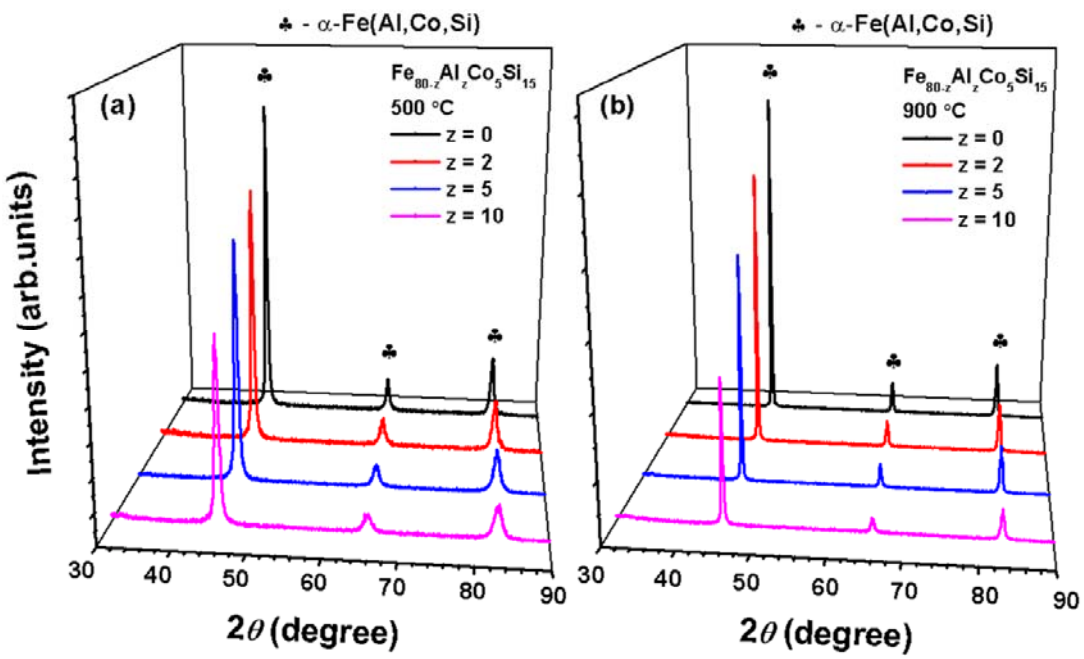

Figure 7.02. Room temperature XRD patterns of $Fe_{80-z}Al_zCo_5Si_{15}$ alloy powders annealed at different temperatures: (a) 500 °C and (b) 900 °C.

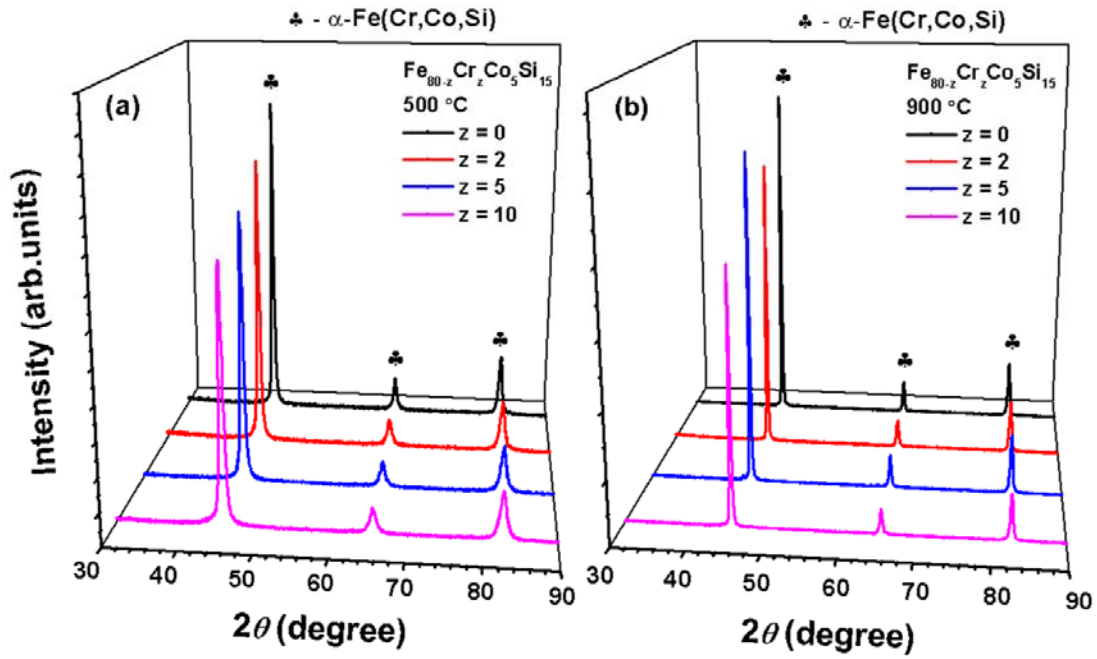

Figure 7.03. Room temperature XRD patterns of $Fe_{80-z}Cr_zCo_5Si_{15}$ alloy powders annealed at different temperatures: (a) 500 °C and (b) 900 °C.

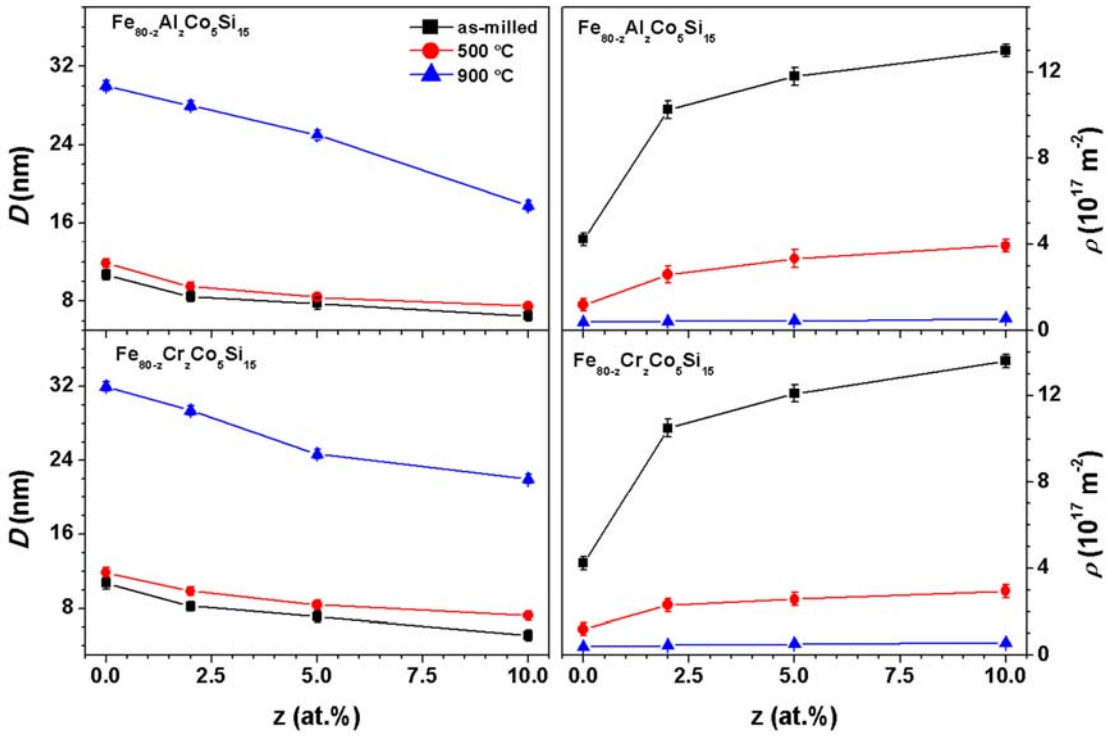

Figure 7.04. Variations of D and ρ of as-milled and annealed $Fe_{80-z}(Al,Cr)_zCo_5Si_{15}$ alloy powders as a function of Al and Cr contents. The representation of the symbols for different annealing temperatures is same in all figures.

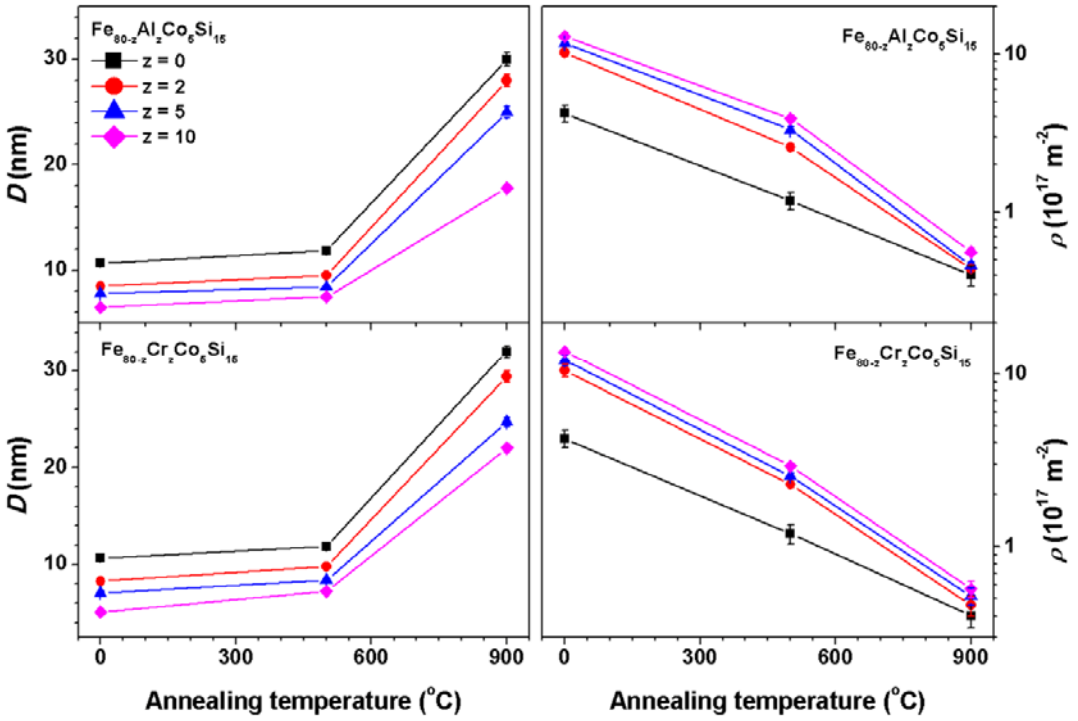

Figure 7.05. Variations of D and ρ of as-milled and annealed $Fe_{80-z}(Al,Cr)_zCo_5Si_{15}$ alloy powders as a function of annealing temperatures. The representation of the symbols for different compositions is same in all figures.

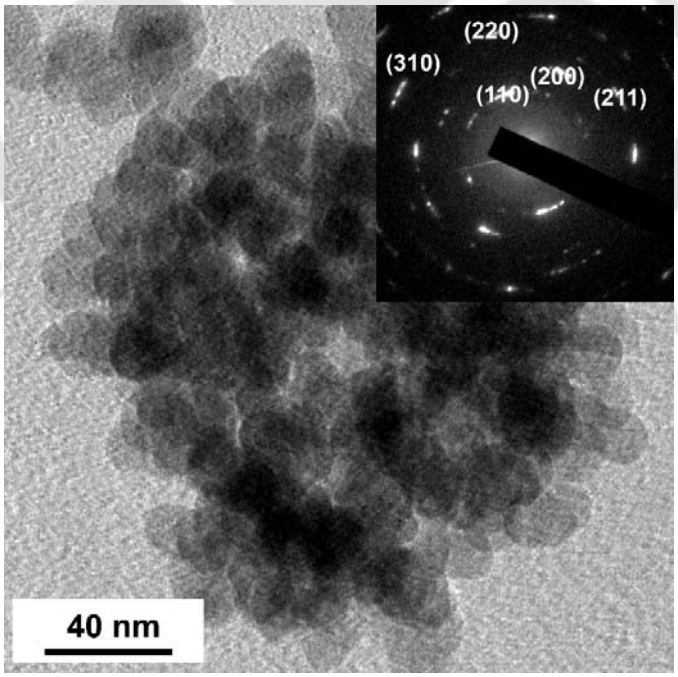

Figure 7.06. BF-TEM micrograph and SAED pattern of $Fe_{70}Al_{10}Co_5Si_{15}$ annealed powders at 900 °C.

Figure 7.04 depicts the variations of D and ρ as a function of substituting elements for the as-milled and annealed samples. In order to realize the effect of annealing temperatures, the variations of D and ρ are also plotted as a function of annealing temperatures in Figure 7.05. It is observed that (i) while the values of D increase slightly for the samples annealed at 500 °C, the samples annealed at 900 °C exhibit a large increase in the D values up to a maximum of 32 nm. Interestingly, the values of D decrease with increasing the substituting elements for the samples annealed at a particular temperature. For example, the values of D decrease from 30 nm to 18 nm and 32 nm to 22 nm for Al and Cr substituted $Fe_{70}(Al,Cr)_{10}Co_5Si_{15}$ samples annealed at 900 °C, respectively. (ii) On the other hand, the values of ρ decrease largely for the samples annealed at 500 °C due to the strain relaxation. On further increasing the annealing temperature to 900 °C, ρ decreases further down by one order. In order to confirm the grain growth of the crystallites, TEM micrographs were obtained. Figure 7.06 depicts typical bright-field TEM (BF-TEM) micrograph and selected area electron diffraction (SAED) pattern for $Fe_{70}Al_{10}Co_5Si_{15}$ sample annealed at 900 °C. BF-TEM micrograph confirms the existence of clear grain structure with the average grain size of about 18.5 nm. The rings present in SAED pattern reveal a nanocrystalline microstructure and match with the Bragg reflections in the XRD patterns. The values of average crystallite size and lattice constant calculated from TEM analysis show a close agreement with those obtained from the XRD data. These results clearly confirm that (i) the substitution of Al and Cr in $Fe_{80-z}(Al,Cr)_zCo_5Si_{15}$ powders helps to control the growth of the crystallites efficiently during the annealing process. (ii) The low temperature annealing at 500 °C reduces the strain largely without much growth of the crystallites. (iii) On the other hand, the high temperature annealing at 900 °C not only induces the growth of the crystallites substantially, but also reduces the strain further from the as-milled powders. These two processes are expected to show sizeable changes in the magnetic properties of the annealed powders. In order to understand the change in the magnetic properties, room temperature M-H loops were measured using VSM and the results are discussed in next section.

7.4. Effect of heat treatment on the magnetic properties:

Figures 7.07 and 7.08 depict room temperature M-H loops of annealed $Fe_{80-z}Al_zCo_5Si_{15}$ and $Fe_{80-z}Cr_zCo_5Si_{15}$ (z = 0, 2, 5 and 10) alloy powders at 500 °C (a) and 900 °C (b), respectively. The M-H loops are typical of soft magnetic materials. To understand the effect of annealing on the magnetic parameters, we have extracted values of H_C from the M-H loops and determined the M_S using power series fitting as described in eqn.(4.09).

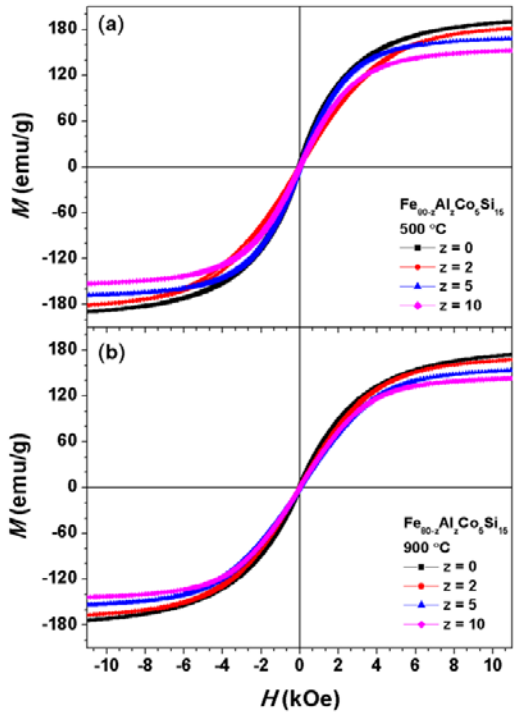

Figure 7.07. Room temperature $M - H$ loops of $Fe_{80-z}Al_zCo_5Si_{15}$ alloy powders annealed at different temperatures: (a) 500 °C and (b) 900 °C.

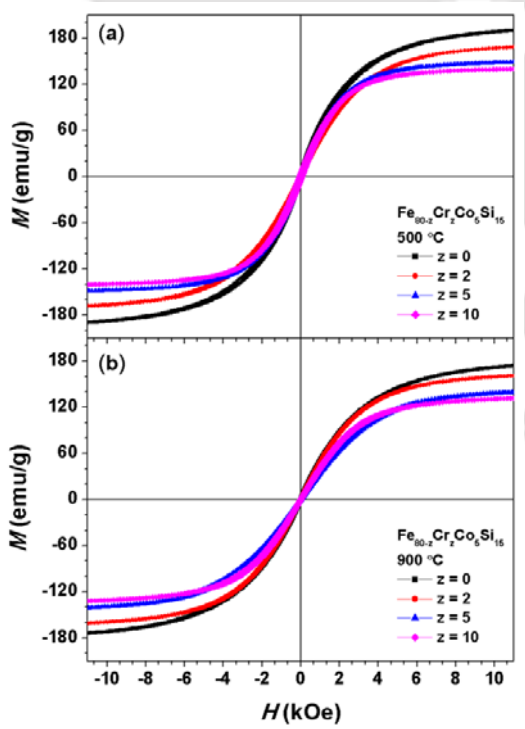

Figure 7.08. Room temperature $M - H$ loops of $Fe_{80-z}Cr_zCo_5Si_{15}$ alloy powders annealed at different temperatures: (a) 500 °C and (b) 900 °C.

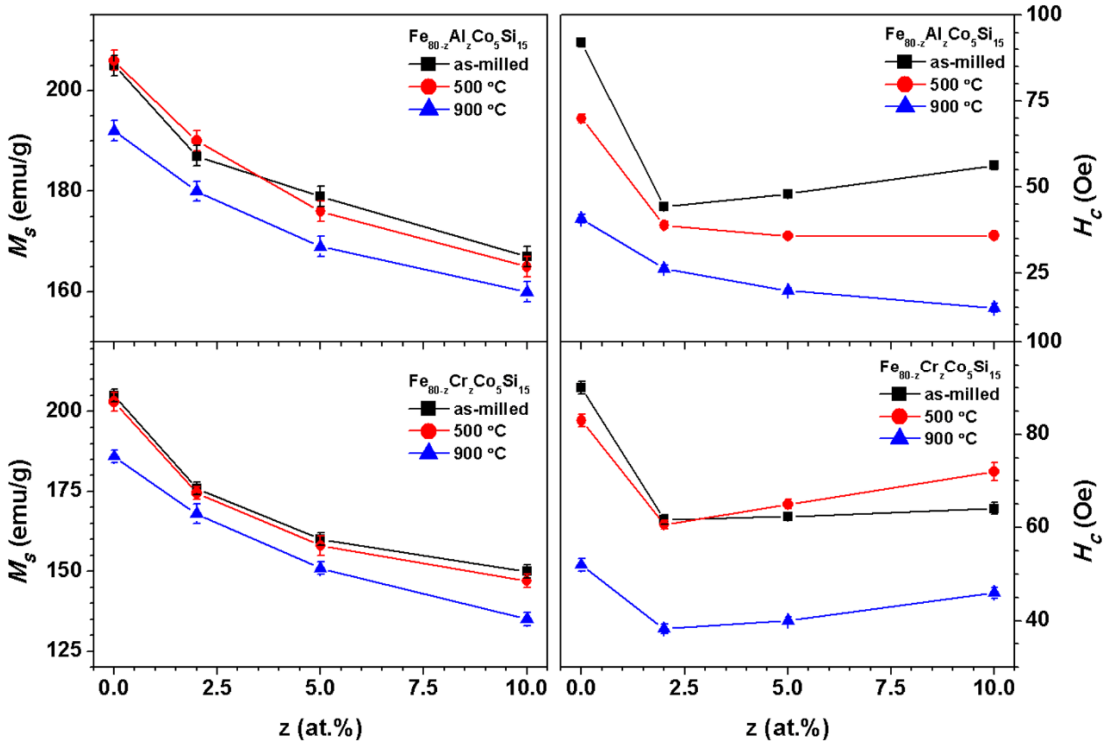

Figure 7.09. Variations of M_S and H_C of as-milled and annealed $Fe_{80-z}(Al,Cr)_zCo_5Si_{15}$ alloy powders at different temperatures.

Figure 7.09 displays the variations of M_S and H_C as a function of substituting elements for all samples. It is observed that (i) the M_S of the as-milled samples decreases from 205 emu/g to 167 emu/g and 147 emu/g for Al and Cr substituted $Fe_{80-z}(Al,Cr)_zCo_5Si_{15}$ alloy powders, respectively. (ii) With increasing the annealing temperature to 500 °C, the values of M_S show a weak change or almost no change as compared to as-milled powders. This could be probably due to the release of strain accumulated in the as-milled powders without much crystallite growth as shown in Figure 7.04. (iii) On the other hand, the samples annealed at 900 °C exhibit a significant decrease of magnetization for all the compositions. This might be correlated to occurrence of atomic ordering [CABL1977, KALI20082, ZHOU2008]. On the other hand, H_C of the Al and Cr substituted $Fe_{80-z}(Al,Cr)_zCo_5Si_{15}$ as-milled powders has been observed to be in the range of 90 Oe to 56 Oe and 90 Oe to 64 Oe, respectively. Such high H_C is mainly attributed to the different contributions such as dislocation density, grain refinement and compositional dependent grain boundary formation as discussed in Chapter 6. With increasing the annealing temperature, a significant decrease in H_C has been observed for all the samples, except for the $Fe_{80-z}Cr_zCo_5Si_{15}$ samples annealed at 500 °C, which show a slight increase in H_C

at higher Cr substitution. However, the relative decrease in coercivity with increasing annealing temperature strongly depends on the Al and Cr content in $Fe_{80-z}(Al,Cr)_zCo_5Si_{15}$ annealed powders.

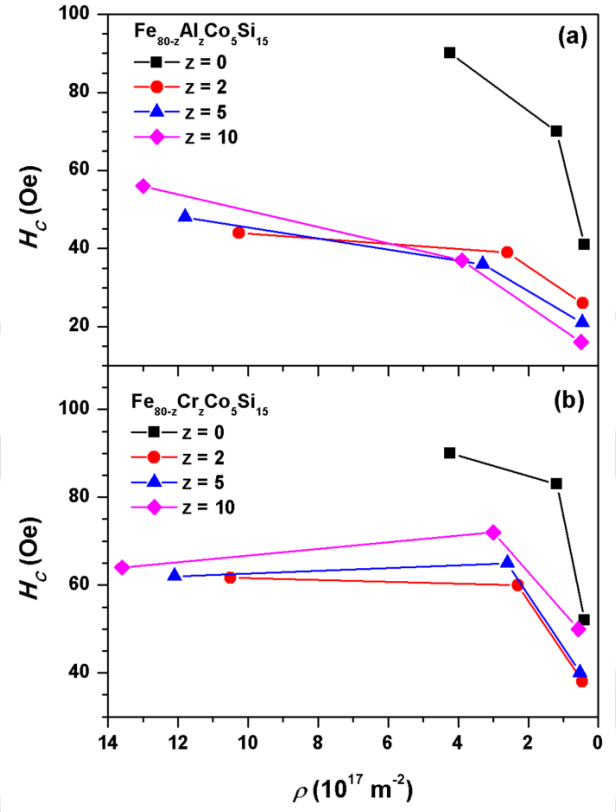

Figure 7.10. Variations of H_C as a function of ρ for $Fe_{80-z}(Al,Cr)_zCo_5Si_{15}$ alloy powders.

In order to understand the observation variation of H_C with annealing temperatures, H_C has been plotted as a function of average dislocation density in Figure 7.10 for $Fe_{80-z}(Al,Cr)_zCo_5Si_{15}$ samples with different Al and Cr contents. According to Neel's theory [NEEL1946], H_C of the mechanically alloyed powders is expected to be proportional to ρ when the magnetostatic energy is higher than the anisotropy energy. However, we have not observed a linear variation of H_C in the presently investigated samples. There exists a compositional dependent non-linear variation of H_C with ρ. While the annealed samples without Al and Cr substitution exhibit large variation of H_C with dislocation density, the relative decrease in H_C with ρ in Al and Cr substituted $Fe_{80-z}(Al,Cr)_zCo_5Si_{15}$ samples is reduced significantly. This could be attributed to the difference in the relaxation behavior and enhancement in the grain growth which reduces the density of dislocations in the annealed samples. It may be noted that amongst all samples of the present investigation, $Fe_{70}Al_{10}Co_5Si_{15}$ powders annealed at 900 °C

yielded the lowest value of H_C of 14 Oe and moderate M_S of 160 emu/g. Kalita et al. [KALI20082] reported that $Fe_{75}Si_{15}Al_{10}$ sample prepared by mechanical alloying process and annealed at 950 °C exhibited the lowest H_C of 9 Oe, but with the low M_S value of 85 emu/g. A comparison between these data reveals that although the existence of Co increases H_C of the samples from 9 to 14 Oe, the magnetization of the sample increases almost double, i.e., from 85 emu/g to 160 emu/g. This reveals that the choice of the substitution element is very much important on tuning the soft magnetic properties of the Fe-Si based nanocrystalline alloys.

7.5. Summary:

We have presented the effect of annealing on the structural and magnetic properties of nanocrystalline $Fe_{80-z}(Al,Cr)_zCo_5Si_{15}$ (z = 0 – 10) alloy powders prepared by mechanical alloying process in a planetary ball mill as a function of Al and Cr substitution and annealing temperatures in this chapter. The following features of the annealed samples could be drawn:

- Annealing of mechanically alloyed as-milled powders at elevated temperatures has significant effects on their structure and soft magnetic properties.
- Upon annealing, the average crystallite size increases and dislocation density decreases with increasing annealing temperatures. Furthermore, the substitution of Al and Cr in $Fe_{80-z}(Al,Cr)_zCo_5Si_{15}$ powders helps to control the crystallite growth efficiently during annealing process.
- The average magnetization decreased slightly after annealing which could be attributed to the atomic ordering. Coercivity of the samples has been observed to be dominated by the dislocation density.
- Although annealing causes considerable improvement of the soft magnetic properties of the mechanically alloyed $Fe_{80-z}(Al,Cr)_zCo_5Si_{15}$ powders, the residual defects present in the annealed powders result the coercivity of 14 to 40 Oe in the mechanically alloyed powders.
- Systematic correlations between structural and magnetic properties have been observed for these annealed $Fe_{80-z}(Al,Cr)_zCo_5Si_{15}$ powders prepared by mechanical alloying process. However, the structural and magnetic parameters are strongly dependent on the alloy composition.
- $Fe_{70}Al_{10}Co_5Si_{15}$ powders annealed at 900 °C yielded the lowest coercivity of 14 Oe among the powders studied in this work and moderate magnetization of 160 emu/g.

This could be attributed to optimum nanocrystalline microstructure with fine crystallites of about 18 nm with reduced dislocation density by the annealing process.

- The observed results show a promising approach to control the growth of the average crystallite size efficiently in the annealed nanocrystalline alloys by proper choice of suitable substituting elements and to improve the soft magnetic properties of mechanically alloyed Fe-Si based nanocrystalline alloys.

Chapter 8

Summary and scope for future work

The overall summary of the salient results obtained on the structural and magnetic properties of (a) $Fe_{100-x}Si_x$ ($5 \leq x \leq 50$) binary alloys, (b) $Fe_{100-x-y}Co_ySi_x$ ($x = 10$ and 15, $y = 0 – 20$) ternary alloys (c) $Fe_{95-x-z}(Al,Cr)_zCo_5Si_x$ ($x = 10$ and 15, $z = 0 – 10$) quaternary alloys and (d) annealed quaternary alloys of $Fe_{80-z}(Al,Cr)_zCo_5Si_{15}$ with $z = 0 – 10$ is listed in this chapter. Highlights of the current investigations and the possibilities for future work are also summarized below:

8.1. Summary of the results:

Nanocrystalline $Fe_{100-x}Si_x$ ($5 \leq x \leq 50$) binary alloys, $Fe_{100-x-y}Co_ySi_x$ ($x = 10$ and 15, $y = 0 – 20$) ternary alloys and $Fe_{95-x-z}(Al,Cr)_zCo_5Si_x$ ($x = 10$ and 15, $z = 0 – 10$) quaternary alloys with the formation of body centered cubic non-equilibrium solid solutions of α-Fe(Si), α-Fe(Co,Si), α-Fe(Al,Co,Si) and α-Fe(Cr,Co,Si), respectively were synthesized by mechanical alloying of elemental powders of appropriate compositions. All the mechanical alloying process was done using a planetary ball mill under high purity Ar gas atmosphere. A systematic study of the evolution of structure and magnetic properties of the binary, ternary and quaternary alloy powders was carried out to understand the milling characteristics and effect of the substituting elements. The as-milled $Fe_{80-z}(Al,Cr)_zCo_5Si_{15}$ with $z = 0 – 10$ quaternary alloys powders were subsequently heat treated at elevated temperatures under high vacuum conditions in a furnace and the changes occurring in the structure and magnetic properties of the annealed powders were evaluated.

Structural evolution during the course of milling was analyzed using Williamson-Hall plot and Modified Williamson-Hall plot methods. It has been observed that the modified Williamson-Hall method used for the estimation of average crystallite size and dislocation density from the broadening of X-ray reflections of the mechanically alloyed powders was found to be more applicable as compared to the conventional Williamson-Hall plot method for the presently investigated samples. During the milling process, the average crystallite size of the powders decreases gradually to the order of around 10 nm while the average dislocation density increases to the order of 10^{17} m^{-2} for the milling time period of above 30 hours. Further, the alloying of Fe and Si has been found to be nearly complete with formation of non-equilibrium solid solutions of α-Fe(Si). However, the milling time required for forming the non-equilibrium solid solution increases with increasing Si content. This is mainly due to the delay in the dissolution of Si in Fe matrix under the present preparation conditions. Occurrence of atomic disorder during the milling process has been evidenced from the changes of the lattice constant and saturation magnetization of the powders. The coercivity of the powders

increased with increasing milling time periods, which has been understood as a consequence of large amount of dislocations and particle size refinement during the course of milling. The presence of dislocations and grain boundaries increases the possibility of domain wall pinning in the milled samples. High Curie temperature of the powders as compared to melt-spun ribbons of similar compositions has been attributed to the excessive internal strain in the milled powders. Curie temperature decreases at a rate of 1.45 K per at.% Si with increasing Si in Fe-Si solid solution. Though the correlation between the structure and magnetic properties of Fe-Si powders has been found to be similar, the structural and magnetic parameters of each set of samples are distinctly different and strongly dependent on the alloy compositions.

To improve soft magnetic properties such as saturation magnetization and Curie temperature, Co substituted $Fe_{100-x-y}Co_ySi_x$ alloy powders were prepared using planetary ball milling and then characterized. The formation of non-equilibrium α-Fe(Co,Si) solid solution could be obtained for all the $Fe_{100-x-y}Co_ySi_x$ (x = 10 and 15, y = 0 – 20) samples within 40 hours of milling under the milling speed of 600 rpm. The lattice constant was increasing with increasing Co content up to 10 at. % due to the substitution of Co in Fe matrix and then decreases with increasing Co above 10 at.%. The amount of decrease in lattice constant strongly dependent on the Si content. This was attributed to the delay in the dissolution of Co into Fe lattice by the introduction of more Si. The average crystallite size was found to be in the range of 7 to 11 nm, but increases initially up to 10 at.% Co substitution and then decreases with the further increase in Co content. On the other hand, the dislocation density is found to be of the order of $10^{17}m^{-2}$, but decreases slightly with increasing Co substitution up to 10 at.% and then increases for high Co content. The fraction of grain boundaries also exhibits a similar variation as that of dislocation density with increasing Co content. However, the amount of variation strongly depends on the Si content. The substitution of Co in $Fe_{100-x-y}Co_ySi_x$ increases both saturation magnetization and coercivity due to atomic ordering. Thermomagnetization studies at high temperatures revealed that Curie temperature increases at a rate of 4 K per at.% Co for the Co substitution up to 10 at.%, but the rate of increase in Curie temperature drops down to 1.4 K per at.% Co for higher Co substitution. Furthermore, the crystallization temperature decreases with increasing Co content resulting an increase in magnetization data at high temperature with increasing Co content above 5 at.%. A systematic correlation between structural and magnetic properties has been observed for these Fe-Co-Si alloys and the variation of structural and magnetic parameters has been found to be dependent on the alloy composition.

In order to refine the average crystallite size in the nanocrystalline microstructure and to improve the soft magnetic properties, the influence of additional substitutional elements like Al and Cr on the control of nanocrystalline microstructure and resulting magnetic properties of nanocrystalline $Fe_{95-x-z}(Al,Cr)_zCo_5Si_x$ alloy powders prepared by mechanical alloying process were investigated. The formation of non-equilibrium α-Fe(Al,Co,Si) and α-Fe(Cr,Co,Si) solid solution could be obtained for all the $Fe_{95-x-z}(Al,Cr)_zCo_5Si_x$ (x = 10 and 15, z = 0 – 10) samples within 40 hours of milling carried out under 600 rpm speed. The average crystallite size decreases down to about 6 nm and the dislocation density increases with increasing Al and Cr contents. But the amount of variations depends on the parent system. Although the lattice constant increases with increasing Al and Cr content, the actual variation of lattice constant is significantly low as compared to their binary counter parts due to the compositional dependent dissolution process. While the Al substitution decreases the M_S almost linearly, the substitution of Cr in $Fe_{95-x-z}(Al,Cr)_zCo_5Si_x$ alloy powders decreases the M_S largely due to the formation of various types of exchange interactions. The coercivity behavior of the quaternary alloys depends on the density of dislocations, grain refinement and compositional dependent grain boundary formation, resulting no direct correlation between coercivity and effective magnetic anisotropy as observed for nanocrystalline alloys prepared by melt spun technique. The observed results show a promising approach to reduce average crystallite size considerably in the as-milled nanocrystalline alloys by proper choice of suitable substituting elements.

In order to release the strain in the as-milled nanocrystalline alloy powders and to improve the soft magnetic properties, the effect of annealing on the structural and magnetic properties of nanocrystalline $Fe_{80-z}(Al,Cr)_zCo_5Si_{15}$ (z = 0 – 10) alloy powders has been investigated. Annealing of mechanically alloyed as-milled powders at elevated temperatures has significant effects on their structure and soft magnetic properties. Upon annealing, the average crystallite size increases and dislocation density decreases with increasing annealing temperatures. Furthermore, the substitution of Al and Cr in $Fe_{80-z}(Al,Cr)_zCo_5Si_{15}$ powders helps to control the crystallite growth efficiently during annealing process. The average magnetization decreased slightly after annealing due to atomic ordering. Coercivity of the samples has been observed to be dominated mainly by the dislocation density. Although annealing causes considerable improvement of the soft magnetic properties of the mechanically alloyed $Fe_{80-z}(Al,Cr)_zCo_5Si_{15}$ powders, the residual defects present in the annealed powders result the coercivity of 14 to 40 Oe in the mechanically alloyed powders. Systematic correlations

between structural and magnetic properties have been observed for these annealed $Fe_{80-z}(Al,Cr)_zCo_5Si_{15}$ powders, but the structural and magnetic parameters are strongly dependent on the alloy composition. $Fe_{70}Al_{10}Co_5Si_{15}$ powders annealed at 900 °C yielded the lowest coercivity of 14 Oe among the powder samples studied in this work and moderate magnetization of 160 emu/g in the mechanically alloyed quaternary alloys. This improvement could be attributed to optimum nanocrystalline microstructure with fine crystallites of about 18 nm with reduced dislocation density by the annealing process. Although the observed results has shown a promising approach to control the growth of the average crystallite size efficiently in the annealed nanocrystalline alloys by proper choice of suitable substituting elements and had improved the soft magnetic properties of mechanically alloyed Fe-Si based nanocrystalline alloys, the dislocation density introduced during the milling could not be entirely relieved by the annealing process.

The present studies have brought out several interesting results which contribute to the understanding of the evolution of magnetic properties of Fe-Si based alloy powders during milling and subsequent heat treatment. These studies have also revealed the strong correlation between structure and magnetic properties of Fe-Si and Fe-Si based alloy powders as well as the possibility of improving the soft magnetic properties of mechanically alloyed Fe-Al-Co-Si powders by proper choice of substituting elements and optimum annealing conditions.

8.2 Scope for future work:

The present investigations on as-milled and annealed powders of Fe-Si based alloys have revealed that there are several aspects of interest in these materials. A study of the local atomic environment of Fe in powders milled for various time periods would help in understanding (i) the mixing of substituting elements such as Si, Co, Al and Cr in Fe and (ii) the manner in which Si enter in Fe matrix for binary alloys and Si, Co, Al or Cr enter in Fe matrix for quaternary alloys while forming the solid solution. This would help in understanding the competition between the Si and other substituting elements in the dissolution process. Mössbauer studies on the disordered and ordered Fe-Si, Fe-Co-Si and Fe-(Al,Cr)-Co-Si powders would reveal the magnetic interactions in these structures and might provide insights on reducing the magnetic hardening in these powders. Field cooled and zero field cooled low temperature investigations of these powders would also help in the understanding of the nature of the magnetically ordered and disordered phases at low temperatures. $Fe_{70}Al_{10}Co_5Si_{15}$ powders annealed at 900 °C yielded the lowest coercivity of 14 Oe among the powders studied in this work and moderate

magnetization of 160 emu/g in the mechanically alloyed quaternary alloys. Although this is found to be one of the challenging results, the obtained behaviors suggest that the fine tuning of composition in quaternary alloys and optimization of milling and annealing conditions may help in further improving the soft magnetic properties of mechanically alloyed Fe-Al-Co-Si powders. Rapid annealing or microwave annealing may help in reducing the growth of the average crystallite size increased during the annealing process. Additionally, it is worthy to investigate green compacted and sintered pellets of the above powders towards developing materials better suited for applications.

References

[AGUI2009] Aguilar C, Martinez V, Navea L, Pavez O, Santander M, J. Alloys Compd. 471 (2009) 336.

[AGUI2010] Aguilar C, Ordonezb S, Guzmanc D, Rojasd P.A, J. Alloys Compd. 504 (2010) 102.

[ALBA1987] Albanese-Kotar N.F, Mikkola D.E, Mater. Sci. Eng. 91 (1987) 233.

[ALBE1978] Alben R, Becker J.J, Chi M.C, J. Appl. Phys. 49 (1978) 1653.

[AZZA2006] Azzaza S, Alleg S, Moumeni H, Nemamcha A.R, Rehspringer J.L, Greneche J.M, J. Phys.: Condens. Matter 18 (2006) 7257.

[BAHR2006] Bahrami A, Hosseini H.R.M, Abachi P, Miragheai S, Mater. Lett. 60 (2006) 1068.

[BAHR2013] Bahrami A.H, Ghayour H, Sharafi S, Powder Tech. 249 (2013) 7.

[BARR1900] Barrett W.F, Brown W, Hadfild R.A, Sci. Trans. R. Dublin Soc. 7 (1900) 7.

[BECK1991] Beckman O, Lundgren L, In: Handbook of Magnetic Materials, Buschow K. H. J (Edt.), Vol. 6, Elsevier, Amsterdam (1991) 181.

[BENS2009] Bensebaa Z, Bouzabata B, Otmani A, J. Alloys Compd. 469 (2009) 24.

[BENS2010] Bensebaa Z, Bousabata B, Otmani A, Djekoun A, Kihal A, Greneche J. M, J. Magn. Magn. Mater. 322 (2010) 2099.

[BERK1969] Berkowitz A.E, Kneller E, Magnetism and Metallurgy, Academic Press, New York (1969).

[BITO1997] Bitoh T, Makino A, Hatanai T, Inoue A, J. Appl. Phys. 81 (1997) 4634.

[BLAN2006] Blanco D.M, Gorria P, Blanco J.A, J. Magn. Magn. Mater. e339 - e341 (2006) 300.

[BLOC1932] Bloch F, Z. Phys. 74 (1932) 295.

[BLUN2001] Blundell S, Magnetism in Condensed Matter, Oxford University Press, New York (2001).

[BOLL1983] Boll R, Hildnger H.R, IEEE Trans. Magn. 19 (1983) 1946.

[BOUK2012] Boukherroub N, Guittoum A, Souami N, Akkouche K, Boutarfaia S, EJP Web Conf. 29 (2012) 00010.

[BOZO1951] Bozorth R.M, Ferromagnetism, IEEE Press, England (1951) 77.

[BOZO1993] Bozorth R.M, Ferromagnetism, IEEE Press, New York (1993).

[BROW1940] Brown W.F, Phys. Rev. 58 (1940) 736.

[BROW1941] Brown W.F, Phys. Rev. 60 (1941) 132.

[BROW1970] Brown Jr., Brown W.F, IEEE Trans. Magn. 6 (1970) 121.

[CABL1977] Cable J.W, David L, Parra R, Phys. Rev. B 16B (1977) 1132.

[CAHN1983] Cahn R.W, Physical Metallurgy, 3rd edition, Elsevier Science Publishers, B.V. (1983).

[CARM1991] Carmona F, Gonzalez J.M, Martin A, Martin V.E, J. Magn. Magn. Mater. 101 (1991) 119.

[CHIT2011] Chitsazan B, Shokrollahi H, Behvandi A, Ghaffari M, J. Magn. Magn. Mater. 323 (2011) 1128.

[CHRI2013] Christensen R.M, The Theory of Materials Failure, Oxford University Press, Oxford (2013) 218.

[COEY1996] Coey J.M.D, Rare-Earth Iron Permanent Magnets, University Press, Oxford (1996).

[COEY2010] Coey J.M.D, Magnetism and Magnetic Materials, Cambridge university press, Cambridge (2010).

[COTT1981] Cottrell A.H, The Mechanical Properties of Matter, Krieger, FL (1981).

[CULL1972] Cullity B.D, Introduction to Magnetic Materials, Addison-Wesley, Reading, Massachusetts (1972).

[CULL2001] Cullity B.D, Stock S.R, Elements of X-ray diffraction, 3rd Ed., Pearson Education, Boston (2001).

[CZIC2006] Czichos H, Saito T, Smith L, Springer Handbook of materials measurement methods, Springer, Germany (2006).

[DAVI1987] Davis R.M, Koch C.C, J. Mater. Sci. Eng. 21 (1987) 305.

[DEME2013] Demetrio K.B, Klein A.N, Schaeffer L, Consoni D.R, Martinelli A.E, Bendo T, Mater. Res. 16 (2013) 1030.

[DILL1963] Dillon J.F, In: Magnetism III, Rado G.T, Shul H (Edts.), Vol.3, Academic Press, New York (1963).

[DING2001] Ding J, Li Y, Chen L.F, Deng C.R, J. Alloys Compd. 314 (2001) 262.

[DUSW2005] Du S.W, Ramanujan R.V, J. Magn. Magn. Mater. 292 (2005) 286.

[ESCO1991] Escorial A.G, Adeva P, Cristina M.C, Martin A, Carmona F, Cebollada F, Martin V.E, Leonato M, Mater. Sci. Eng. A 134 (1991) 1394.

[FALL1936] Fallot M, Ann. Physique 6 (1936) 305.

[FECH1992] Fecht H.J, Nanostruct. Mater. 11 (1992) 125.

[FECH2004] Fechova E, Kollar P, Fuzer J, Kovac J, Petrovic P, Kavekansky V, Mater. Sci. Eng. B 107 (2004) 155.

[FISH1990] Fish G.E, Proceedings of IEEE 78 (1990) 978.

[FUJI1991] Fujii Y, Fujita H, Seki A, Tomida T, J. Appl. Phys. 70 (1991) 6241.

[GIRO1987] Giron S, Briones F, Vincent L.J, Phil. Mag. Part B 56 (1987) 449.

[GLEI1989] Gleiter H, Prog. Mater. Sci. 33 (1989) 233.

[GOME1993] Gomez-Polo C, Vazquez M, J. Magn. Magn. Mater. 118 (1993) 86.

[GOME2014] Gomez-Esparza C.D, Lopez F.J.B-, Rodriguez C.R.S, Guel I.E., Aquino J.A.M, Ramirez J.M.H, Sanchez R.M, J. Alloys Compd 615 (2014) S317.

[GORR1996] Gorria P, Orue I, Gubieda M.L.F, Plazaola F, Zabala N, Barandiaran J.M, J. Magn. Magn. Mater. 157-158 (1996) 203.

[GORR2005] Gorria P, Blanco D.M, Perez M.J, Blanco J.A, Smith R.I, J. Magn. Magn. Mater. 294 (2005)159.

[GORR2006] Gorria P, Blanco D.M, Iglesias R, Palacios S.L, Perez M.J, Blanco J.A, Barquín L.F, Hernando A, Gonzalez M.A, J. Magn. Magn. Mater. 300 (2006) 229.

[GORR2009] Gorria P, Blanco D.M, Perez M.J, Blanco J.A, Hernando A, Laguna-Marco M.A, Haskel D, Souza-Neto N, Smith R.I, Marshall W.G, Garbarino G, Mezouar M, Martinez A.F, Chaboy J, Barquin L.F, Castrillon J.A.R, Alonso J.I.G, Moldovan M, Zhang J, Liobet A, Jiang J.S, Phy. Rev. B 80 (2009) 064421.

[GUES2008] Guessasma S, Fenineche N, J. Magn. Magn. Mater. 320 (2008) 450.

[GUIT2008] Guittoum A, Layadi A, Bourzami A, Tafat H, Souami N, Bourtafaia S, Lacour D, J. Magn. Magn. Mater. 320 (2008) 1385.

[HEIS1928] Heisenberg V.W, fur. Z, Phys. 49 (1928) 619.

[HERN19951] Hernando A, Navarro I, Gorria P, Phys. Rev. B 51 (1995) 3281.

[HERN19952] Hernando A, Vazquez M, Kulik T, Prados C, Phys. Rev. B 51 (1995) 3581.

[HERN1998] Hernando A, Marin P, Vazquez M, Barandiaran J.M, Herzer G, Phys. Rev. B 58 (1998) 336.

[HERN2005] Hernando A, Martin P, Lopez M, Kulik T, Verga L.K, Hadjipanayis G, Phys. Rev. B 69 (2005) 052501.

[HERZ1990] Herzer G, IEEE Trans. Magn. 26 (1990) 1397.

[HERZ1993] Herzer G, Physica Scripta T 49 (1993) 307.

[HERZ1995] Herzer G, Scr. Metall. Mater. 33 (1995) 1741.

[HERZ1996] Herzer G, Proceedings of the NATO Advanced Study Institute on Magnetic Hysteresis in Novel Materials 338 (1996) 711.

[HERZ2005] Herzer G, Properties and Applications of Nanocrystalline Alloys from Amorphous Precursors, NATO Science Series II: Mathematics, Physics and Chemistry, Idzikowski B, Svec P, Miglierini M (Edts.), Vol. 184, Kluwer Academic Publishers, Dordrecht (2005).

[HONO2002] Hono K, Prog. Mater. Sci. 47 (2002) 621.

[HUBE2009] Hubert A, Schafer R, Magnetic Domains: the Analysis of Magnetic Microstructures, Springer, New York (2009).

[HULL2001] Hull D, Bacon D.J, Introduction to Dislocations, 4th Ed., Pergamon Press, Oxford (2001).

[IDZI2005] Idzikowski B, Svec P, Miglierini M, Properties and Applications of Nanocrystalline Alloys from Amorphous Precursors, NATO Science Series, The Netherlands (2005).

[INOU2001] Inoue A, Hashimoto K, Amorphous and Nanocrystalline Materials: Preparation, Properties and Applications, Springer-Verlag, New York (2001).

[JANA1977] Janak J, Phys. Rev. B 16 (1977) 255.

[JILE1991] Jiles D, Introduction to Magnetism and Magnetic Materials, Chapman and Hall, Newyork (1991).

[JILE1997] Jiles D, Introduction to Magnetism and Magnetic Materials, Chapman and Hall, Boca Raton (1997).

[JOHN1996] Johnson M, Bloemen P, den Broeder F, de Vries J, Rep. Prog. Phys. 59 (1996) 1409.

[KALI20081] Kalita M.P.C, Perumal A, Srinivasan A, J. Magn. Magn. Mater. 320 (2008) 2780.

[KALI20082] Kalita M.P.C, Ph.D. Thesis, Indian Institute of Technology Guwahati, India (2008).

[KALI20083] Kalita M.P.C, Perumal A, Srinivasan A, J. Phys. D: Appl. Phys. 41 (2008) 165002.

[KALI20084] Kalita M.P.C, Perumal A, Srinivasan A, Pandey B, Verma H.C, J. Nanosci. Nanotechnol. 8 (2008) 4314.

[KALI2009] Kalita M.P.C, Perumal A, Srinivasan A, J. Phys. D: Appl. Phys. 42 (2009) 105001.

[KELL1987] Kelly A, Macmillan N.H, Strong Solids, Oxford Uni Press, Oxford (1987).

[KHAJ2011] Khajepour M, Sharafi S, J. Alloys Compd. 509 (2011) 7729.

[KIMS2006] Kim S.-H, Lee Y.J, Lee B.-H, Lee K.H, Narasimhan K, Kim Y.D, J. Alloys Compd. 424 (2006) 204.

[KIMY2000] Kim Y.D, Chung J.Y, Kim J, Jeon H, Mater. Sci. Eng. A 291 (2000) 17.

[KITT1949] Kittel C, Rev. Mod. Phys. 21 (1949) 541.

[KITT1956] Kittel C, Galt J.K In: Solid State Physics, Eherenreich H, Seitz F, Turnbull D (Edts.), Academic Press, New York (1956).

[KITT2004] Kittel C, Introduction to Solid state Physics, 7th Ed., Wiley, Singapore (2004).

[KOCH1993] Koch C. C, Nanostruct. Mater. 2 (1993) 109.

[KOCH2002] Koch C.C, Nanostructured materials: Processing, properties and potential applications, Noyes Publications, New York (2002).

[KOHO1994] Kohomoto O, Yamaguchi N, Mori T, J. Mater. Sci. 29 (1994) 3221.

[KOOH2008] Koohkan R, Sharafi S, Shokrollahi H, Janghorban K, J. Magn. Magn. Mater. 320 (2008) 1089.

[KRON1959] Kronmuller H, Z. Physik. 154 (1959) 574.

[KRON1987] Kronmuller H, Phys. Stat. Sol. (b) 144 (1987) 385.

[KRON1988] Kronmuller H, Durst K.-D, Sagawa M, J. Magn. Magn. Mater. 74 (1988) 291.

[KRON2003] Kronmuller H, Fahnle M, Micromagnetism and the Microstructure of Ferromagnetic Solids, Cambridge University Press, United Kingdom (2003).

[KRON2007] Kronmuller H, Parkin S, Handbook of Magnetism and Advanced Magnetic Materials, 5 Vol. set, John Wiley and Sons (2007).

[KUHR1993] Kuhrt C, Schultz L, IEEE Trans. Magn. 29 (1993) 2667.

[LAND1935] Landau L, Lifshitz E, Phys. Z. Sowjetunion 8 (1935) 153.

[LARE2009] Larentiev M.Y, Dudarev S.L, Manh D.N, J. Nucl. Mater. 386-388 (2009) 22.

[LIEB1976] Liebermann, H.; Graham, C. IEEE Trans. Magn. 12 (1976) 921.

[LIUY2006] Liu Y, Sellmyer D.J, Shindo D, Handbook of Advanced Magnetic Materials,Vol. 1 and 3, Springer Science (2006).

[LOFF1999] Loffler J.F, Braun H.B, Wagner W, J. Appl. Phys. 85 (1999) 5187.

[LOUD2011] Loudjani N, Bensebaa N, Dekhil L, Alleg S, Suñol J.J, J. Magn. Magn. Mater. 323 (2011) 3063.

[LUK1996] Lu K, Mater. Sci. Eng. R16 (1996) 161.

[LUL1998] Lu L, Lai M.O, Mechanical Alloying, Kluwer Academic, Boston (1998).

[MAGE1952] Mager A, Ann. Phys. 6 F (1952) 15.

[MAKI1994] Makino A, Suzuki K, Inoue A, Hirotsu Y, Masumoto T, J. Magn. Magn. Mater. 133 (1994) 329.

[MAKI1995] Makino A, Inoue A, Masumoto T, Mat Trans JIM 36 (1995) 924.

[MANG1978] Mangin P, Marchal G, J. Appl. Phys. 49 (1978) 1709.

[MARI2000] Marin P, Hernando A, J. Magn. Magn. 215-216 (2000) 729.

[MARI2001] Mariadassou C.D, Bessais L, Greneche J.M, Phys. Rev. B 65 (2001) 014419.

[MCHE1999] McHenry M.E, Willard M.A, Laughlin D.E, Prog. Mater. Sci. 44 (1999) 291.

[MHAD2010] Mhadhbi M, Khitouni M, Escoda L, Sunol J.J, Mater. Lett. 64 (2010) 1802.

[MILT1992] Milton O, The materials science of thin films, Academic Press, United Kingdom (1992).

[MIRA2008] Miraghaei S, Abachi P, Hosseini H.R.M, Bahrami A, J. Mater. Proc. Tech. 203(2008) 554.

[MISH2009] Mishra D, Perumal A, Saravanan P, Babu D. A, Srinivasan A, J. Magn. Magn. Mater. 321 (2009) 4097.

[MISH2010] Mishra D, Magnetic Properties of Co and Mn Substituted Fe-Zr-B Alloy Prepared by Melt Spinning and Mechanical Alloying Processes, Thesis (PhD) Indian Institute of Technology Guwahati, India (2010).

[MISH2011] Mishra D, Saravanan P, Perumal A, Srinivasan A, J. Appl. Phys. 109 (2011) 07A306.

[MOOR1984] Moorjani K, Coey J.M.D, Metallic Glasses, Elsevier, Amsterdam (1984).

[MORL2011] Morley S.A, Porter N.A, Marrows C.H, Phys. Status. Solid (RRL), 5 (2011) 429.

[MULL1994] Muller M, Mattern N, J. Magn. Magn. Mater. 136 (1994) 79.

[NEEL1946] Neel L, Annales Uni. Grenoble 22 (1946) 299.

[NEEL1951] Neel L, J. de Phys. Rad. 12 (1951) 339.

[OHAN1987] O'Handley R.C, J. Appl. Phys. 62 (1987) R15.

[OHAN2000] O'Handley R.C, Modern Magnetic Materials: Principles and Applications, Wiley, New York (2000).

[OHIT2007] Ohita M, Yoshizawa Y, Jpn. J. Appl. Phys. 46 (2007) L477.

[PANI1994] Panina L, Mohri K, Appl. Phys. Lett. 65 (1994) 1189.

[PARK1997] Park J.R, Suh S.J, Kim K.Y, Noh T.H. IEEE Trans. Magn. 33 (1997) 3799.

[PEPP2001] Pepperhoff W, Acet M, Constitution and Magnetism of Iron and its Alloys, Springer, Heidelberg (2001).

[PERE1996] Perez R.J, Huang B.L, Crawford P.J, Sharif A.A, Lavernia E. J, Nanostruct. Mater. 7 (1996) 47.

[PETR2002] Petrov Y.I, Shafranovsky E.A, Krupyanskii Y.F, Essine S.V, J. Appl. Phys. 91 (2002) 352.

[PILA2008] Pilarczyk W, Nowosielski R, Pilarczyk A, J. Achiv. Mater. Manu. Eng. 30 (2008) 141.

[RAJA2000] Raja M.M, Chattopadhyay K, Majumder B, Narayanasamy N.A, J. Alloys Compd. 297 (2000) 199.

[RODR2008] Rodriguez R.R, Alcazar G.A.P, Sanchez H, Grenecheb J.M, Microelec. Journal 39 (2008) 1311.

[SCHA2009] Schafer R, The Magnetic Microstructure of Nanostructured Materials, In: Nanoscale Magnetic Materials and Applications, Liu J.P, Fullerton E, Gutfleisch O, Sellmyer D.J (Edts.), Springer Science (2009).

[SCHI1996] Schilling P.J, He J.H, Cheng J, Ma E, Appl. Phys. Lett. 68 (1996) 767.

[SELL2006] Sellmyer D, Skomski R, Advanced Magnetic Nanostructures, Springer, New York (2006).

[SHEN1992] Shen T.D, Wang K.Y, Quan M.X, Wang J.T, J. Mater. Sci. Lett. 11 (1992) 1576.

[SHEN2005] Shen T.D, Schwarz R.B, Thompson J.D, Phys. Rev. B 72 (2005) 014431.

[SHIG1974] Shiga M, AIP Conf. Proc. 18 (1974) 463.

[SKOM1998] Skomski R, J. Appl. Phys. 83 (1998) 6503.

[SKOM19991] Skomski R, Coey J.M.D, Permanent Magnetism, Institute of Physics, Bristol (1999).

[SKOM19992] Skomski R, Coey J, Coey J.M.D, Tilley D.R, Studies in condensed matter physics, Institute of Physics, London (1999).

[SLAT1936] Slater J.C, Phys. Rev. 49 (1936) 537.

[SONG1999] Song H.W, Guo S.R, Hu Z.Q, Nanostruct. Mater. 11 (1999) 203.

[SONI2001] Soni P.R, Mechanical alloying: Fundamental and applications, Cambridge International Science Publishing, UK (2001).

[STEV1999] Stevulova N, Buchal A, Petrovic P, Tkacova K, Sepelak V, J. Magn. Magn. Mater. 203 (1999) 190.

[STON1938] Stoner E, Proc. R. Soc. A 165 (1938) 372.

[STON1993] Stoner E.C, Phil. Mag. 15 (1993) 1080.

[SUNO2008] Sunol J.J, Escoda L, Fort J, Perez J, Pujol T, Mater. Lett. 62 (2008) 1673.

[SURY2001] Suryanarayana C, Prog. Mater. Sci. 46 (2001) 1.

[SURY2004] Suryanarayana C, Mechanical alloying and Milling, Marcel Dekker, New York (2004).

[SUZU1990] Suzuki K, Kataoka N, Inoue A, Makino A, Masumoto T, Mater. Trans. JIM 31 (1990) 743.

[SUZU19911] Suzuki K, Makino A, Inoue A, Masumoto T, J. Appl. Phys. 70 (1991) 3232.

[SUZU19912] Suzuki K, Makino A, Inoue A, Kataoka N, Masumoto T, Mater. Trans. JIM 32 (1991) 93.

[SUZU1996] Suzuki K, Cadogan J.M, Sahajwalla V, Inoue A, Masumoto T, J. Appl. Phys. 79 (1996) 5149.

[SVOB2004] Svoboda J, Magnetic Techniques for the treatment of materials, Kluwer Academic Publishers, The Netherlands (2004).

[TAGH2011] Taghvaei A.H, Ebrahimi A, Ghaffari M, Janghorban K, J. Magn. Magn. Mater. 323 (2011) 150.

[UMCY2004] Um C.-Y, McHenry M.E, IEEE Trans. Magn. 40 (2004) 2724.

[UNGA19991] Ungar T, Tichy G, Physica Status Solidi A 171 (1999) 425.

[UNGA19992] Ungar T, Dragomir I, Revesz A, Borbely A, J. Appl. Cryst. 32(1999) 992.

[VARG2001] Varga L.K, Mazaleyrat F, Kovac J, Kakay A, Mater. Sci. Engg. A 304-306 (2001) 946.

[VACC1981] Vaccari J. A., Des. Eng. 52 (1981) 53.

[VISS2006] Visscher P.B, Coarse-graining and Hierarchical Simulation of Magnetic Materials: the Fast Multipole Method, In: Handbook of Advanced Magnetic Materials, Liu Y, Sellmyer D.J, Shindo D (Edts.), Springer, US (2006).

[VOJT1974] Vojtechovsky K, Zemcik T, Czech J. Phys. B 24 (1974) 171.

[WALI1994] Waliszewski J, Dobrzynski L, Malinowski A, Satula D, Szymanski K, Prandl W, Bruckel T, Scharpf O, J. Magn. Magn. Mater. 132 (1994) 349.

[WILL1953] Williamson G.K, Hall W.H, Acta Met. 1 (1953) 22.

[WITK2006] Witkin D.B, Lavernia E.J, Prog. Mater. Sci. 51 (2006) 1.

[YOSH1988] Yoshizawa Y, Oguma S, Yamauchi K, J. Appl. Phys. 64, (1988) 6044.

[YOSH2001] Yoshizawa Y, Scripta Mater. 44 (2001) 1321.

[YOUS2012] Yousefi M, Sharafi S, Mater. Design 37 (2012) 325.

[YOUS2014] Yousefi M, Sharafi S, Mehrolhosseiny A, Adv. Pow. Tech. 25 (2014) 752.

[ZENG2007] Zeng Q, Baker I, McCreary V, Yan Z, J. Magn. Magn. Mater. 318 (2007) 28.

[ZHAN2004] Zhang D.L, Prog. Mater. Sci. 49 (2004) 537.

[ZHOU1996] Zhou T, Zhang J, Xu J, Yu Z, Gu G, Wang D, Huang H , Du Y , Wang J, Jiang Y, J. Magn. Magn. Mater. 164 (1996) 219.

[ZHOU1999] Zhou T.J, Yu Z, Du Y. W, J. Magn. Magn. Mater. 202 (1999) 354.

[ZHOU2000] Zhou T.J, Yu Z, Du Y. W, Appl. Phys. A 70 (2000) 75.

[ZHOU2008] Zhou T.D, Deng L.J, Liang D.F, Acta Metall. Sin. (Eng. Lett.) 21 (2008) 191.

[ZOLL2012] Zollinger J, Adam O, Daloz D, IOP Conf. Ser.: Mater. Sci. Eng. 27 (2012) 012078.

[ZUOB2004] Zuo B, Saraswati N, Sritharan T, Hng H.H, Mater. Sci. Engg. A 371 (2004) 210.

[ZUOB2005] Zuo B, Sritharan T, Acta Mater. 53(2005) 1233.

Publications

LIST OF PUBLICATIONS:

Published:

[1]. Structural and magnetic properties of Al and Cr substituted nanocrystalline $Fe_{80}Si_{15}Co_5$ alloy powders
P. C. Shyni and A. Perumal
Physics Express (2014, Accepted and Available online).

[2]. Thermomagnetic properties of nanocrystalline Fe–Si alloys with high Si content
P.C. Shyni and A. Perumal
Physica B 448 (2014) 60.

[3]. Structural and magnetic properties of $Fe_{100-x}Si_x$ ($0 \leq x \leq 40$) nanocrystalline alloy powders
P. C. Shyni and A. Perumal
IEEE Transactions on Magnetics 50 (2014) 2101904.

[4]. Effects of composition and milling on the structural and magnetic properties of mechanically alloyed $Fe_{100-x}Si_x$ ($x = 0 – 50$) powders
P. C. Shyni and A. Perumal
Proceedings of Processing and Fabrication of Advanced Materials XXI (PFAM-21) IIT Guwahati, December 10-13, 2012.

Under communication:

[5]. Effect of annealing on the microstructural and magnetic properties of mechanically alloyed Fe-(Al,Cr)-Si-Co powders
P. C. Shyni and A. Perumal

[6]. Structural and magnetic properties of Co substituted Fe-Si alloy powders produced by mechanical milling
P. C. Shyni and A. Perumal

PAPERS PRESENTED IN CONFERENCES:

[1]. Synthesis and annealing of nanocrystalline Fe-Si-Co alloy powders
P. C. Shyni and A. Perumal

Presented in the International Conference on Magnetic Materials and Applications (ICMAGMA-2014), September 15-17, 2014, Pondicherry University, Pondicherry, India.

[2]. Magnetic properties of $Fe_{100-x-y}Co_xSi_y$ nanocrystalline powders at elevated temperatures

P. C. Shyni and A. Perumal

Presented in the International Conference on Magnetic Materials and Applications 2013 (MagMA-2013), December 5-7, 2013, IIT Guwahati, Guwahati, India.

[3]. Structural and magnetic properties of $Fe_{100-x}Si_x$ ($0 < x < 40$) nanocrystalline alloy powders

P. C. Shyni and A. Perumal

Presented in the 3rd International Symposium on Advanced Magnetic Materials and Applications (ISAMMA 2013) July 21-25, 2013, Taichung, Taiwan.

[4]. Effects of composition and milling on the structural and magnetic properties of mechanically alloyed $Fe_{100-x}Si_x$ ($x = 0 – 50$) powders

P. C. Shyni and A. Perumal

Presented in the Twenty first International Symposium on Processing and Fabrication of Advanced Materials (XXI PFAM), December 10-13, 2012, IIT Guwahati, India.

[5]. Role of nanostructure on the magnetic properties

A. Perumal, Akhilesh Kr. Singh, **P. C. Shyni**, K. Bhagaban, Anabil Gayen

Invited for presentation in National Seminar on Nanoscience and Nanotechnology, August 31-September 01, 2012, MC College, Barpeta, India.

[6]. Enhanced soft magnetic properties in multilayer structured amorphous Fe-Ta-C films

D. Mishra, Akhilesh Kr. Singh, **P. C. Shyni**, D. Sharma, and A. Perumal

Presented in International Conference on Magnetism and Magnetic Materials (55th MMM Conference), November 14-18, 2010, Atlanta, USA.

PUBLICATIONS OUTSIDE THESIS WORK:

[1]. Finite size effects in magnetic and optical properties of antiferromagnetic NiO nanoparticles

Bhagaban Kisan, **P. C. Shyni**, Samar Layek, H. C. Verma, David Hesp, Vinod Dhanak, Satheesh Krishnamurthy and A. Perumal

IEEE Transaction on Magnetics 50 (2014) 2300704.

[2]. Enhanced soft magnetic properties in multilayer structured amorphous Fe-Ta-C films

D. Mishra, Akhilesh Kr. Singh, **P. C. Shyni**, D. Sharma, and A. Perumal

Journal of Applied Physics 109 (2011) 07A304.